

The University of Saskatchewan
Department of Computer Science

Technical Report #2010-01



Stiffness analysis of cardiac electrophysiological models

Raymond J. Spiteri*

Ryan C. Dean†

Abstract

The electrophysiology in a cardiac cell can be modelled as a system of ordinary differential equations. The efficient solution of these systems is important because they must be solved many times as sub-problems of tissue- or organ-level simulations of cardiac electrophysiology. The wide variety of existing cardiac cell models encompasses many different properties, including the complexity of the model and the degree of stiffness. Accordingly, no single numerical method can be expected to be the most efficient for every model. In this report, we perform a detailed study of the stiffness properties of a range of cardiac cell models and discuss the implications for their numerical solution. The analysis of the data generated allows us to see the impact of stiffness on the performance of several numerical methods.

1 Introduction

The electrophysiological behaviour in myocardial tissue can be modelled by means of differential equations, often as a combination of ordinary and partial differential equations. Ionic currents at the myocardial cell level are described by a model consisting of ordinary differential equations (ODEs). These ionic currents are coupled via a model consisting of partial differential equations (PDEs) to describe the flow of electricity across the heart. A PDE model, such as the bidomain model, coupled with an ionic model can be used to simulate the electrical activity in the heart. For a thorough introduction, see [42] or [50].

Coupled ODE/PDE models are often solved separately via an algorithm called operator splitting. In this algorithm, the solution process alternates between solving the ODEs and the PDEs separately. In this context, the solution of each system is an important sub-problem of the overall solution process, each posing challenges to solving the overall problem efficiently. One such challenge is that the ionic model is usually a stiff, non-linear set of ODEs that must be solved for each node in the simulation. Moreover, a fine spatial discretization is required to produce useful data [54], and so another challenge is the magnitude of the system required for a realistic simulation. Inefficiencies in solving the ionic model, for example, are dramatically magnified as simulations become larger. The use of reduced, computationally inexpensive ionic models (e.g., [52]) illustrate the difficulty in efficiently performing simulations. In this study, we generate stiffness data and perform a systematic stiffness analysis of 37 verified ionic cell models from the CellML model repository [27] and show how this analysis can lead to application or design of appropriate methods for their efficient numerical solution.

*Department of Computer Science, University of Saskatchewan, Saskatoon, SK S7N 5C9. e-mail: spiteri@cs.usask.ca. This work was partially supported by grants from MITACS and NSERC.

†Department of Computer Science, University of Saskatchewan, Saskatoon, SK S7N 5C9. e-mail: rcd144@mail.usask.ca. This work was partially supported by grants from MITACS and NSERC.

A wide range of ionic models exists. Most models are based upon the Hodgkin–Huxley (HH) model for the giant squid axon [21]. The FitzHugh–Nagumo (FHN) model [17, 33], a simplification of the HH model with two ODEs, is often used as an inexpensive ionic model, albeit usually in a form modified to more accurately model cardiac action potentials; see, e.g., [4, 25, 43, 53]. Modern models, on the other hand, usually add detail to the HH model or subsequent models; e.g., the model of Iyer et al. (2004) of human left-ventricular epicardial myocytes consists of 67 ODEs. There is also variety in the type of cardiac cell modelled, including models of cells in the atria, ventricles, sinoatrial node, and Purkinje fibres, as well as in the species being modelled, e.g., human, canine, rabbit, etc.

The wide variety of ionic models has significant implications for efficiently obtaining their numerical solution. The simplest models, such as FHN, are non-stiff [50]. In such a case, the use of a non-stiff numerical method is the most appropriate to obtain a solution efficiently. Cell models more detailed than FHN tend to be stiff and require the use of a stiff numerical method to obtain a solution efficiently [50]. However, stiffness is a subtle effect and challenging to definitively characterize. The distinction between stiff and non-stiff models is not clear cut in general; it depends on aspects such as the dichotomy of the time scales involved and the accuracy required of the approximate solution. We find there is a considerable difference in the degree of stiffness across the range of ionic models even for typical accuracy requirements. For example, [29] demonstrates the marked difference in the degree of stiffness between the models of Courtemanche et al. [11] and Winslow et al. [56]. Both are stiff, detailed, second-generation models, but the most well-suited numerical method is different in each case.

In this study, we analyse the stiffness of a wide range of cardiac electrophysiological models. We examine the eigenvalues of the Jacobian of the solutions for the 37 ionic cell models considered. These eigenvalues are often related to the stiffness of the model [19], and in fact a stiff initial-value problem is sometimes defined in terms of the eigenvalues of the Jacobian, e.g., [50]. We show how this information can be used to apply or design a numerical method for a specific ionic cell model. We give special focus to numerical methods commonly used in cardiac electrophysiological simulations and demonstrate the efficiency gains that are possible through the use of eigenvalue data.

The rest of this report is organized as follows. In Section 2, we give a brief outline of ionic cell models and an overview of the particular models used in this study. In Section 3, we give a brief overview of the concept of stiffness. We also present the extreme eigenvalue data generated for the models considered and discuss the implications for model stiffness. Finally, in Section 4, we summarize the conclusions reached based on our observations.

2 Cardiac electrophysiological models

2.1 Ionic current models

Small-scale processes that occur at the level of the individual cells in the heart can be modelled using ODEs. Such models can be used to simulate the behaviour of electrical activity in an isolated cell, or, when coupled with a PDE model, can be used to provide the ionic current to tissue- or organ-level simulations. The simplest of these models are called *first-generation models*. A first-generation model contains enough detail to reproduce an action potential, but it has a simplified description of the underlying physiological details [50]. Some popular examples of first-generation models are the FHN model and the 1991 Luo–Rudy model (LR) [28]. More complex models, called *second-generation models*, contain all of the details included in

first-generation models and as many fine-scaled physiological details as possible [50]. Most modern models can be classified as second-generation models because the most useful simulations tend to require details on the finest level [50]. Although first-generation models have less detail, their advantage is that they are computationally inexpensive relative to second-generation models.

The heart consists of different types of excitable cells, each having their own properties [42]. As such, most models are suited to particular type of cell in the heart. Normally, the electrical activity in the heart is initiated by a spontaneous electrical pulse emanating from specialized tissue called the sinoatrial node. From the sinoatrial node, electricity spreads to the atrial myocardium [42]. From the atria, the activation wave spreads to the atrioventricular node, the Purkinje fibres, and, finally, to the ventricles. There are models for each of these regions of the heart. In particular, there are numerous models of the atria and the ventricles. On the other hand, there are relatively few models of the atrioventricular node; see, e.g., [42], for a detailed list of dozens of cardiac electrophysiological models classified in this way.

As an example of a first-generation model, we consider the LR model, sometimes called the Luo–Rudy Phase 1 model. The LR model describes guinea pig ventricular tissue and consists of 8 ODEs. For an individual cardiac cell, we have that the transmembrane potential, V_m , satisfies [28]

$$\frac{dV_m}{dt} = -\frac{1}{C_m}(I_{ion} + I_{st}), \quad (1)$$

where C_m is the membrane capacitance, I_{ion} is the total transmembrane ionic current, and I_{st} is the stimulus current. The LR model contains six gating variables that determine the flow of current. The evolution of each gating variable y is governed by a nonlinear ODE involving rate parameters $\alpha_y = \alpha_y(V_m)$ and $\beta_y = \beta_y(V_m)$ in the general form

$$\frac{dy}{dt} = \frac{y_\infty - y}{\tau_y}, \quad (2)$$

where

$$y_\infty = \frac{\alpha_y}{\alpha_y + \beta_y} \quad \text{and} \quad \tau_y = \frac{1}{\alpha_y + \beta_y}.$$

The range of each gating variable is $[0, 1]$. When $y = 0$, the gate is completely closed, allowing no current to flow. When $y = 1$, the gate is completely open, allowing current to flow without being inhibited by the gate [42]. The remaining ODE in the LR model describes calcium concentration in the cell:

$$\frac{d([\text{Ca}]_i)}{dt} = -10^{-4}I_{si} + 0.07(10^{-4} - [\text{Ca}]_i), \quad (3)$$

where $[\text{Ca}]_i$ is the intracellular calcium concentration and I_{si} is the slow inward calcium current [28]. The 6 gating equations of the form (2) are coupled with (1) and (3) to form the complete LR model. Full details of the model can be found in [28].

As an example of a second-generation model, we consider the model of Winslow et al. [56]. This model describes canine ventricular tissue and consists of 33 ODEs. The transmembrane potential is again given by equation (1), and there are eight gating equations in the form of equation (2).

The following equations are related to the calcium concentration:

$$\begin{aligned}
\frac{dP_{C_1}}{dt} &= -k_a^+ [\text{Ca}^{2+}]_{\text{ss}}^n P_{C_1} + k_a^- P_{O_1}, \\
\frac{dP_{O_1}}{dt} &= k_a^+ [\text{Ca}^{2+}]_{\text{ss}}^n P_{C_1} - k_a^- P_{O_1}, -k_b^+ [\text{Ca}^{2+}]_{\text{ss}}^m P_{O_1} \\
&\quad + k_b^- P_{O_2} - k_c^+ P_{O_1} + k_c^- P_{C_2}, \\
\frac{dP_{O_2}}{dt} &= k_b^+ [\text{Ca}^{2+}]_{\text{ss}}^m P_{O_1} - k_b^- P_{O_2}, \\
\frac{dP_{C_2}}{dt} &= k_c^+ P_{O_1} - k_c^- P_{C_2}.
\end{aligned}$$

The following system describes the membrane current of calcium through the L-type channels:

$$\begin{aligned}
\frac{dC_0}{dt} &= \beta C_1 + \omega C_{\text{Ca}0} - (4\alpha + \gamma) C_0, \\
\frac{dC_1}{dt} &= 4\alpha C_0 + 2\beta C_2 + \frac{\omega}{b} C_{\text{Ca}1} - (\beta + 3\alpha + \gamma a) C_1, \\
\frac{dC_2}{dt} &= 3\alpha C_1 + 3\beta C_3 + \frac{\omega}{b^2} C_{\text{Ca}2} - (2\beta + 2\alpha + \gamma a^2) C_2, \\
\frac{dC_3}{dt} &= 2\alpha C_2 + 4\beta C_4 + \frac{\omega}{b^3} C_{\text{Ca}3} - (3\beta + \alpha + \gamma a^3) C_3, \\
\frac{dC_4}{dt} &= \alpha C_3 + gO + \frac{\omega}{b^4} C_{\text{Ca}4} - (4\beta + f + \gamma a^4) C_4, \\
\frac{dO}{dt} &= fC_4 - gO, \\
\frac{dO_{\text{Ca}}}{dt} &= f' C_{\text{Ca}4} - g' O_{\text{Ca}}, \\
\frac{dC_{\text{Ca}0}}{dt} &= \beta' C_{\text{Ca}1} + \gamma C_0 - (4\alpha' + \omega) C_{\text{Ca}0}, \\
\frac{dC_{\text{Ca}1}}{dt} &= 4\alpha' C_{\text{Ca}0} + 2\beta' C_{\text{Ca}2} + \gamma a C_1 - \left(\beta' + 3\alpha' + \frac{\omega}{b} \right) C_{\text{Ca}1}, \\
\frac{dC_{\text{Ca}2}}{dt} &= 3\alpha' C_{\text{Ca}1} + 3\beta' C_{\text{Ca}3} + \gamma a^2 C_2 - \left(2\beta' + 2\alpha' + \frac{\omega}{b^2} \right) C_{\text{Ca}2}, \\
\frac{dC_{\text{Ca}3}}{dt} &= 2\alpha' C_{\text{Ca}2} + 4\beta' C_{\text{Ca}4} + \gamma a^3 C_3 - \left(3\beta' + \alpha' + \frac{\omega}{b^3} \right) C_{\text{Ca}3}, \\
\frac{dC_{\text{Ca}4}}{dt} &= \alpha' C_{\text{Ca}3} + \gamma a^4 C_4 - \left(4\beta' + f' + \frac{\omega}{b^4} \right) C_{\text{Ca}4},
\end{aligned}$$

Intracellular calcium buffering is described by

$$\begin{aligned}
\frac{d[\text{HTRPNCa}]}{dt} &= k_{\text{htrpn}}^+ [\text{Ca}^{2+}]_i ([\text{HTRPN}]_{\text{tot}} - [\text{HTRPNCa}]) \\
&\quad - k_{\text{htrpn}}^- [\text{HTRPNCa}], \\
\frac{d[\text{LTRPNCa}]}{dt} &= k_{\text{ltrpn}}^+ [\text{Ca}^{2+}]_i ([\text{LTRPN}]_{\text{tot}} - [\text{LTRPNCa}]) \\
&\quad - k_{\text{ltrpn}}^- [\text{LTRPNCa}],
\end{aligned}$$

where the k -coefficients are constants.

Finally, intracellular ionic concentrations are described by

$$\begin{aligned}
\frac{d[\text{Na}^+]_i}{dt} &= -(I_{Na} + I_{Na,b} + 3I_{NaCa} + 3I_{NaK}) \frac{A_{cap} C_{sc}}{V_{myo} F}, \\
\frac{d[\text{K}^+]_i}{dt} &= -(I_{Kr} + I_{Ks} + I_{to1} + I_{K1}, \\
&\quad + I_{Kp} + I_{Ca,K} - 2I_{NaK}) \frac{A_{cap} C_{sc}}{V_{myo} F}, \\
\frac{d[\text{Ca}^{2+}]_i}{dt} &= \beta_i \left[J_{xfer} - J_{up} - J_{trpn} \right. \\
&\quad \left. - (I_{Ca,b} - 2I_{NaCa} + I_{p(Ca)}) \frac{A_{cap} C_{sc}}{2V_{myo} F} \right], \\
\frac{d[\text{Ca}^{2+}]_{ss}}{dt} &= \beta_{ss} \left(J_{rel} \frac{V_{JSR}}{V_{myo}} - J_{xfer} \frac{V_{myo}}{V_{ss}} - I_{Ca} \frac{A_{cap} C_{sc}}{2V_{myo} F} \right), \\
\frac{d[\text{Ca}^{2+}]_{JSR}}{dt} &= \beta_{JSR} (J_{tr} - J_{rel}), \\
\frac{d[\text{Ca}^{2+}]_{NSR}}{dt} &= J_{up} \frac{V_{myo}}{V_{NSR}} - J_{tr} \frac{V_{JSR}}{V_{NSR}}.
\end{aligned}$$

We refer the reader to [56] for the remaining details.

2.2 Models used

In this study, we consider 37 different ionic models, including some that are variations of a given model. This represents a wide variety of models in terms of type of cardiac cell, species modelled, degree of stiffness, and level of detail. Model data were obtained from the CellML model repository [27]. The CellML representation of models was used to generate Matlab code via a python script. To ensure the faithfulness of the code to the model, two specific considerations were made. First, apart from one exception, we used only models considered to be faithful to the published model according to CellML’s curation guidelines, i.e., models marked with a gold star on the CellML website. The exception was for the Puglisi–Bers model [41] because we already had reliable code as part of other work [46]. Second, reference solutions were obtained with the generated Matlab code and were verified to be the same as reference solutions obtained with JSim [1], an independent software package capable of parsing CellML files.

A detailed formulation of all models is omitted for the sake of brevity. The reader is instead referred to the original model papers or to the CellML repository, which contains a concise formulation of each model. A summary of each of the models used in this study is presented in Table 1 including, for each model, the name used for it in this report, a reference to the original paper, a brief description of the model, and the number of ODEs in the model.

For each model, the set of default parameters in CellML was used. All models contain adjustable parameters; e.g., the model of Pandit et al. (2001) has a parameter that determines if the model should take into account the influence of diabetes. Because adjusting parameters to the models requires intricate knowledge of each of the model and increases the chance of human error, we did not vary any of these parameters unless separate CellML files were provided for variations on the same model. This was the case for the model of Sakmann

Table 1: Summary of models used. Three variants (endocardial cell, epicardial cell, and M-cell) exist for each of the models marked with an asterisk.

Model	Reference	ODEs	Description
Beeler–Reuter (1977)	[7]	8	Canine ventricular model
Bondarenko et al. (2004)	[9]	41	Mouse ventricular model
Courtemanche et al. (1998)	[11]	21	Human atrial model
Demir et al. (1994)	[13]	27	Rabbit sinoatrial node model
Demir et al. (1999)	[12]	29	Rabbit sinoatrial node model
DiFrancesco–Noble (1985)	[14]	16	Mammal Purkinje fibre model
Dokos et al. (1996)	[15]	18	Rabbit sinoatrial node model
Faber–Rudy (2000)	[16]	19	Guinea pig ventricular model
FitzHugh–Nagumo (1961)	[17, 33]	2	Nerve membrane model
Fox et al. (2002)	[18]	13	Canine ventricular model
Hilgemann–Noble (1987)	[20]	15	Rabbit atrial model
Hund–Rudy (2004)	[22]	29	Canine ventricular model
Jafri et al. (1998)	[23]	31	Guinea pig ventricular model
Luo–Rudy (1991)	[28]	8	Guinea pig ventricular model
Maleckar et al. (2008)	[30]	30	Human atrial model
McAllister et al. (1975)	[32]	10	Canine Purkinje fibre model
Noble (1962)	[34]	4	Mammal Purkinje fibre model
Noble–Noble (1984)	[35]	15	Rabbit sinoatrial node model
Noble et al. (1991)	[36]	17	Guinea pig ventricular model
Noble et al. (1998)	[37]	22	Guinea pig ventricular model
Nygren et al. (1998)	[38]	29	Human atrial model
Pandit et al. (2001)	[39]	26	Rat left-ventricular model
Pandit et al. (2003)	[40]	26	Rat left-ventricular model
Puglisi–Bers (2001)	[41]	17	Rabbit ventricular model
Sakmann et al. (2000)*	[45]	21	Guinea pig ventricular model
Stewart et al. (2009)	[48]	20	Human Purkinje fibre model
Ten Tusscher et al. (2004)*	[51]	17	Human ventricular model
Ten Tusscher et al. (2006)*	[52]	19	Human ventricular model
Wang–Sobie (2008)	[55]	35	Neonatal mouse ventricular model
Winslow et al. (1999)	[56]	33	Canine atrial model
Zhang et al. (2000)	[58]	15	Rabbit sinoatrial node model

et al. (2000) and the two models of Ten Tusscher et al. studied here. For these three models, endocardial, epicardial, and M-cell variants of the model were in the CellML repository and thus included in this study.

3 Stiffness

We are concerned with the characterization of stiffness in various ionic cell models. Arguably, there is no universally accepted definition of stiffness. For example, Hairer and Wanner state that “stiff equations are problems for which explicit methods don’t work” [19, pg. 2]. Lambert [26] describes stiffness as a phenomenon rather than a property because the concept of property implies the requirement of a precise mathematical definition. In this report, we say that a problem is stiff with respect to a given method when stability requirements force the method to take a smaller step-size than that dictated by accuracy requirements. This is similar to the definition of stiffness used by Ascher and Petzold [6]. This can be seen as a pragmatic definition because it frames stiffness in terms of the associated computational consequences. Generally, the step-size required for a stiff problem is much smaller than accuracy requirements dictate, resulting in a numerical solution that is much more accurate (and hence more costly) than desired. For efficiency, we would like that a step-size be chosen based only the accuracy requirements.

Despite the absence of a universally accepted definition, there is a large body of knowledge regarding the suitability of particular methods for both stiff and non-stiff problems. Numerical methods for the solution of ODEs can generally be put into two groups, stiff and non-stiff. The placement of a particular method in a certain group is based on the method’s relative performance on stiff and non-stiff problems. Consider, for example, forward Euler (FE) and backward Euler (BE) methods [6, ch. 3]. One step with FE is computationally inexpensive. So when the step-size is dictated by accuracy considerations, FE is more efficient than BE. However, FE has a relatively small region of absolute stability. An attempt to solve a stiff problem with FE requires a small step-size, and overall the numerical solution process is less efficient than if we use a method with a larger stability region. Hence, FE is classified as a non-stiff method. On the other hand, BE has a large stability region. Despite the fact that each step of BE is more expensive than FE because a system of nonlinear equations must generally be solved at each step, the overall performance trade-off is favourable: the step-size can be increased by more than enough to offset the extra cost per step. Hence, BE is classified as a stiff method. This analysis illustrates that choosing the proper type of method to solve the ODEs can be critical to achieve acceptable performance.

Related to the stiffness of a general initial-value problem (IVP)

$$\frac{dy}{dt} = \mathbf{f}(t, \mathbf{y}), \quad \mathbf{y}(0) = \mathbf{y}_0, \quad t \in [t_0, t_f], \quad (4)$$

are the eigenvalues of the Jacobian $\mathbf{J} = \frac{\partial \mathbf{f}}{\partial \mathbf{y}}(t, \mathbf{y})$ over time. These eigenvalues can give us an indication of a problem’s stiffness. In particular, eigenvalues with large negative real parts are likely to lead to stiff problems on their corresponding time intervals. Similarly, problems that have one or more eigenvalues with positive real parts are likely to be non-stiff. Problems that have eigenvalues with large imaginary parts also tend to be difficult to solve by standard solvers, but the highly oscillatory nature of the solutions to the associated linearized problem does not make the problems stiff according to the classical description of stiffness. In Section 3.1, we find the eigenvalues of the Jacobian of each of the models introduced in Section 2.2 and discuss the implications for stiffness. In Section 3.2, we discuss numerical experiments with stiff and non-stiff methods to illustrate the eigenvalue discussion.

3.1 Eigenvalue Data

For each model in Section 2.2, we found the eigenvalues of the Jacobian in the following way. First, a reference solution was generated using Matlab’s `ode15s` [31]. This was done by lowering the error tolerances for successive approximations until two approximations were identical for at least 10 significant digits at 100 equally spaced output points. Code representing the derivative of each model was created via automatic differentiation using `AdiMat` [8]. We found a value for the Jacobian at every 1 ms of simulated time using the derivative code with the reference solution, and we found the eigenvalues of each of these Jacobians with Matlab’s `eig` function.

The extreme values in the set of eigenvalues associated with a model are of particular interest because they offer a worst-case look at the stiffness properties. At each point in time considered, we found the maximum and minimum values of both the real and complex parts of the eigenvalues. The extreme values across the solution interval of these minimum and maximum values are reported in Table 2 along with the percentage of time at least one pair of complex eigenvalues was present. As we can see, there is a wide range of behaviours encompassed by these models, from models such as FHN and Beeler–Reuter that do not have relatively large negative eigenvalues to models such as Wang–Sobie and that of Maleckar et al. that have moderately large negative eigenvalues to the model of Pandit et al. (2003) that has extremely large negative eigenvalues.

Although not apparent from these tables, we note that problems may not be stiff everywhere in their respective intervals of integration. Accordingly it may be possible to use different integration methods that are more appropriate at different times. We also note integration methods that use a constant step size are subject to the constraints imposed by the worst-case behaviour of stiffness and hence tend to perform poorly.

Figures demonstrating the extreme values of these eigenvalues are presented in Appendix A.

3.2 Numerical Experiments

3.2.1 Overview

We now discuss numerical experiments to show how the results presented in Section 3.1 can be utilized. We describe numerical experiments for 8 integration methods for ionic cell models: FE, the Rush–Larsen (RL) [44] method, and the recently proposed second-order generalization of RL (GRL2) [49]. The primary goal of these experiments is not to find the most efficient numerical method possible but rather to illustrate how the stiffness of particular models affects the performance of different numerical methods. A secondary goal of these experiments is to demonstrate the suitability of numerical methods to particular ionic models according to their degree of stiffness.

For each numerical method, we aim to balance the requirements for accuracy and efficiency. To quantify the error in a solution, we use the *relative root mean square error* (RRMS) error of the transmembrane potential:

$$RRMS := \sqrt{\frac{1}{N} \frac{\sum_{i=1}^N (V_i - \hat{V}_i)^2}{\sum_{i=1}^N \hat{V}_i^2}},$$

where V_i is the numerical approximation and \hat{V}_i is the reference solution at time t_i as described above. For each model and numerical method considered, we maximize the step-size while producing a solution that

Table 2: Extreme values of the eigenvalues for each model. The minimum real part of the set of eigenvalues is denoted $\min(\text{Re}(\lambda))$, and the maximum real part of the set of eigenvalues is denoted $\max(\text{Re}(\lambda))$. Similarly, the minimum and maximum imaginary parts are denoted $\min(\text{Im}(\lambda))$ and $\max(\text{Im}(\lambda))$. The percentage of the solution interval in which there is at least one pair of complex eigenvalues is also reported.

Model	$\min(\text{Re}(\lambda))$	$\max(\text{Re}(\lambda))$	$\min(\text{Im}(\lambda))$	$\max(\text{Im}(\lambda))$	% Complex
Beeler–Reuter (1977)	-8.20E+1	-3.968E-3	0.00E+0	0.00E+0	0
Bondarenko (2004)	-8.49E+3	4.51E+0	-2.80E+0	2.80E+0	64
Courtemanche et al. (1998)	-1.29E+2	1.87E-1	-4.50E+0	4.50E+0	82
Demir et al. (1994)	-2.24E+4	4.57E+0	-7.35E+0	7.35E+0	100
Demir et al. (1999)	-3.45E+4	4.81E+2	-6.50E+1	6.50E+1	66
DiFrancesco–Noble (1985)	-2.62E+4	8.24E+1	-3.21E+0	3.21E+0	31
Dokos et al. (1996)	-2.99E+4	2.49E-15	-6.39E+1	6.39E+1	100
Faber–Rudy (2000)	-1.83E+2	1.36E-17	0.00E+0	0.00E+0	0
FitzHugh–Nagumo (1961)	-4.38E-1	1.78E-1	-4.59E-2	4.59E-2	45
Fox et al. (2002)	-4.38E+2	4.44E-2	-4.18E-1	4.18E-1	65
Hilgemann–Noble (1987)	-2.86E+4	1.81E-14	-7.71E+1	7.71E+1	21
Hund (2004)	-1.95E+2	2.69E-2	-1.57E-3	1.57E-3	4
Jafri et al. (1998)	-1.12E+3	2.31E-7	-1.91E-2	1.91E-2	52
Luo–Rudy (1991)	-1.51E+2	7.01E-2	-4.11E-2	4.11E-2	74
Maleckar et al. (2008)	-4.16E+4	2.42E+2	-3.42E+2	3.42E+2	28
McAllister et al. (1975)	-8.18E+1	-4.79E-4	-2.85E-2	2.85E-2	100
Noble (1962)	-9.79E+3	-1.92E+0	0.00E+0	0.00E+0	0
Noble–Noble (1984)	-6.56E+3	1.35E-15	-1.36E+1	1.36E+1	100
Noble et al. (1991)	-3.88E+4	1.78E-12	0.00E+0	0.00E+0	0
Noble et al. (1998)	-3.60E+4	-6.32E-7	-8.41E+0	8.41E+0	9
Nygren et al. (1998)	-4.03E+4	1.22E-1	-3.88E+2	3.88E+2	22
Pandit et al. (2001)	-8.89E+4	2.20E-14	0.00E+0	0.00E+0	0
Pandit et al. (2003)	-3.90E+9	6.83E+0	-8.09E-5	8.09E-5	17
Puglisi–Bers (2001)	-1.67E+1	1.29E+0	-1.52E-1	1.52E-1	35
Sakmann et al. (2000) – Endocardial	-2.93E+4	6.02E-1	-5.21E+1	5.21E+1	100
Sakmann et al. (2000) – Epicardial	-2.93E+4	3.59E+1	-5.24E+1	5.24E+1	100
Sakmann et al. (2000) – M-cell	-2.93E+4	1.03E+2	-5.20E+1	5.20E+1	100
Stewart et al. (2009)	-1.38E+2	3.34E+0	-1.56E+0	1.56E+0	92
Ten Tusscher et al. (2004) – Endocardial	-1.17E+3	1.16E-1	-4.67E+0	4.67E+0	17
Ten Tusscher et al. (2004) – Epicardial	-1.17E+3	1.12E-1	-4.73E+0	4.73E+0	18
Ten Tusscher et al. (2004) – M-cell	-1.16E+3	1.12E-1	-4.73E+0	4.73E+0	22
Ten Tusscher et al. (2006) – Endocardial	-1.26E+3	1.94E-8	0.00E+0	0.00E+0	0
Ten Tusscher et al. (2006) – Epicardial	-1.26E+3	1.92E-8	0.00E+0	0.00E+0	0
Ten Tusscher et al. (2006) – M-cell	-1.26E+3	1.92E-8	0.00E+0	0.00E+0	0
Wang–Sobie (2008)	-1.22E+2	1.23E+0	-1.23E+0	1.23E+0	46
Winslow et al. (1999)	-1.84E+4	1.53E+0	-4.22E-1	4.22E-1	63
Zhang et al. (2000)	-2.22E+4	1.29E+2	-1.00E+2	1.00E+2	89

has less than 5% RRMS error. For each combination of numerical method and model, we report the result for the step-size with the least execution time and less than 5% RRMS error.

We used constant step sizes in our experiments to reflect the typical use of the cell models within a tissue-scale simulation. As mentioned, these simulations typically employ operator splitting, and constant equal step sizes are used for integrating both the PDEs and the ODEs. The use of variable step sizes for the integration of the ODEs over long time intervals can generally be expected to be more efficient than the use of constant steps [46] and hence would likely be more effective in a scenario where a fully coupled (i.e., unsplit) integration approach is used; see e.g., [57].

We placed two additional requirements on the step-size. First, the maximum step-size allowed was equal to the length of time in which the stimulus current was applied. The cases for which this maximum was reached are denoted with a dagger in Tables 3–6. Second, the step-size was adjusted at up to three points in time in order to resolve important events: the start of the application of stimulus current, the end of the application of stimulus current, and the end point of the simulation. If the integration was to step past one of these three points, the step-size would be adjusted, for that step only, to land on the point exactly. This was done mainly because a discontinuous stimulus application can introduce errors that are avoidable if the points at which the discontinuities occur are resolved.

3.2.2 Methods

The first method used in our experiments is the explicit first-order FE method. Applied to the general IVP (4), one step of FE from $(t_{n-1}, \mathbf{y}_{n-1})$ to (t_n, \mathbf{y}_n) is given by

$$\begin{aligned}\mathbf{y}_n &= \mathbf{y}_{n-1} + \Delta t_n \mathbf{f}(t_{n-1}, \mathbf{y}_{n-1}), \\ t_n &= t_{n-1} + \Delta t_n,\end{aligned}$$

where $\mathbf{y}_n \approx \mathbf{y}(t_n)$ and $t_n = t_{n-1} + \Delta t_n$. It is a popular method in practice mainly due to the ease of implementation.

FE belongs to the more general family of *explicit Runge–Kutta* (ERK) methods; see, e.g., [6]. ERK methods use more function evaluations (or stages) in a given step and combine them to produce a higher order of accuracy than FE. Because of their bounded stability regions, they are generally considered to be effective on non-stiff problems. In our experiments, we use the three well-known, higher-order ERK methods as representative candidates for commonly used ERK methods: the two-stage, second-order trapezoidal (TRAP) method, the two-stage, second-order mid-point (MID) method, and the classical four-stage, fourth-order ERK (ERK4) method; see e.g. [6].

A non-standard yet popular method in cell model simulation is the RL method. The RL method advances the solution to the gating equations (2) using

$$y_n = y_\infty + (y_{n-1} - y_\infty)e^{-\frac{\Delta t_n}{\tau_y}}, \quad (5)$$

which represents the exact solution of (2) *assuming all variables besides y are constant*. FE is then used to advance the solution of the remaining equations. This method is an effective stiff solver for the Luo–Rudy model [47]; i.e., the step-size can be chosen based on accuracy considerations. RL is generally one of the most popular methods in practice due to its good stability properties and ease of implementation. However, this method is only first-order accurate and thus suffers from the usual drawbacks of low-order methods.

The second non-standard method that we investigate is the GRL2 method developed by Sundnes et al. [49]. GRL2 decouples and linearizes the ODE system consisting of m ODEs around a point $\mathbf{y} = \boldsymbol{\eta}$ to obtain

$$\frac{dy_i}{dt} = f_i(\boldsymbol{\eta}) + \frac{\partial}{\partial y_i} f_i(\boldsymbol{\eta})(y_i - \eta_i), \quad y_i(t_n) = \eta_i, \quad (6)$$

for $i = 1, 2, \dots, m$, where the subscript i denotes component i of a vector. The exact solution of (6) is given by

$$y_i(t) = \eta_i + \frac{a}{b} \left(e^{b(t-t_n)} - 1 \right), \quad i = 1, 2, \dots, m, \quad (7)$$

where $a = f_i(\boldsymbol{\eta})$ and $b = \partial f_i(\boldsymbol{\eta})/\partial y_i$. The numerical solution \mathbf{y}_{n+1} at time $t = t_{n+1}$ is then obtained in two steps:

1. Let $\eta_i = y_{n,i}$. Estimate the solution at time $t_{n+1/2}$ with

$$y_{n+1/2,i} = \eta_i + \frac{a}{b} \left(e^{b(\Delta t_n/2)} - 1 \right), \quad i = 1, 2, \dots, m. \quad (8)$$

2. Let $\bar{\mathbf{y}}_{n+1/2}$ be $\mathbf{y}_{n+1/2}$ with component i replaced by $y_{n,i}$. For each i , set $\boldsymbol{\eta} = \bar{\mathbf{y}}_{n+1/2}$ and compute the numerical solution at time t_{n+1} from

$$y_{n+1,i} = \eta_i + \frac{a}{b} \left(e^{b\Delta t_n} - 1 \right), \quad i = 1, 2, \dots, m. \quad (9)$$

GRL2 and RL treat the gating equations (2) in a similar manner. The main difference is that GRL2 integrates the non-gating equations with an exponential formula based on local linearization, whereas RL uses FE. GRL2 is verified to be second order in [5].

We note that care must be taken in the implementation of GRL2 to ensure efficiency, in particular regarding the computation of $\partial \mathbf{f}/\partial \mathbf{y}$. For example, the finite-difference approximation of $\partial f_i(\boldsymbol{\eta})/\partial y_i$ is performed via

$$\partial f_i(\boldsymbol{\eta})/\partial y_i \approx \frac{f_i(\eta^1, \dots, \eta^{i-1}, \eta_i + \delta, \eta^{i+1}, \dots, \eta^m) - f_i(\boldsymbol{\eta})}{\delta}, \quad (10)$$

where $\delta = 10^{-8}$ for double-precision calculations. Without careful implementation, this could add another m full ODE right-hand side function evaluations per step, making the method prohibitively expensive for all but the simplest models. Moreover, we note that a full ODE right-hand-side function evaluation is not needed for each $\partial f_i(\boldsymbol{\eta})/\partial y_i$. Also in practice, if $|\partial f_i(\boldsymbol{\eta})/\partial y_i| < \delta$, the limit as $\partial f_i(\boldsymbol{\eta})/\partial y_i \rightarrow 0$ is used instead of (7):

$$y_i(t) = \eta_i + a(t - t_n), \quad i = 1, \dots, m. \quad (11)$$

For the results reported here for GRL2, we used a finely tuned version of the cell model code. This code had the ability to return the value of the right-hand side of any particular ODE in the system and would compute only the information required for the individual ODE. This fine tuning was necessary for GRL2 to be competitive.

Finally, we also consider two specialized methods, called ROCK2 and ROCK4. These methods are ERK methods constructed to maximize the segment of the negative real axis in their stability regions. This construction is meant to improve the efficiency of these methods relative to standard ERK methods for mildly stiff problems with real eigenvalues. See [3] and [2] for more details on these methods.

3.2.3 Results

For each pair of a model given in Section 2.2 and a method given in Section 3.2.2, we find a maximum step size to 3 significant digits subject to the conditions given in Section 3.2.1. With this information, we performed an experiment to determine the best execution time possible for a combination of a model with a method. All numerical experiments were performed in Matlab on an iMac with 2.8 GHz Intel Core Duo processor with 4 GB DDR SD RAM running at 667 MHz. Except for the model of Pandit et al. (2003), we report the minimum of 100 runs of each combination of a method and model. Because the model of Pandit et al. (2003) required significant run times with the methods used, the execution time reported is the minimum of 10 runs. In all cases, we ensured that the variance of the times recorded for a given combination was small.

Results for FE and the higher-order ERK methods TRAP, MID, and ERK4 are presented in Tables 3 and 4. Results for RL, GRL2, ROCK2, and ROCK4 are presented in tables Tables 5 and 6. From these tables, we see only FE, RL, and GRL2 are the most efficient on any model. For these 3 methods on the models considered, the non-standard methods RL and GRL2 generally outperform FE. RL is the most efficient in 18 cases, GRL2 is the most efficient in 15 cases, and FE is the most efficient in 4 cases. GRL2 can usually take a larger step than RL, which can in turn usually take a larger step than FE. However, GRL2 generally has a higher cost per step than RL, which in turn has a higher cost per step than FE. We see that generally the increases in acceptable step sizes for GRL2 and RL are large enough to more than offset the added cost per step when compared with FE. The situation for GRL2 compared with RL is less clear, with each being the most efficient on roughly an equal number of models. These results further support the findings in [49] for the competitiveness of GRL2 as a method for the integration of cell models, albeit at the expense of a non-trivial implementation. In four cases FE was the most efficient method: FHN, Noble (1962), Pandit et al. (2001), and Pandit et al. (2003). In these cases, the increase maximum step size for RL or GRL2 offers little or no improvement in performance relative to FE due to the higher cost per step. Except for a few cases, all the higher-order ERK methods (including ROCK2 and ROCK4) underperformed relative to FE. We also performed experiments with other implicit-explicit Runge–Kutta (IMEX-RK) methods; see, e.g., [46] and references therein. In particular, we examined the solution of the model of Pandit et al. (2003) with three IMEX-RK methods: ARK3(2)4L[2]SA and ARK5(3)8L[2]SA from [24], denoted ARK3 and ARK5, and the uniformly accurate BHR553 scheme from [10] with $\gamma = \gamma_2 \approx 0.57281606$. Results for experiments with these methods is presented in Table 7. As could have been anticipated based on the stiffness characteristics of the models and previous investigations [46], all of these IMEX-RK methods outperformed FE (and hence also RL and GRL2) on this model, with ARK3 coming in about 30 times faster than FE.

Table 3: Largest step sizes Δt and corresponding execution times in seconds of FE and TRAP yielding less than 5% RRMS error.

Model	FE		TRAP	
	Δt	Time	Δt	Time
Beeler–Reuter (1977)	2.53E-2	5.19E-2	2.46E-2	1.15E-1
Bondarenko et al. (2004)	2.13E-4	3.81E+0	2.13E-4	8.38E+0
Courtemanche et al. (1998)	1.94E-2	4.27E+0	1.94E-2	1.11E+1
Demir et al. (1994)	5.95E-2	1.74E-2	5.53E-2	4.11E-2
Demir et al. (1999)	5.97E-2	2.13E-2	5.54E-2	5.07E-2
DiFrancesco–Noble (1985)	7.85E-2	8.59E-2	7.66E-2	1.77E-1
Dokos et al. (1996)	7.30E-2	3.44E-2	6.91E-2	8.02E-2
Faber–Rudy (2000)	1.12E-2	1.69E-1	1.12E-2	5.91E-1
FitzHugh–Nagumo (1961)	5.00E-1 [†]	3.93E-3	5.00E-1 [†]	8.64E-3
Fox et al. (2002)	4.60E-3	4.11E-1	4.60E-3	7.59E-1
Hilgemann–Noble (1987)	6.25E-2	1.69E-1	6.21E-2	3.12E-1
Hund–Rudy (2004)	1.11E-2	1.75E-1	1.11E-2	3.22E-1
Jafri et al. (1998)	5.77E-4	6.18E+0	5.77E-4	1.18E+1
Luo–Rudy (1991)	1.34E-2	3.61E-1	1.46E-2	6.15E-1
Maleckar et al. (2008)	5.02E-2	1.09E-1	5.31E-2	2.02E-1
McAllister et al. (1975)	2.46E-2	1.21E-1	2.11E-2	2.37E-1
Noble (1962)	2.03E-1	7.63E-3	2.13E-1	1.23E-2
Noble–Noble (1984)	2.04E-1	1.82E-1	1.78E-1	4.63E-1
Noble et al. (1991)	5.15E-2	3.00E-2	5.34E-2	4.96E-2
Noble et al. (1998)	5.58E-2	5.25E-2	5.70E-2	8.99E-2
Nygren et al. (1998)	5.36E-2	1.02E-1	5.30E-2	1.87E-1
Pandit et al. (2001)	2.91E-4	8.85E+0	2.91E-4	2.04E+1
Pandit et al. (2003)	1.08E-2	4.20E+4	1.08E-2	1.66E+5
Puglisi–Bers (2001)	1.08E-2	4.43E-1	1.23E-2	7.23E-1
Sakmann et al. (2000) – Endocardial	6.90E-2	4.73E-2	6.83E-2	8.94E-2
Sakmann et al. (2000) – Epicardial	6.90E-2	5.11E-2	6.81E-2	8.92E-2
Sakmann et al. (2000) – M-cell	6.86E-2	5.12E-2	6.77E-2	9.06E-2
Stewart et al. (2009)	1.50E-2	4.35E-1	1.45E-2	8.43E-1
Ten Tusscher et al. (2004) – Endocardial	1.78E-3	1.75E+0	1.70E-3	3.38E+0
Ten Tusscher et al. (2004) – Epicardial	1.78E-3	1.75E+0	1.70E-3	3.38E+0
Ten Tusscher et al. (2004) – M-cell	1.76E-3	1.25E+0	1.71E-3	2.48E+0
Ten Tusscher et al. (2006) – Endocardial	1.62E-3	1.33E+0	1.55E-3	2.53E+0
Ten Tusscher et al. (2006) – Epicardial	2.14E-3	9.79E-1	1.55E-3	2.07E+0
Ten Tusscher et al. (2006) – M-cell	2.14E-3	9.79E-1	1.56E-3	2.14E+0
Wang–Sobie (2008)	1.66E-2	5.95E-2	1.63E-2	1.06E-1
Winslow et al. (1999)	1.07E-4	1.70E+1	1.07E-4	3.55E+1
Zhang et al. (2000)	9.90E-2	5.19E-2	9.95E-2	1.01E-1

Table 4: Largest step sizes Δt and corresponding execution times in seconds of MID and ERK4 yielding less than 5% RRMS error.

Model	MID		ERK4	
	Δt	Time	Δt	Time
Beeler–Reuter (1977)	2.53E-2	1.00E-1	3.41E-2	1.45E-1
Bondarenko et al. (2004)	2.13E-4	8.38E+0	2.99E-4	1.16E+1
Courtemanche et al. (1998)	2.07E-2	1.07E+1	2.68E-2	2.32E+1
Demir et al. (1994)	5.67E-2	4.01E-2	7.55E-2	5.85E-2
Demir et al. (1999)	5.67E-2	4.28E-2	7.56E-2	7.23E-2
DiFrancesco–Noble (1985)	7.92E-2	1.63E-1	1.06E-1	2.35E-1
Dokos et al. (1996)	6.93E-2	8.00E-2	9.52E-2	1.13E-1
Faber–Rudy (2000)	1.12E-2	4.55E-1	1.55E-2	4.48E-1
FitzHugh–Nagumo (1961)	5.00E-1 [†]	8.64E-3	5.00E-1 [†]	1.52E-2
Fox et al. (2002)	4.60E-3	7.59E-1	6.51E-3	1.00E+0
Hilgemann–Noble (1987)	6.26E-2	3.12E-1	8.62E-2	4.31E-1
Hund–Rudy (2004)	1.11E-2	3.21E-1	1.54E-2	4.57E-1
Jafri et al. (1998)	6.60E-4	1.82E+1	7.25E-4	2.06E+1
Luo–Rudy (1991)	1.46E-2	6.15E-1	1.86E-2	1.14E+0
Maleckar et al. (2008)	4.91E-2	2.09E-1	6.82E-2	2.81E-1
McAllister et al. (1975)	2.19E-2	2.48E-1	3.49E-2	3.19E-1
Noble (1962)	2.02E-1	1.26E-2	8.38E-2	1.76E-2
Noble–Noble (1984)	1.77E-1	4.60E-1	2.41E-1	6.64E-1
Noble et al. (1991)	5.15E-2	5.13E-2	7.38E-2	6.94E-2
Noble et al. (1998)	5.58E-2	9.31E-2	7.92E-2	1.26E-1
Nygren et al. (1998)	5.21E-2	1.87E-1	7.19E-2	2.56E-1
Pandit et al. (2001)	2.91E-4	2.04E+1	4.03E-4	2.75E+1
Pandit et al. (2003)	1.08E-2	1.66E+5	2.82E-2	3.09E+5
Puglisi–Bers (2001)	1.27E-2	6.84E-1	1.48E-2	1.19E+0
Sakmann et al. (2000) – Endocardial	6.90E-2	8.85E-2	9.47E-2	1.26E-2
Sakmann et al. (2000) – Epicardial	6.90E-2	8.80E-2	9.46E-2	1.25E-1
Sakmann et al. (2000) – M-cell	6.87E-2	8.92E-2	9.40E-2	1.27E-1
Stewart et al. (2009)	1.51E-2	8.17E-1	2.02E-2	1.14E+0
Ten Tusscher et al. (2004) – Endocardial	1.78E-3	3.23E+0	2.36E-3	4.58E+0
Ten Tusscher et al. (2004) – Epicardial	1.79E-3	3.23E+0	2.37E-3	4.58E+0
Ten Tusscher et al. (2004) – M-cell	1.78E-3	2.44E+0	2.37E-3	3.46E+0
Ten Tusscher et al. (2006) – Endocardial	1.62E-3	2.46E+0	2.24E-3	3.35E+0
Ten Tusscher et al. (2006) – Epicardial	1.54E-3	1.75E+0	4.75E-3	2.09E+0
Ten Tusscher et al. (2006) – M-cell	1.53E-3	1.79E+0	4.73E-3	2.26E+0
Wang–Sobie (2008)	1.66E-2	1.05E-1	2.27E-2	1.46E-1
Winslow et al. (1999)	1.07E-4	3.55E+1	1.30E-4	5.51E+1
Zhang et al. (2000)	9.95E-2	1.01E-1	1.32E-1	1.35E-1

Table 5: Largest step sizes Δt and corresponding execution times in seconds of RL and GRL2 yielding less than 5% RRMS error.

Model	RL		GRL2	
	Δt	Time	Δt	Time
Beeler–Reuter (1977)	8.49E-1	9.83E-3	8.58E-1	3.09E-2
Bondarenko et al. (2004)	2.50E-4	4.13E+0	1.40E-2	1.85E+0
Courtemanche et al. (1998)	3.45E-1	4.79E-1	9.95E-1	2.07E-1
Demir et al. (1994)	3.45E-1	4.79E-1	9.95E-1	2.07E-1
Demir et al. (1999)	9.66E-2	1.71E-2	2.49E-1	8.24E-2
DiFrancesco–Noble (1985)	6.62E-1	7.66E-2	9.99E-1	2.67E-1
Dokos et al. (1996)	7.64E-1	3.37E-3	9.99E-1	8.35E-2
Faber–Rudy (2000)	9.51E-1	4.60E-3	6.35E-1	1.38E-1
FitzHugh–Nagumo (1961)	N/A	N/A	5.00E-1 [†]	3.19E-2
Fox et al. (2002)	6.37E-1	3.11E-2	7.74E-1	7.70E-2
Hilgemann–Noble (1987)	8.06E-2	9.56E-2	9.96E-2	6.23E-2
Hund–Rudy (2004)	4.17E-2	5.35E-2	6.20E-1	4.26E-1
Jafri et al. (1998)	5.89E-4	4.42E+0	1.59E-3	8.38E+0
Luo–Rudy (1991)	2.50E-1	6.94E-2	1.00E+0 [†]	2.31E-2
Maleckar et al. (2008)	7.50E-1	9.44E-2	8.21E-1	3.84E-1
McAllister et al. (1975)	7.06E-1	6.00E-2	2.63E-1	2.32E-1
Noble (1962)	9.41E-2	8.82E-2	2.22E-1	7.89E-2
Noble–Noble (1984)	2.73E-1	1.20E-1	1.00E+0 [†]	4.99E-2
Noble et al. (1991)	1.53E-1	1.21E-2	6.25E-1	9.31E-3
Noble et al. (1998)	1.57E-1	1.50E-2	5.43E-1	2.67E-2
Nygren et al. (1998)	8.88E-2	8.68E-2	9.81E-1	3.65E-2
Pandit et al. (2001)	2.91E-4	1.01E+1	4.98E-4	2.56E+1
Pandit et al. (2003)	1.04E-7	8.37E+4	9.28E-7	8.93E+4
Puglisi–Bers (2001)	4.30E-1	8.35E-2	6.24E-1	4.18E-1
Sakmann et al. (2000) – Endocardial	2.36E-1	1.80E-2	9.71E-1	1.03E-2
Sakmann et al. (2000) – Epicardial	2.36E-1	1.80E-2	9.71E-1	1.03E-2
Sakmann et al. (2000) – M-cell	2.36E-1	1.80E-2	9.71E-1	1.03E-2
Stewart et al. (2009)	1.62E-1	5.60E-2	3.58E-2	8.61E-2
Ten Tusscher et al. (2004) – Endocardial	1.00E+0 [†]	5.43E-3	1.00E+0 [†]	1.30E-2
Ten Tusscher et al. (2004) – Epicardial	1.00E-1 [†]	5.43E-3	1.00E+0 [†]	1.30E-2
Ten Tusscher et al. (2004) – M-cell	2.80E-1	1.29E-2	9.81E-1	2.84E-2
Ten Tusscher et al. (2006) – Endocardial	1.52E-1	6.41E-2	7.80E-1	9.27E-3
Ten Tusscher et al. (2006) – Epicardial	2.80E-1	3.64E-2	8.39E-1	7.06E-3
Ten Tusscher et al. (2006) – M-cell	2.05E-1	4.17E-2	7.77E-1	9.27E-3
Wang–Sobie (2008)	5.26E-2	2.19E-2	4.97E-1	1.61E-2
Winslow et al. (1999)	2.80E-4	8.84E+0	1.34E-3	2.26E+0
Zhang et al. (2000)	1.00E+0 [†]	7.69E-3	1.00E+0 [†]	1.85E-1

Table 6: Largest step sizes Δt and corresponding execution times in seconds of ROCK2 and ROCK4 yielding less than 5% RRMS error.

Model	ROCK2		ROCK4	
	Δt	Time	Δt	Time
Beeler–Reuter (1977)	7.62E–2	1.67E–1	7.97E–2	4.12E–1
Bondarenko et al. (2004)	6.17E–4	5.04E+0	7.24E–4	1.63E+1
Courtemanche et al. (1998)	5.90E–2	7.31E+0	5.99E–2	2.13E+1
Demir et al. (1994)	1.74E–1	8.85E–2	1.81E–1	2.48E–1
Demir et al. (1999)	1.66E–1	1.06E–1	1.76E–1	2.74E–1
DiFrancesco–Noble (1985)	2.50E–1	4.10E–1	2.50E–1	1.14E+0
Dokos et al. (1996)	2.12E–1	1.30E–1	2.15E–2	3.47E–1
Faber–Rudy (2000)	3.42E–2	7.60E–1	3.54E–2	2.08E+0
FitzHugh–Nagumo (1961)	5.00E–1 [†]	4.16E–2	5.00E–1 [†]	1.04E–1
Fox et al. (2002)	1.42E–2	1.67E+0	1.37E–2	5.12E+0
Hilgemann–Noble (1987)	1.91E–1	1.22E–1	1.86E–1	3.56E–1
Hund–Rudy (2004)	3.40E–2	8.02E–1	3.38E–2	2.33E+0
Jafri et al. (1998)	1.30E–3	1.90E+1	1.38E–3	5.45E+1
Luo–Rudy (1991)	5.04E–2	3.91E–1	4.84E–2	1.32E+0
Maleckar et al. (2008)	1.00E+0 [†]	7.76E–1	1.00E+0 [†]	2.24E+0
McAllister et al. (1975)	3.36E–2	6.81E–1	5.32E–2	1.13E+0
Noble (1962)	6.33E–1	2.72E–2	6.91E–1	6.25E–2
Noble–Noble (1984)	5.41E–1	4.79E–2	5.12E–1	1.06E–1
Noble et al. (1991)	1.58E–1	9.32E–2	1.54E–1	3.49E–1
Noble et al. (1998)	1.71E–1	1.08E–1	1.66E–1	2.52E–1
Nygren et al. (1998)	1.54E–1	4.76E–1	1.57E–1	1.33E+0
Pandit et al. (2001)	5.25E–5	2.84E+1	5.25E–4	6.29E+1
Pandit et al. (2003)	8.39E–6	9.74E+4	8.55E–6	4.62E+5
Puglisi–Bers (2001)	6.40E–2	9.22E–1	6.55E–2	1.57E+0
Sakmann et al. (2000) – Endocardial	2.10E–1	2.54E–1	2.05E–1	7.03E–1
Sakmann et al. (2000) – Epicardial	2.10E–1	2.69E–1	2.05E–1	7.32E–1
Sakmann et al. (2000) – M-cell	2.08E–1	2.92E–1	2.03E–1	7.82E–1
Stewart et al. (2009)	4.50E–2	1.88E+0	4.38E–2	5.56E+0
Ten Tusscher et al. (2004) – Endocardial	5.23E–3	7.50E+0	5.29E–3	2.97E+1
Ten Tusscher et al. (2004) – Epicardial	5.23E–3	7.50E+0	5.29E–3	2.97E+1
Ten Tusscher et al. (2004) – M-cell	2.23E–3	1.54E+1	2.23E–3	4.03E+1
Ten Tusscher et al. (2006) – Endocardial	4.50E–3	6.12E+0	4.50E–3	1.75E+1
Ten Tusscher et al. (2006) – Epicardial	5.35E–3	4.73E+0	4.65E–3	1.40E+1
Ten Tusscher et al. (2006) – M-cell	4.25E–3	6.62E+0	4.66E–3	1.38E+1
Wang–Sobie (2008)	5.07E–2	2.72E–1	4.94E–2	7.55E–1
Winslow et al. (1999)	1.13E–3	8.21E+1	1.15E–3	2.44E+2
Zhang et al. (2000)	2.96E–1	1.28E–1	3.40E–1	3.60E–1

Table 7: Largest step sizes Δt and corresponding execution times in seconds of ARK3, ARK5, and BHR553 yielding less than 5% RRMS error when solving the model of Pandit et al. (2003).

ARK3		ARK5		BHR553	
Δt	Time	Δt	Time	Δt	Time
2.50E-3	1.39E+3	8.50E-4	9.06E+3	1.15E-3	6.06E+3

4 Conclusions

In this report, we examined the eigenvalues of the Jacobian of a variety of cardiac electrophysiological models. In particular, we examined the consequences for stiffness that arise from these eigenvalues and demonstrated how they affect the performance of various numerical methods.

The extremes of these eigenvalues were presented in Section 3.1. The wide range of cardiac electrophysiological models led to considerable differences in the eigenvalues from one model to another. One can infer from these data that there is a large variation in the stiffness properties among the models. At one extreme is the non-stiff FitzHugh–Nagumo model; at the other is the highly stiff model of Pandit et al. (2003). The data suggest that most cell models are moderately stiff for the typical accuracies required.

Numerical experiments with 8 integration methods (denoted FE, TRAP, MID, ERK4, RL, GRL2, ROCK2, and ROCK4) for cell models were discussed in Section 3.2. The non-standard methods GRL2 and RL were found to outperform the other ERK methods on 33 of the 37 models considered. Individually, each of RL and GRL2 was the most efficient method on roughly an equal number of models. This observation lends support to the effectiveness of the recently proposed GRL2 method, albeit at the cost of a non-trivial implementation. RL seems to generally strike a good balance between efficient integration and ease of implementation. Nonetheless, these methods did not perform satisfactorily on all models. In particular, all the methods considered face a severe step-size restriction due to stiffness for the models of Winslow et al. and Pandit et al. (2003). For the model of Pandit et al. (2003), we found that IMEX-RK methods generally performed much better, with reductions in CPU time of up to 30.

References

- [1] <http://bioeng.washington.edu/jsim/>.
- [2] A. Abdulle. Fourth order Chebyshev methods with recurrence relation. *SIAM J. Sci. Comput.*, 23(6):2041–2054, 2002.
- [3] A. Abdulle and A. A. Medovikov. Second order Chebyshev methods based on orthogonal polynomials. *Numer. Math.*, 90(1):1–18, 2001.
- [4] R. R. Aliev and A. V. Panfilov. A simple two-variable model of cardiac excitation. *Chaos, Solitons and Fractals*, 7(3):293–301, 1996.
- [5] R. Artebrant, J. Sundnes, O. Skavhaug, and A. Tveito. A second order method of Rush-Larsen type. Technical report, Simula Research Laboratory, 2008.
- [6] U. M. Ascher and L. R. Petzold. *Computer methods for ordinary differential equations and differential-algebraic equations*. Society for Industrial and Applied Mathematics (SIAM), Philadelphia, PA, 1998.

- [7] G. W. Beeler and H. Reuter. Reconstruction of the action potential of ventricular myocardial fibres. *J Physiol*, 268(1):177–210, 1977.
- [8] C. H. Bischof, H. M. Bückner, and A. Vehreschild. A macro language for derivative definition in ADi-Mat. In *Automatic differentiation: applications, theory, and implementations*, volume 50 of *Lect. Notes Comput. Sci. Eng.*, pages 181–188. Springer, Berlin, 2006.
- [9] V. E. Bondarenko, G. P. Szigeti, G. C. L. Bett, S-J. Kim, and R. L. Rasmusson. Computer model of action potential of mouse ventricular myocytes. *Am J Physiol Heart Circ Physiol*, 287(3):H1378–403, 2004.
- [10] S. Boscarino and G. Russo. On a class of uniformly accurate imex Runge–Kutta schemes and applications to hyperbolic systems with relaxation. *SIAM J. Sci. Comput.*, 31(3):1926–1945, 2009.
- [11] M. Courtemanche, R. J. Ramirez, and S. Nattel. Ionic mechanisms underlying human atrial action potential properties: insights from a mathematical model. *Am. J. Physiol.*, 275(1):H301–H321, 1998.
- [12] S. S. Demir, J. W. Clark, and W. R. Giles. Parasympathetic modulation of sinoatrial node pacemaker activity in rabbit heart: a unifying model. *Am J Physiol*, 276(6 Pt 2):H2221–44, 1999.
- [13] S. S. Demir, J. W. Clark, C. R. Murphey, and W. R. Giles. A mathematical model of a rabbit sinoatrial node cell. *Am J Physiol*, 266(3 Pt 1):C832–52, 1994.
- [14] D. DiFrancesco and D. Noble. A model of cardiac electrical activity incorporating ionic pumps and concentration changes. *Philos Trans R Soc Lond B Biol Sci*, 307(1133):353–98, 1985.
- [15] S. Dokos, B. Celler, and N. Lovell. Ion currents underlying sinoatrial node pacemaker activity: a new single cell mathematical model. *J Theor Biol*, 181(3):245–72, 1996.
- [16] G. M. Faber and Y. Rudy. Action potential and contractility changes in $[Na(+)](i)$ overloaded cardiac myocytes: a simulation study. *Biophys J*, 78(5):2392–404, 2000.
- [17] R. FitzHugh. Impulses and Physiological States in Theoretical Models of Nerve Membrane. *Biophys. J.*, 1(6):445–466, 1961.
- [18] J. J. Fox, J. L. McHarg, and Jr Gilmour, R. F. Ionic mechanism of electrical alternans. *Am J Physiol Heart Circ Physiol*, 282(2):H516–530, 2002.
- [19] E. Hairer and G. Wanner. *Solving Ordinary Differential Equations II: Stiff and Differential-Algebraic Problems*. Springer-Verlag, Berlin, second edition, 1996.
- [20] D. W. Hilgemann and D. Noble. Excitation-contraction coupling and extracellular calcium transients in rabbit atrium: reconstruction of basic cellular mechanisms. *Proc R Soc Lond B Biol Sci*, 230(1259):163–205, 1987.
- [21] A.L. Hodgkin and A.F. Huxley. A quantitative description of membrane current and its application to conduction and excitation in nerve. *J. Physiol. (Lond)*, 117(4):500–544, 1952.
- [22] T. J. Hund and Y. Rudy. Rate dependence and regulation of action potential and calcium transient in a canine cardiac ventricular cell model. *Circulation*, 110(20):3168–74, 2004.
- [23] M. S. Jafri, J. J. Rice, and R. L. Winslow. Cardiac Ca^{2+} dynamics: the roles of ryanodine receptor adaptation and sarcoplasmic reticulum load. *Biophys J*, 74(3):1149–68, 1998.
- [24] C. A. Kennedy and M. H. Carpenter. Additive Runge–Kutta schemes for convection-diffusion-reaction equations. *Appl. Numer. Math.*, 44(1-2):139–181, 2003.

- [25] B. Y. Kogan, W. J. Karplus, B. S. Billett, A.T. Pang, H. S. Karagueuzian, and S. S. Kahn. The simplified FitzHugh–Nagumo model with action potential duration restitution: effects on 2-D wave propagation. *Physica D*, 50:327–340, 1991.
- [26] J. D. Lambert. *Numerical methods for ordinary differential systems*. John Wiley & Sons Ltd., Chichester, 1991. The initial value problem.
- [27] C. M. Lloyd, J. R. Lawson, P. J. Hunter, and P. F. Nielsen. The CellML model repository. *Bioinformatics*, 24(18):2122–2123, 2008.
- [28] C. Luo and Y. Rudy. A model of ventricular cardiac action potential. *Circ. Res.*, 68(6):1501–1526, 1991.
- [29] M. C. Maclachlan, J. Sundnes, and R. J. Spiteri. A comparison of non-standard solvers for ODEs describing cellular reactions in the heart. *Comput Methods Biomech Biomed Engin*, 10(5):317–26, 2007.
- [30] M. M. Maleckar, J. L. Greenstein, N. A. Trayanova, and W. R. Giles. Mathematical simulations of ligand-gated and cell-type specific effects on the action potential of human atrium. *Prog Biophys Mol Biol*, 98(2-3):161–70, 2008.
- [31] MathWorks Inc., The. Matlab R2008b. <http://www.mathworks.com/>, 2008.
- [32] R. E. McAllister, D. Noble, and R. W. Tsien. Reconstruction of the electrical activity of cardiac Purkinje fibres. *J Physiol*, 251(1):1–59, 1975.
- [33] J. Nagumo, S. Arimoto, and S. Yoshizawa. An active pulse transmission line simulating nerve axon. *Proceedings of the IRE*, 50(10):2061–2070, 1962.
- [34] D. Noble. A modification of the Hodgkin–Huxley equations applicable to Purkinje fibre action and pace-maker potentials. *J Physiol*, 160(NIL):317–52, 1962.
- [35] D. Noble and S. J. Noble. A model of sino-atrial node electrical activity based on a modification of the DiFrancesco-Noble (1984) equations. *Proc R Soc Lond B Biol Sci*, 222(1228):295–304, 1984.
- [36] D. Noble, S. J. Noble, G. C. Bett, Y. E. Earm, W. K. Ho, and I. K. So. The role of sodium-calcium exchange during the cardiac action potential. *Ann N Y Acad Sci*, 639(NIL):334–53, 1991.
- [37] D. Noble, A. Varghese, P. Kohl, and P. Noble. Improved guinea-pig ventricular cell model incorporating a diadic space, IKr and IKs, and length- and tension-dependent processes. *Can J Cardiol*, 14(1):123–34, 1998.
- [38] A. Nygren, C. Fiset, L. Firek, J. W. Clark, D. S. Lindblad, R. B. Clark, and W. R. Giles. Mathematical model of an adult human atrial cell: the role of K⁺ currents in repolarization. *Circ Res*, 82(1):63–81, 1998.
- [39] S. V. Pandit, R. B. Clark, W. R. Giles, and S. S. Demir. A mathematical model of action potential heterogeneity in adult rat left ventricular myocytes. *Biophys J*, 81(6):3029–3051, 2001.
- [40] S. V. Pandit, W. R. Giles, and S. S. Demir. A mathematical model of the electrophysiological alterations in rat ventricular myocytes in type-I diabetes. *Biophys J*, 84(2 Pt 1):832–841, 2003.
- [41] J. L. Puglisi and D. M. Bers. Labheart: an interactive computer model of rabbit ventricular myocyte ion channels and ca transport. *Am. J. Physiol. Cell Physiol.*, 281(6):C2049–C2060, 2001.
- [42] A. J. Pullan, M. L. Buist, and L. K. Cheng. *Mathematically Modelling the Electrical Activity of the Heart: From Cell to Body Surface and Back Again*. World Scientific, New Jersey, 2005.
- [43] J.M. Rogers and A.D. McCulloch. A collocation–galerkin finite element model of cardiac action potential propagation. *IEEE Trans. Biomed. Eng.*, 41(8):743–757, 1994.

- [44] S. Rush and H. Larsen. A practical algorithm for solving dynamic membrane equations. *IEEE Trans. Biomed. Eng.*, BME-25(4):389–392, 1978.
- [45] B. F. Sakmann, A. J. Spindler, S. M. Bryant, K. W. Linz, and D. Noble. Distribution of a persistent sodium current across the ventricular wall in guinea pigs. *Circ Res*, 87(10):910–4, 2000.
- [46] R. J. Spiteri and R. C. Dean. On the performance of an implicit-explicit Runge–Kutta method in models of cardiac electrical activity. *IEEE Trans. Biomed. Eng.*, 55(5):1488–1495, May 2008.
- [47] R. J. Spiteri and M. C. MacLachlan. An efficient non-standard finite difference scheme for an ionic model of cardiac action potentials. *J. Difference Equ. Appl.*, 9(12):1069–1081, 2003.
- [48] P. Stewart, O. V. Aslanidi, D. Noble, P. J. Noble, M. R. Boyett, and H. Zhang. Mathematical models of the electrical action potential of Purkinje fibre cells. *Philos Transact A Math Phys Eng Sci*, 367(1896):2225–55, 2009.
- [49] J. Sundnes, R. Artebrant, O. Skavhaug, and A. Tveito. A second-order algorithm for solving dynamic cell membrane equations. *IEEE Trans. Biomed. Eng.*, 56(10):2546–2548, 2009.
- [50] J. Sundnes, G. T. Lines, X. Cai, B. F. Nielsen, K.-A. Mardal, and A. Tveito. *Computing the electrical activity in the heart*. Springer-Verlag, Berlin, 2006.
- [51] K. H. W. J. Ten Tusscher, D. Noble, P. J. Noble, and A. V. Panfilov. A model for human ventricular tissue. *Am J Physiol Heart Circ Physiol*, 286(4):H1573–89, 2004.
- [52] K. H. W. J. Ten Tusscher and A. V. Panfilov. Cell model for efficient simulation of wave propagation in human ventricular tissue under normal and pathological conditions. *Phys. Med. Biol.*, 51(23):6141–6156, 2006.
- [53] F. J. L. Van Capelle and D. Durrer. Computer simulation of arrhythmias in a network of coupled excitable elements. *Circ. Res.*, 47:454–466, 1980.
- [54] E. J. Vigmond, R. W. dos Santos, A. J. Prassl, M. Deo, and G. Plank. Solvers for the cardiac bidomain equations. *Prog Biophys Mol Biol*, 96(1-3):3–18, 2008.
- [55] L. J. Wang and E. A. Sobie. Mathematical model of the neonatal mouse ventricular action potential. *Am J Physiol Heart Circ Physiol*, 294(6):H2565–2575, 2008.
- [56] R. L. Winslow, J. Rice, S. Jafri, E. Marbán, and B. O. Rourke. Mechanisms of altered excitation-contraction coupling in canine tachycardia-induced heart failure, ii model studies. *Circ Res.*, 84(5):571–586, 1999.
- [57] Wenjun Ying, D. J. Rose, and C. S. Henriquez. Efficient fully implicit time integration methods for modeling cardiac dynamics. *IEEE Trans. Biomed. Eng.*, 55(12):2701–2711, 2008.
- [58] H. Zhang, A. V. Holden, I. Kodama, H. Honjo, M. Lei, T. Varghese, and M. R. Boyett. Mathematical models of action potentials in the periphery and center of the rabbit sinoatrial node. *Am J Physiol Heart Circ Physiol*, 279(1):H397–421, 2000.

A Plots of eigenvalue data

Figures 1–128 give plots of the eigenvalues over time for all models. In the case of a model with non-zero imaginary parts, four figures are presented: the extreme real part of the eigenvalues over time, the extreme imaginary part of the eigenvalues over time, the extreme real and complex parts over time, and all the eigenvalues over time. In the case of a model with no non-zero imaginary parts, only two figures are presented: the extreme values of the eigenvalues over time and all the eigenvalues over time.

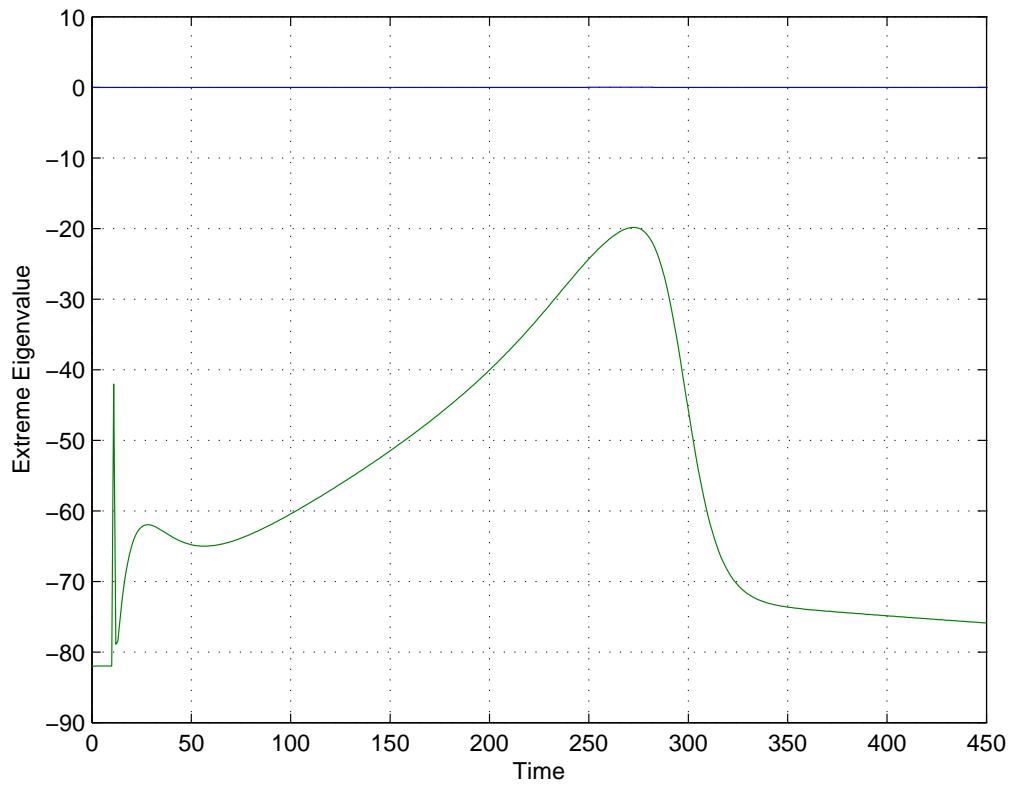


Figure 1: Extreme real eigenvalues in the Beeler–Reuter model.

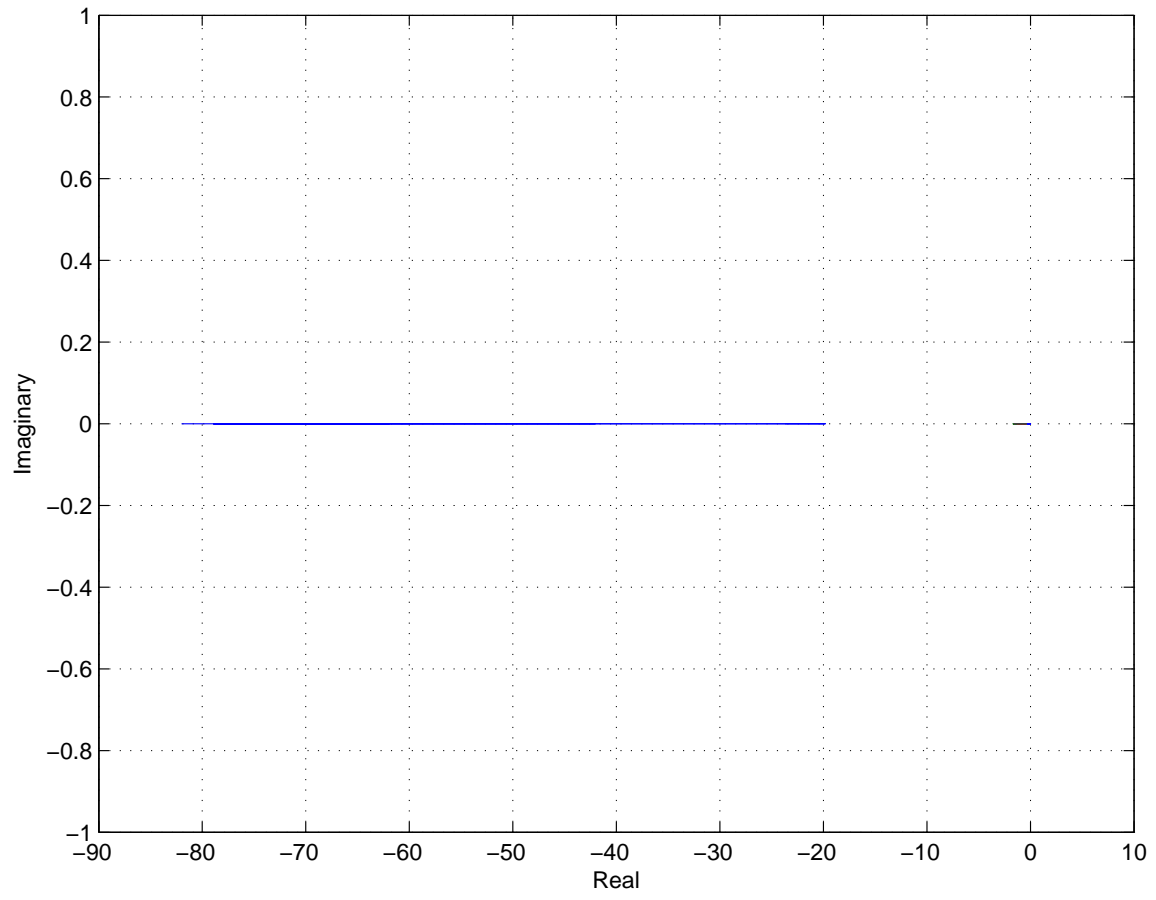


Figure 2: Plot of all eigenvalues at all times measured in the Beeler–Reuter model.

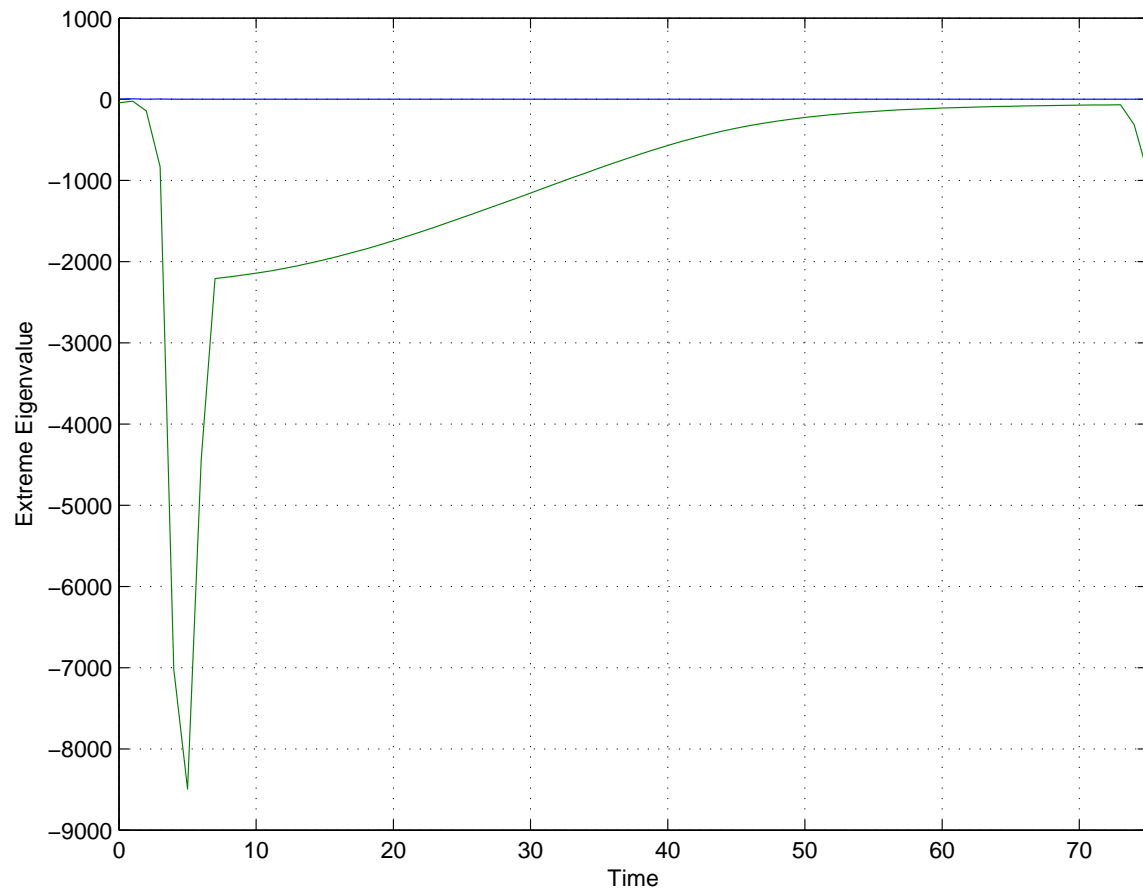


Figure 3: Extreme real eigenvalues in the model of Bondarenko et al.

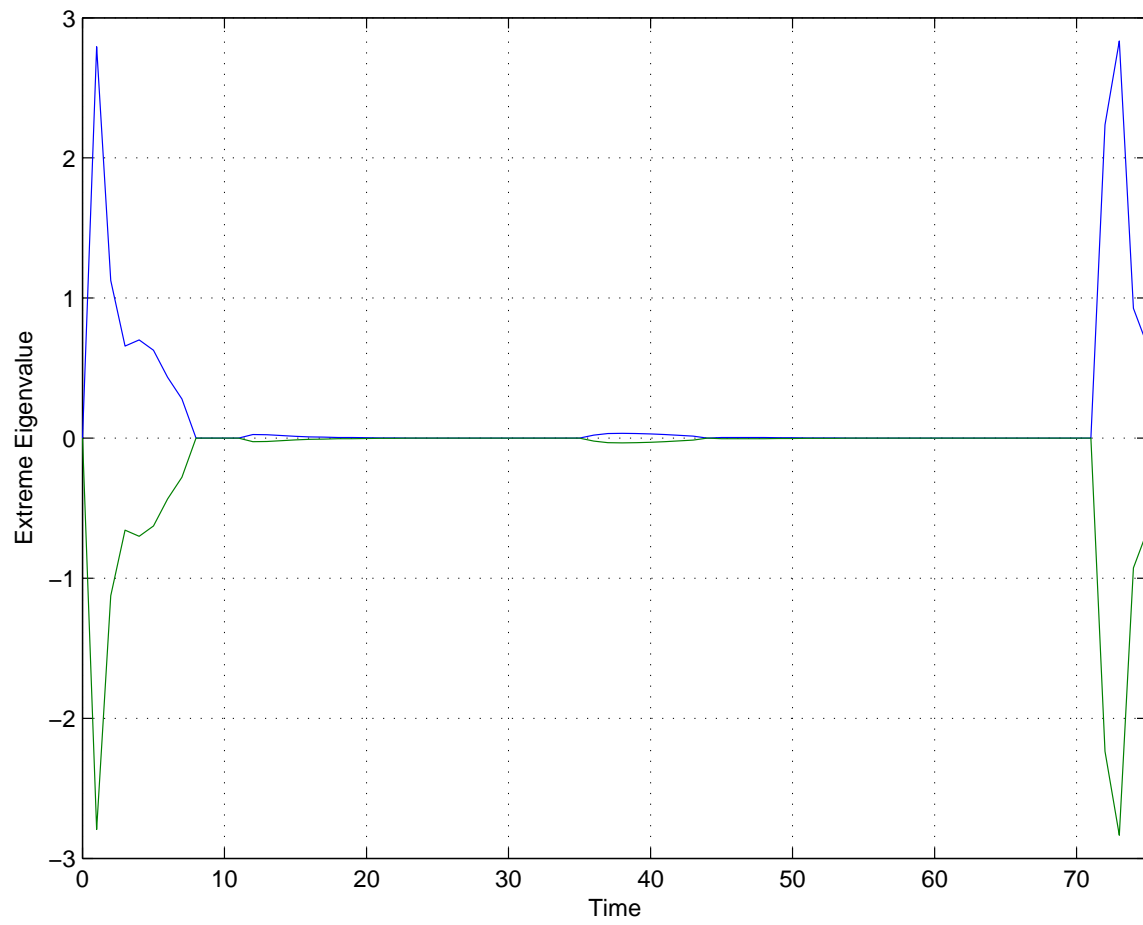


Figure 4: Extreme imaginary eigenvalues in the model of Bondarenko et al.

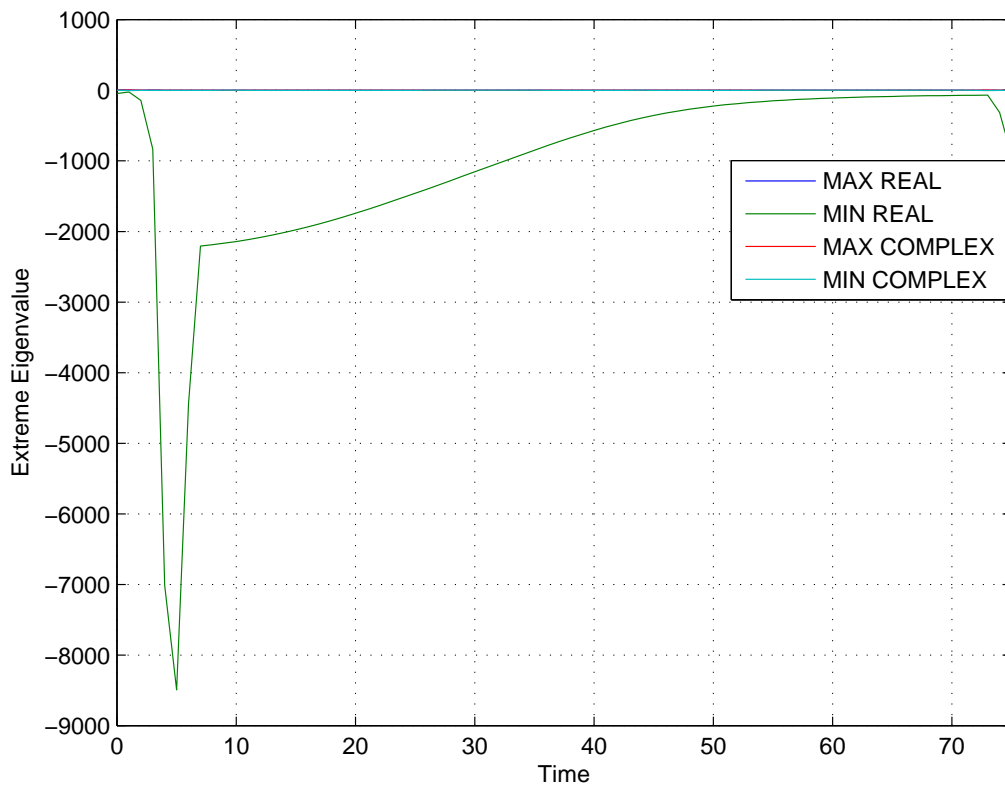


Figure 5: Extreme values of eigenvalues over time in the model of Bondarenko et al.

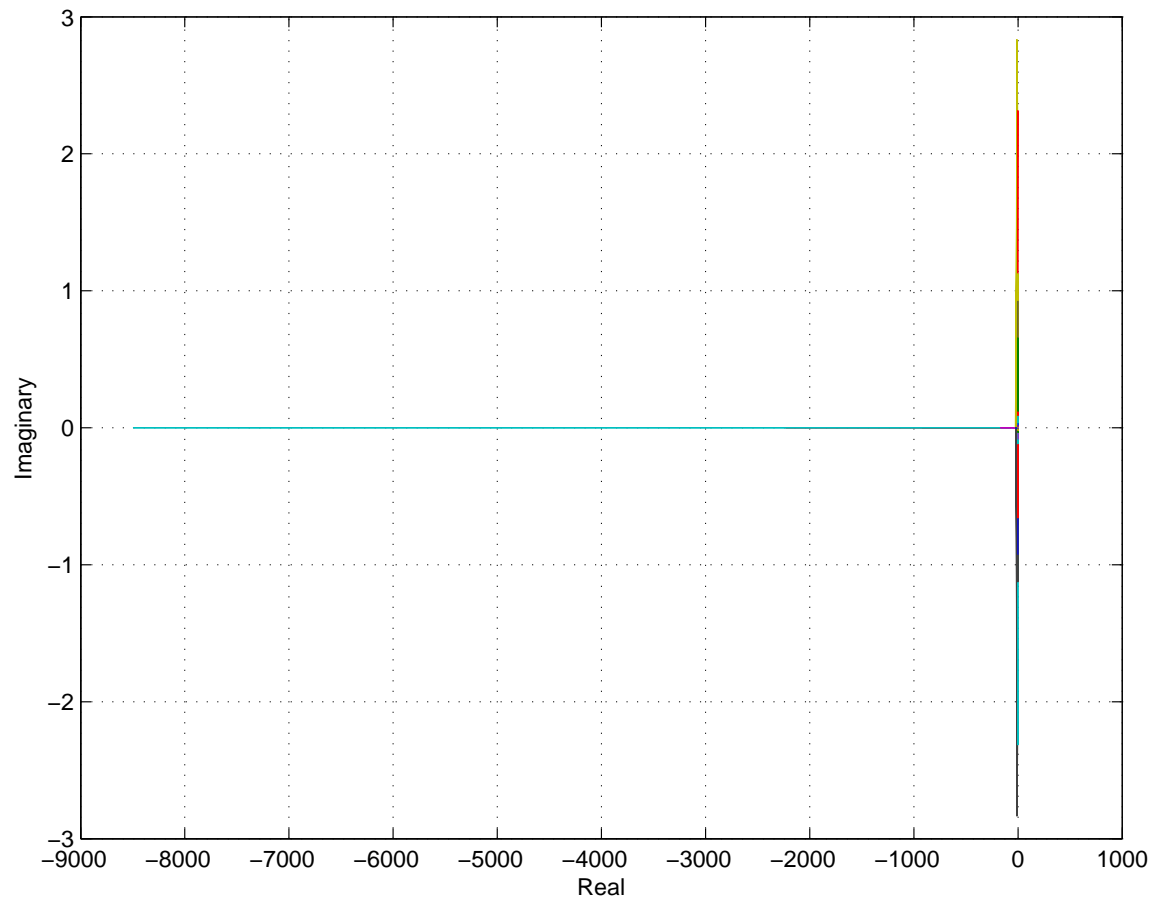


Figure 6: Plot of all eigenvalues at all times measured in the model of Bondarenko et al.

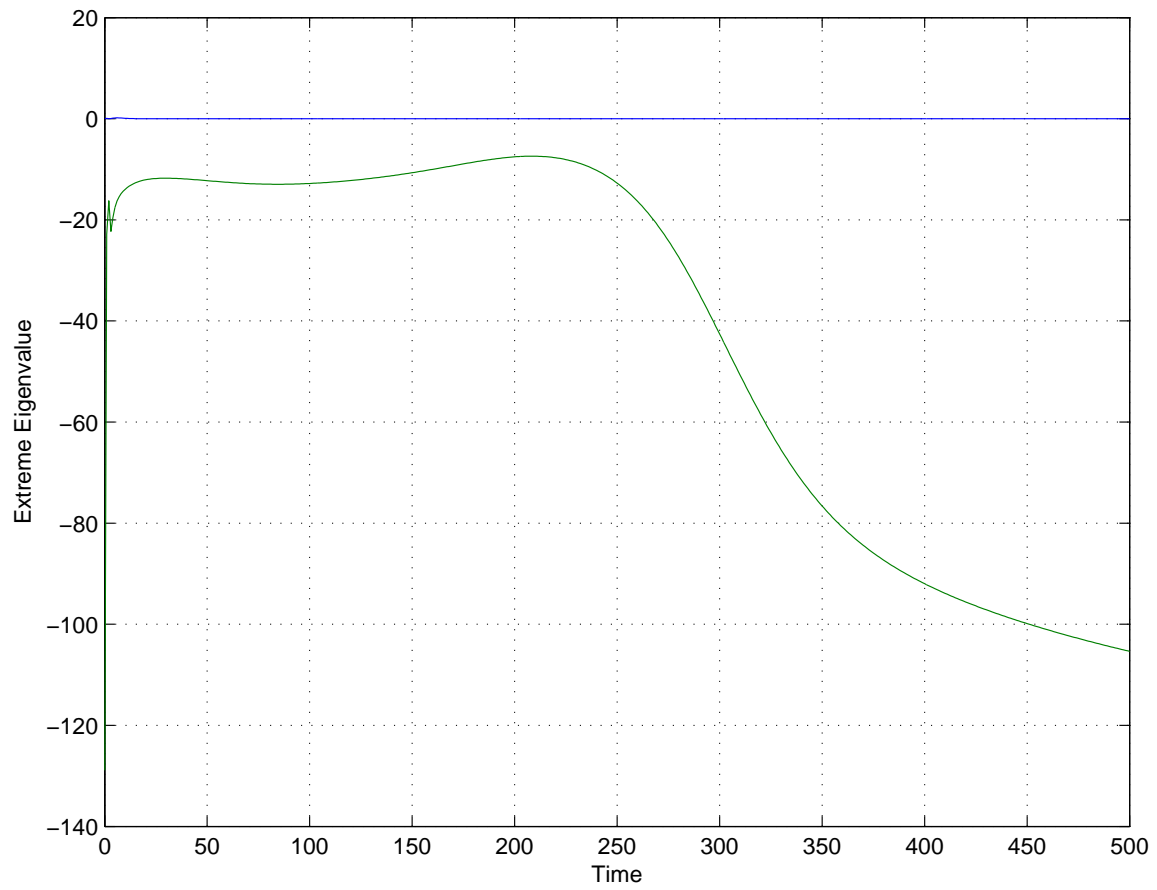


Figure 7: Extreme real eigenvalues in the model of Courtemanche et al.

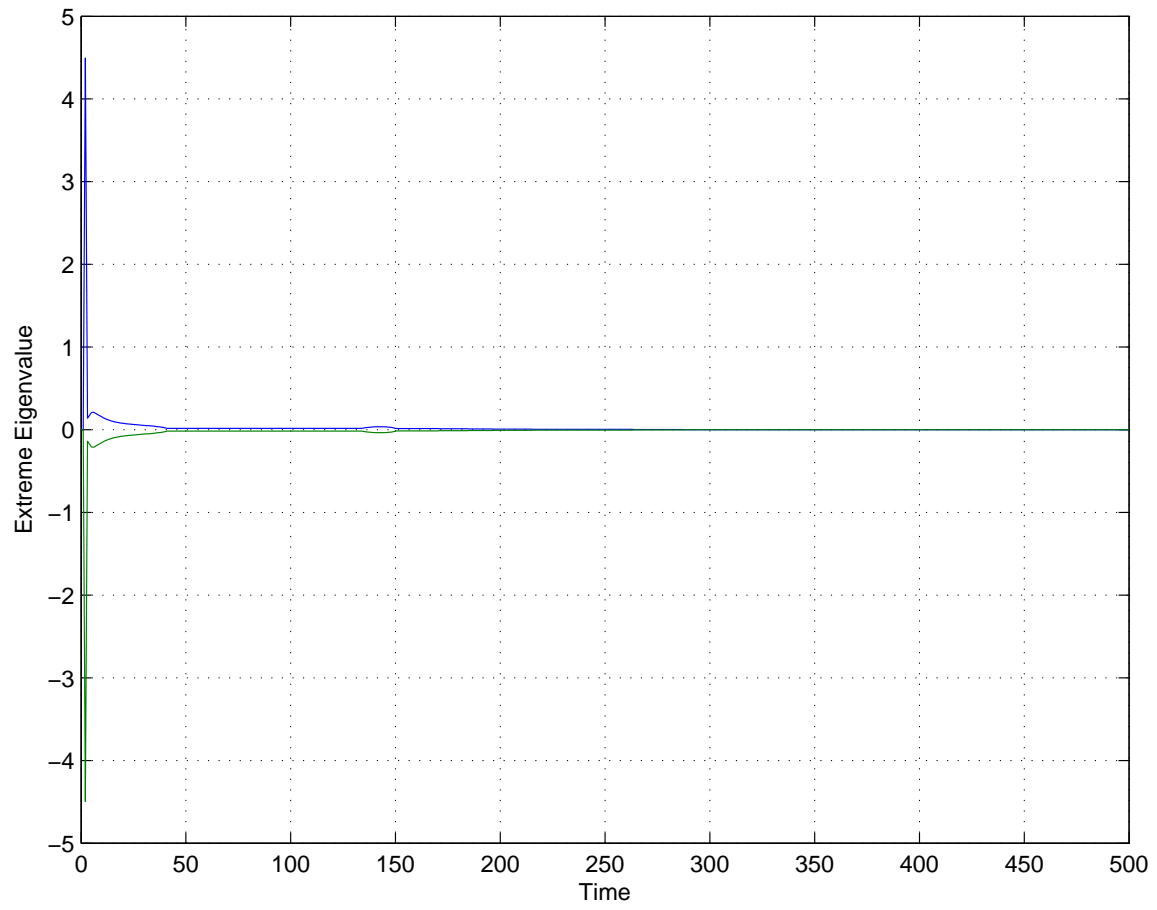


Figure 8: Extreme imaginary eigenvalues in the model of Courtemanche et al.

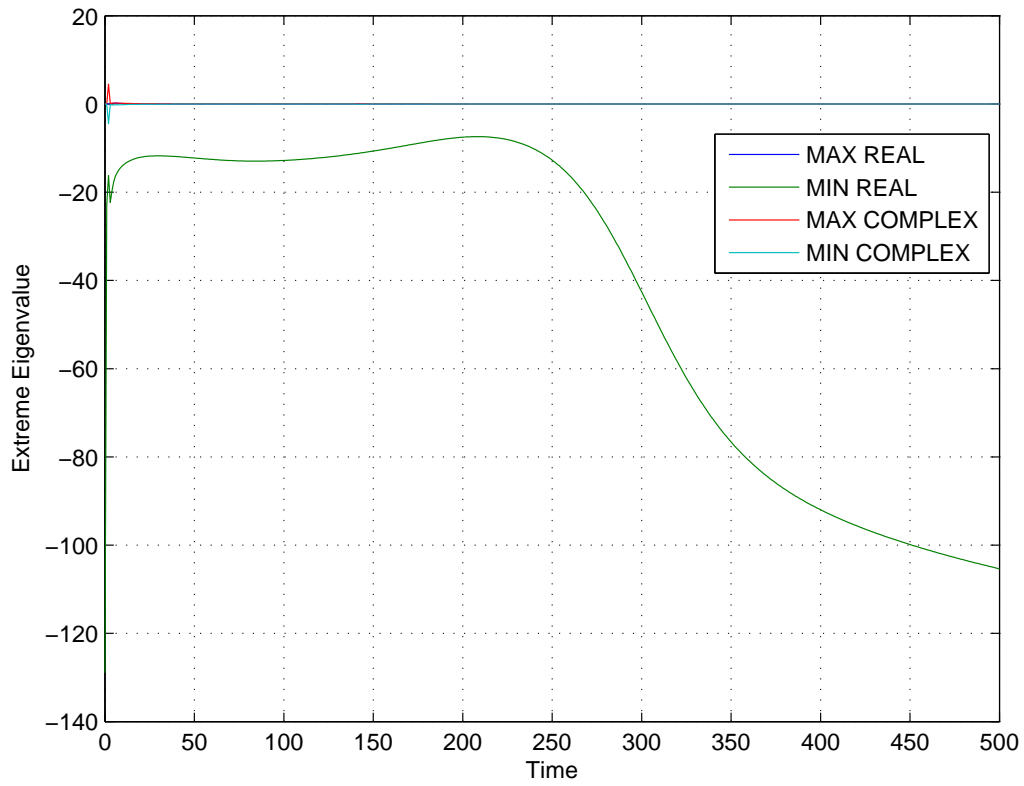


Figure 9: Extreme values of eigenvalues over time in the model of Courtemanche et al.

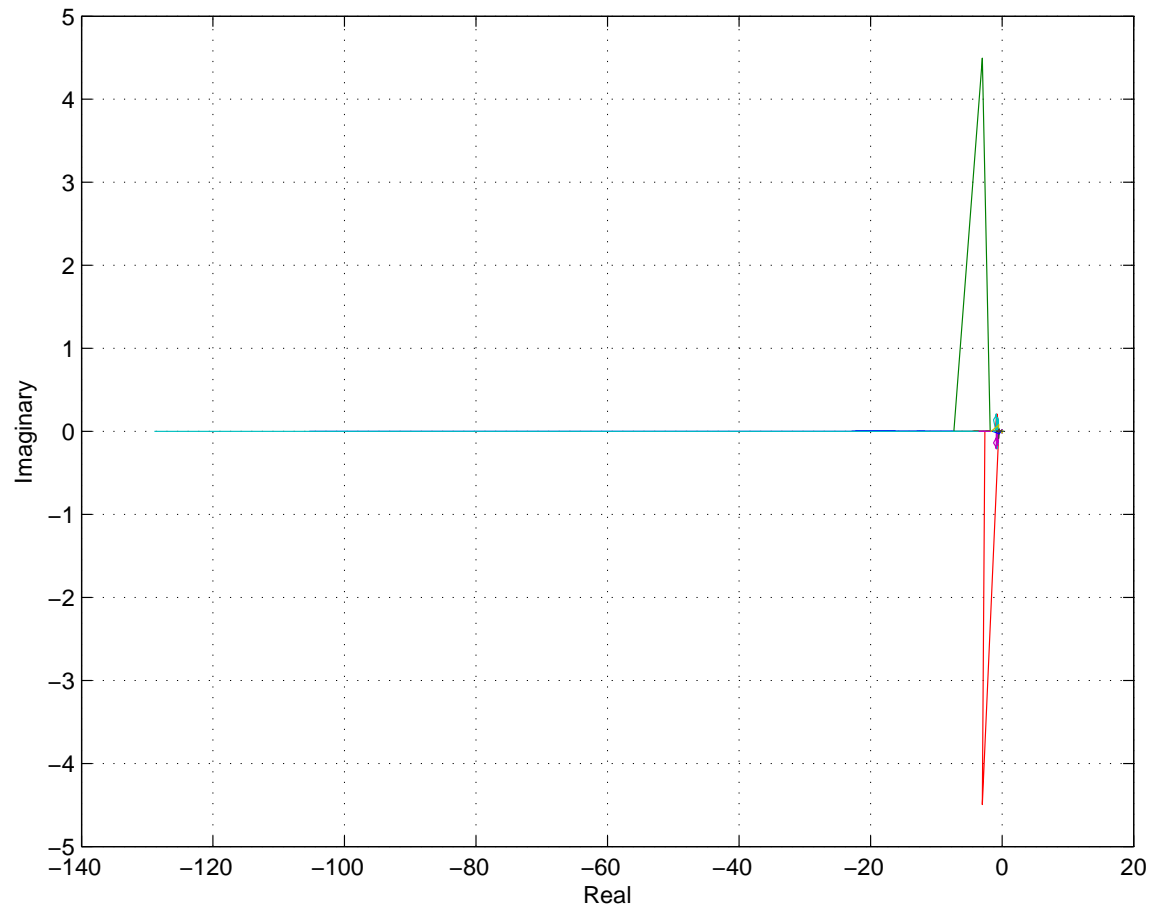


Figure 10: Plot of all eigenvalues at all times measured in the model of Courtemanche et al.

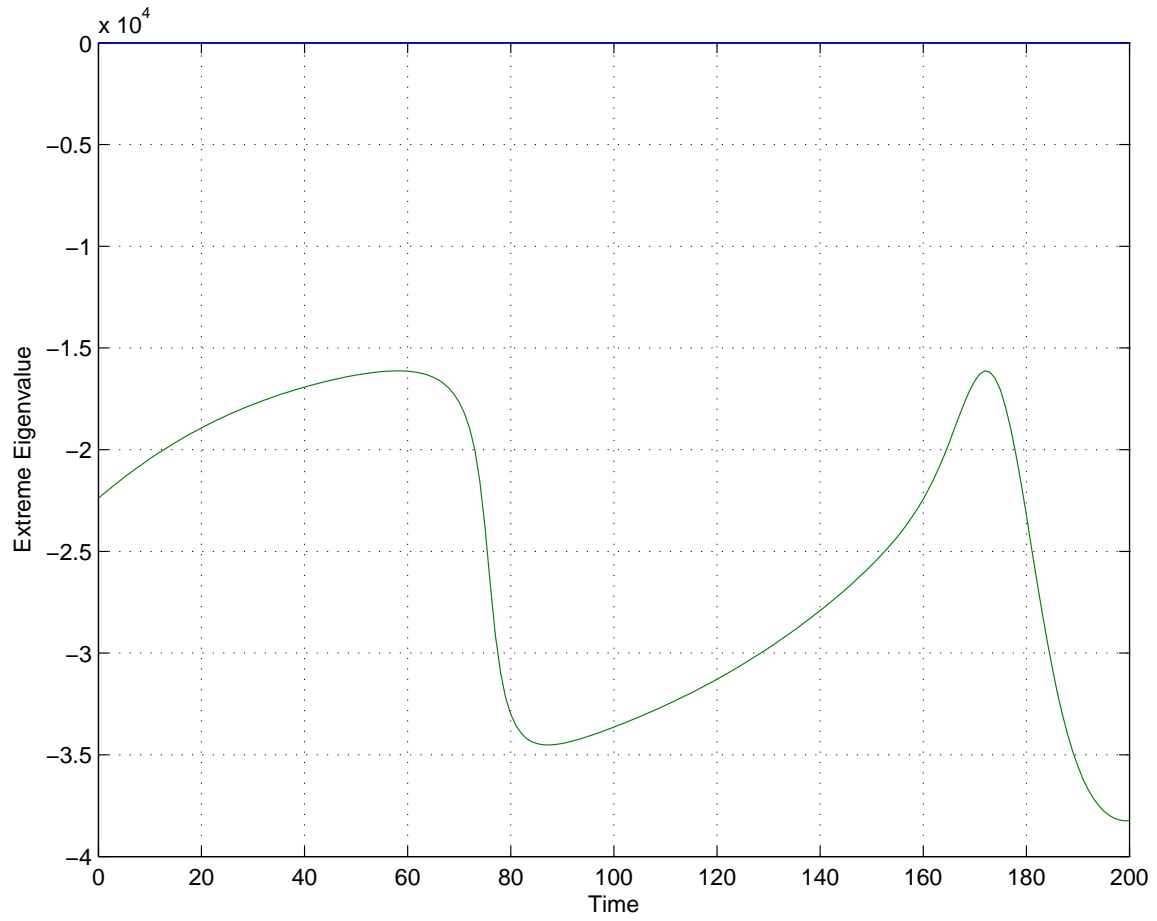


Figure 11: Extreme real eigenvalues in the model of Demir et al. (1994).

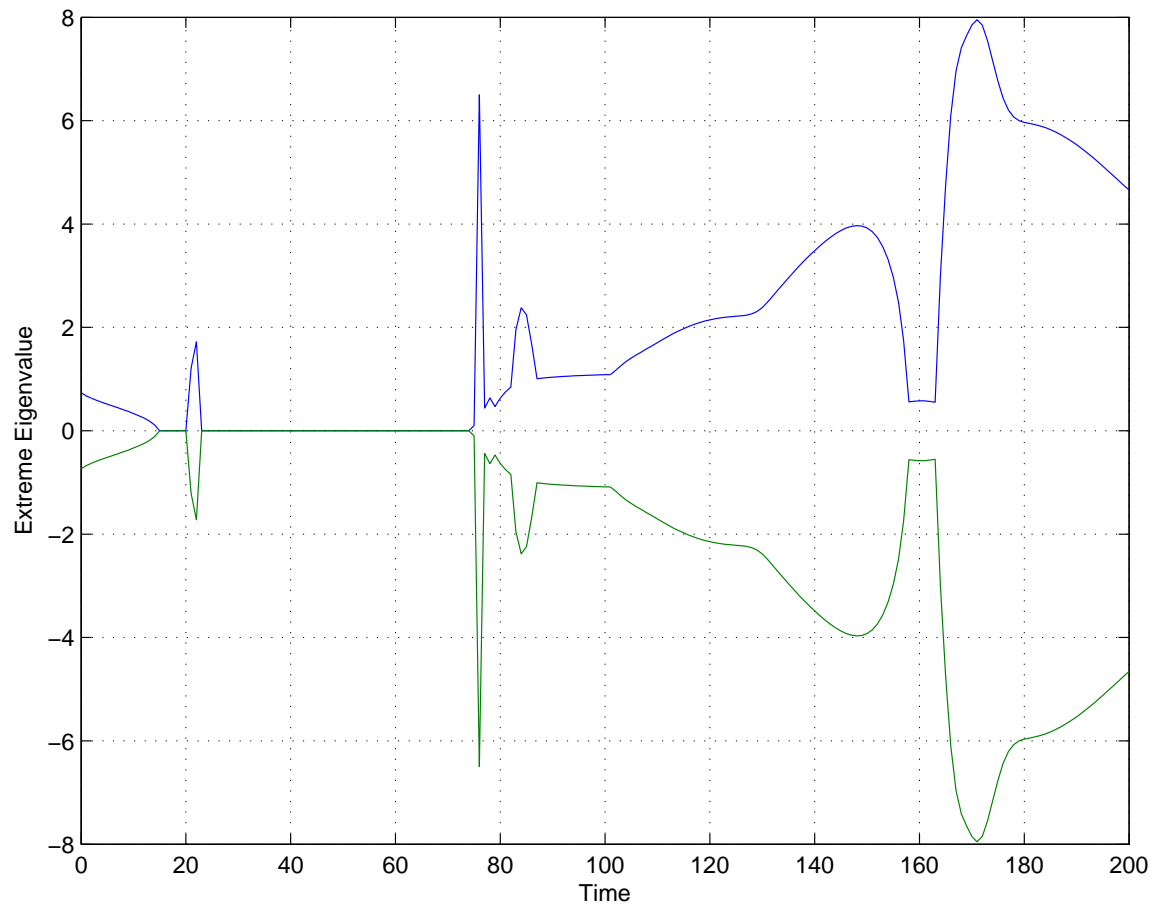


Figure 12: Extreme imaginary eigenvalues in the model of Demir et al. (1994).

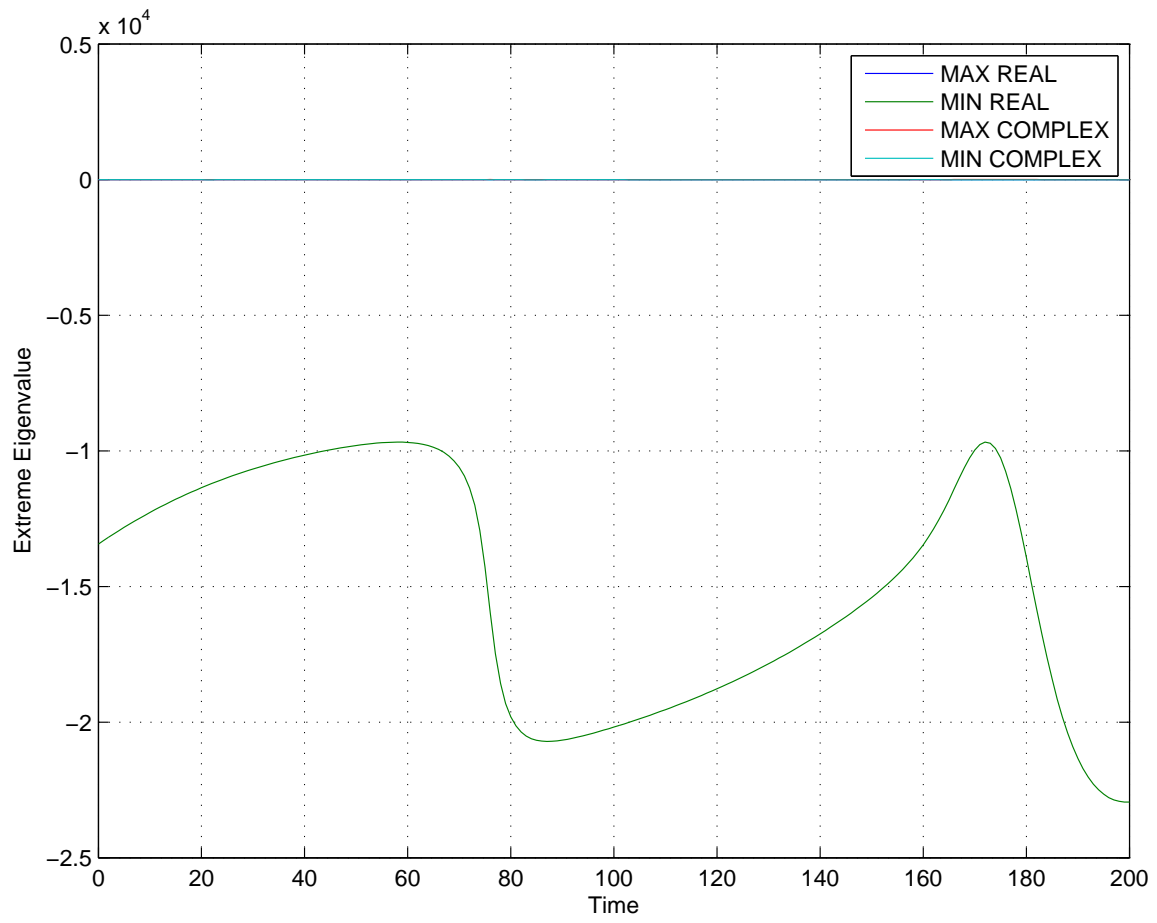


Figure 13: Extreme values of eigenvalues over time in the model of Demir et al. (1994).

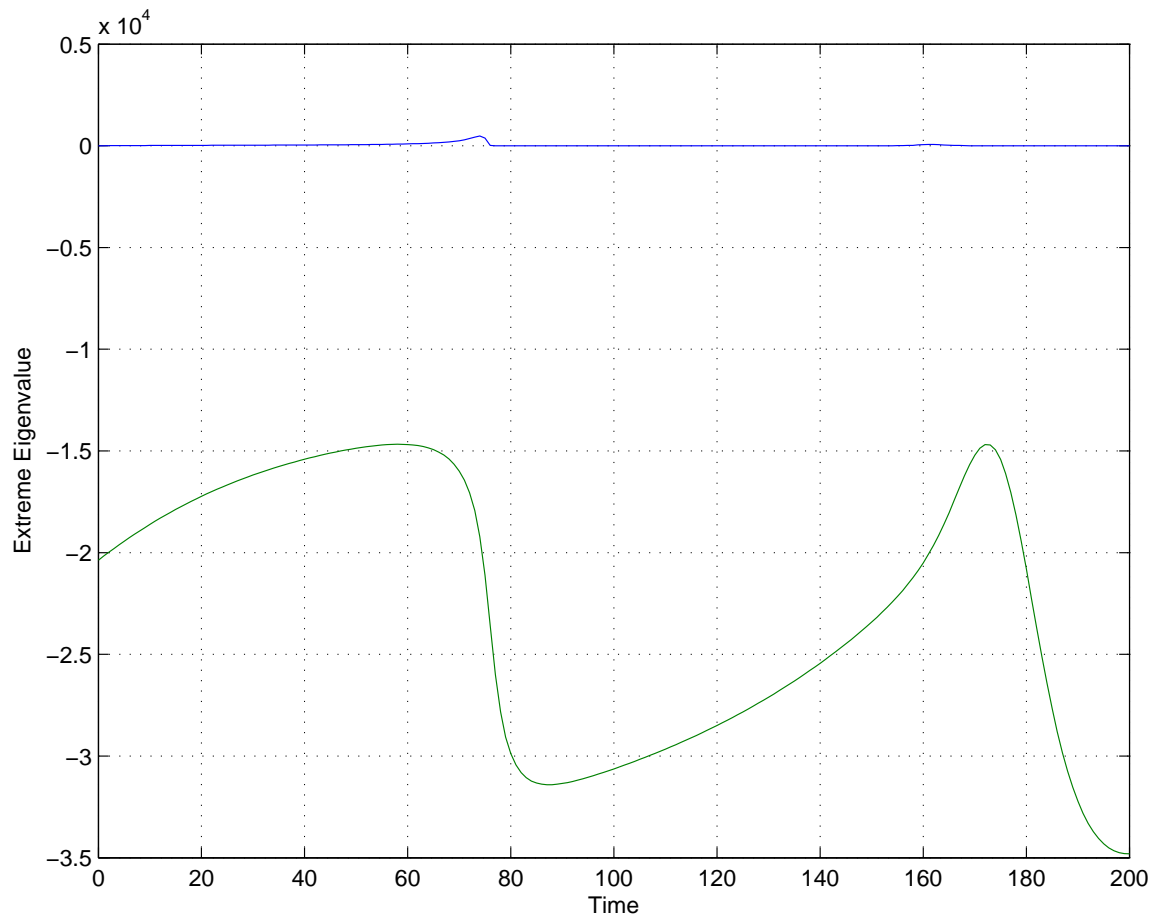


Figure 15: Extreme real eigenvalues in the model of Demir et al. (1999).

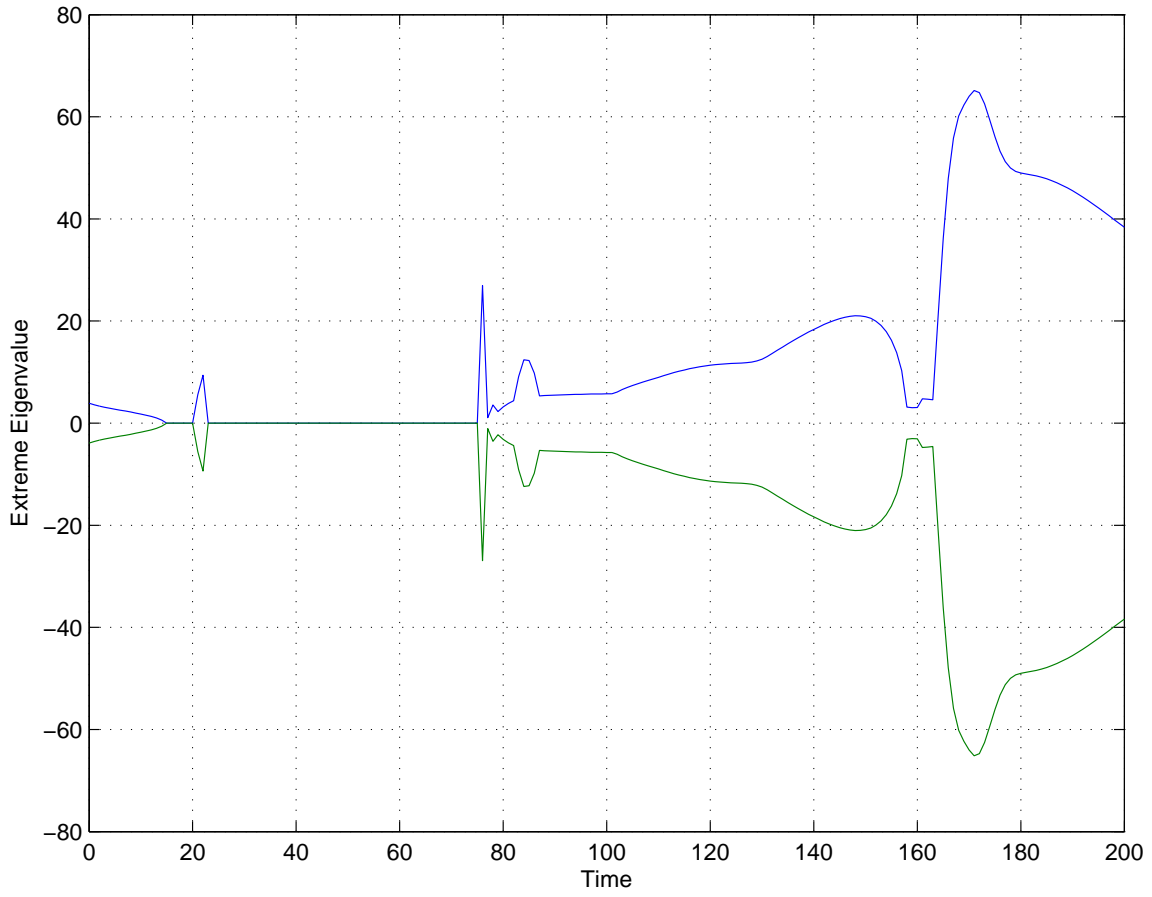


Figure 16: Extreme imaginary eigenvalues in the model of Demir et al. (1999).

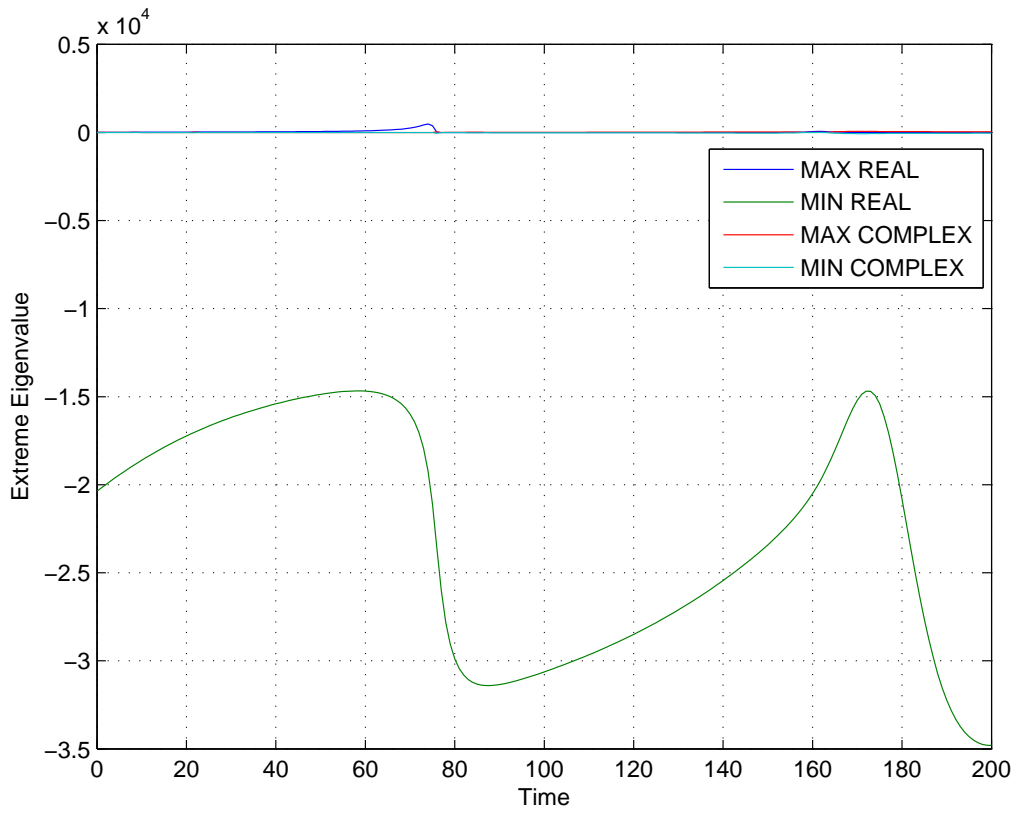


Figure 17: Extreme values of eigenvalues over time in the model of Demir et al. (1999).

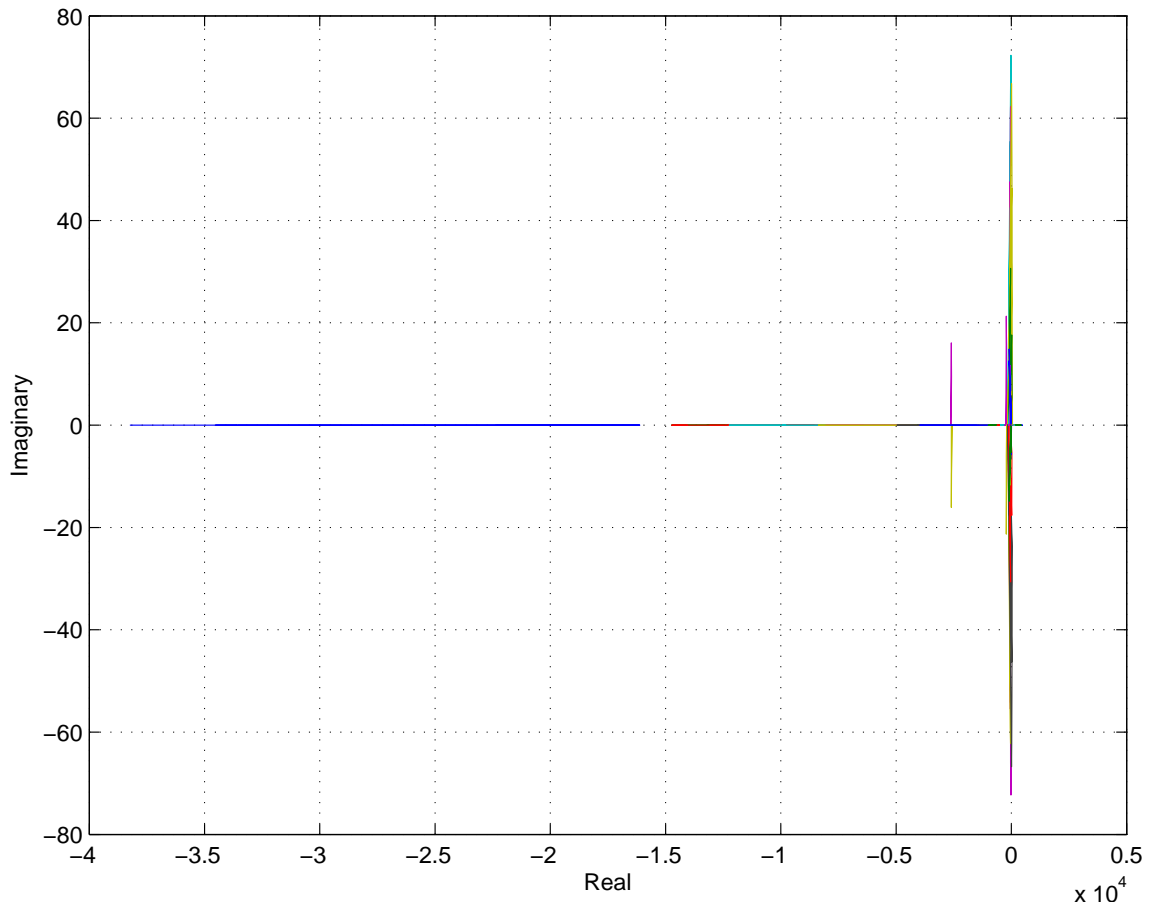


Figure 18: Plot of all eigenvalues at all times measured in the model of Demir et al. (1999).

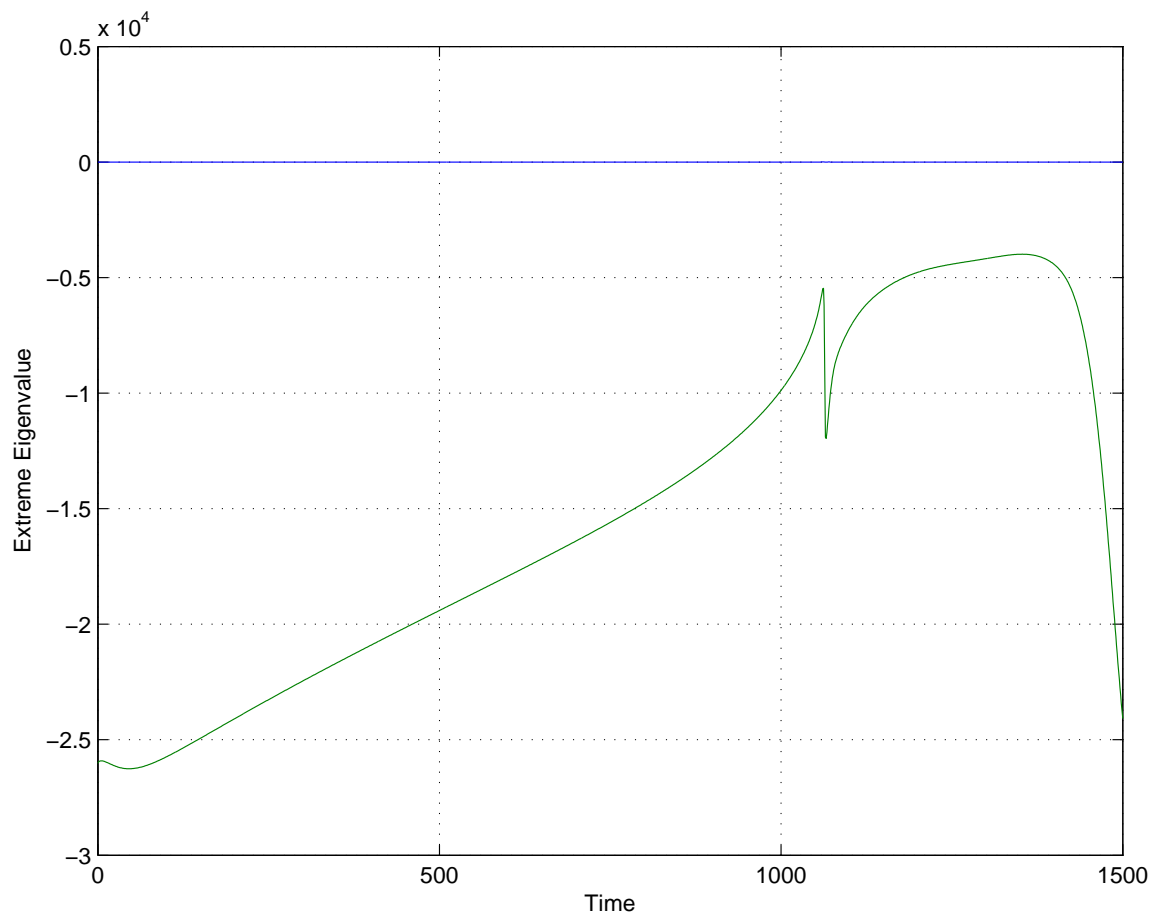


Figure 19: Extreme real eigenvalues in the DiFrancesco–Noble model (1985)

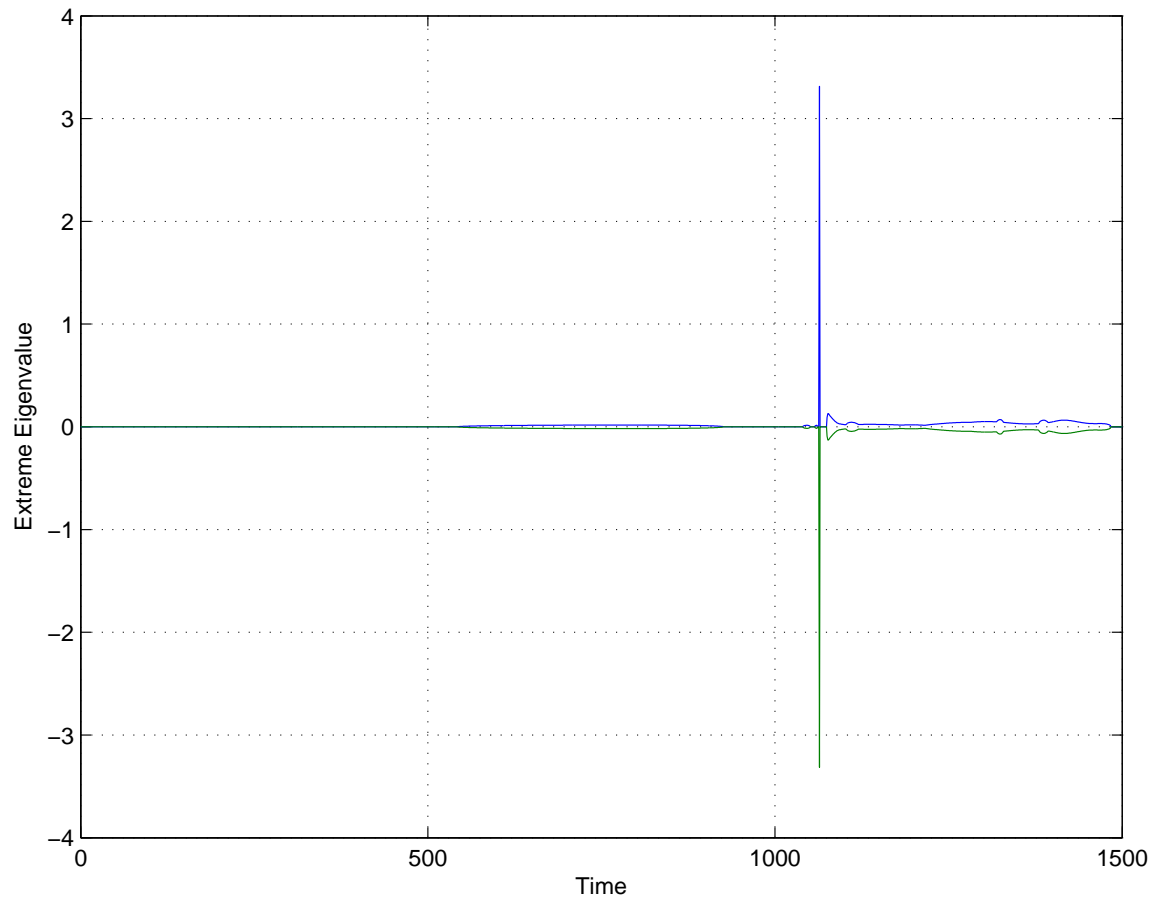


Figure 20: Extreme imaginary eigenvalues in the DiFrancesco–Noble model (1985).

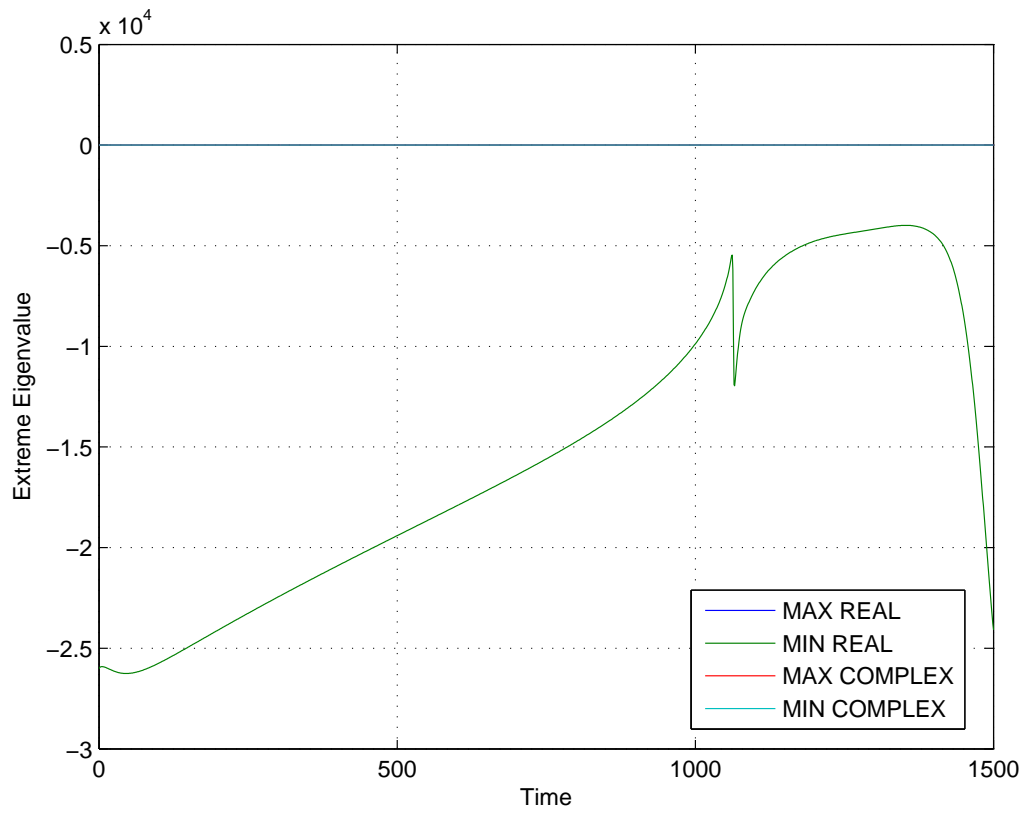


Figure 21: Extreme values of eigenvalues over time in the DiFrancesco–Noble model (1985).

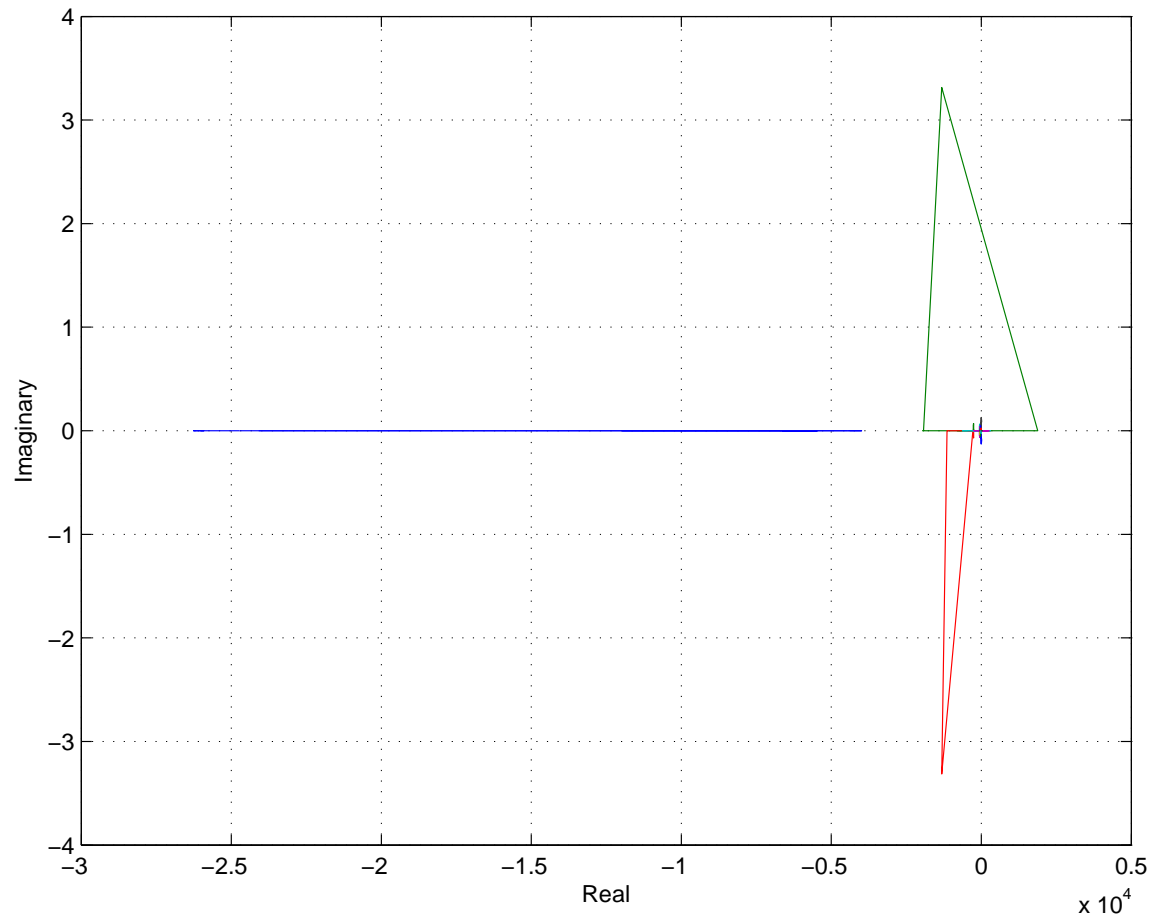


Figure 22: Plot of all eigenvalues at all times measured in the DiFrancesco–Noble model (1985).

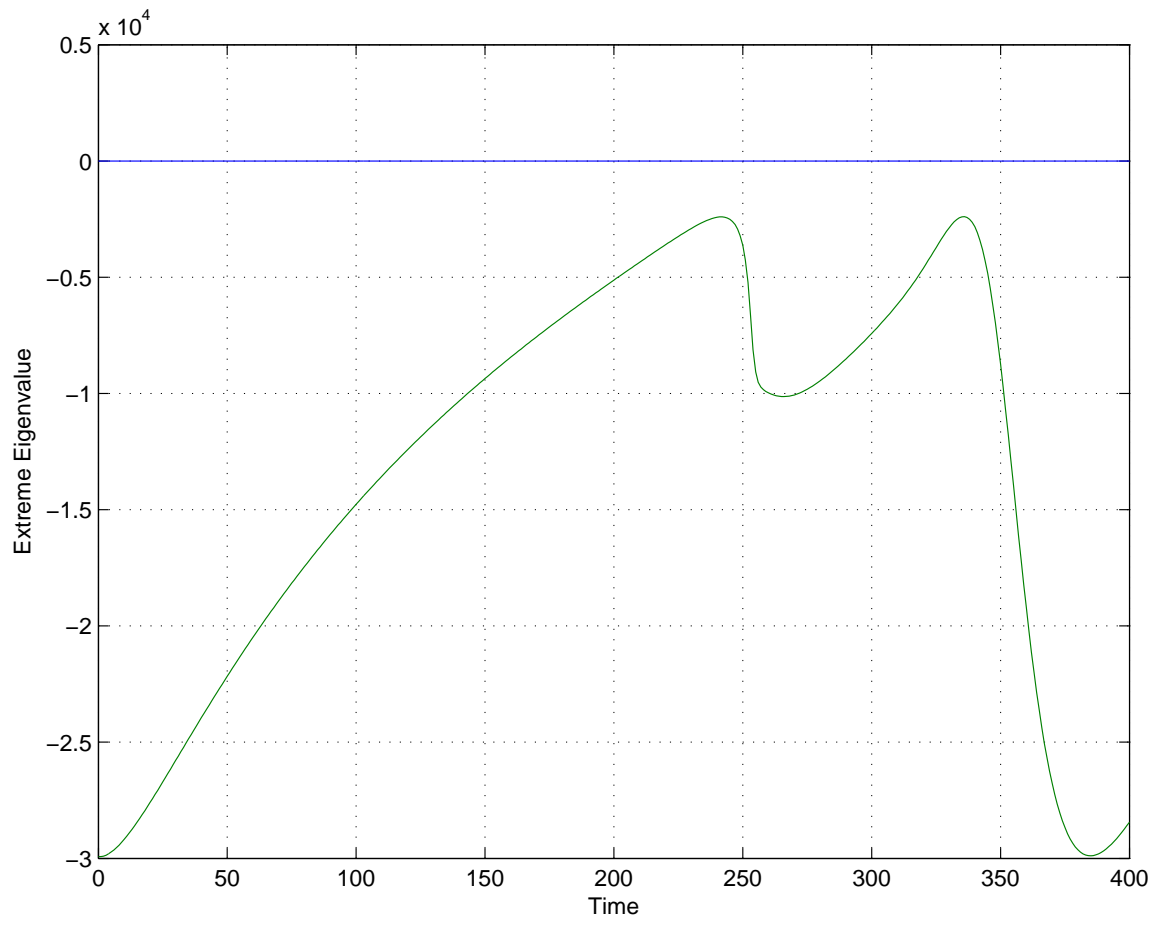


Figure 23: Extreme real eigenvalues in the model of Dokos et al.

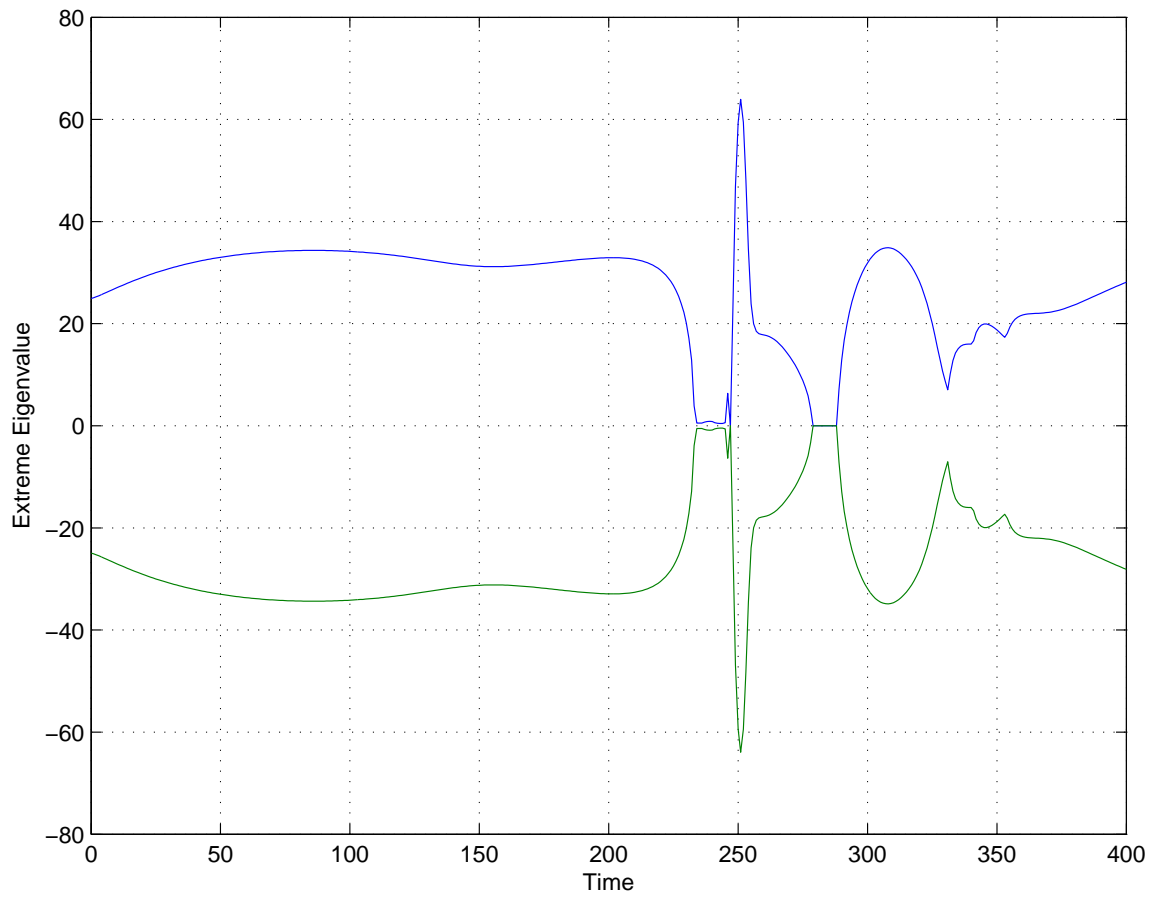


Figure 24: Extreme imaginary eigenvalues in the model of Dokos et al.

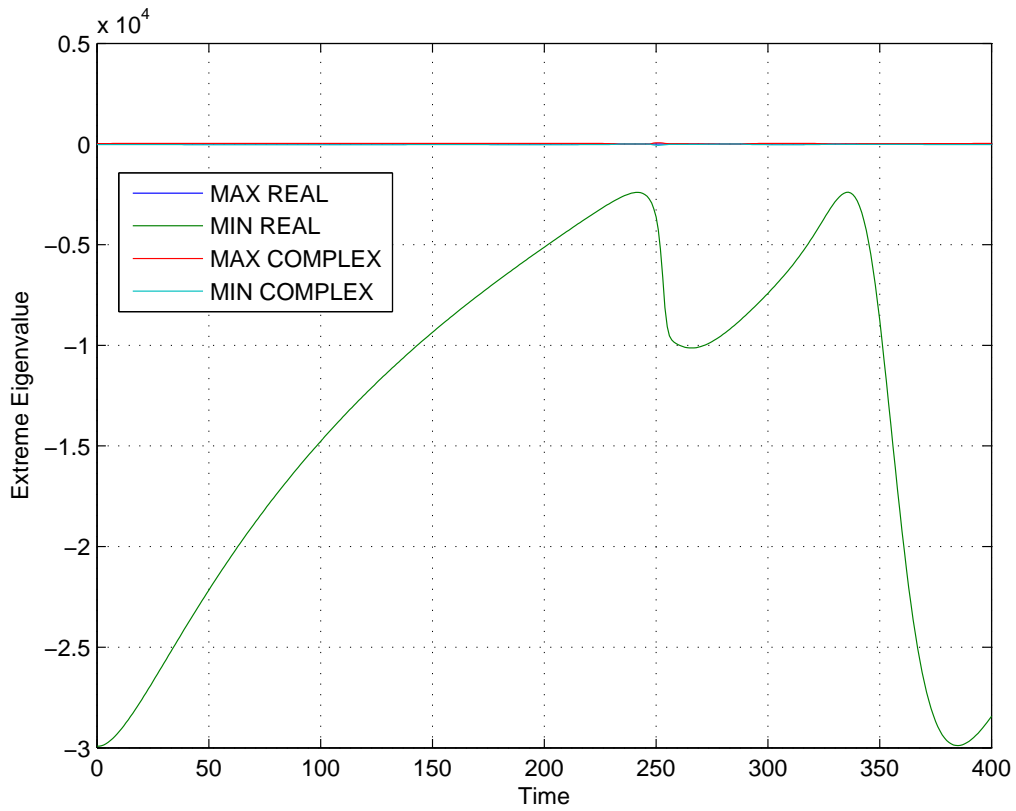


Figure 25: Extreme values of eigenvalues over time in the model of Dokos et al.

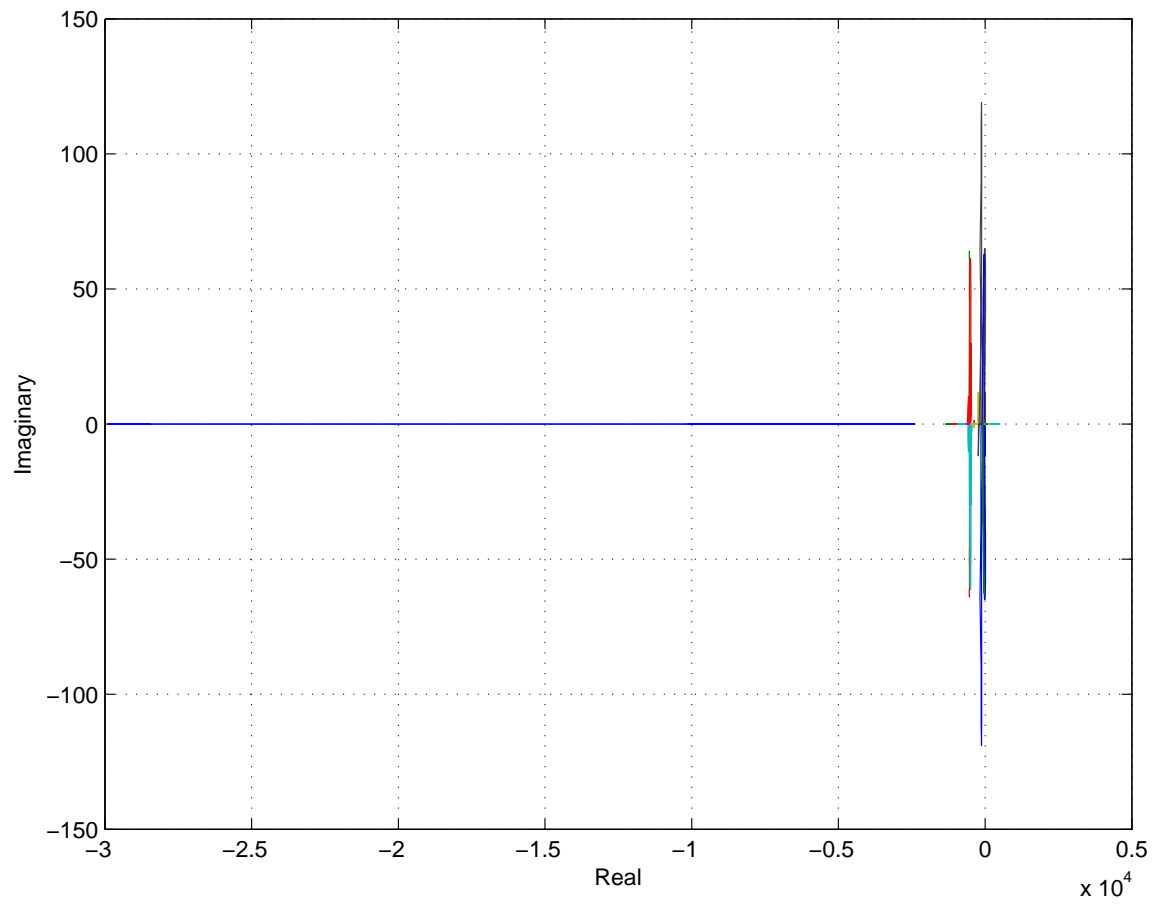


Figure 26: Plot of all eigenvalues at all times measured in the model of Dokos et al.

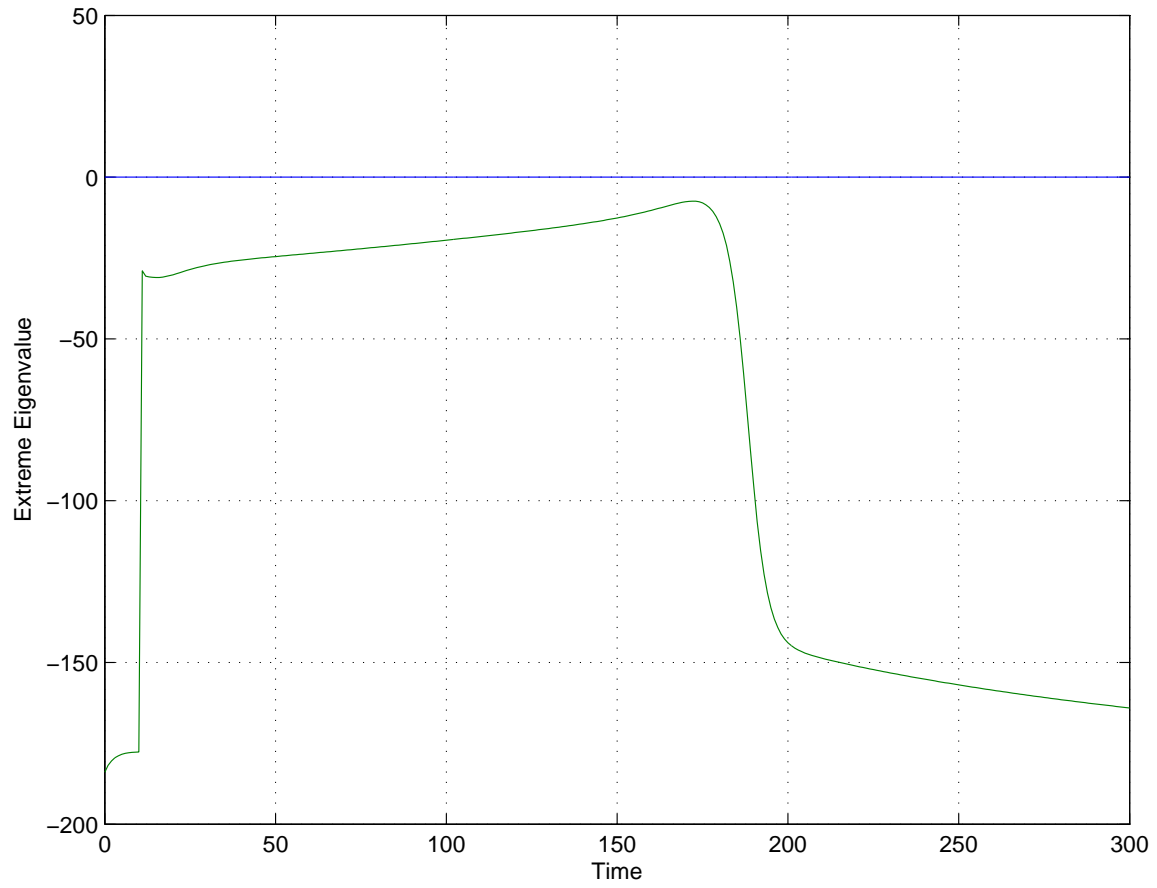


Figure 27: Extreme real eigenvalues in the Faber–Rudy model (2000).

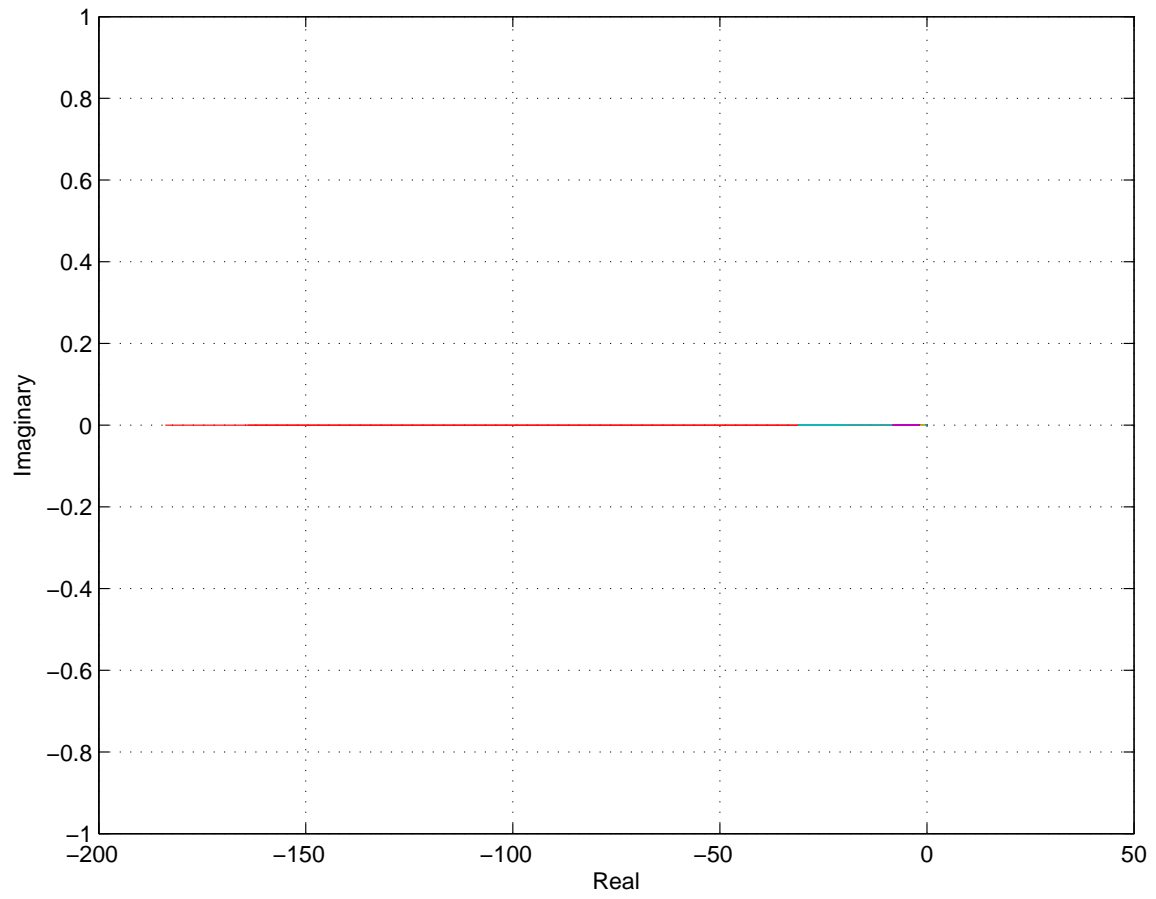


Figure 28: Plot of all eigenvalues at all times measured in the Faber–Rudy model (2000).

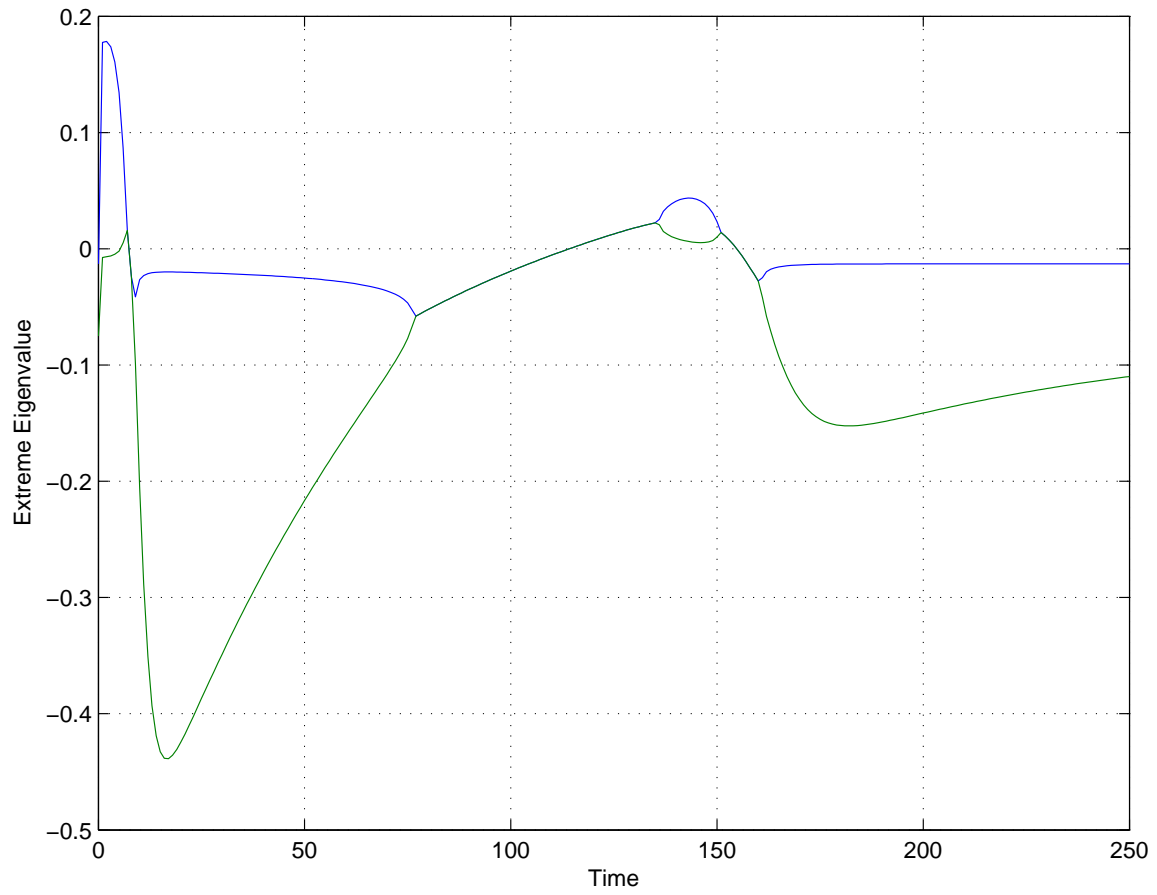


Figure 29: Extreme real eigenvalues in the FitzHugh-Nagumo model (1961).

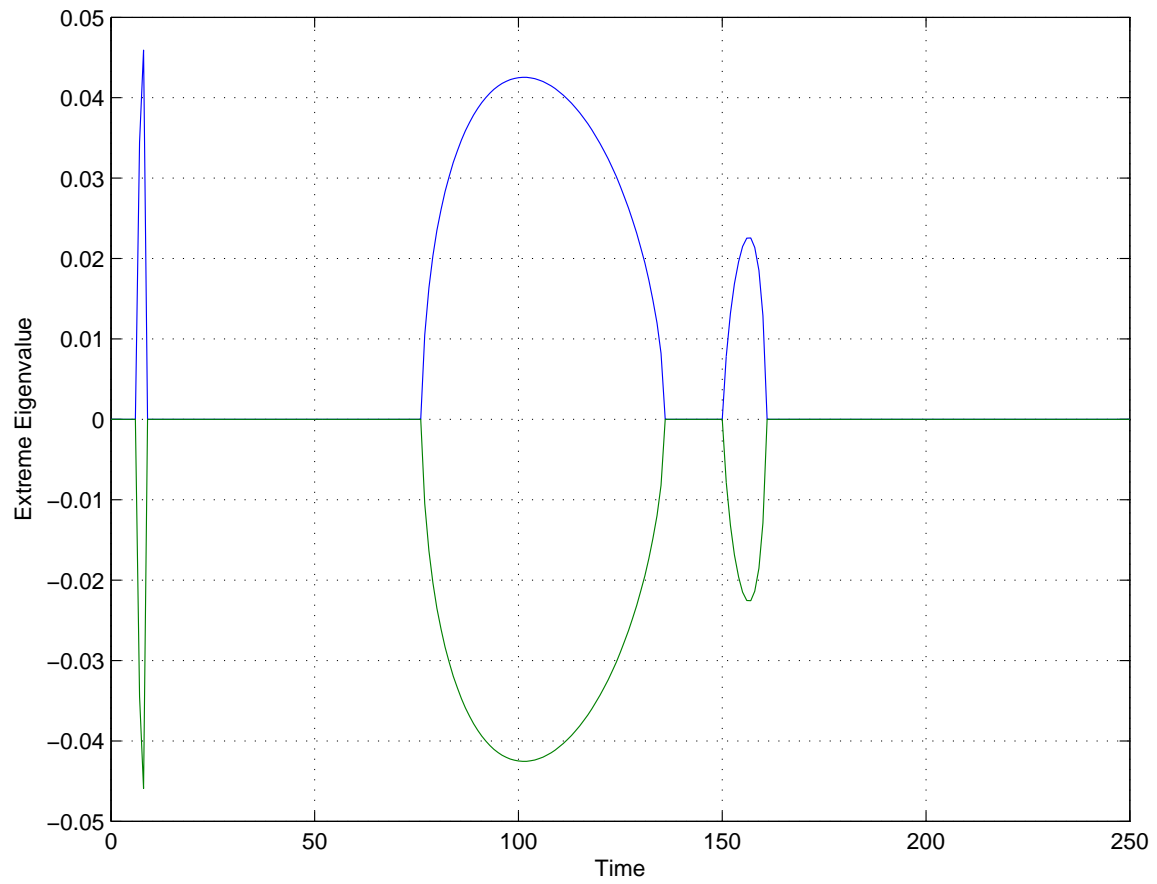


Figure 30: Extreme imaginary eigenvalues in the FitzHugh-Nagumo model (1961).

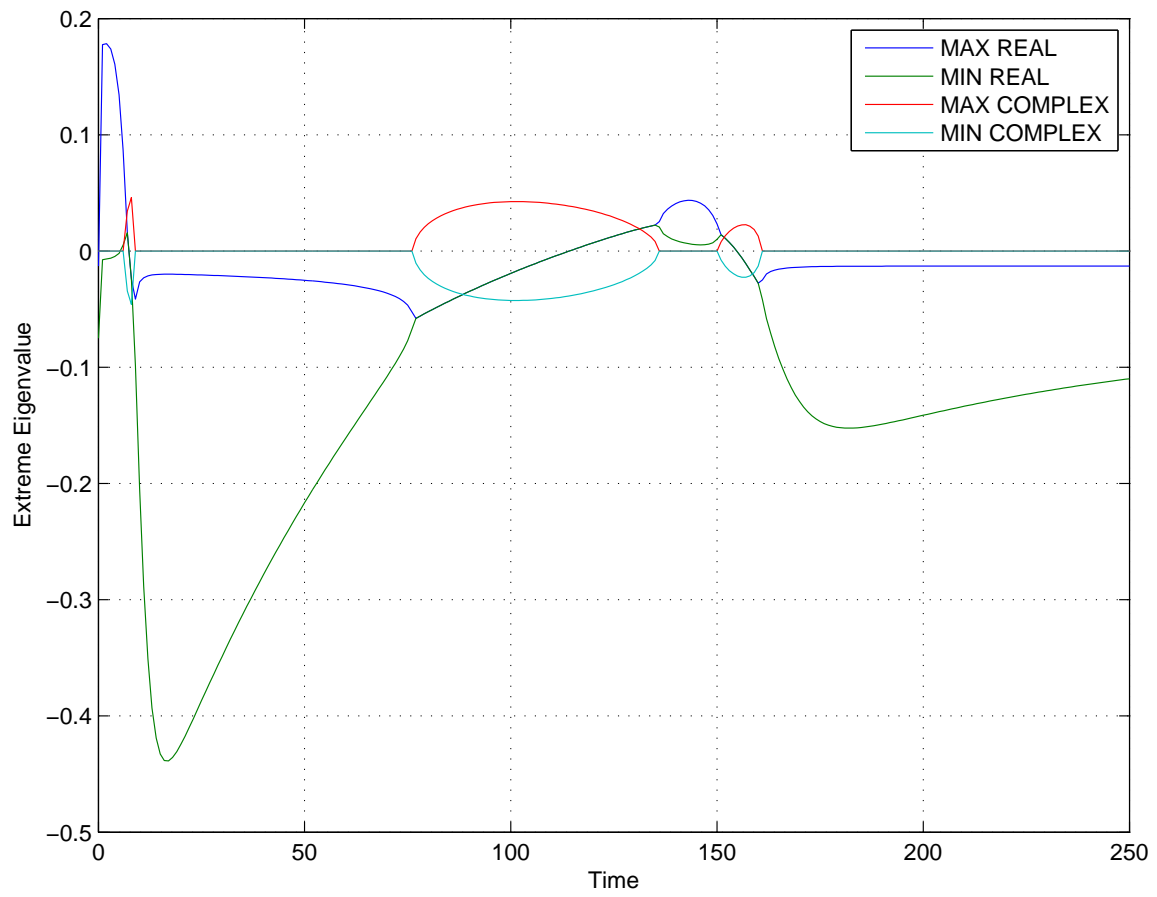


Figure 31: Extreme values of eigenvalues over time in the FitzHugh-Nagumo model (1961).

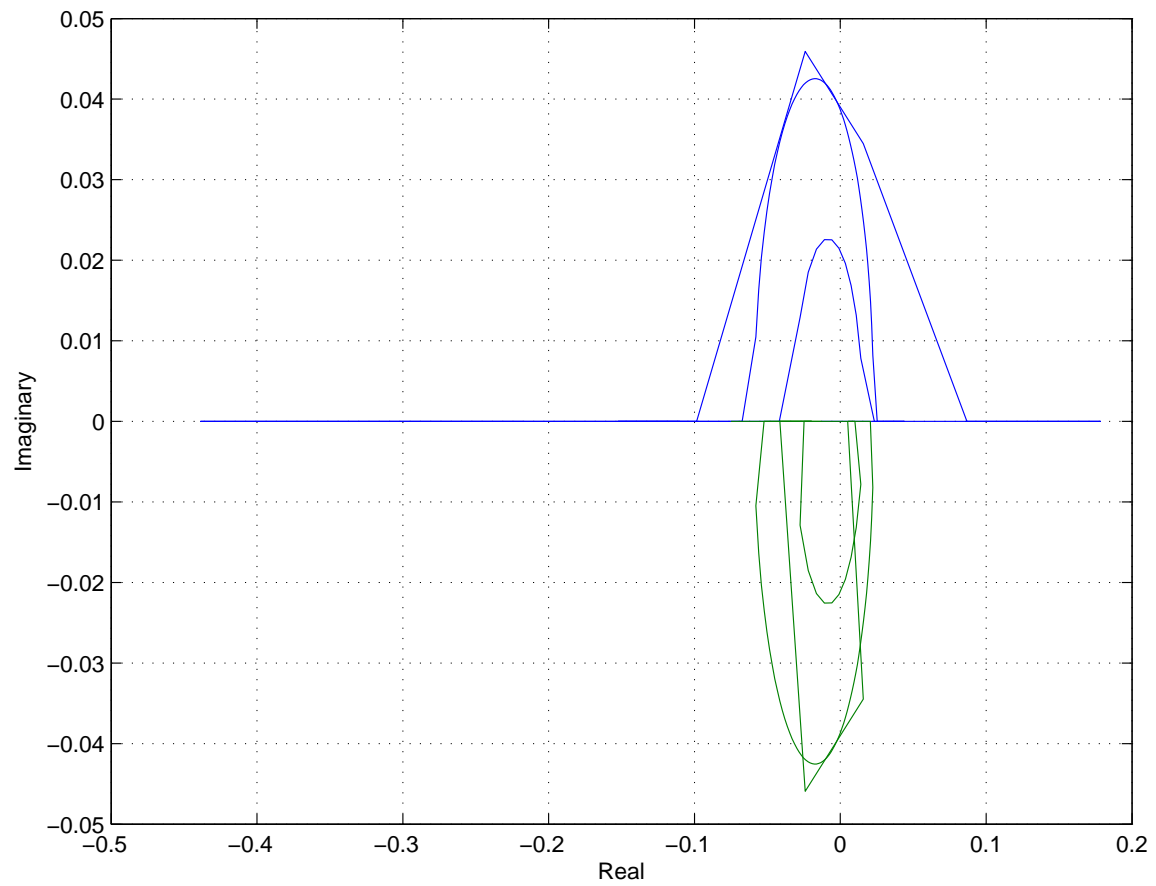


Figure 32: Plot of all eigenvalues at all times measured in the FitzHugh-Nagumo model (1961).

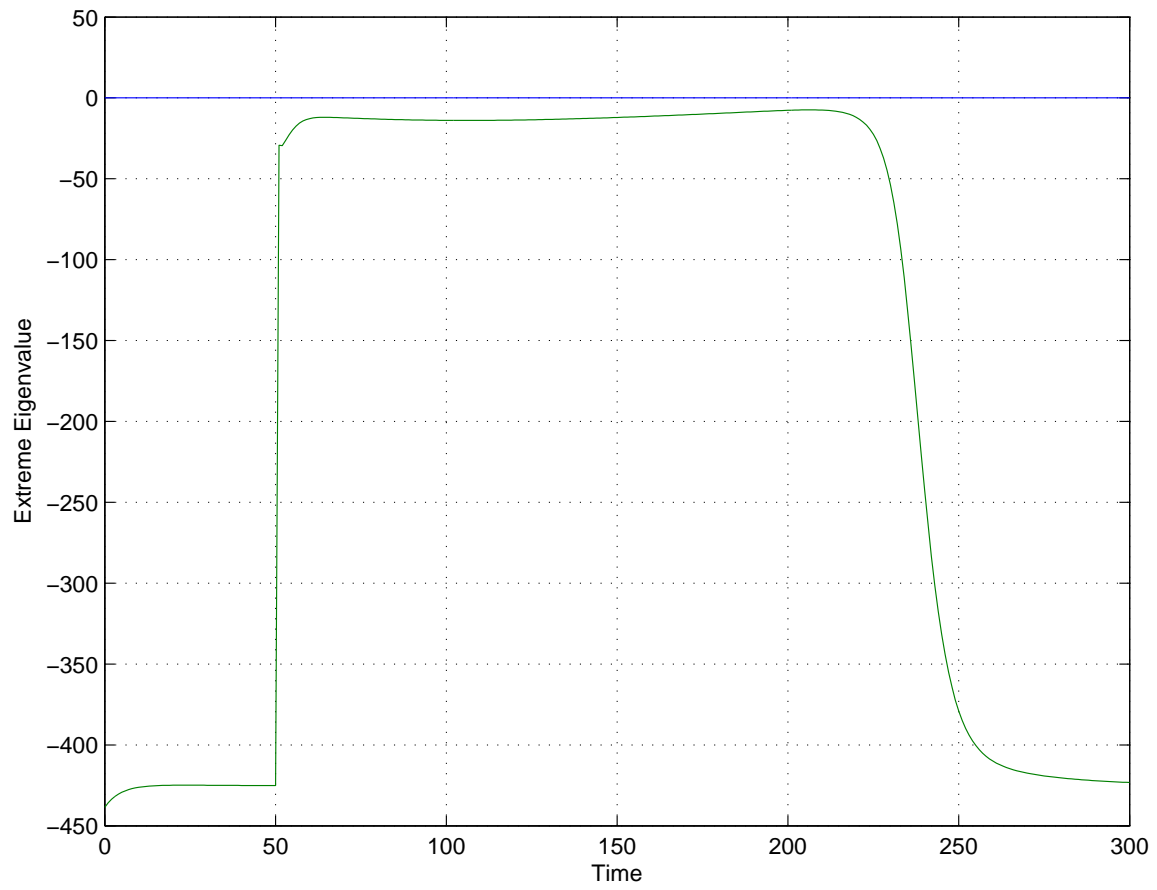


Figure 33: Extreme real eigenvalues in the model of Fox et al. (2002)

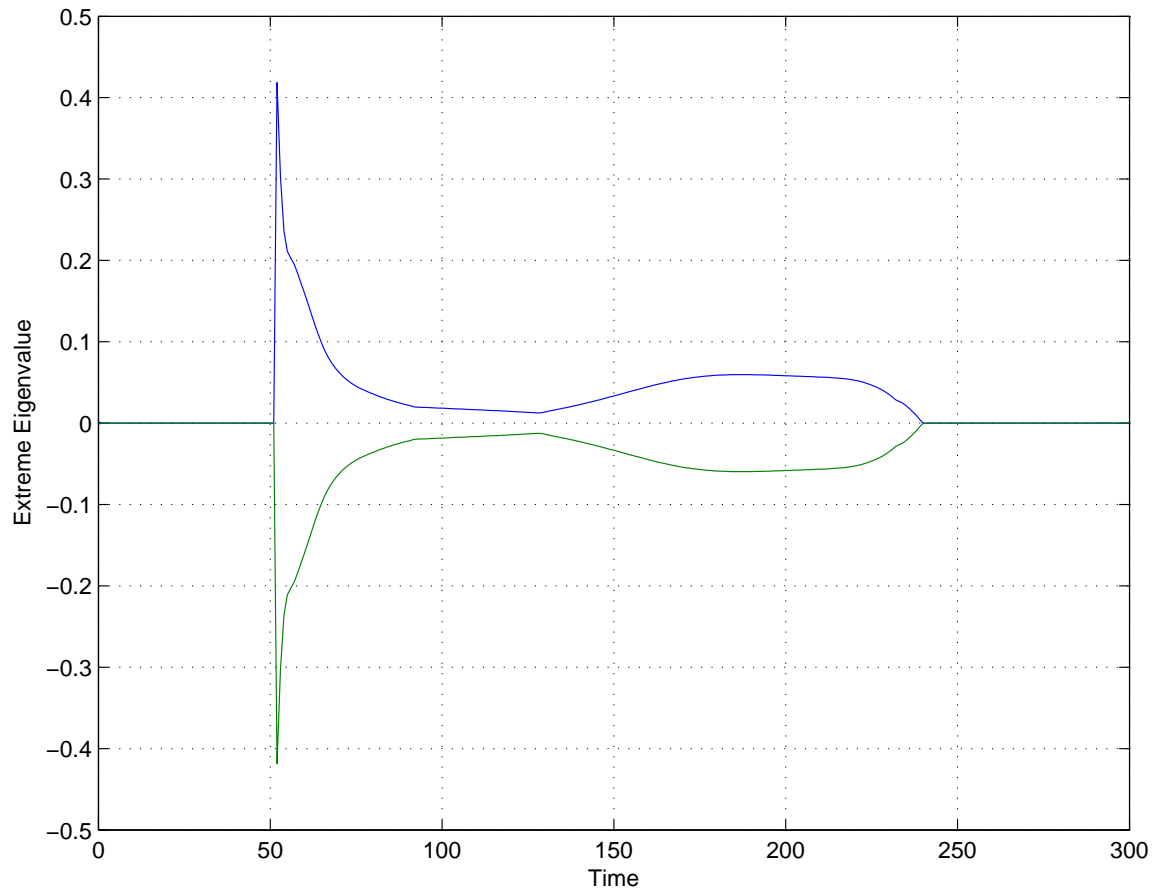


Figure 34: Extreme imaginary eigenvalues in the model of Fox et al. (2002).

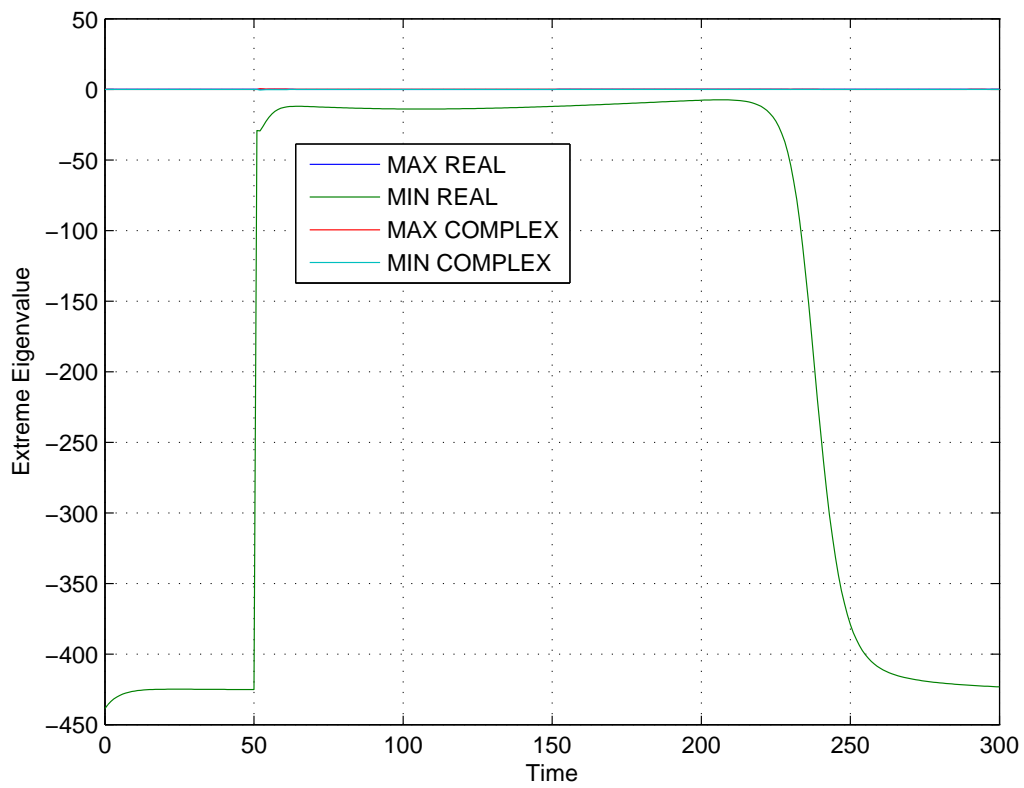


Figure 35: Extreme values of eigenvalues over time in the model of Fox et al. (2002).

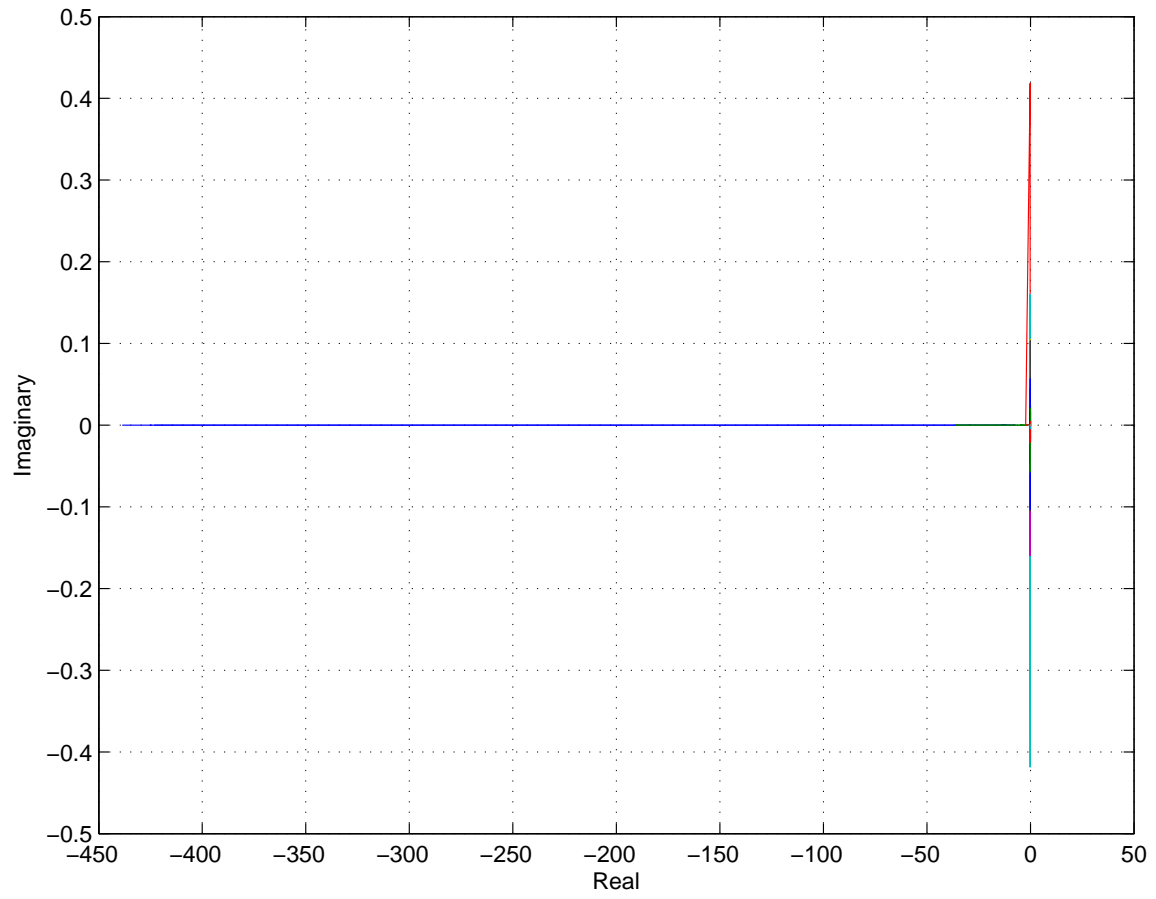


Figure 36: Plot of all eigenvalues at all times measured in the model of Fox et al. (2002).

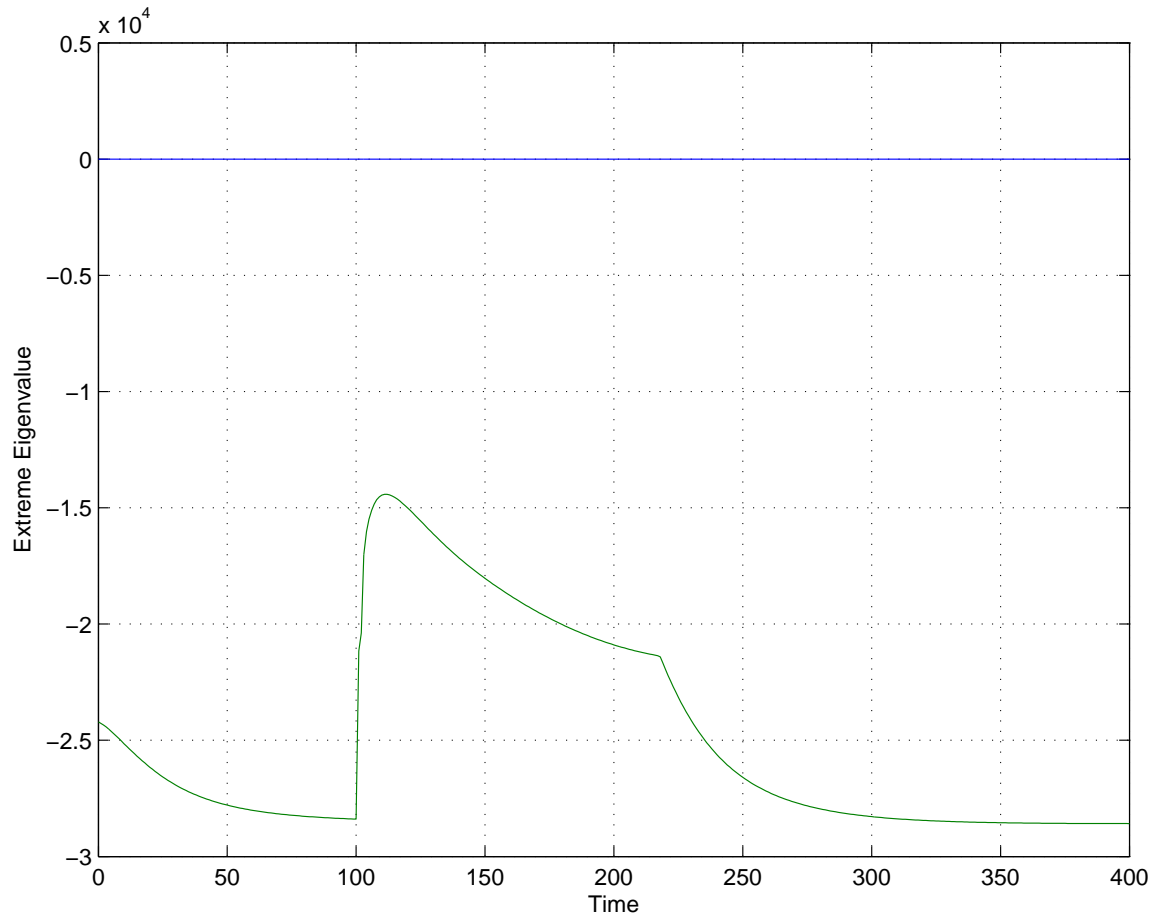


Figure 37: Extreme real eigenvalues in the Hilgemann–Noble model (1987).

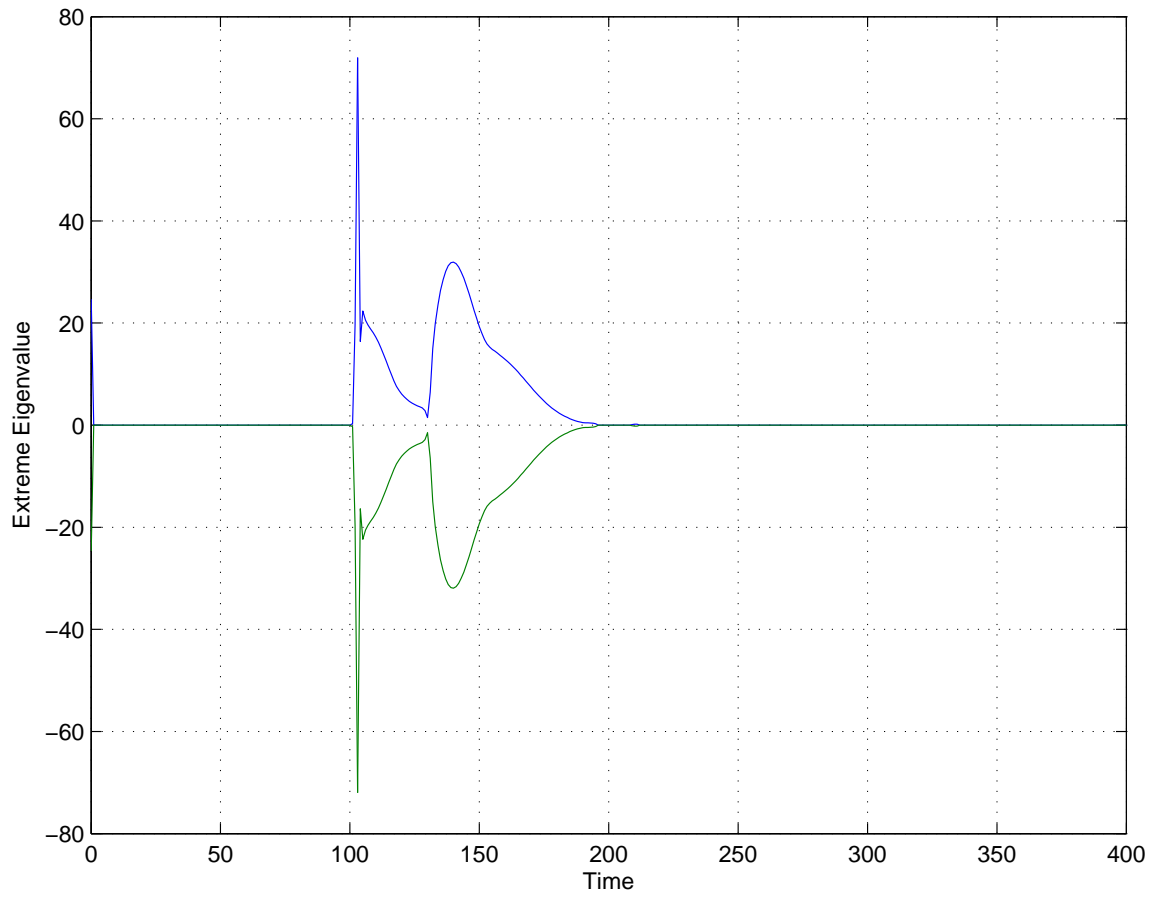


Figure 38: Extreme imaginary eigenvalues in the Hilgemann–Noble model (1987).

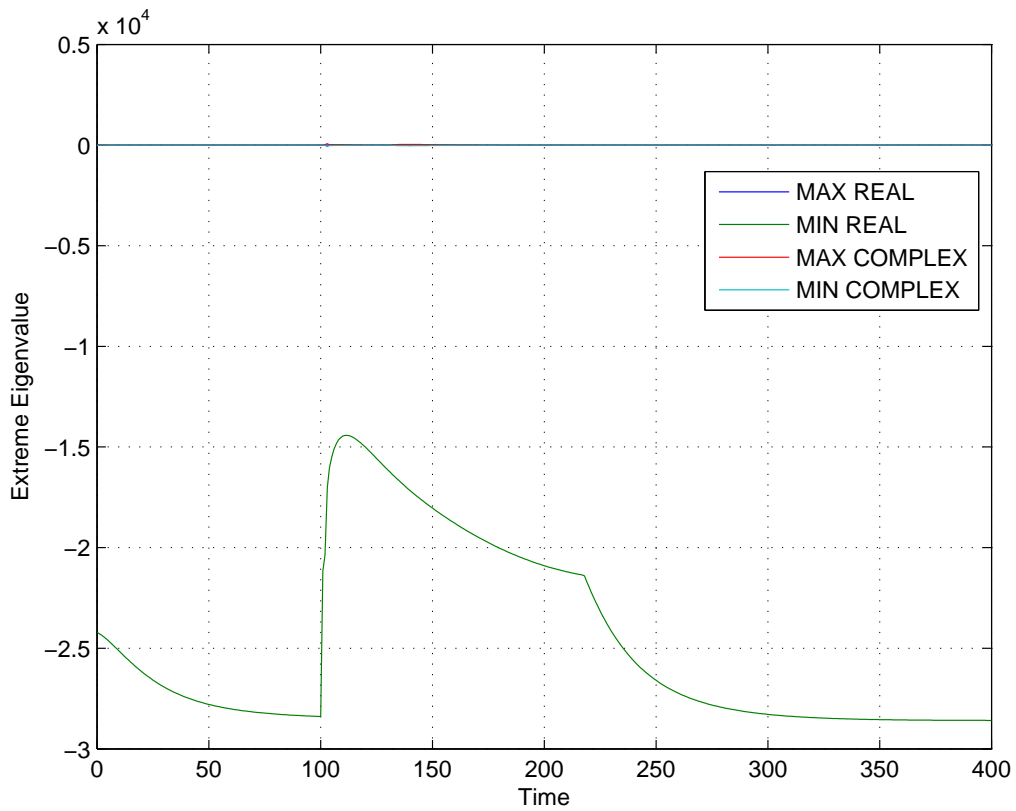


Figure 39: Extreme values of eigenvalues over time in the Hilgemann–Noble model (1987).

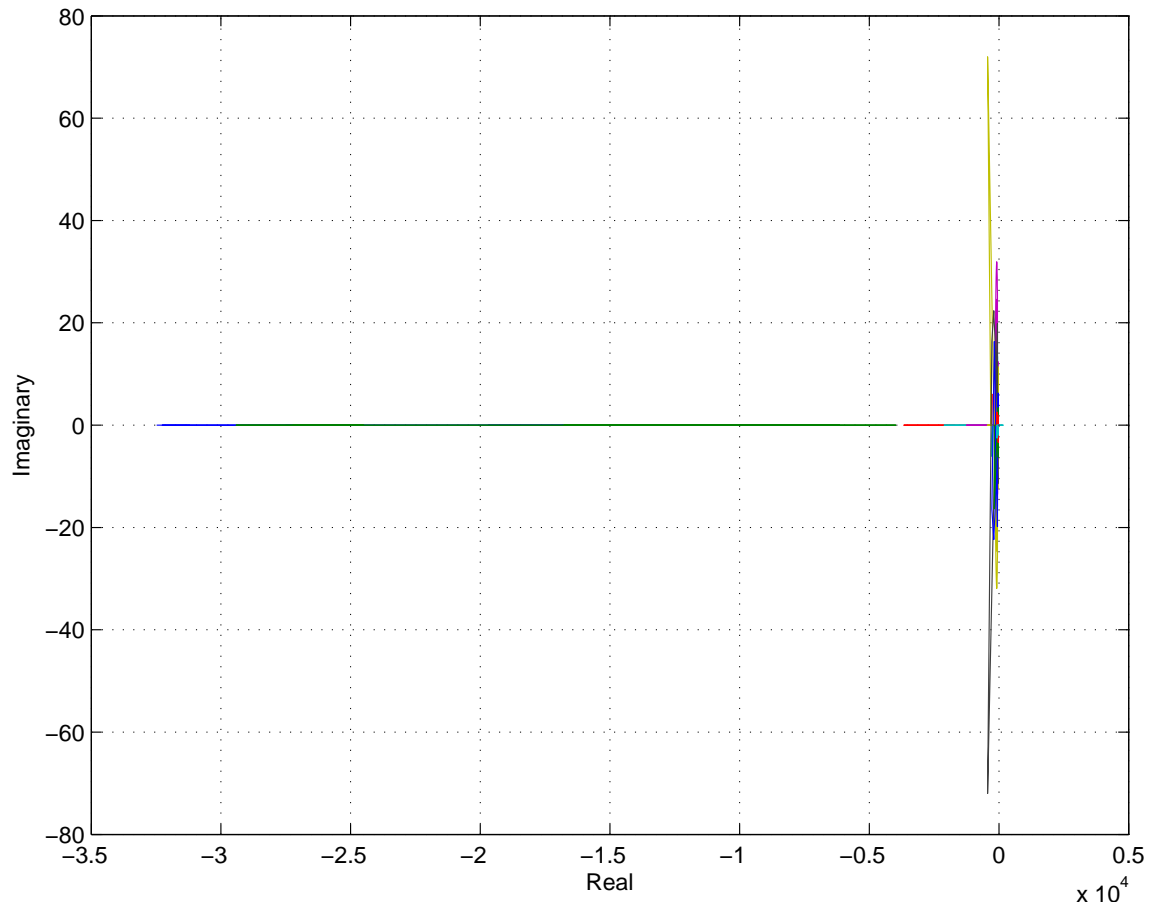


Figure 40: Plot of all eigenvalues at all times measured in the Hilgemann–Noble model (1987).

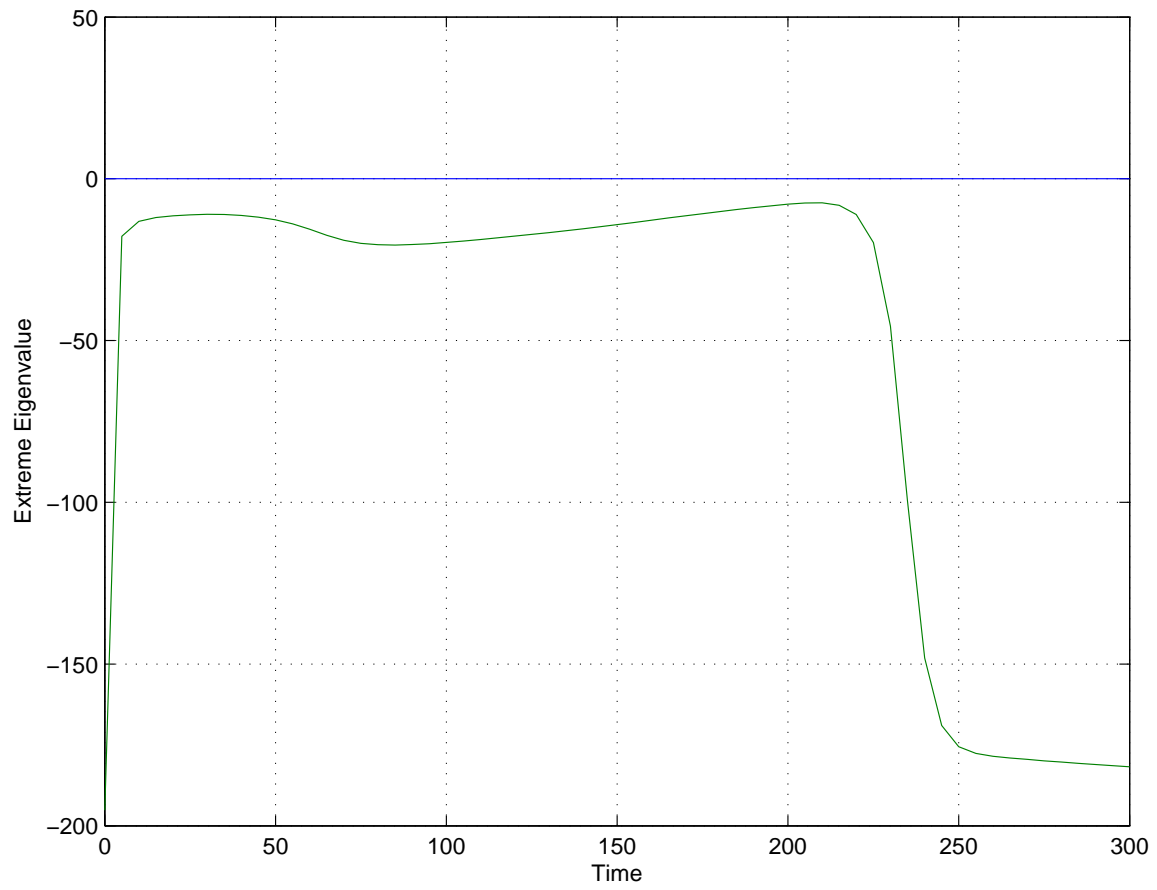


Figure 41: Extreme real eigenvalues in the Hund–Rudy model (2004).

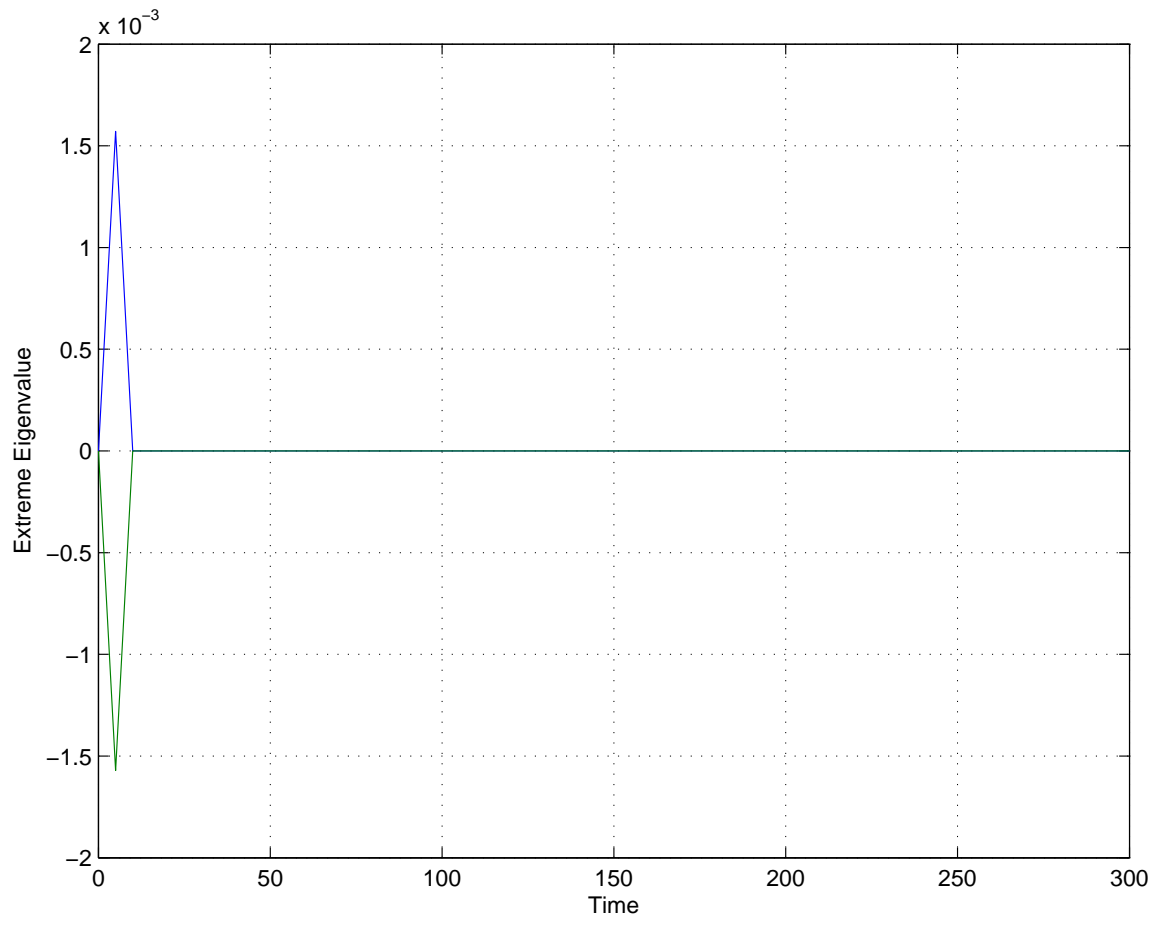


Figure 42: Extreme imaginary eigenvalues in the Hund–Rudy model (2004).

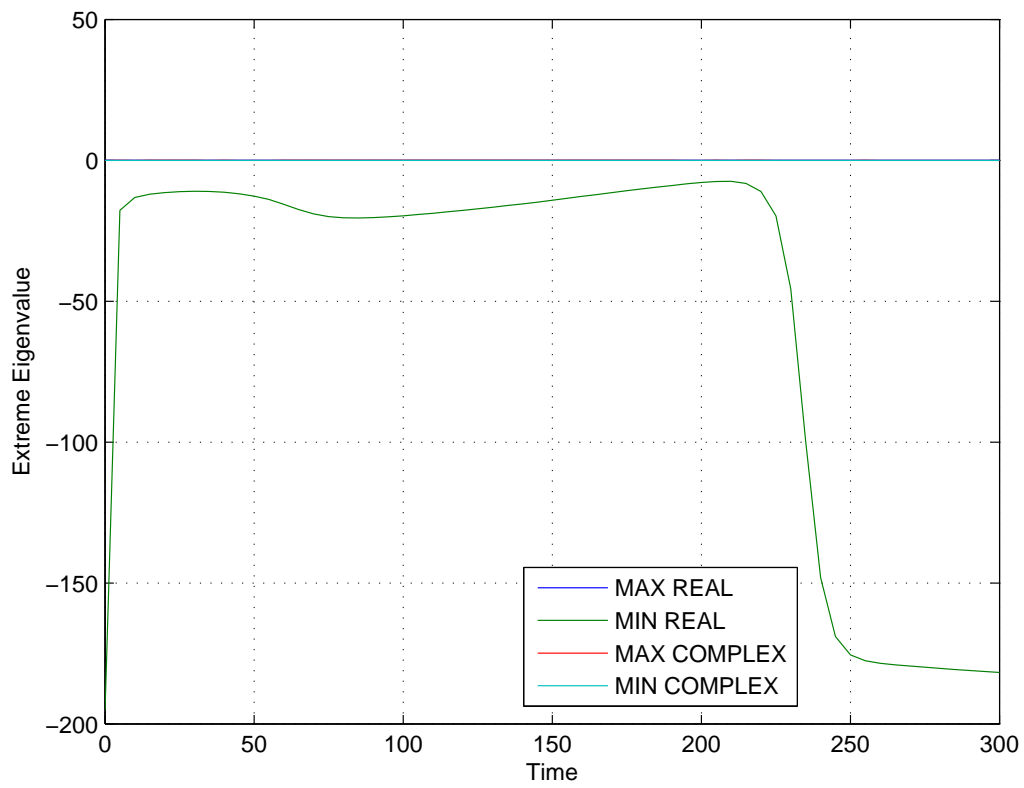


Figure 43: Extreme values of eigenvalues over time in the Hund–Rudy model (2004).

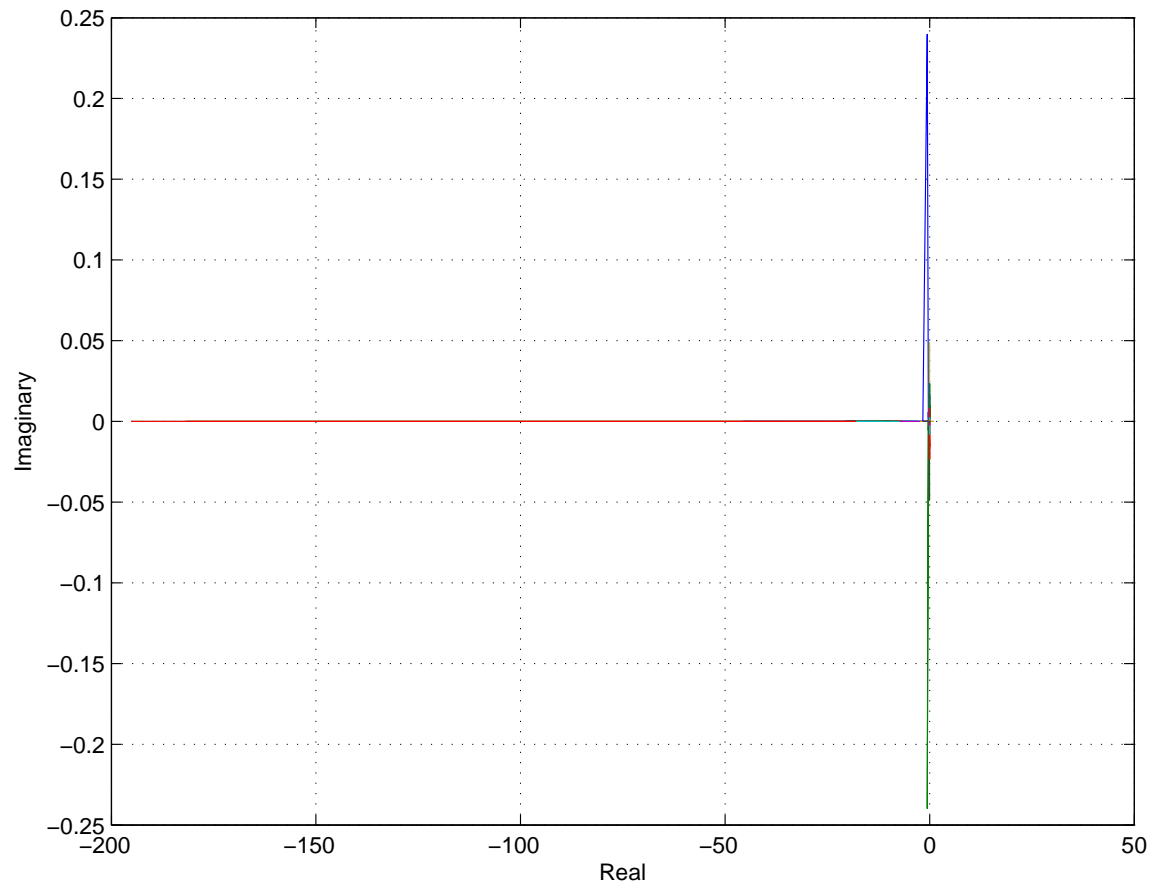


Figure 44: Plot of all eigenvalues at all times measured in the Hund–Rudy model (2004).

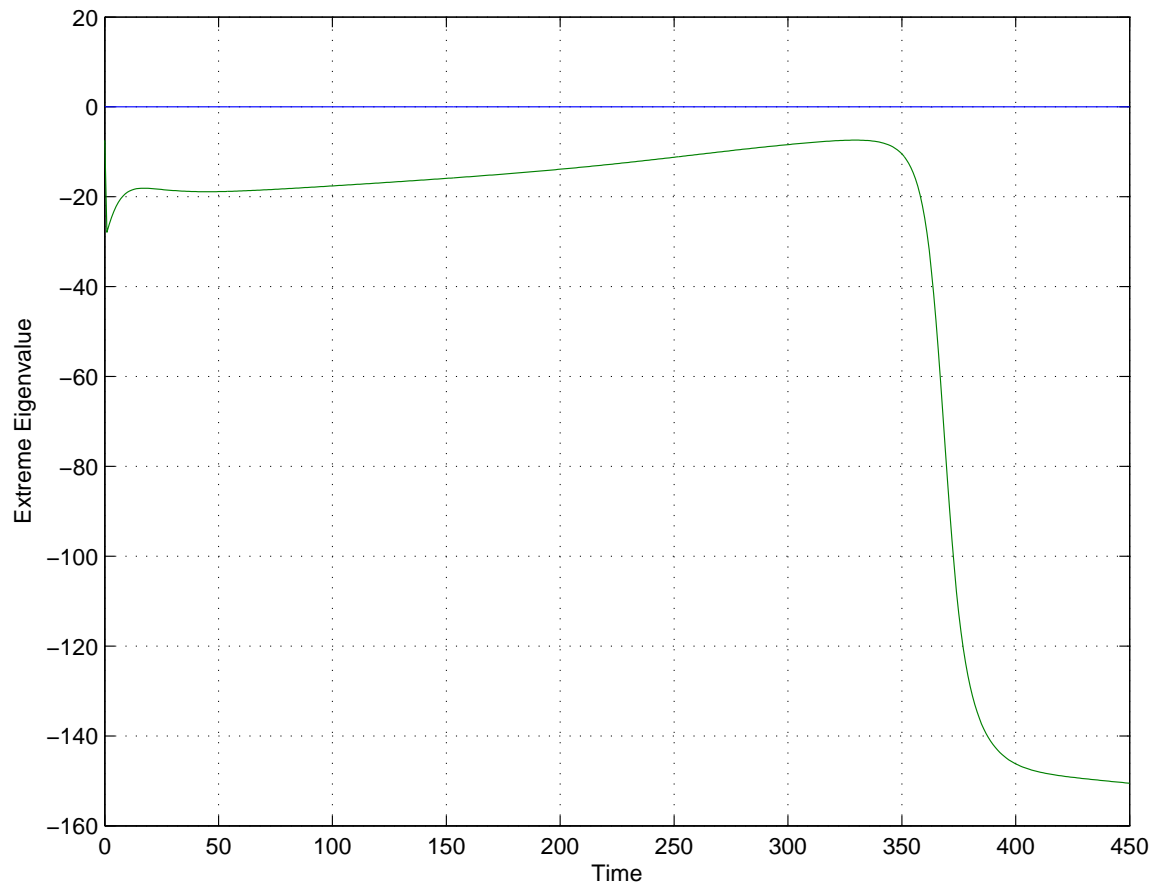


Figure 45: Extreme real eigenvalues in the Luo–Rudy model (1991).

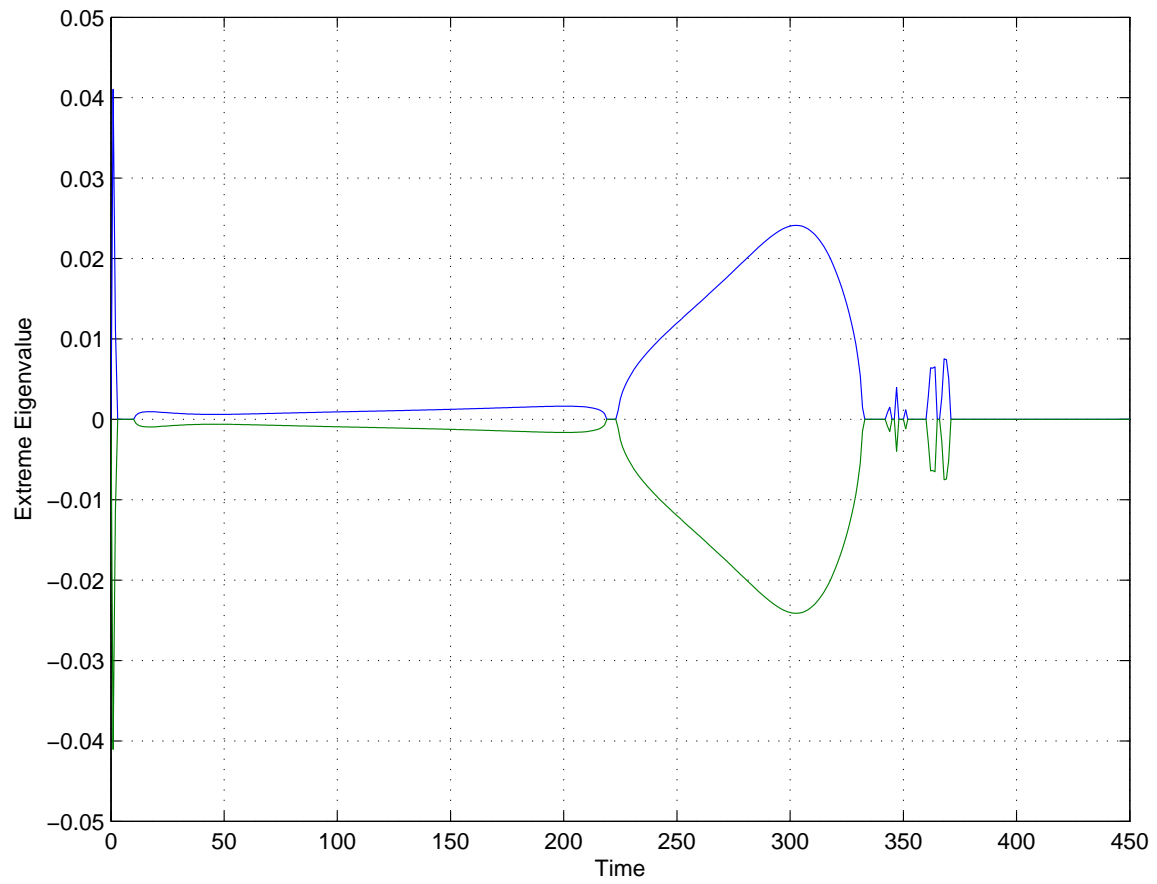


Figure 46: Extreme imaginary eigenvalues in the Luo–Rudy model (1991).

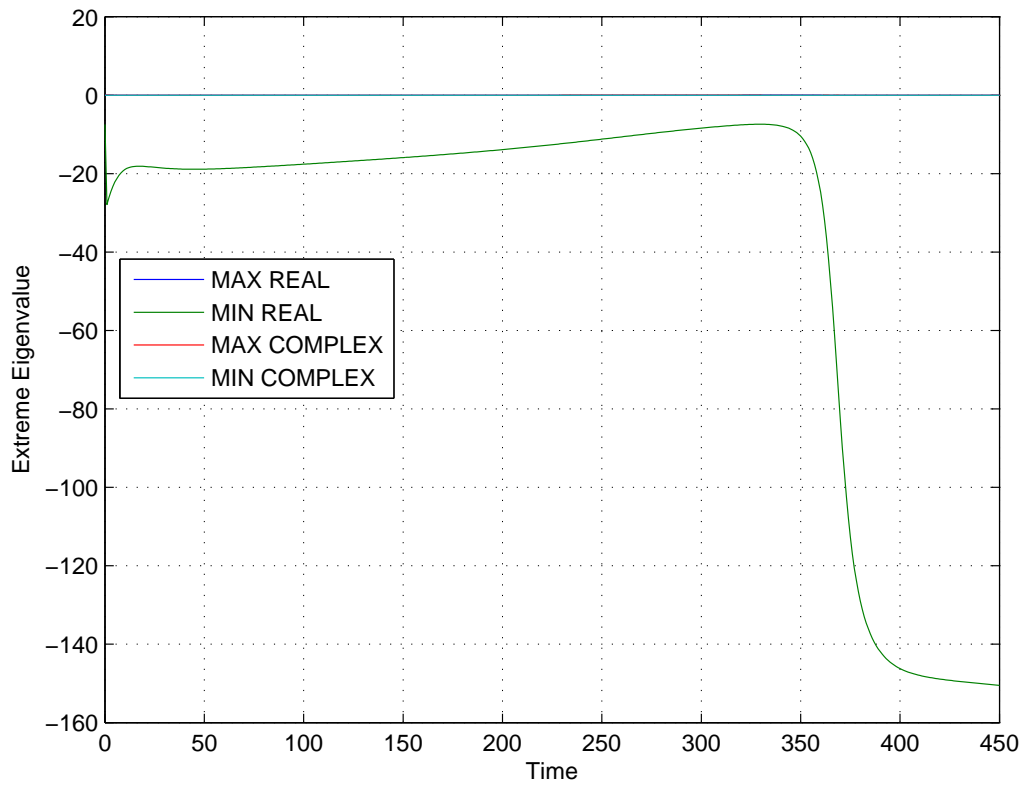


Figure 47: Extreme values of eigenvalues over time in the Luo–Rudy model (1991).

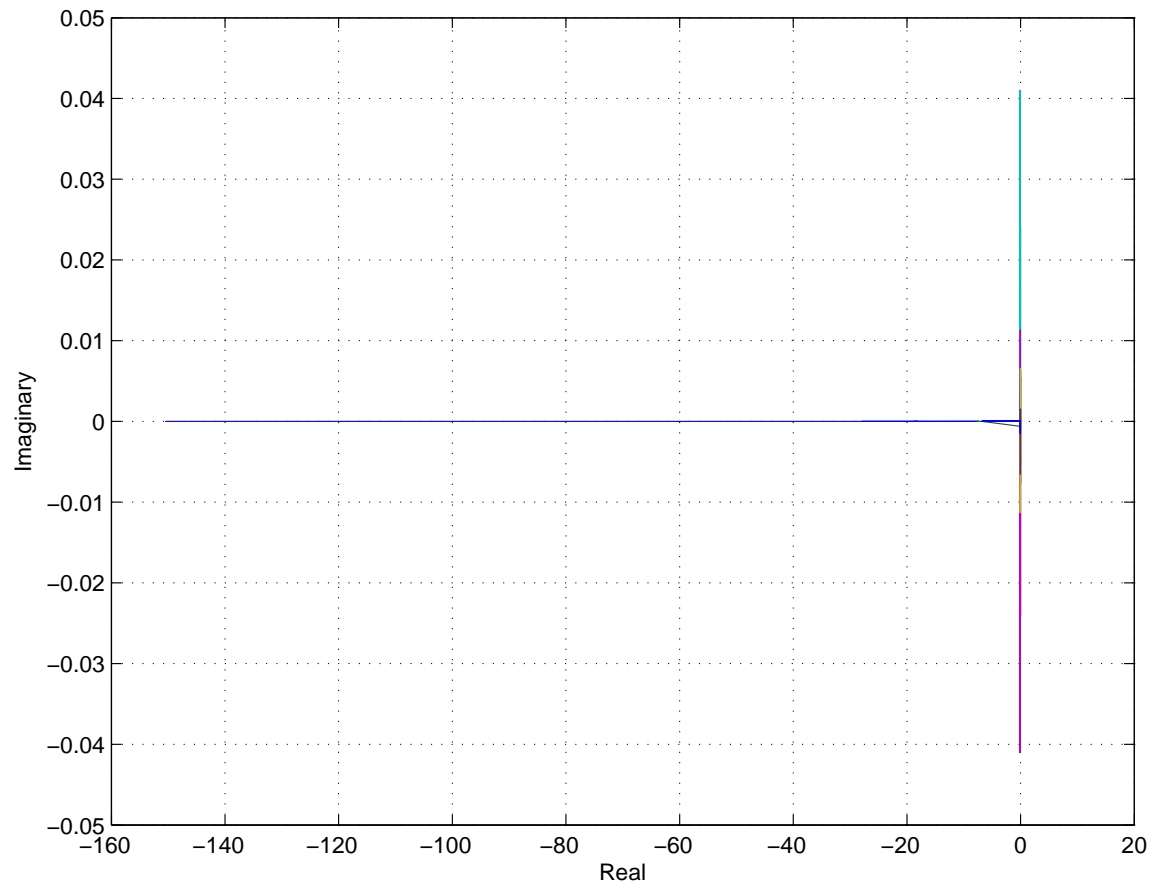


Figure 48: Plot of all eigenvalues at all times measured in the Luo–Rudy model (1991).

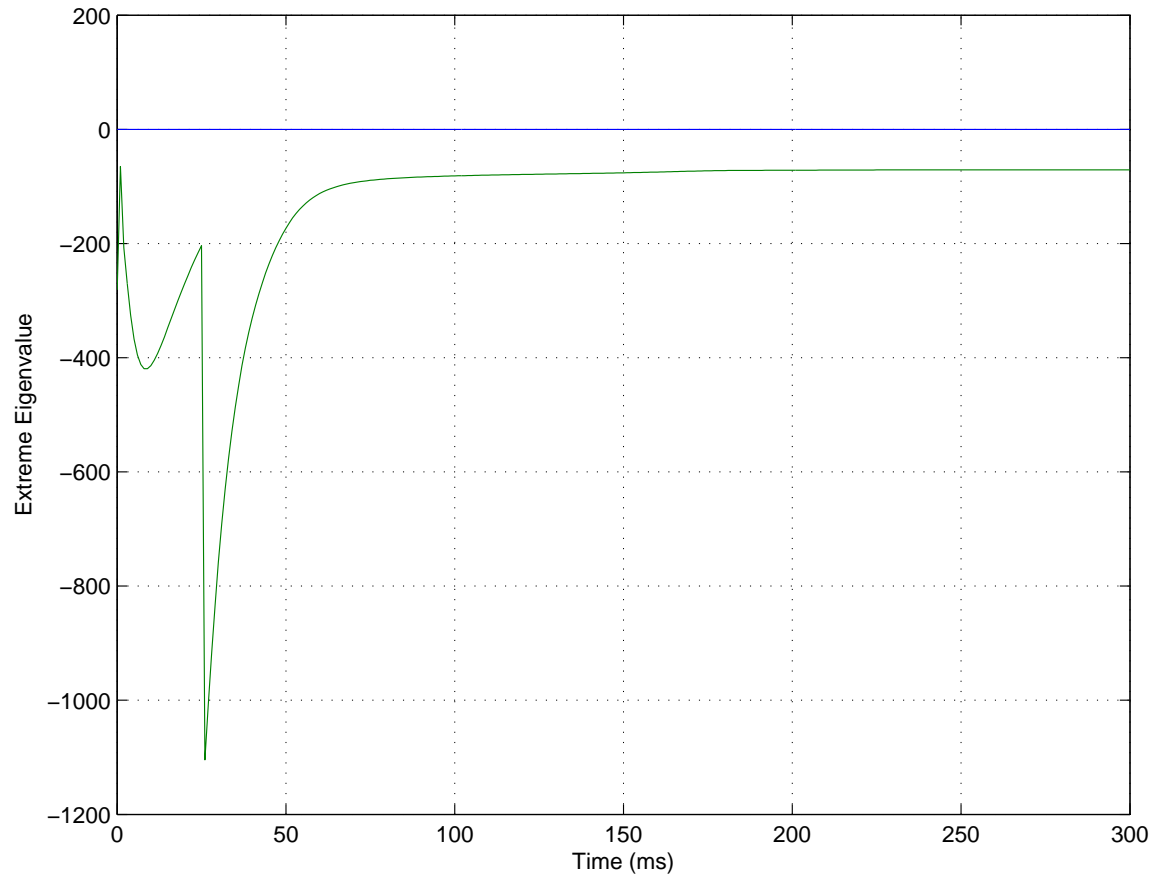


Figure 49: Extreme real eigenvalues in the model of Jafari et al. (1998).

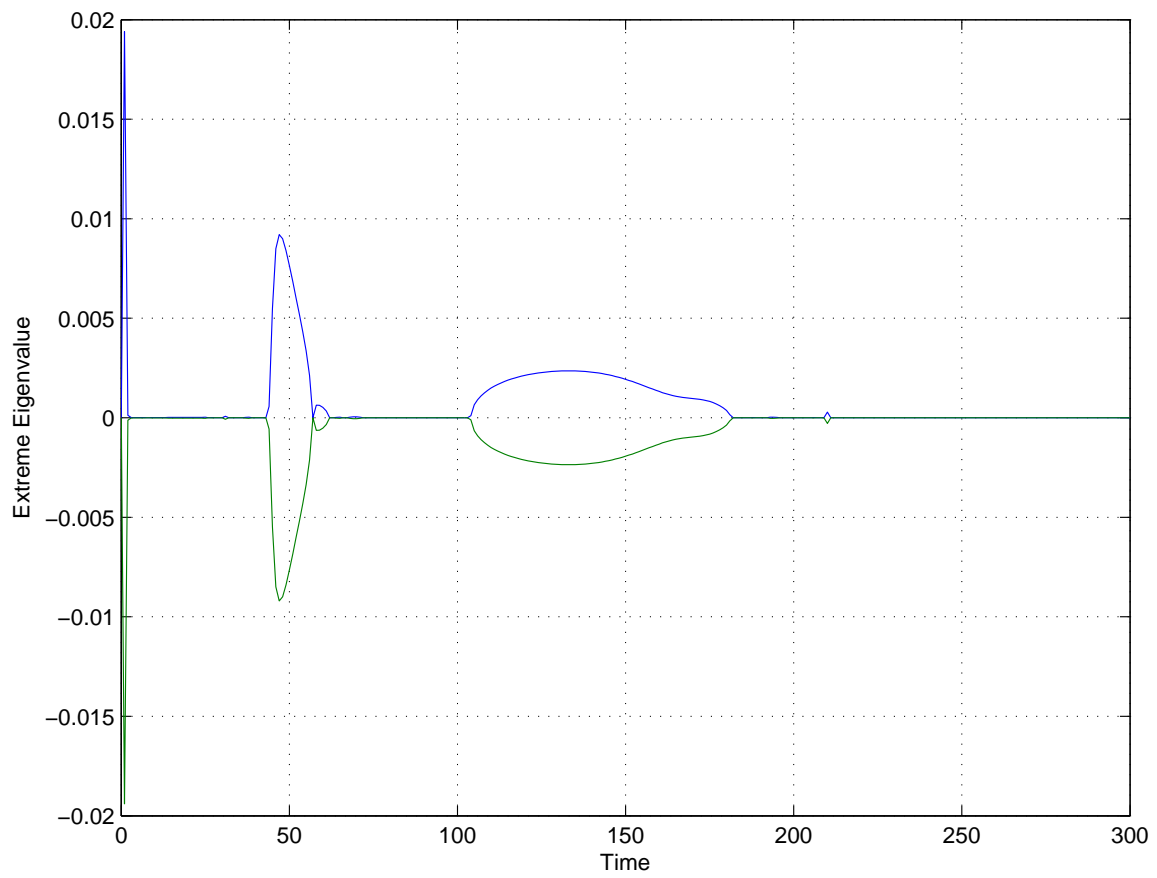


Figure 50: Extreme imaginary eigenvalues in the model of Jafari et al. (1998).

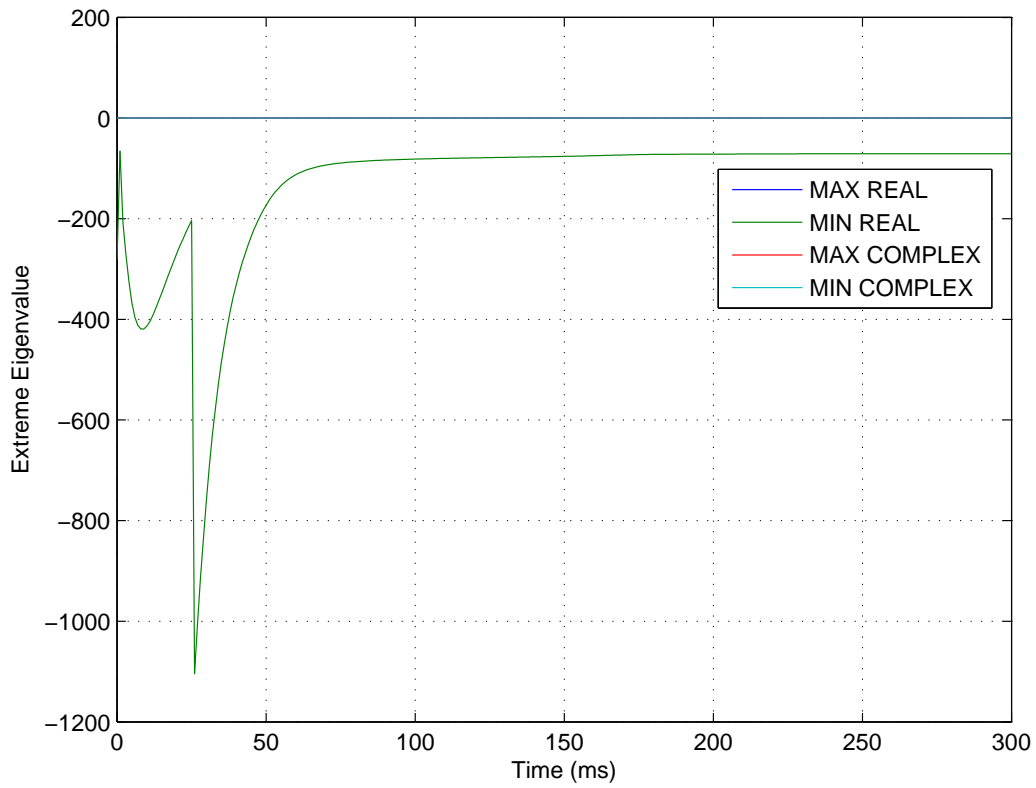


Figure 51: Extreme values of eigenvalues over time in the model of Jafari et al. (1998).

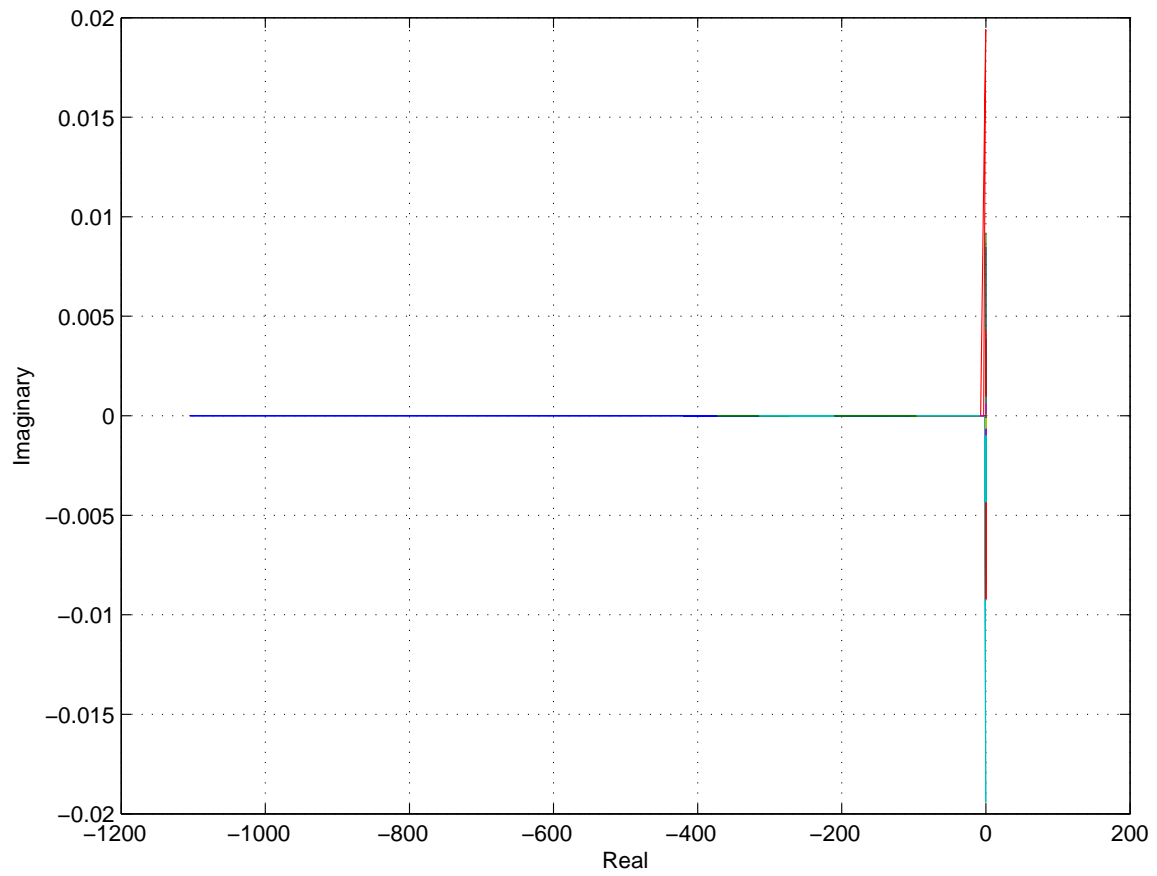


Figure 52: Plot of all eigenvalues at all times measured in the model of Jafari et al. (1998).

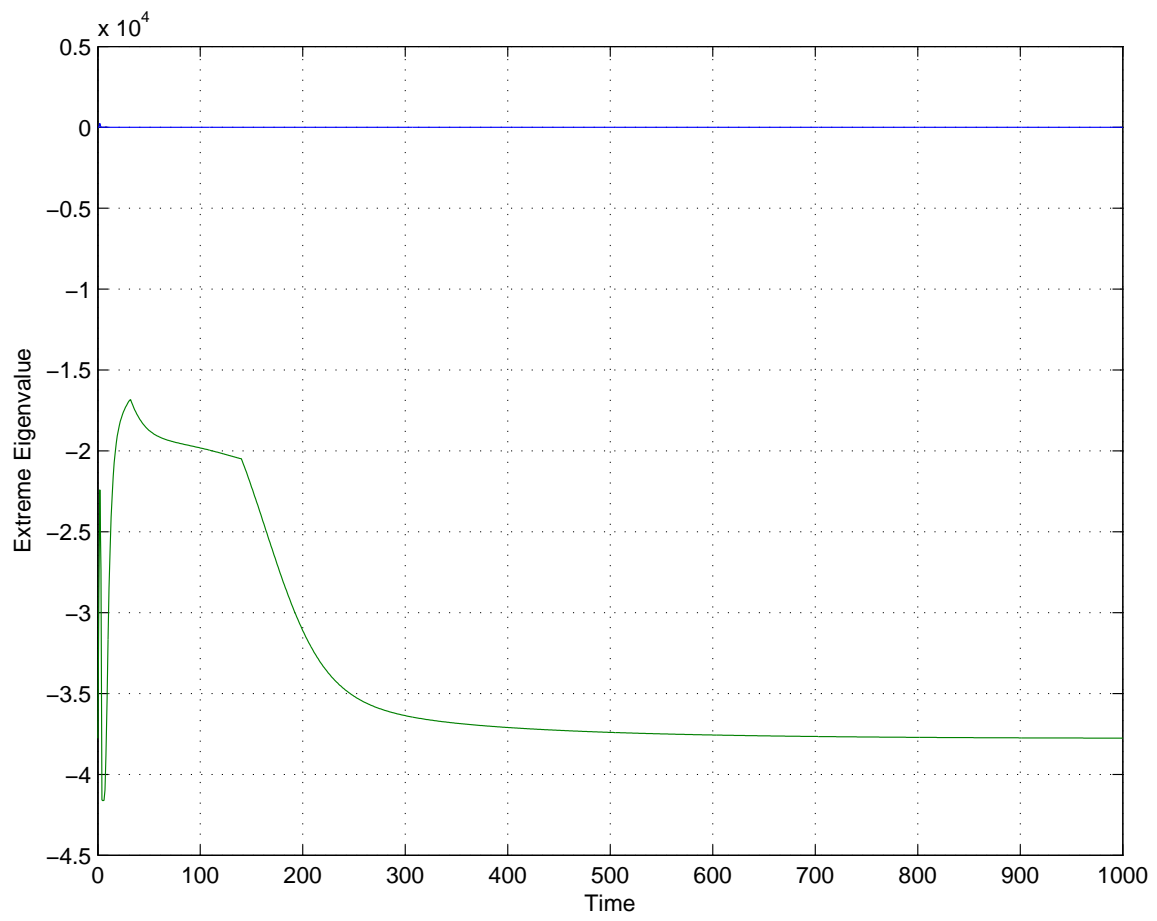


Figure 53: Extreme real eigenvalues in the model of Maleckar et al. (2008)

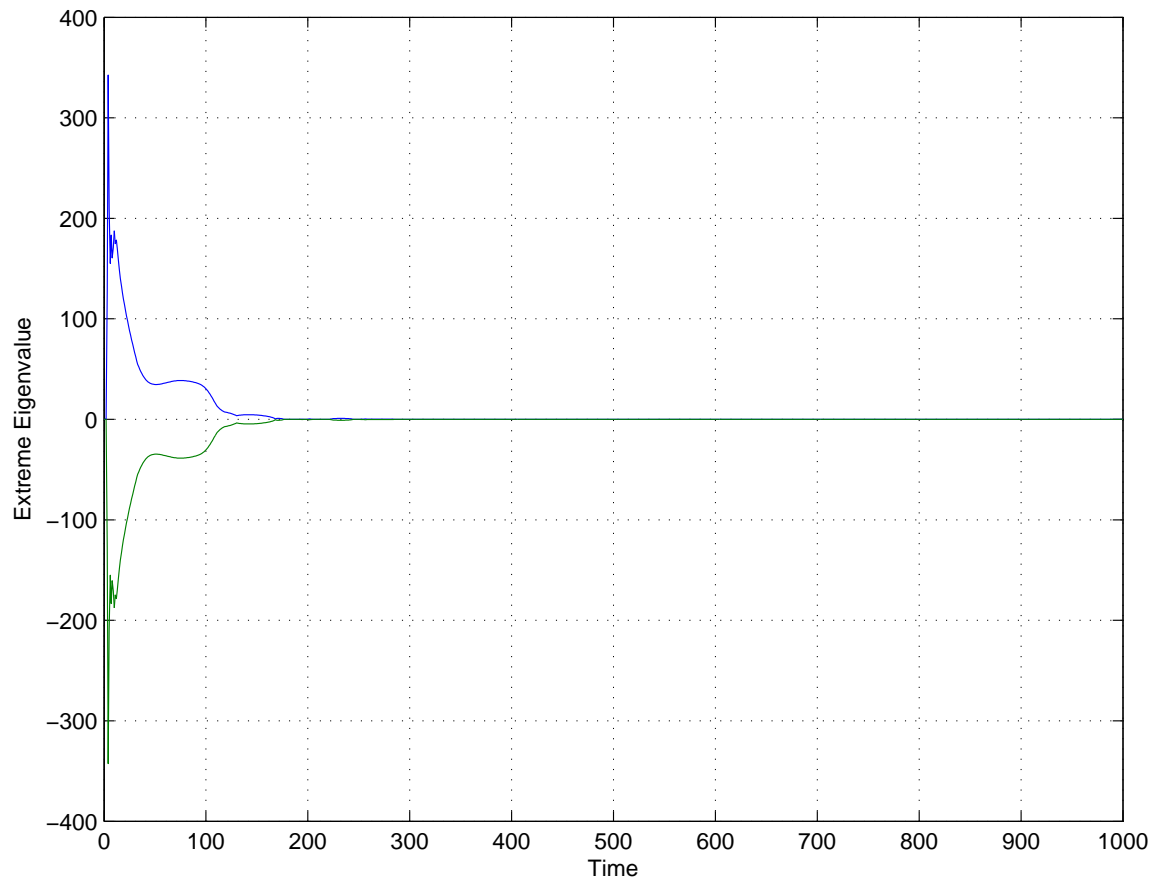


Figure 54: Extreme imaginary eigenvalues in the model of Maleckar et al. (2008).

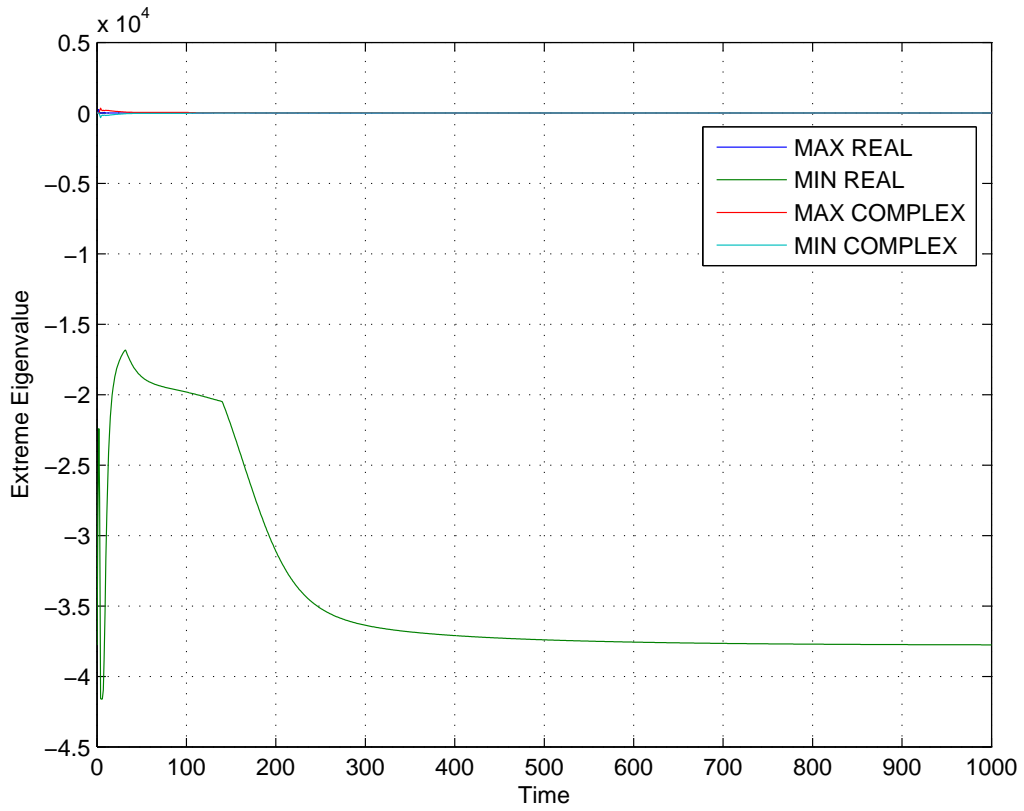


Figure 55: Extreme values of eigenvalues over time in the model of Maleckar et al. (2008).

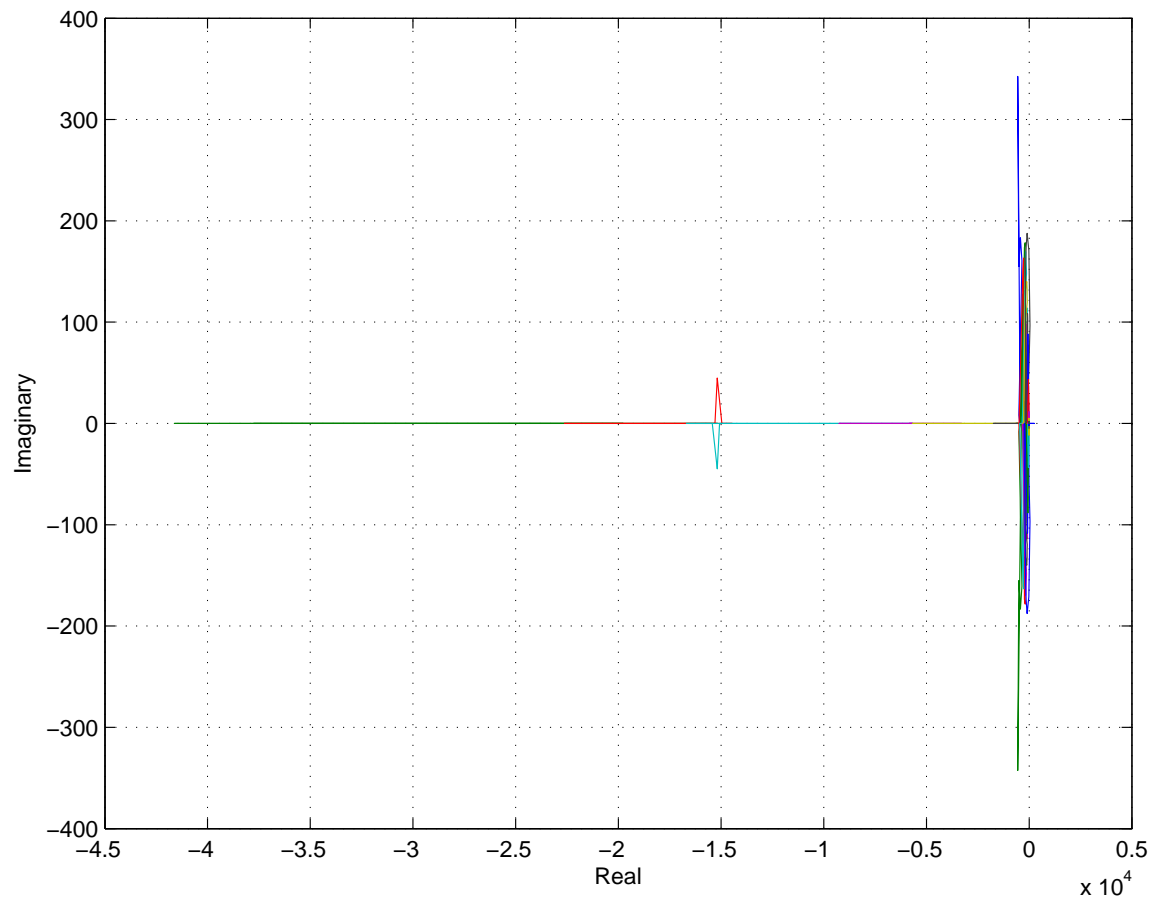


Figure 56: Plot of all eigenvalues at all times measured in the model of Maleckar et al. (2008).

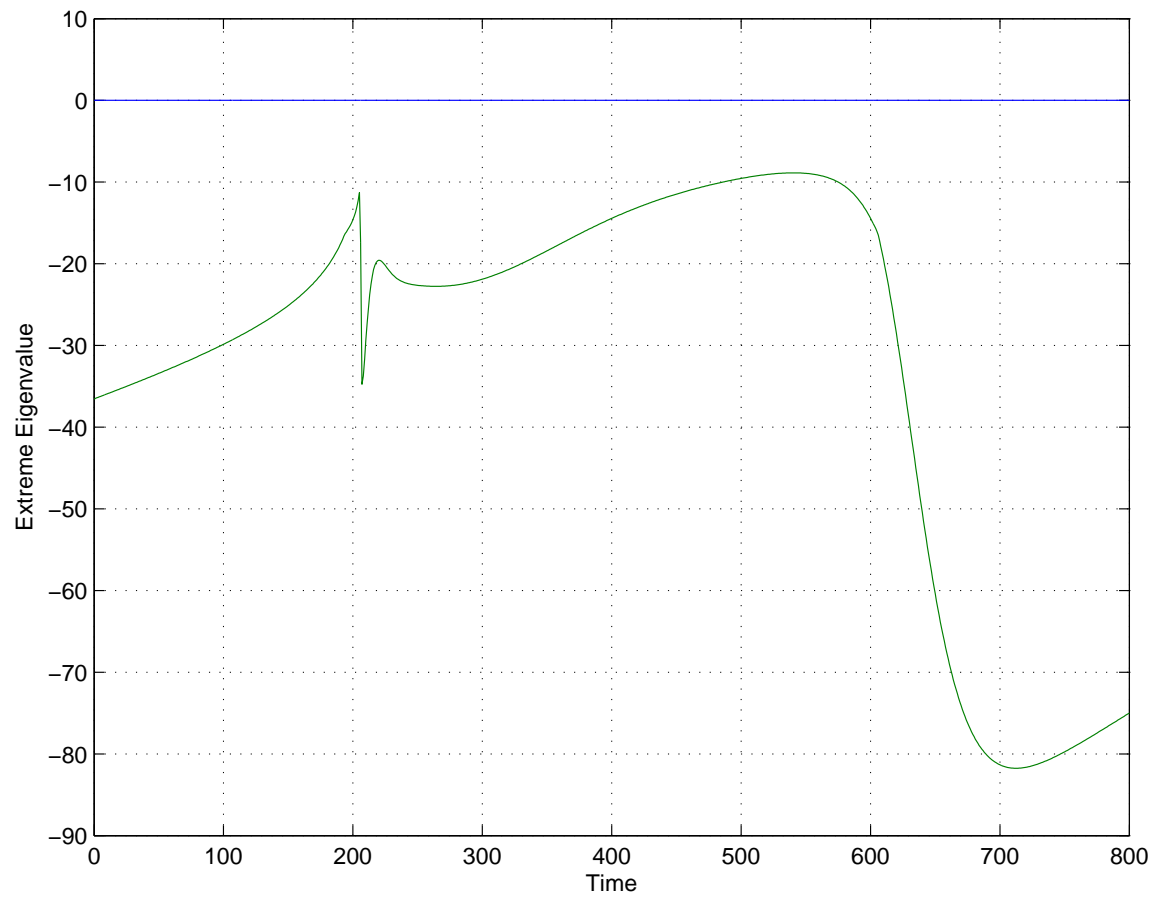


Figure 57: Extreme real eigenvalues in the model of McAllister et al. (1975).

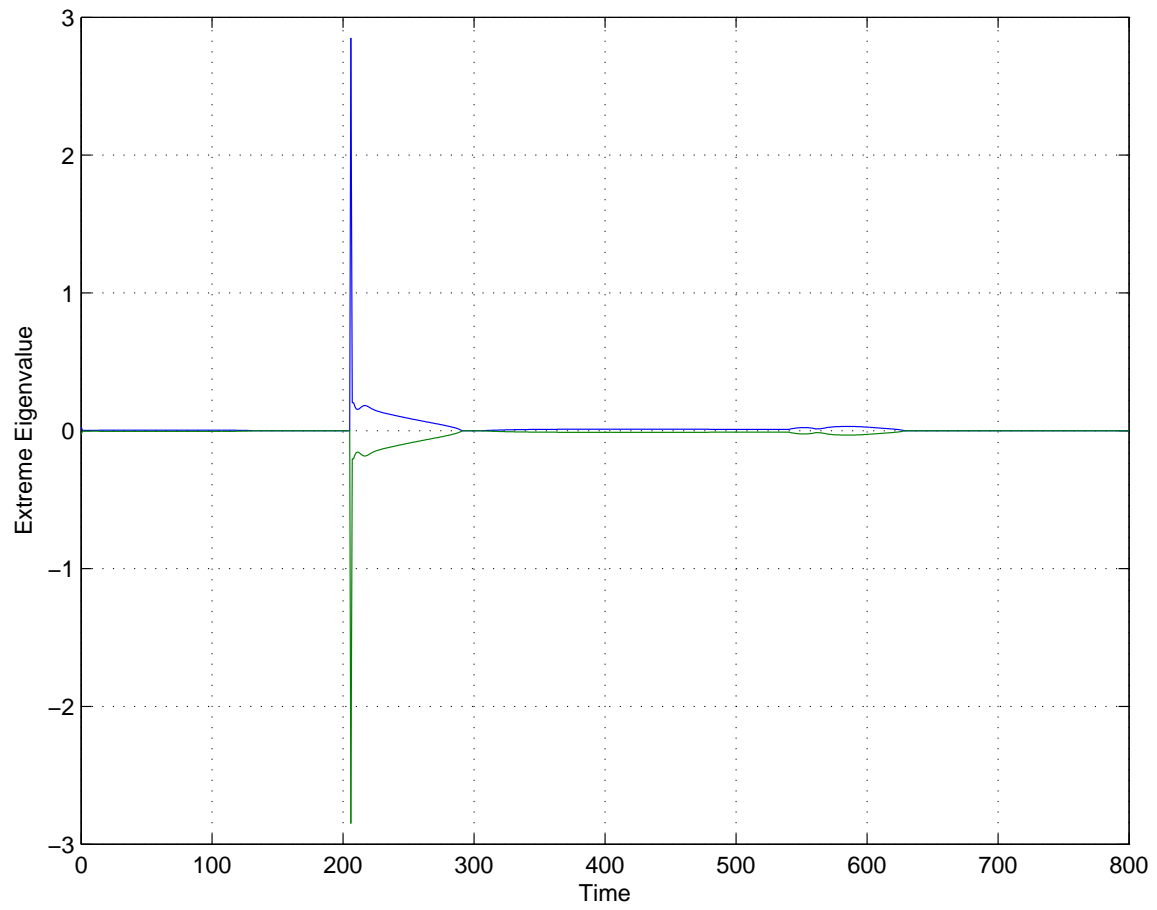


Figure 58: Extreme imaginary eigenvalues in the model of McAllister et al. (1975).

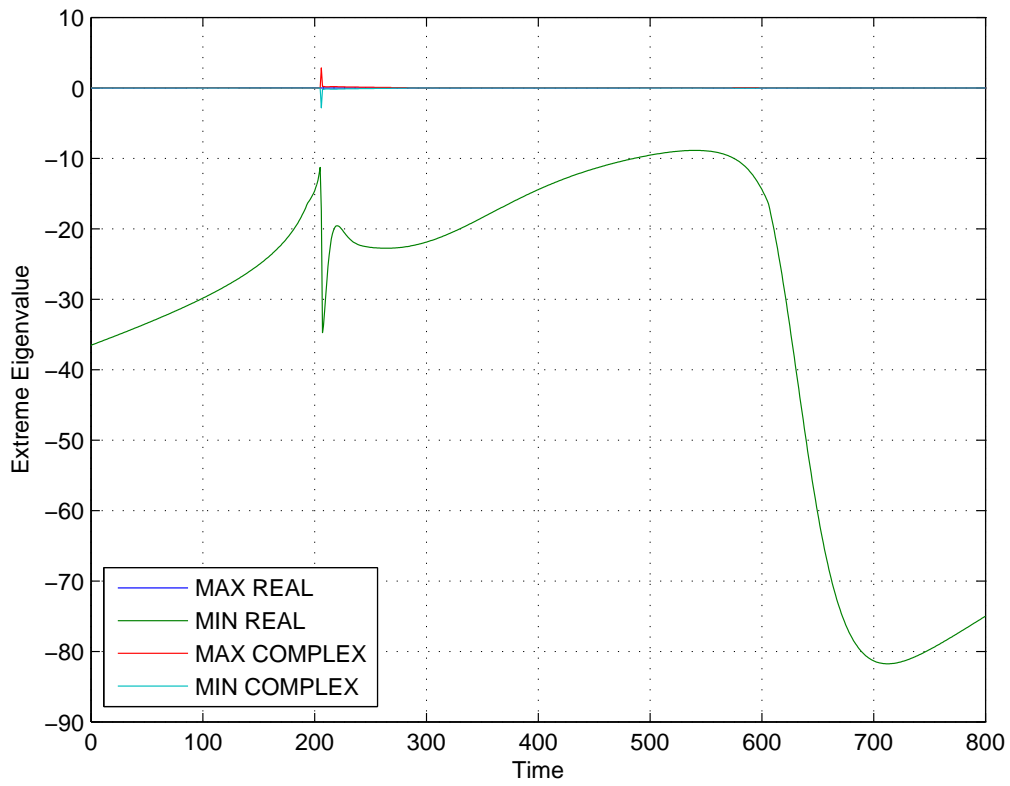


Figure 59: Extreme values of eigenvalues over time in the model of McAllister et al. (1975).

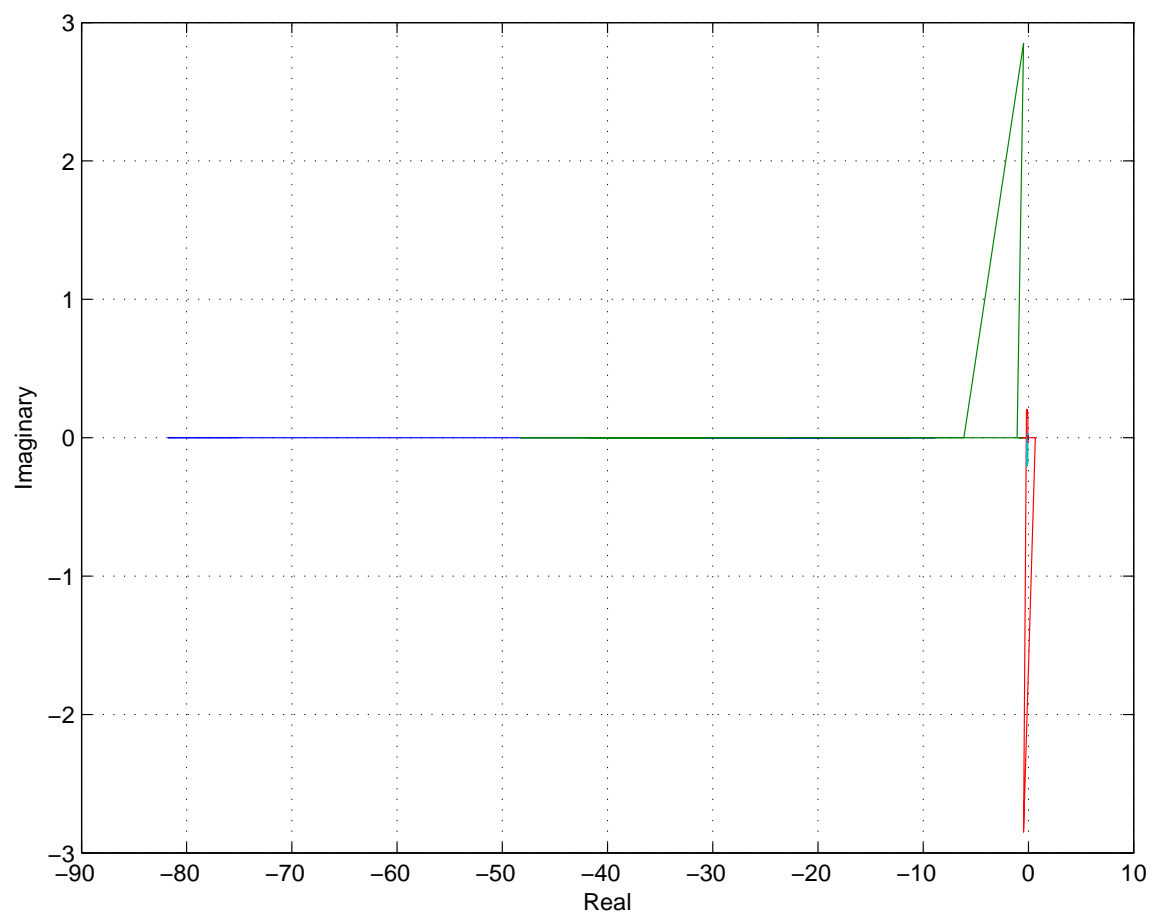


Figure 60: Plot of all eigenvalues at all times measured in the model of McAllister et al. (1975).

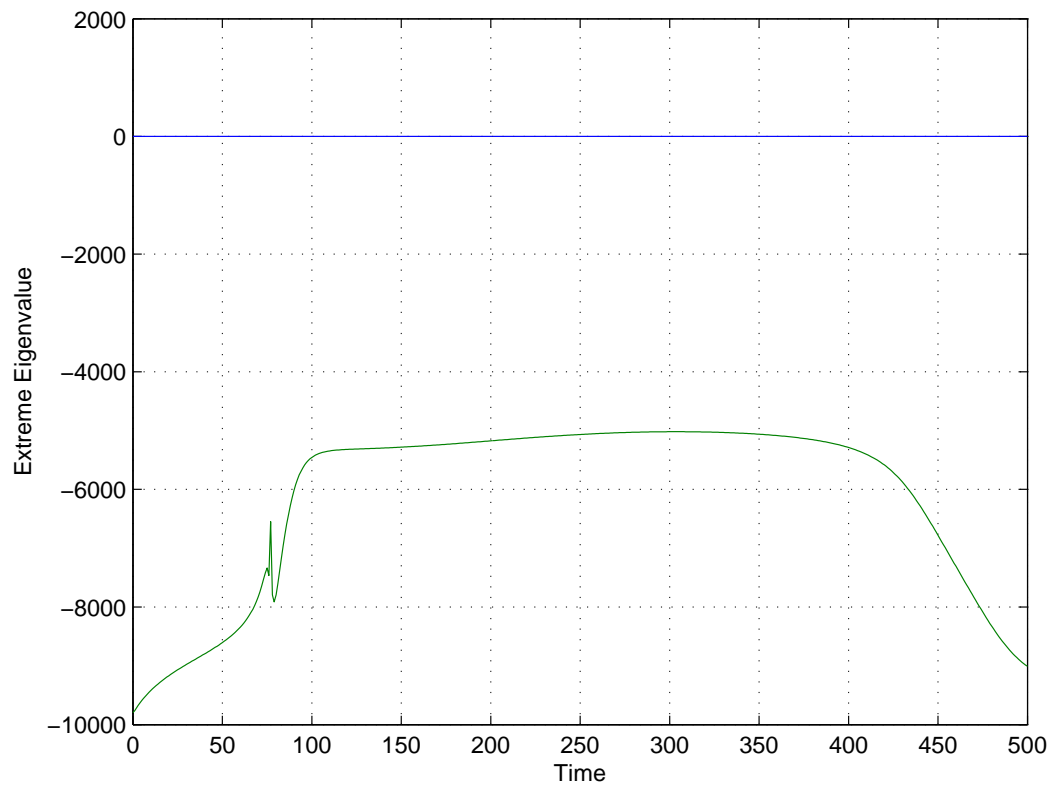


Figure 61: Extreme real eigenvalues in the Noble model (1962).

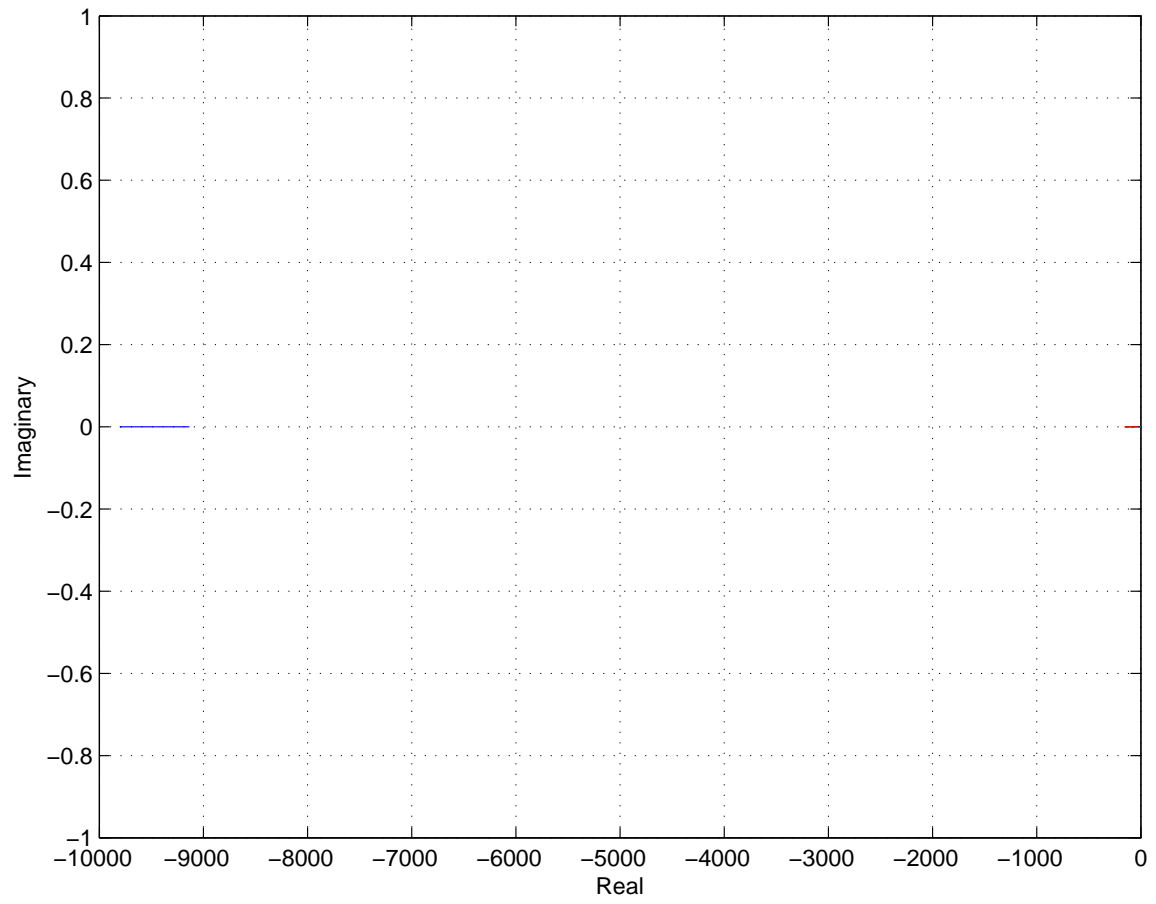


Figure 62: Plot of all eigenvalues at all times measured in the Noble model (1962).

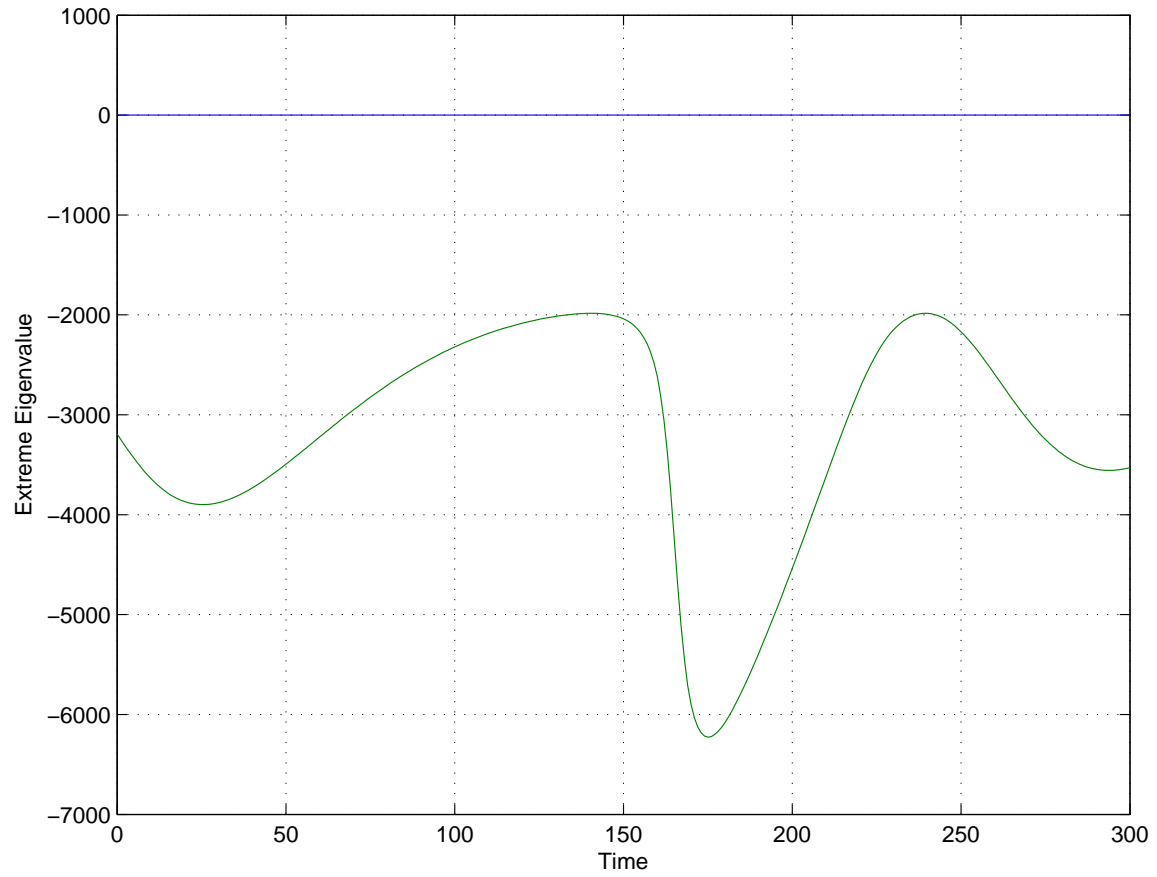


Figure 63: Extreme real eigenvalues in the Noble–Noble model (1984)

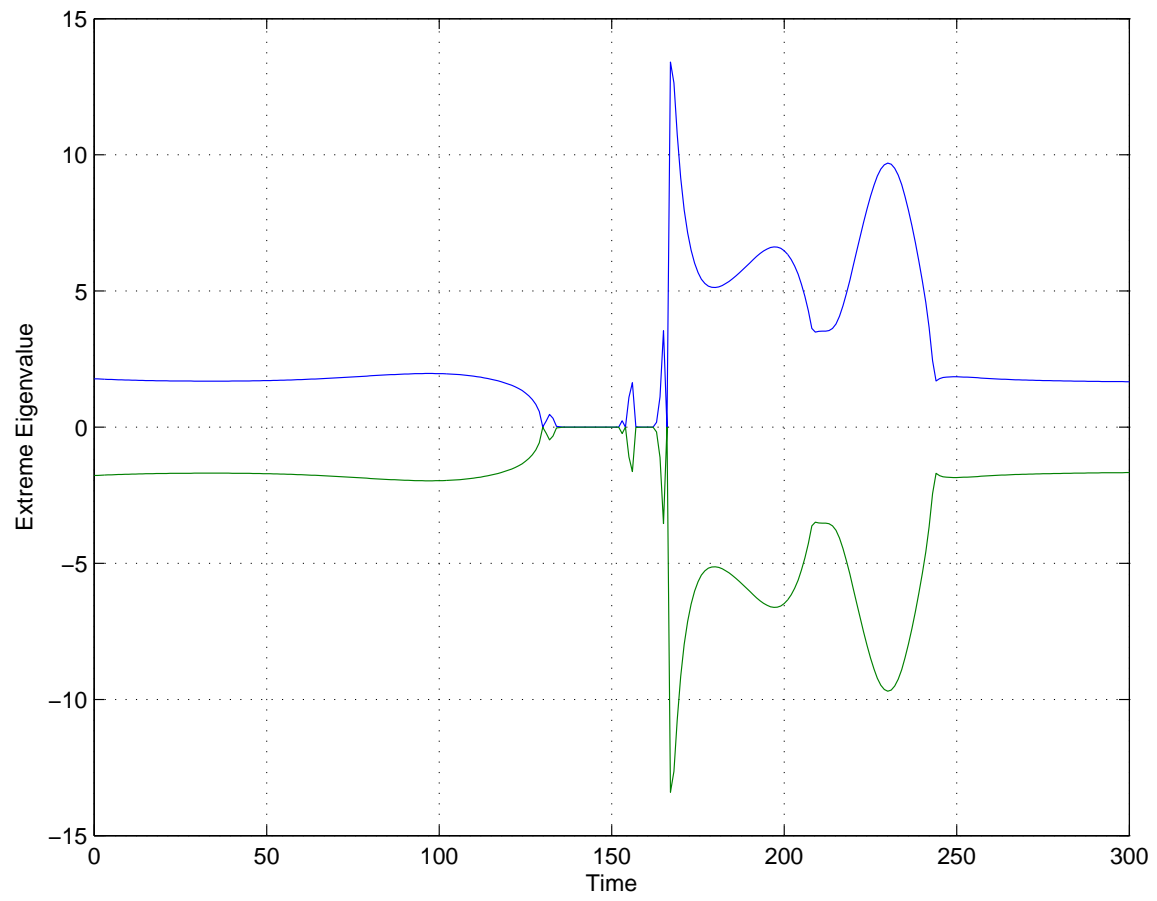


Figure 64: Extreme imaginary eigenvalues in the Noble–Noble model (1984).

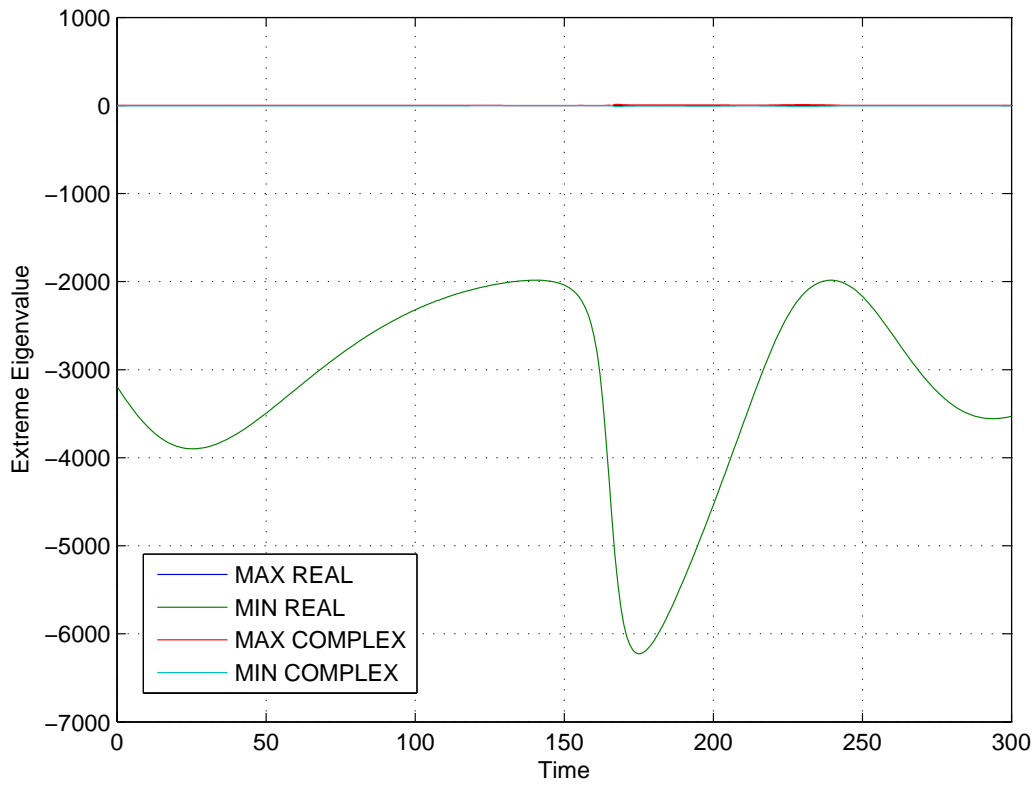


Figure 65: Extreme values of eigenvalues over time in the Noble–Noble model (1984).

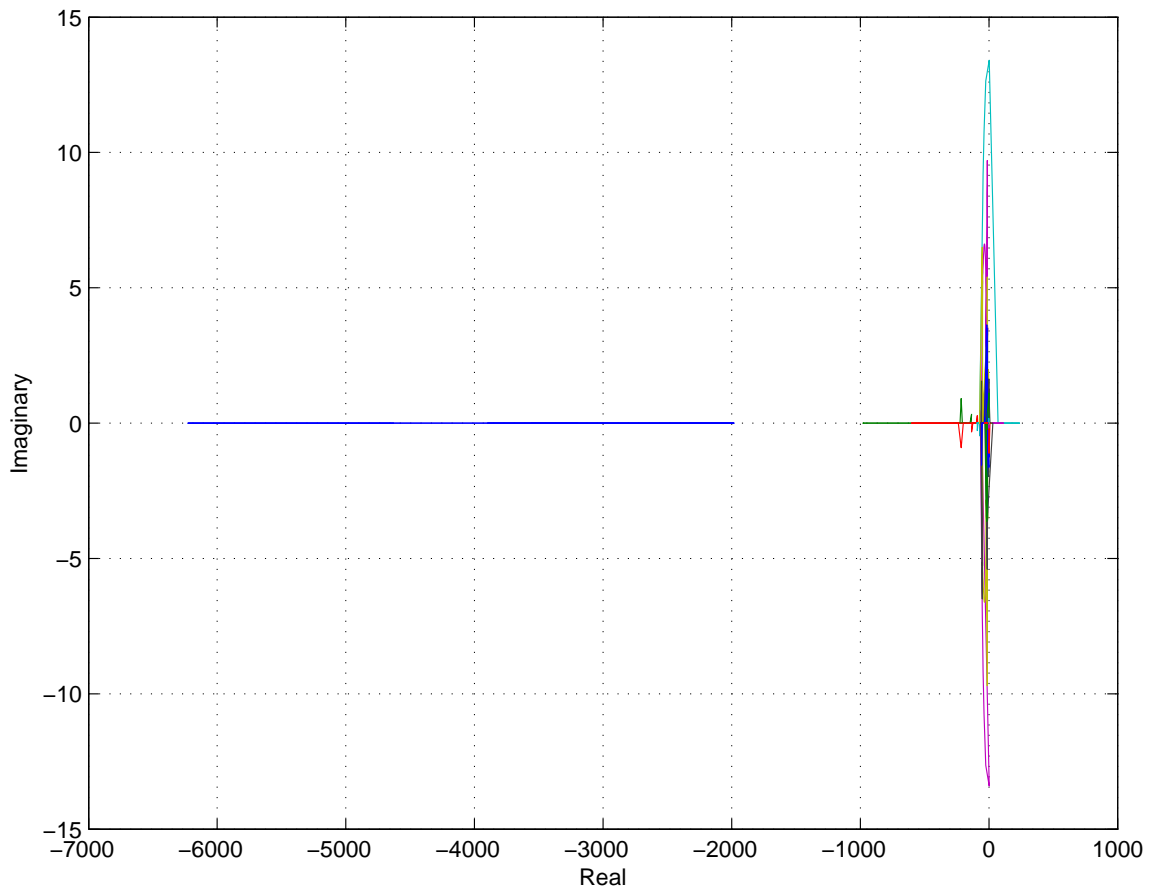


Figure 66: Plot of all eigenvalues at all times measured in the Noble–Noble model (1984).

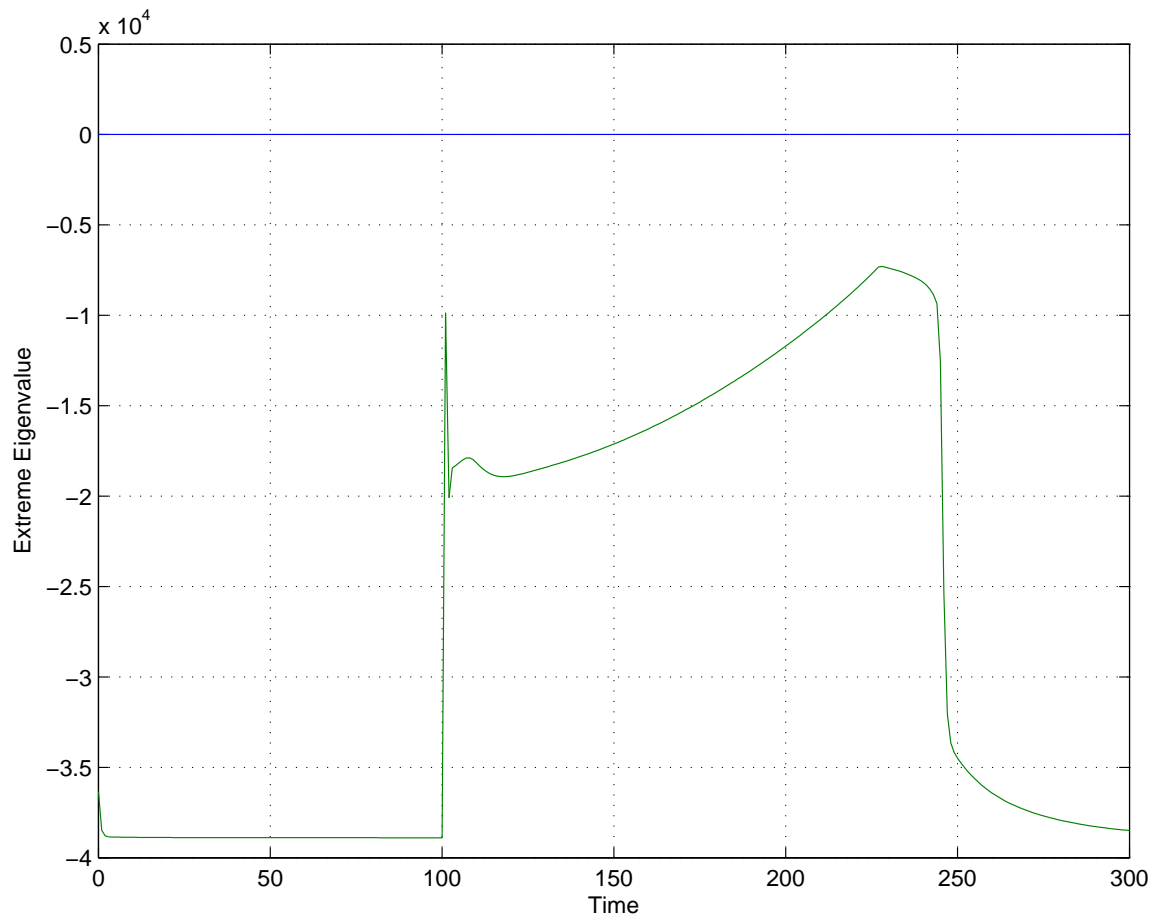


Figure 67: Extreme real eigenvalues in the model of Noble et al. (1991).

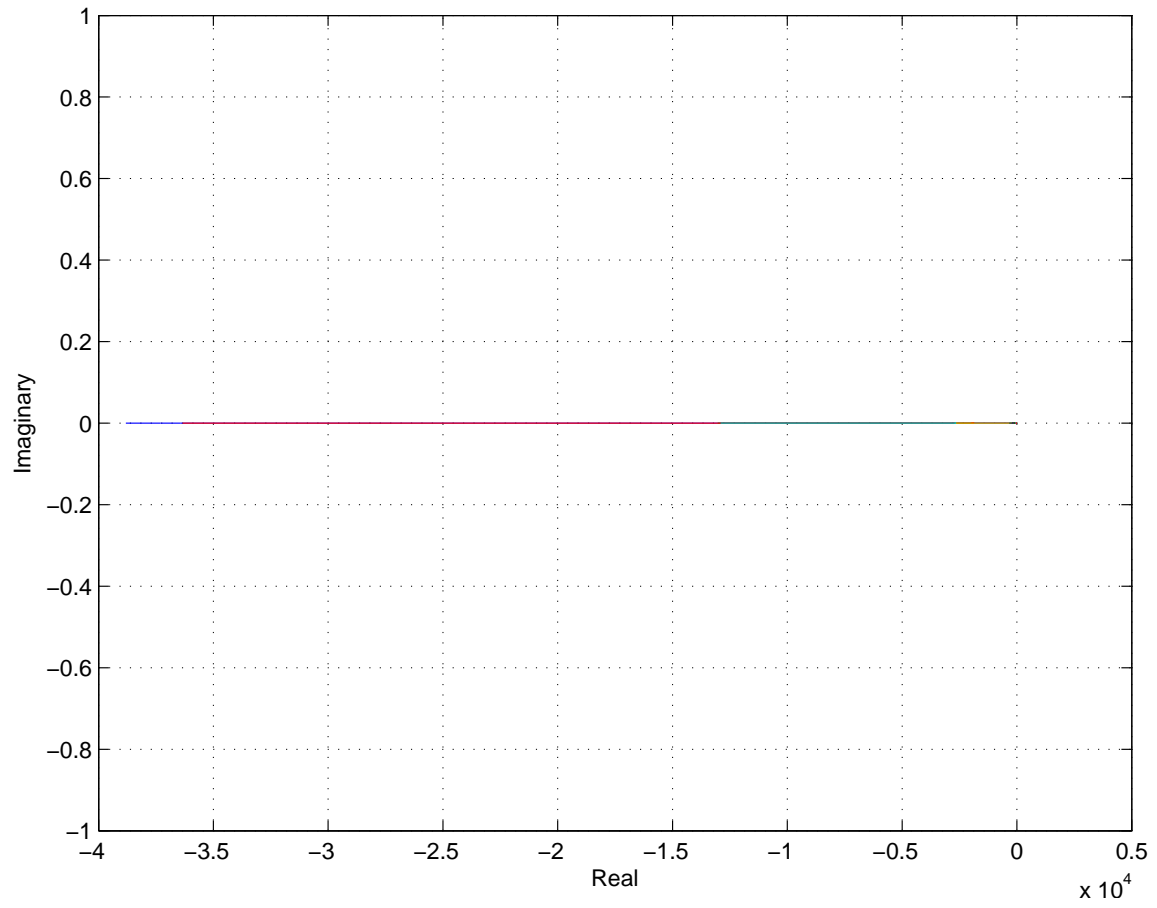


Figure 68: Plot of all eigenvalues at all times measured in the model of Noble et al. (1991).

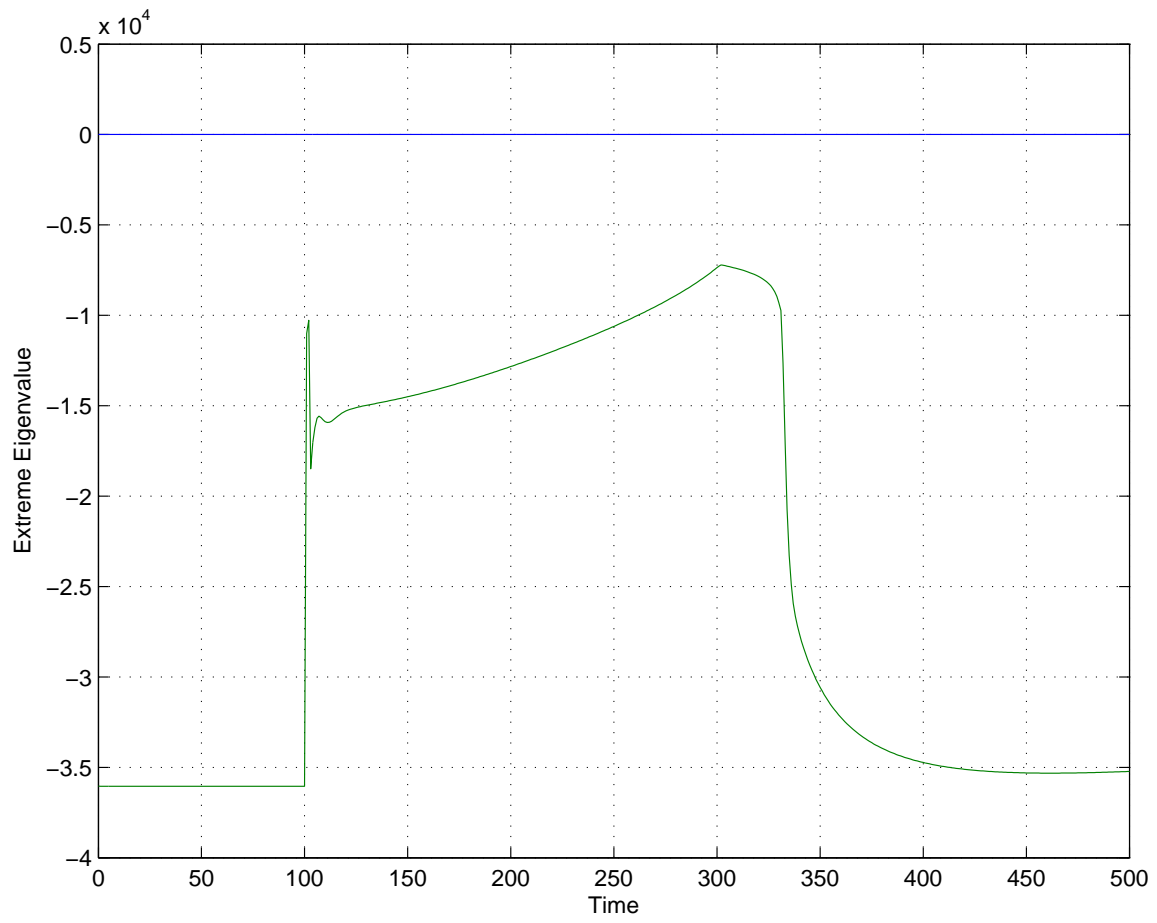


Figure 69: Extreme real eigenvalues in the model of Noble et al. (1998).

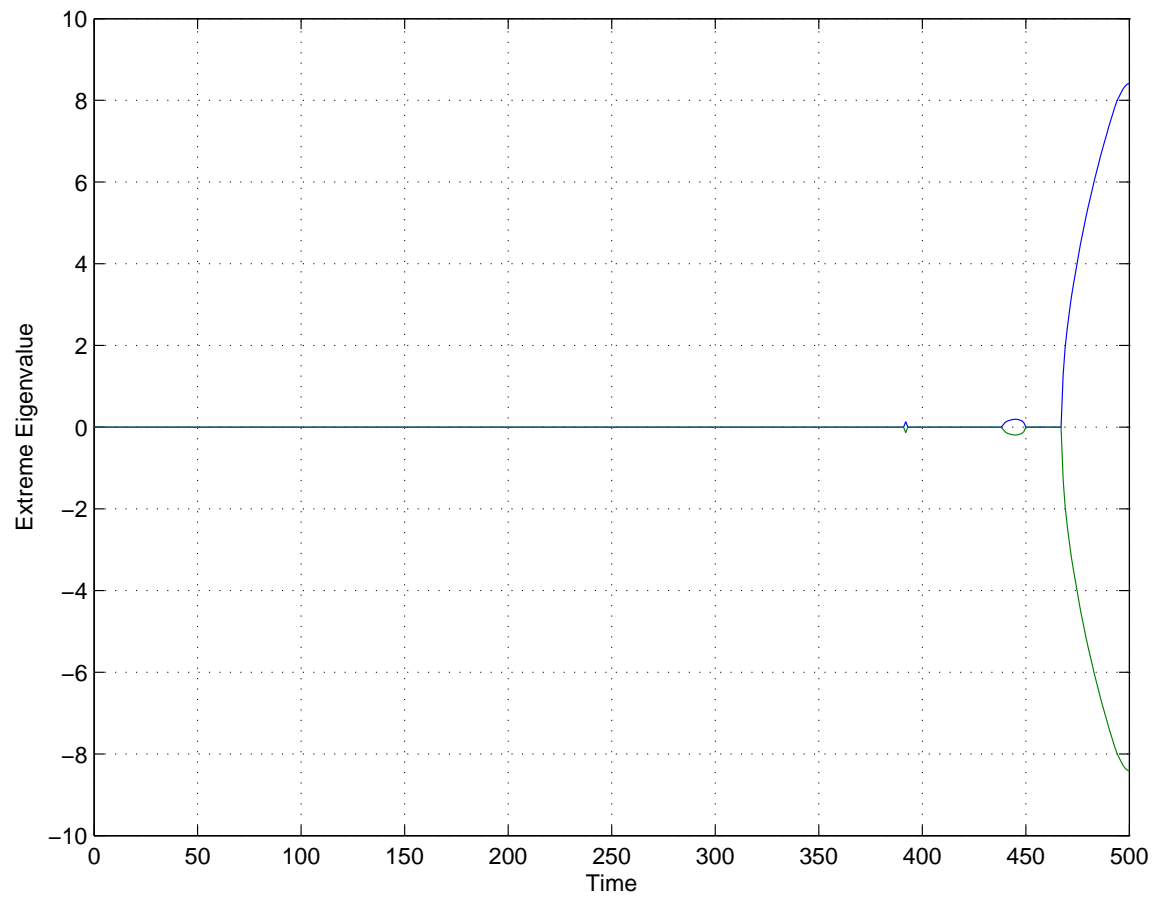


Figure 70: Extreme imaginary eigenvalues in the model of Noble et al. (1998).

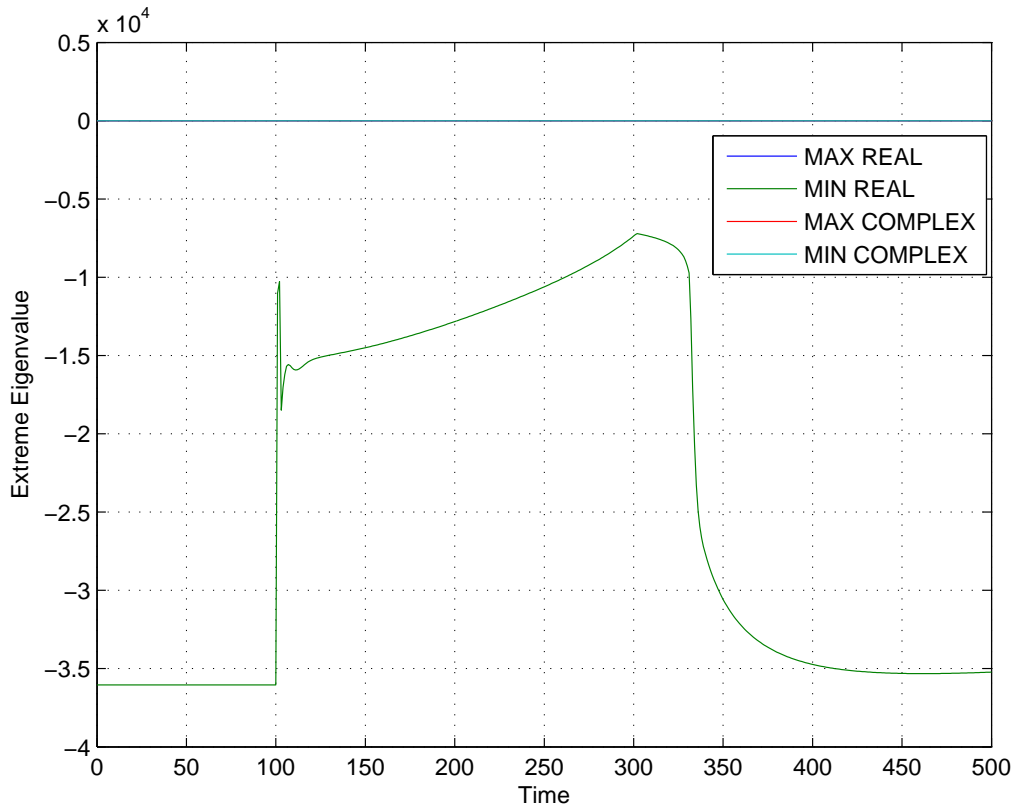


Figure 71: Extreme values of eigenvalues over time in the model of Noble et al. (1998).

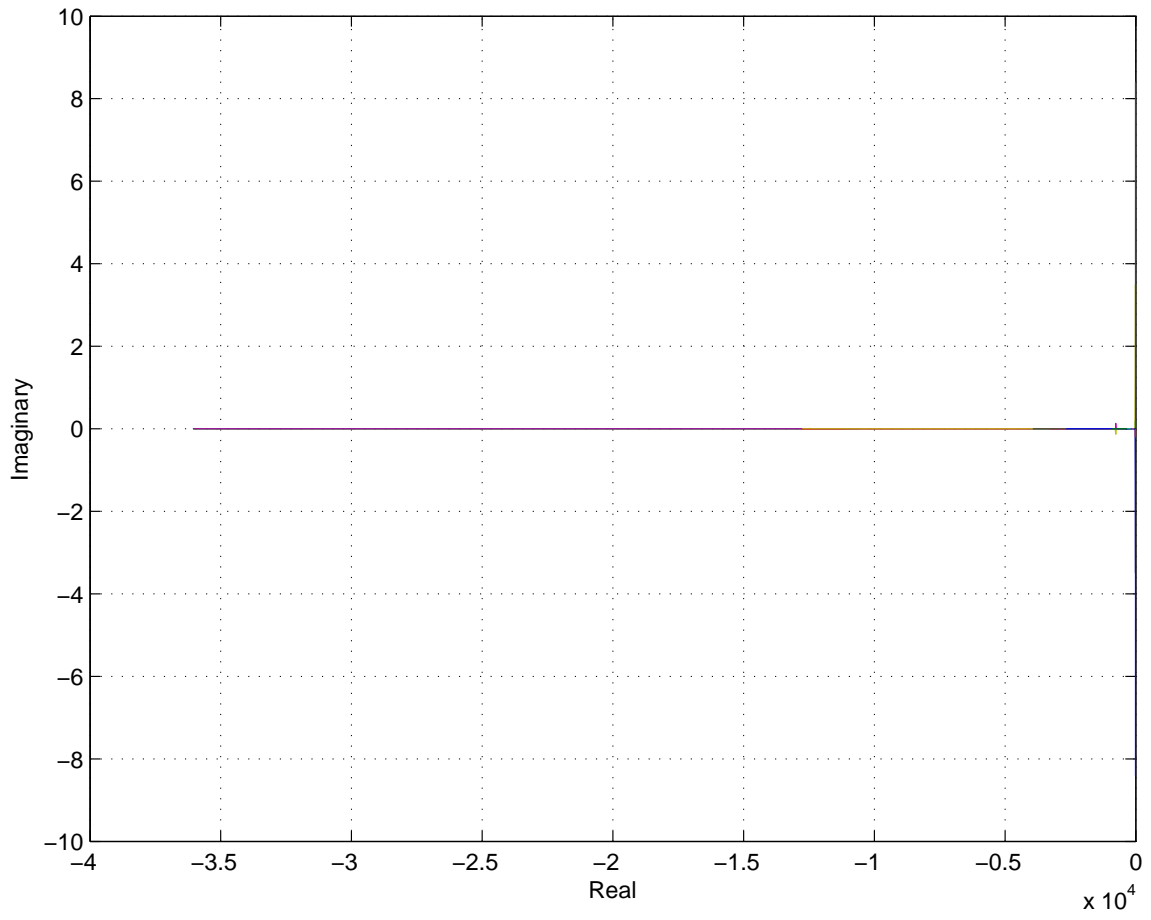


Figure 72: Plot of all eigenvalues at all times measured in the model of Noble et al. (1998).

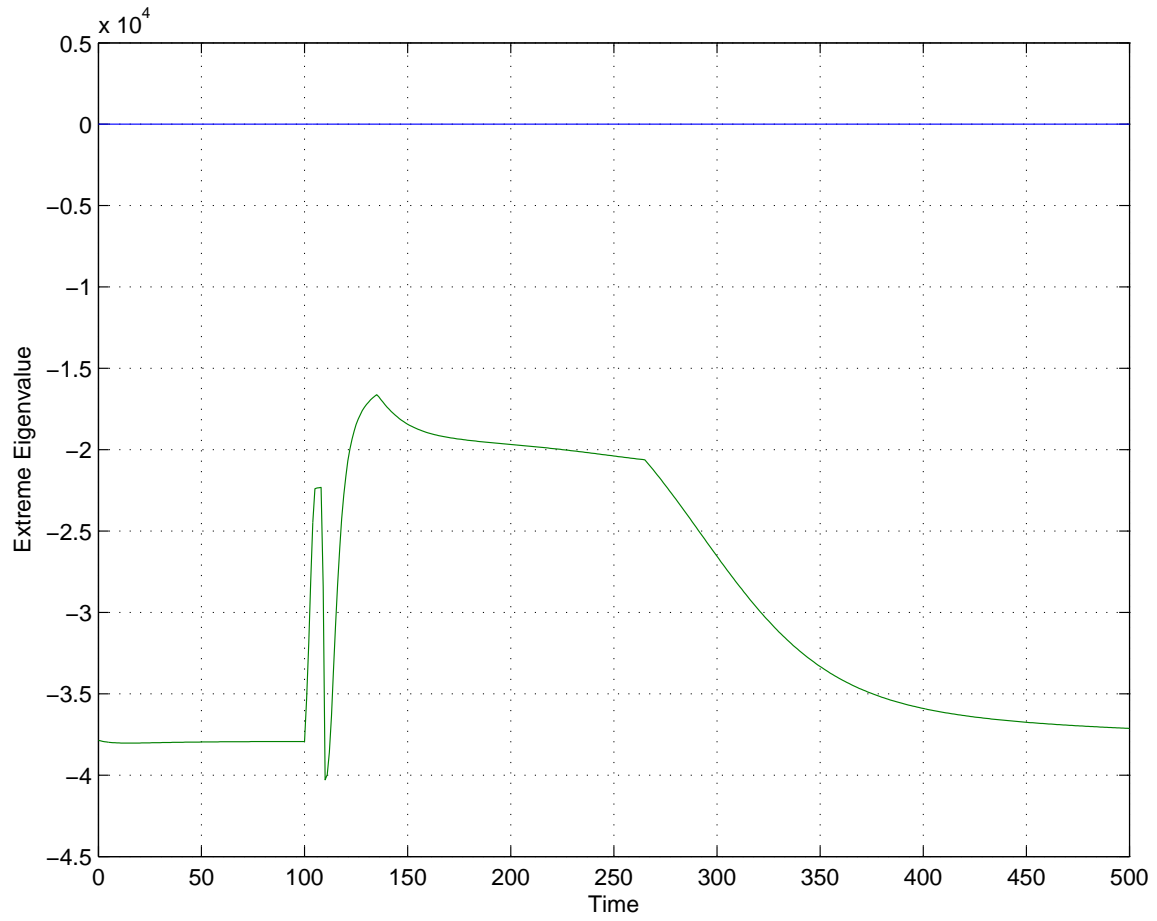


Figure 73: Extreme real eigenvalues in the model of Nygren et al. (1998).

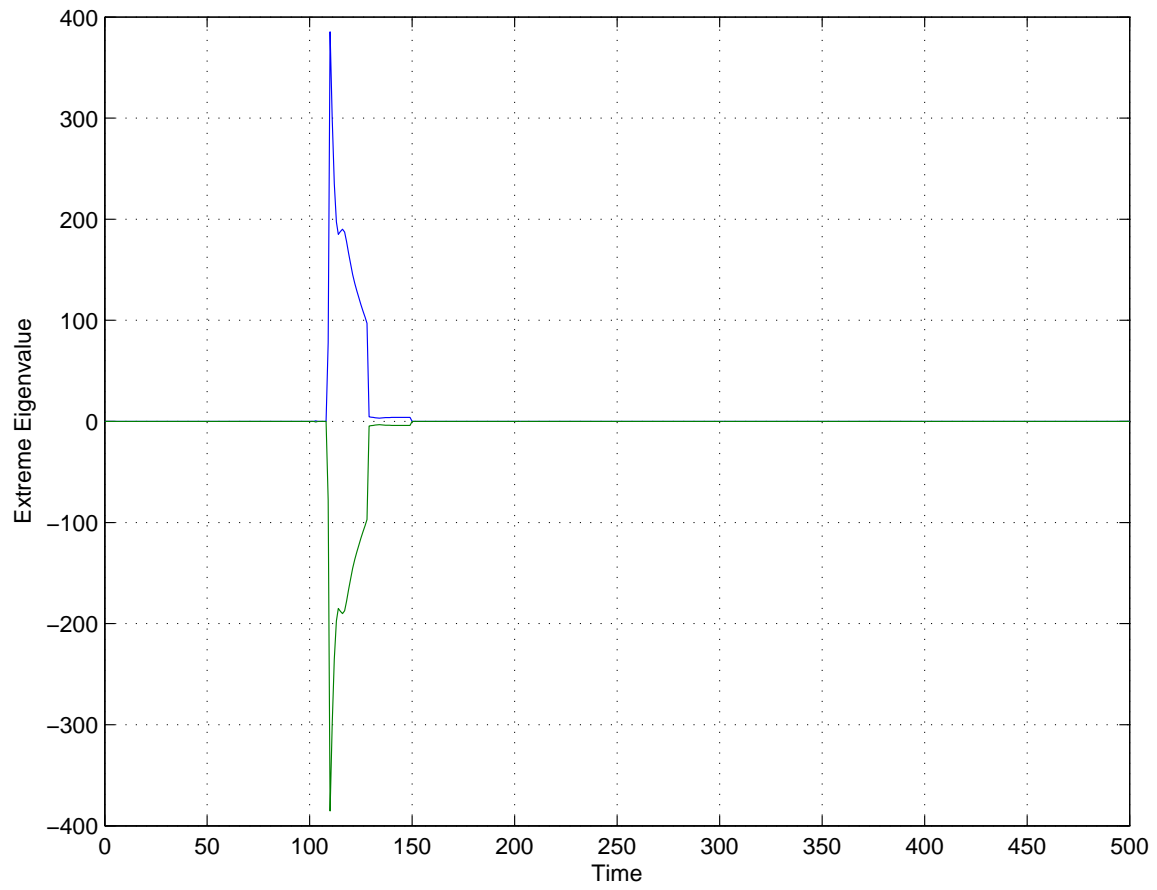


Figure 74: Extreme imaginary eigenvalues in the model of Nygren et al. (1998).

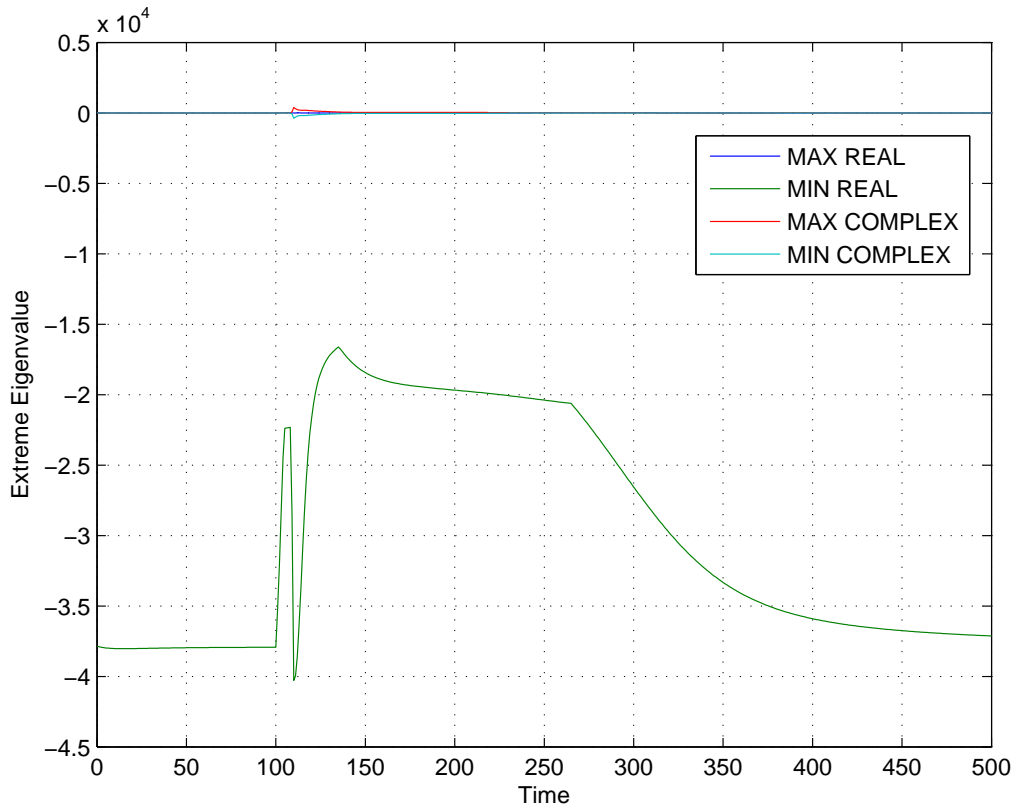


Figure 75: Extreme values of eigenvalues over time in the model of Nygren et al. (1998).

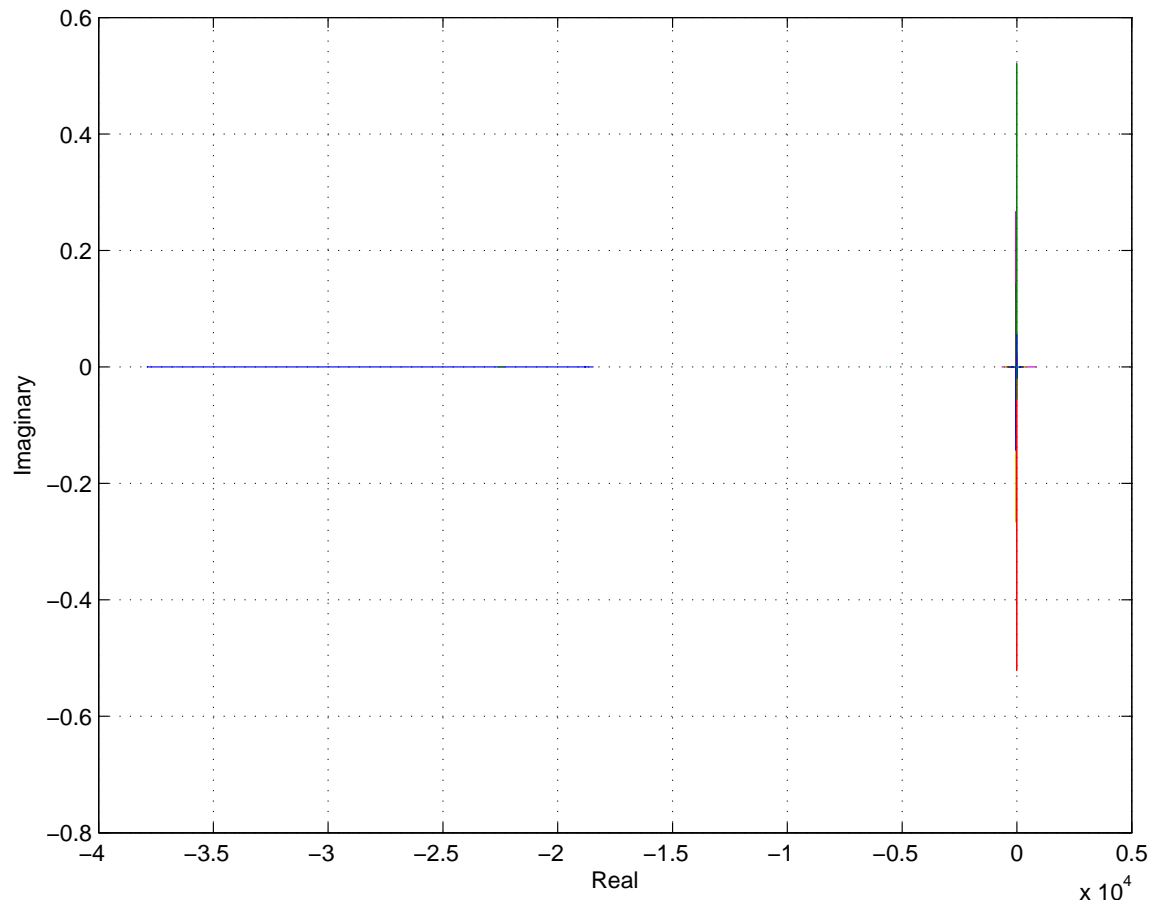


Figure 76: Plot of all eigenvalues at all times measured in the model of Nygren et al. (1998).

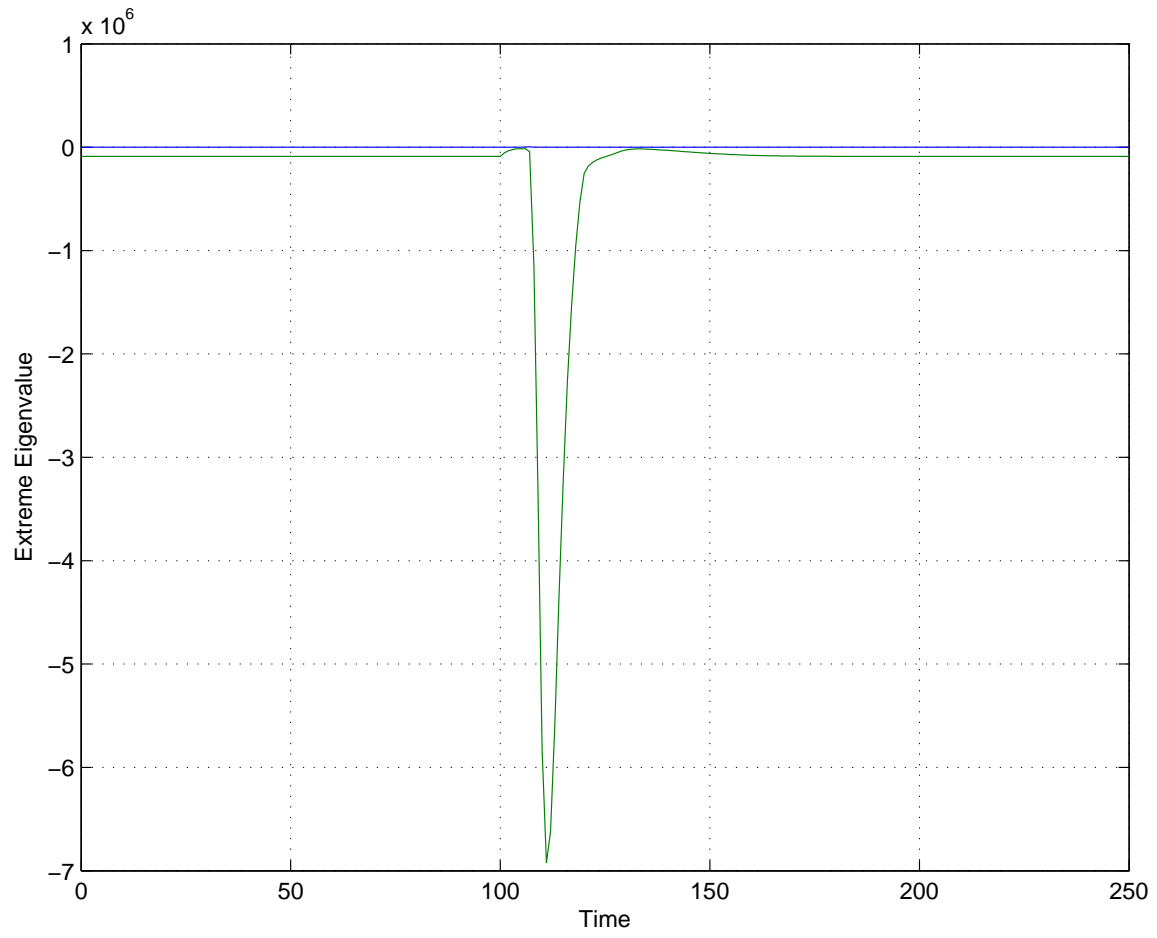


Figure 77: Extreme real eigenvalues in the model of Pandit et al. (2001).

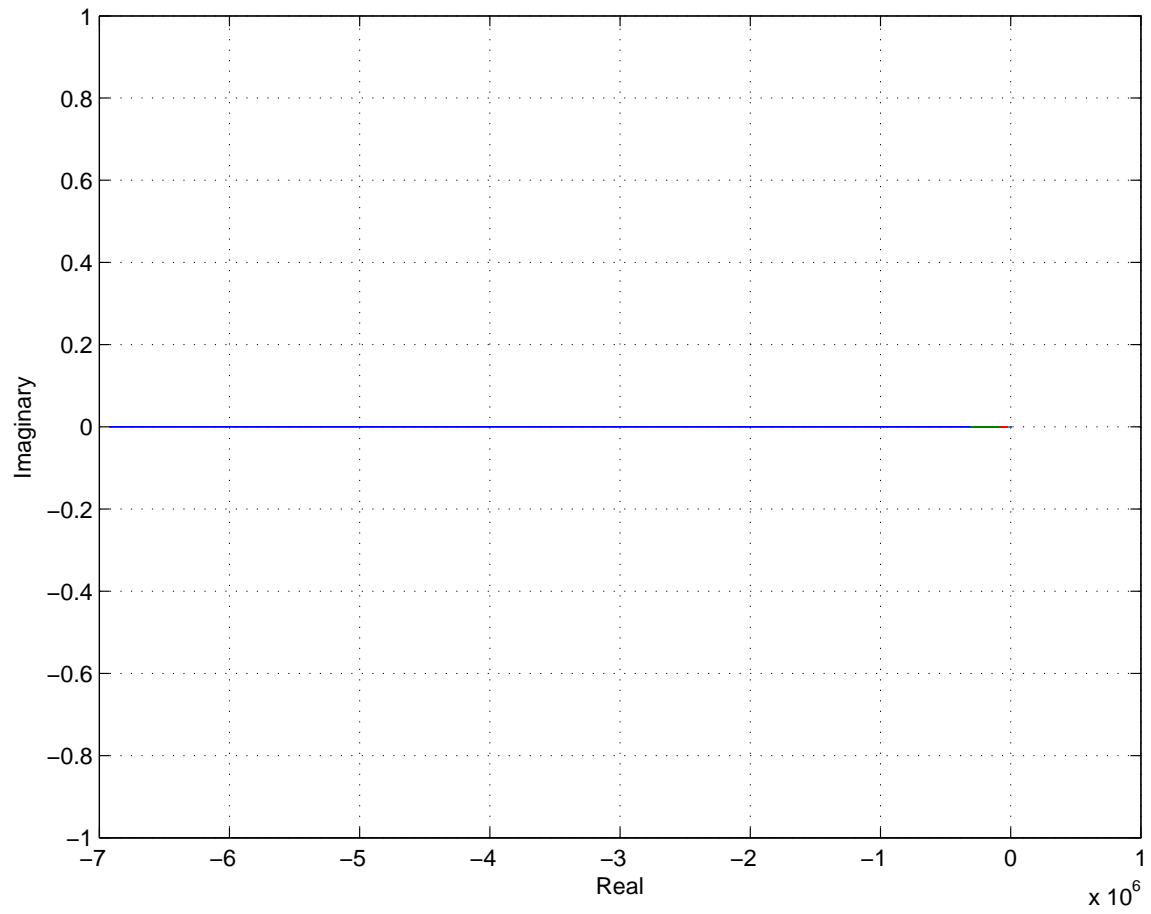


Figure 78: Plot of all eigenvalues at all times measured in the model of Pandit et al. (2001).

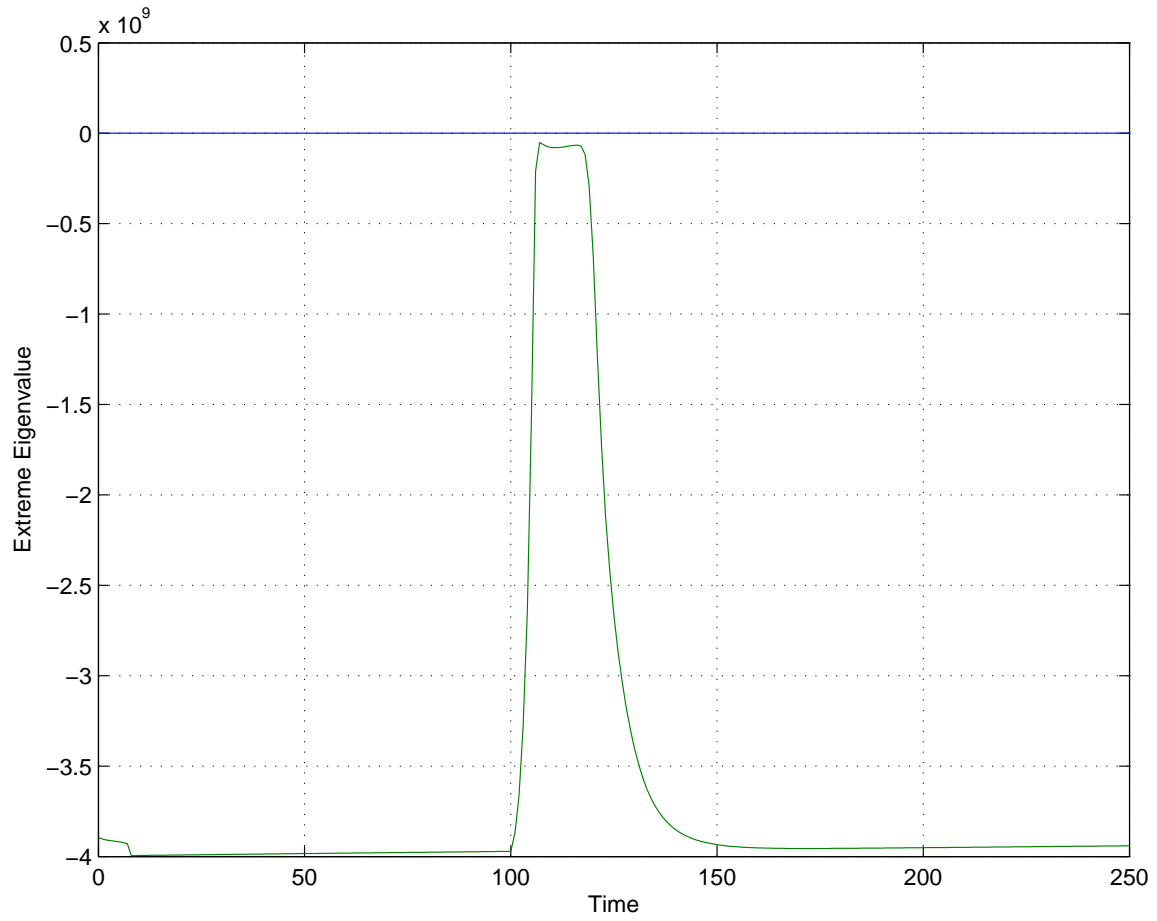


Figure 79: Extreme real eigenvalues in the model of Pandit et al. (2003).

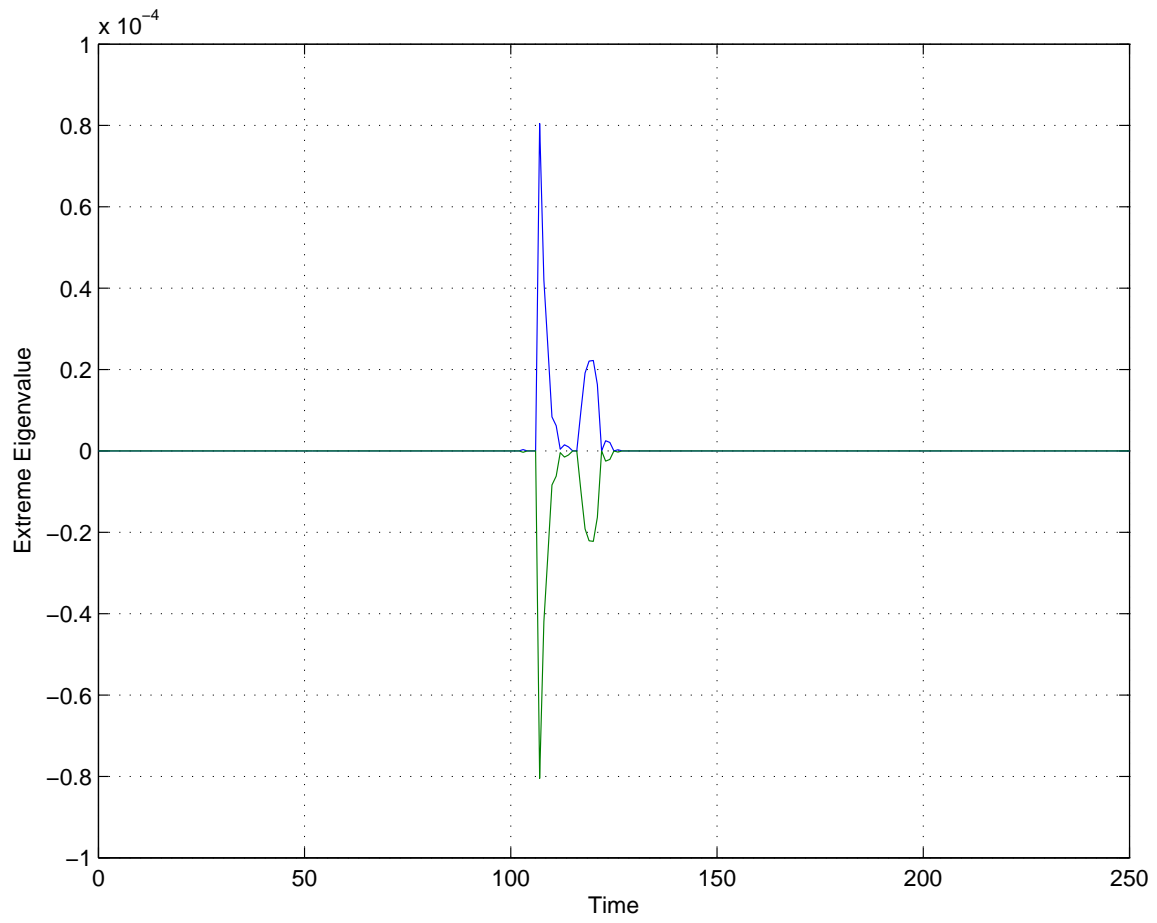


Figure 80: Extreme imaginary eigenvalues in the model of Pandit et al. (2003).

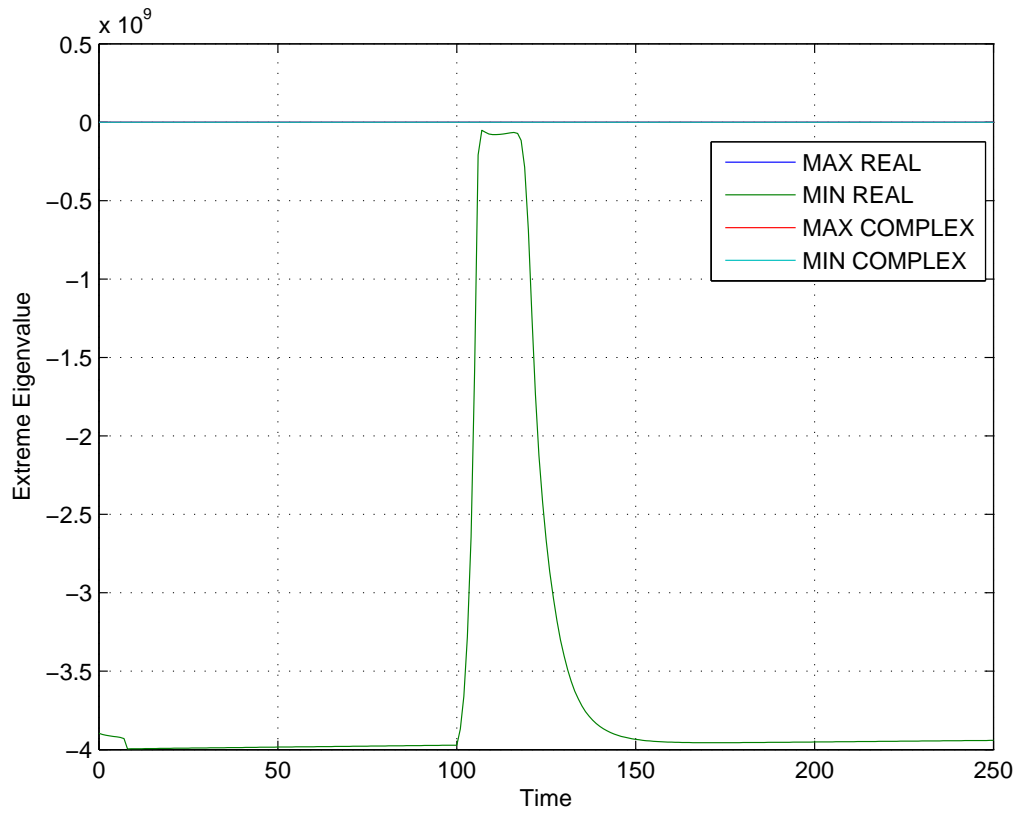


Figure 81: Extreme values of eigenvalues over time in the model of Pandit et al. (2003).

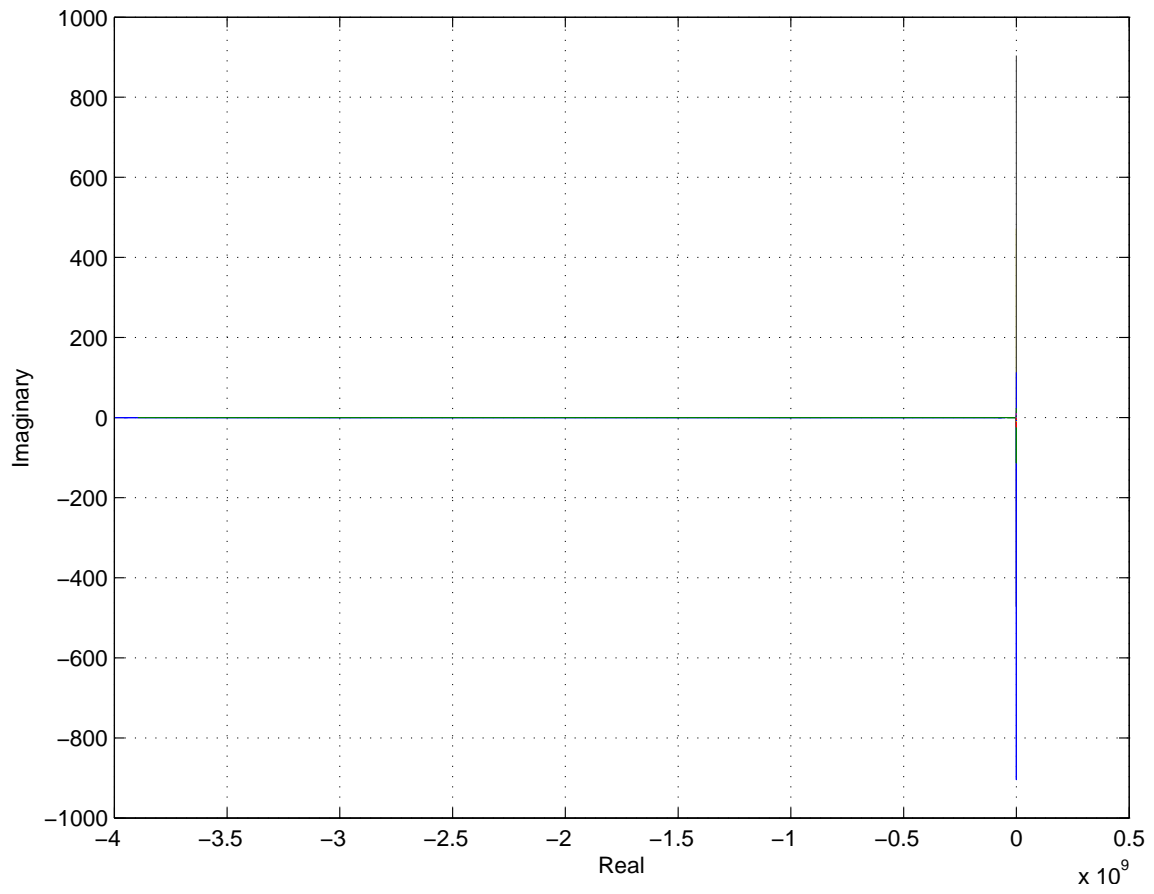


Figure 82: Plot of all eigenvalues at all times measured in the model of Pandit et al. (2003).

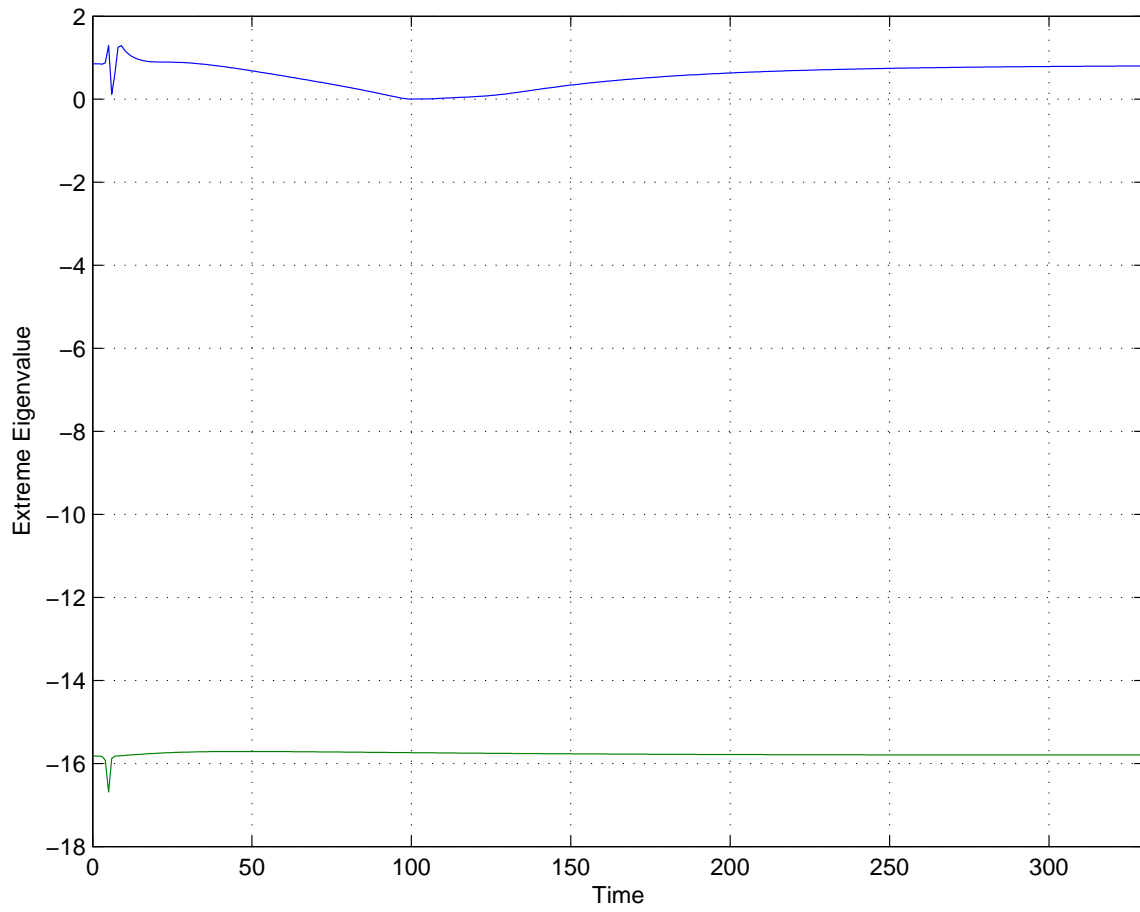


Figure 83: Extreme real eigenvalues in the Puglisi-Bers model

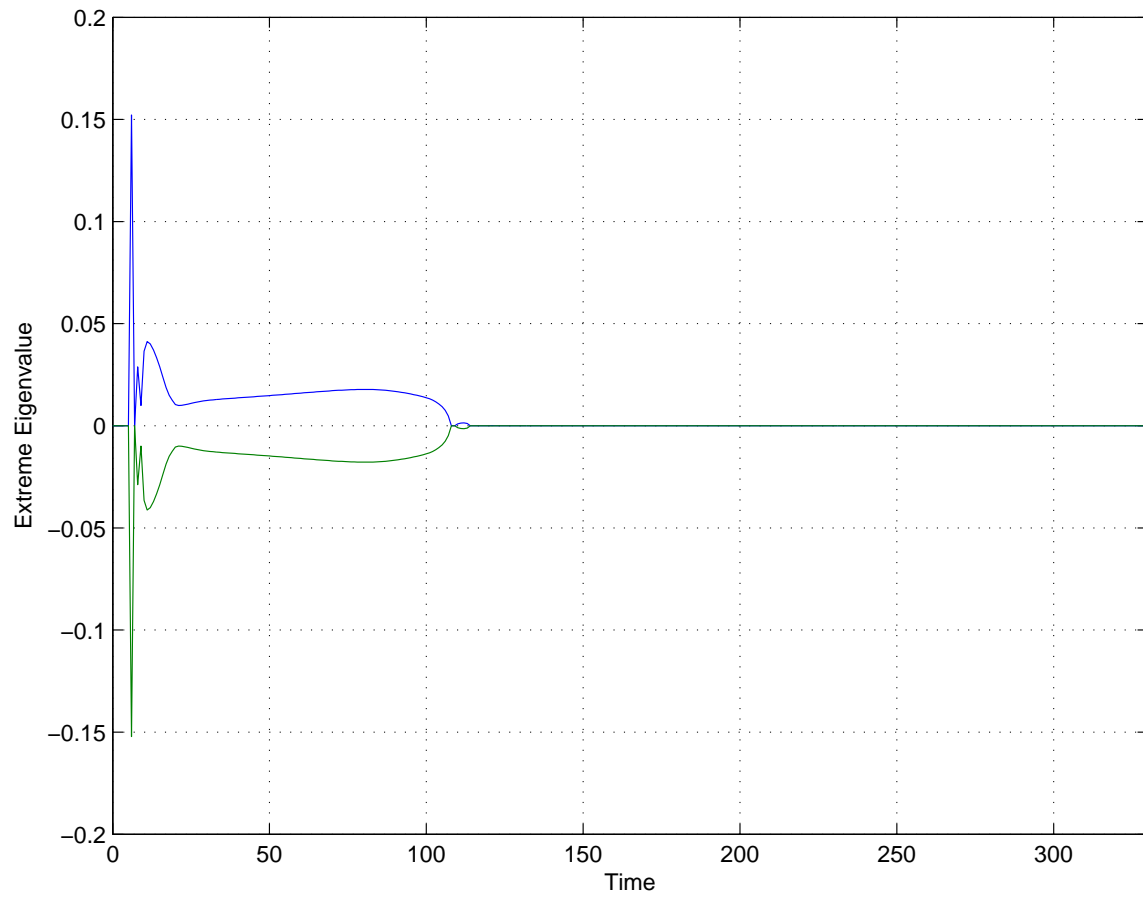


Figure 84: Extreme imaginary eigenvalues in the Puglisi-Bers model

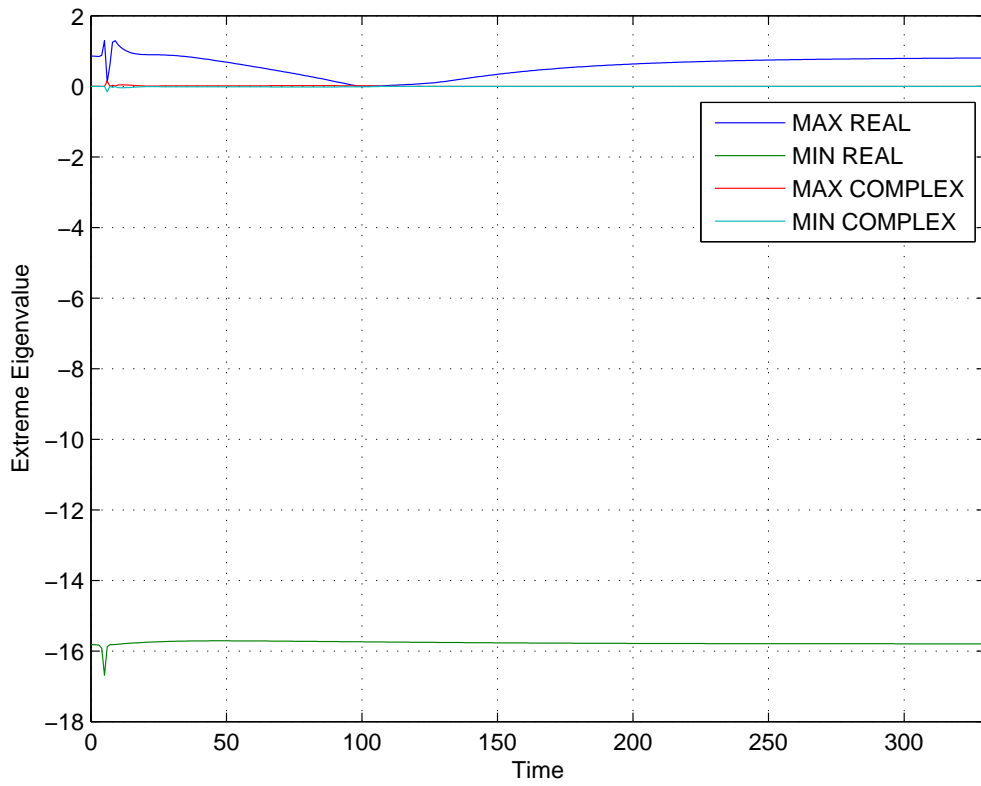


Figure 85: Extreme values of eigenvalues over time in the Puglisi-Bers model.

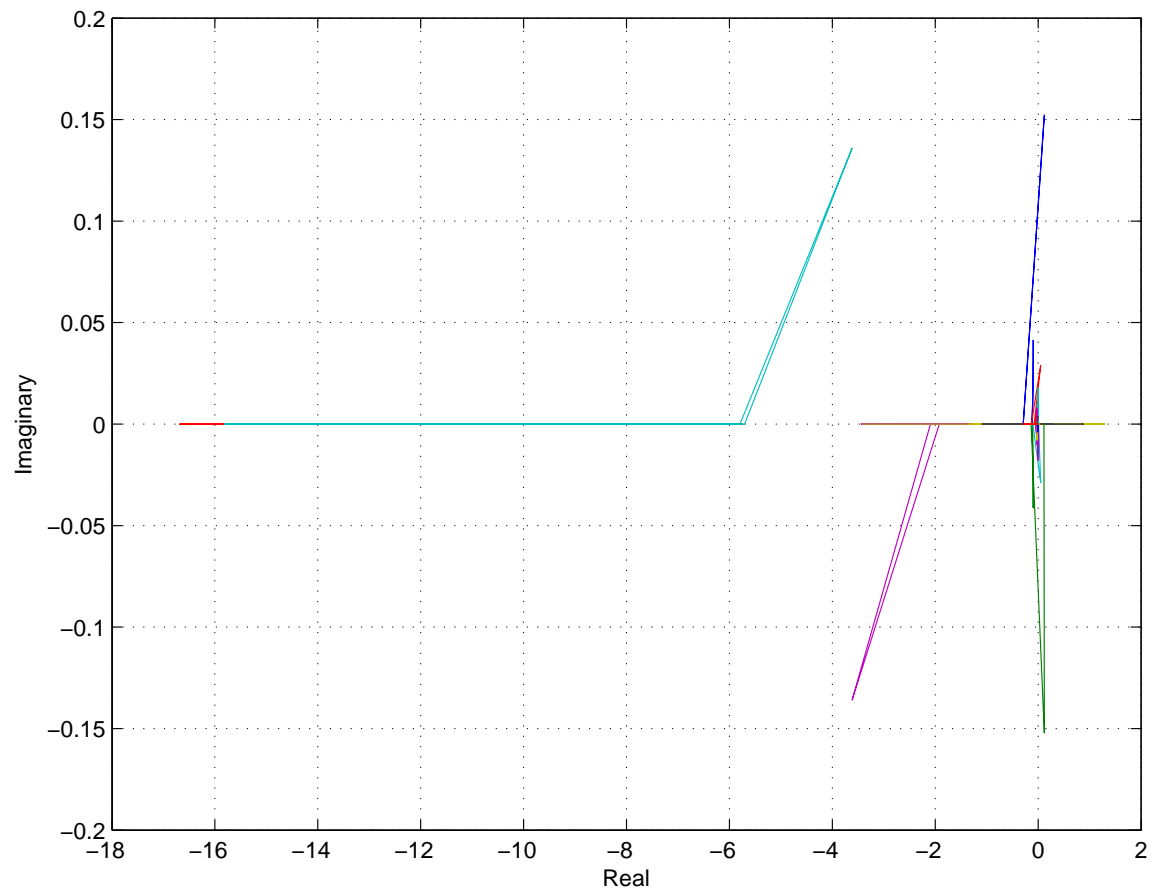


Figure 86: Plot of all eigenvalues at all times measured in the Puglisi–Bers model

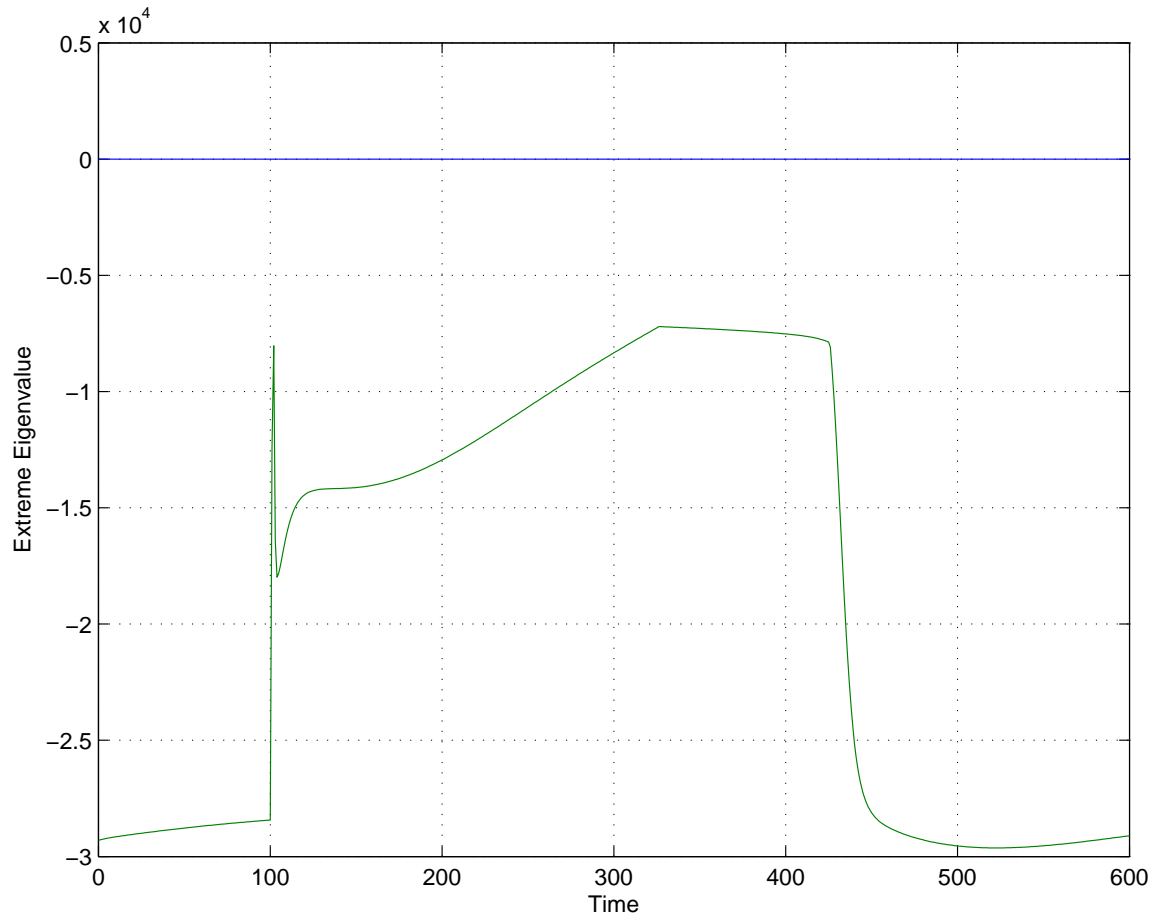


Figure 87: Extreme real eigenvalues in the model of Sakmann et al. (2000) (Endocardial variant)

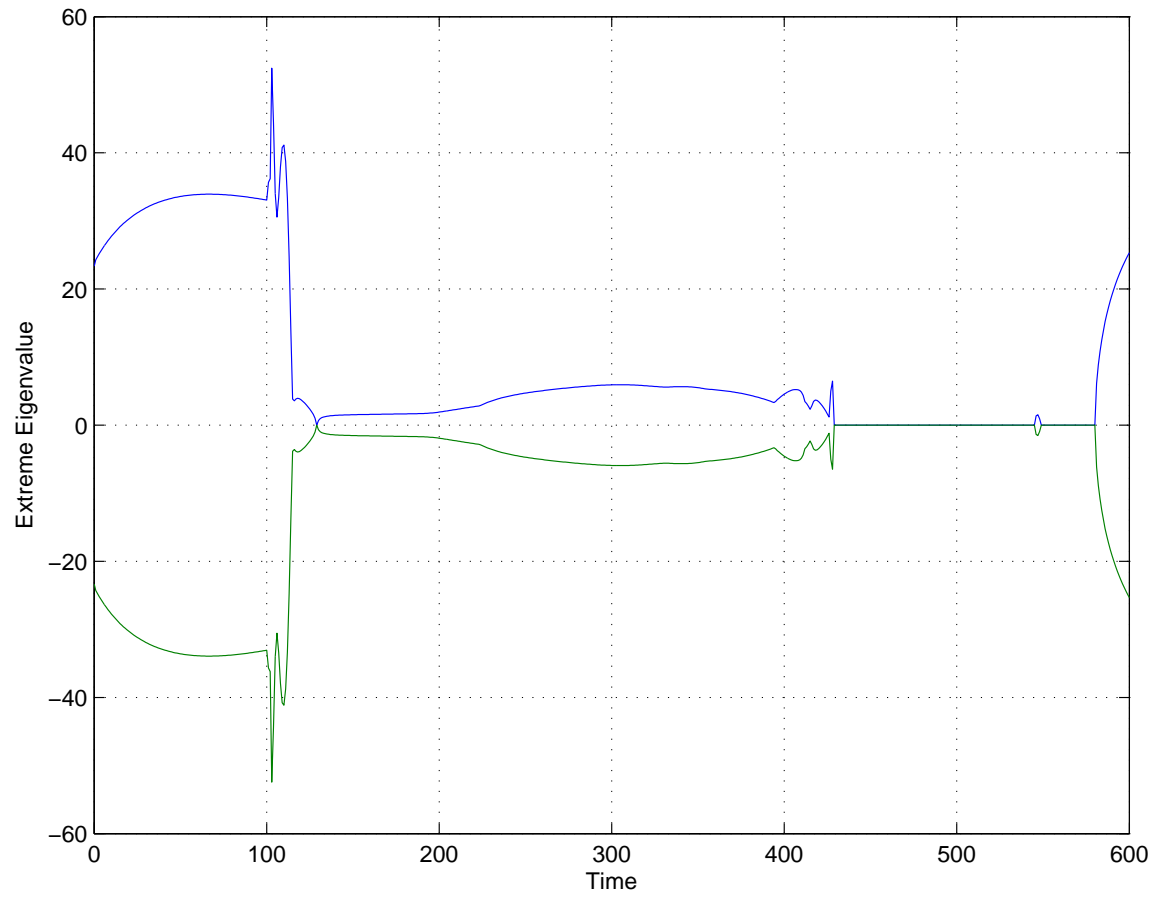


Figure 88: Extreme imaginary eigenvalues in the model of Sakmann et al. (2000) (Endocardial variant)

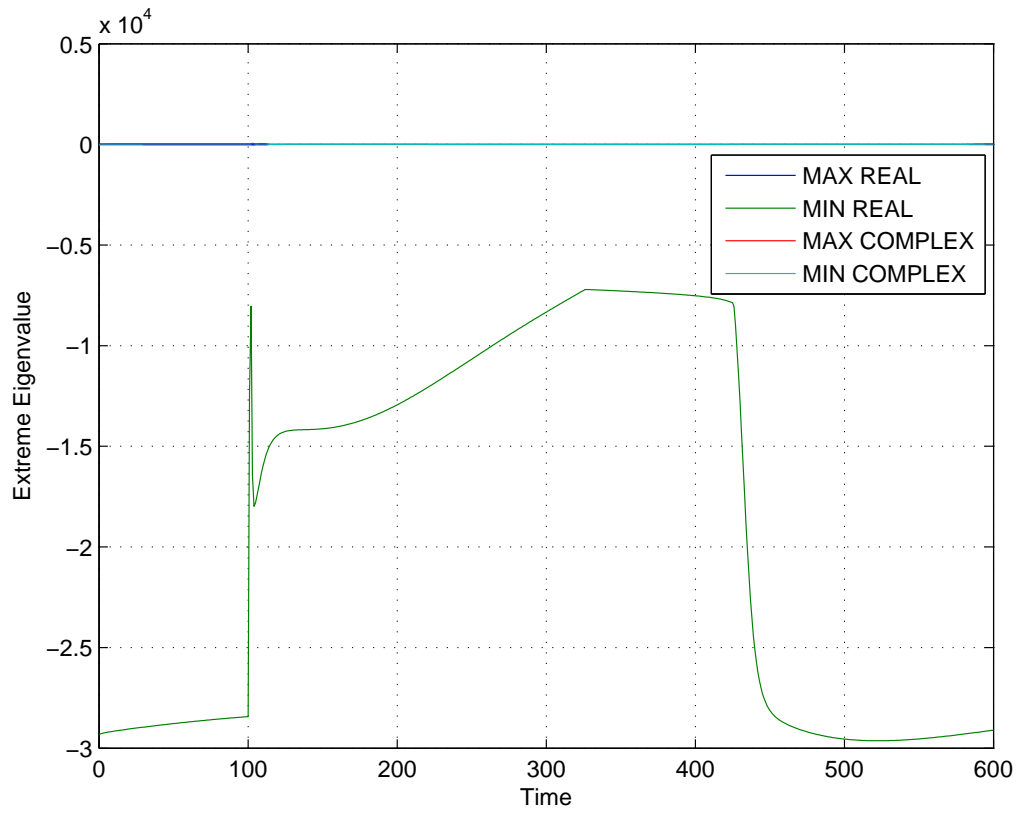


Figure 89: Extreme values of eigenvalues over time in the model of Sakmann et al. (2000) (Endocardial variant)

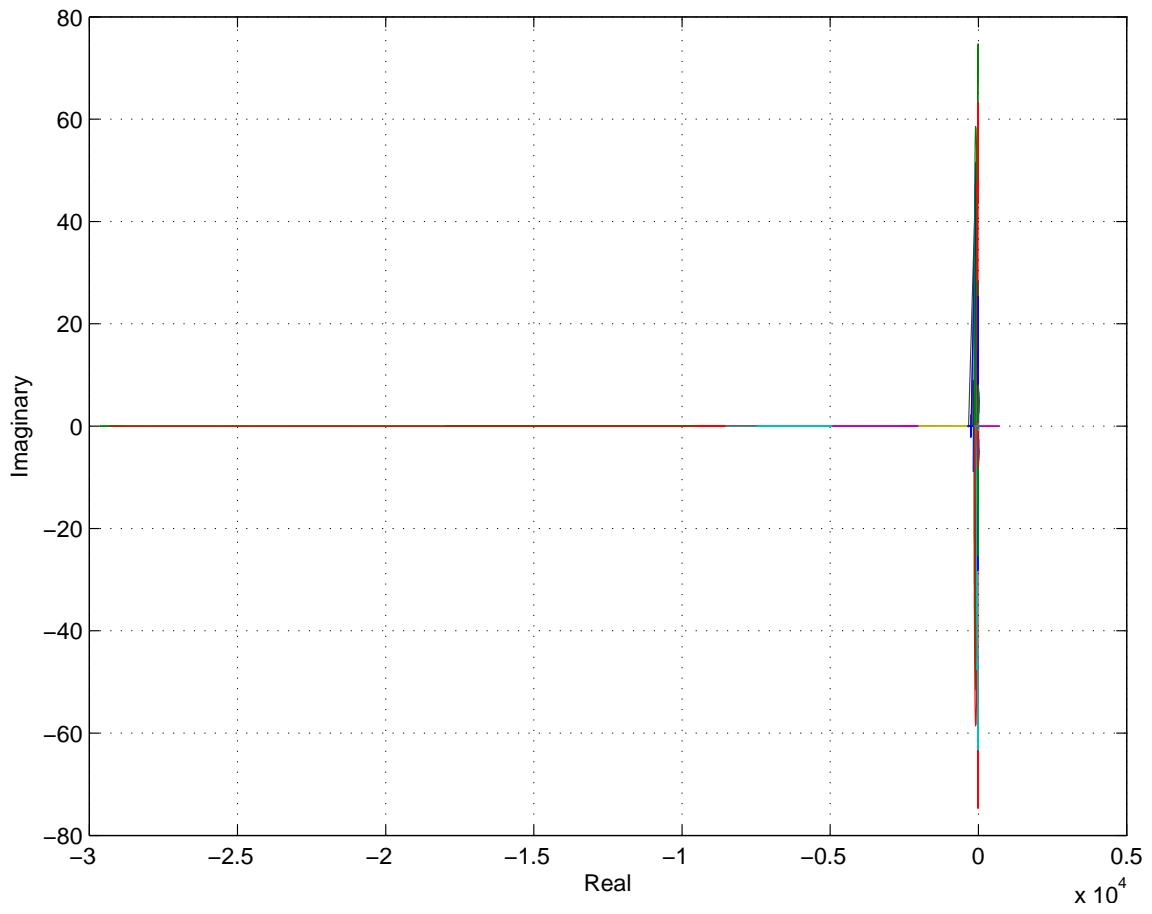


Figure 90: Plot of all eigenvalues at all times measured in the model of Sakmann et al. (2000) (Endocardial variant)

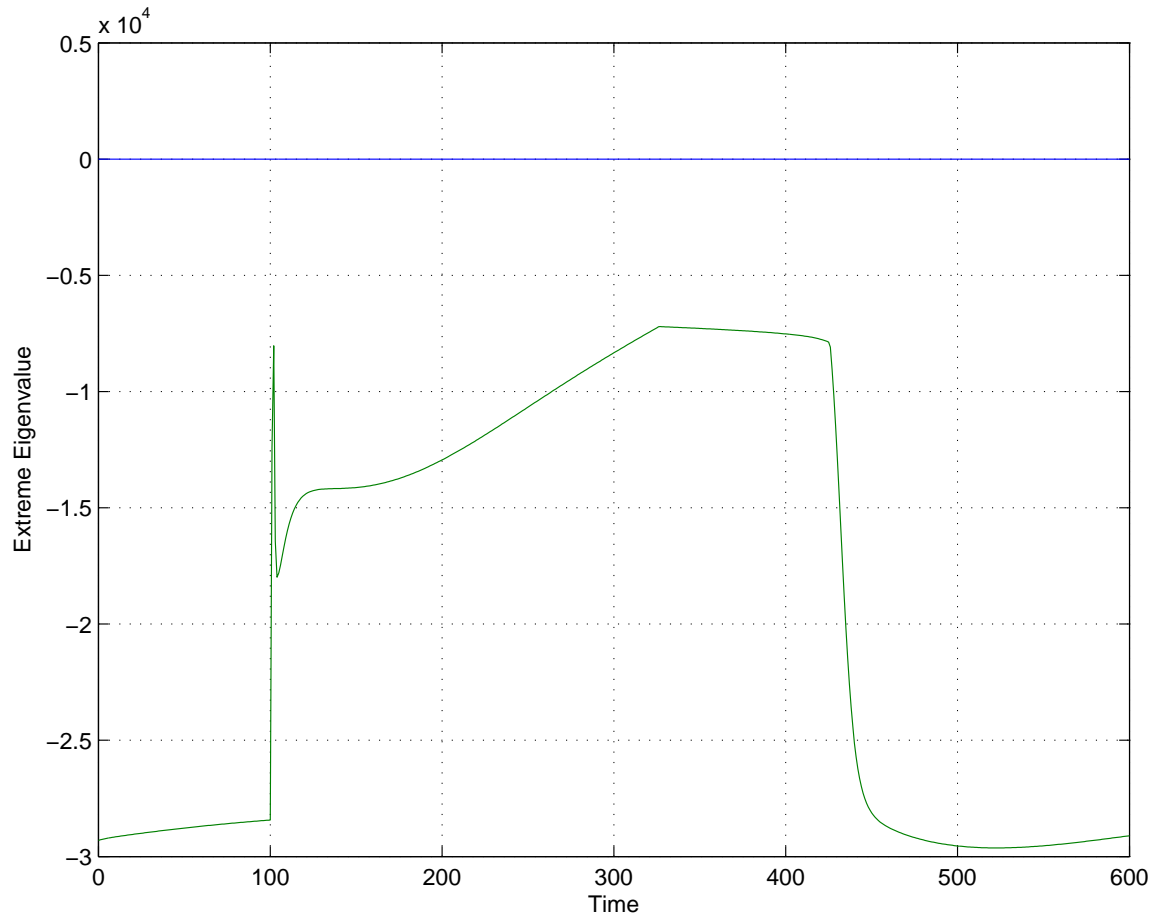


Figure 91: Extreme real eigenvalues in the model of Sakmann et al. (2000) (Epicardial variant)

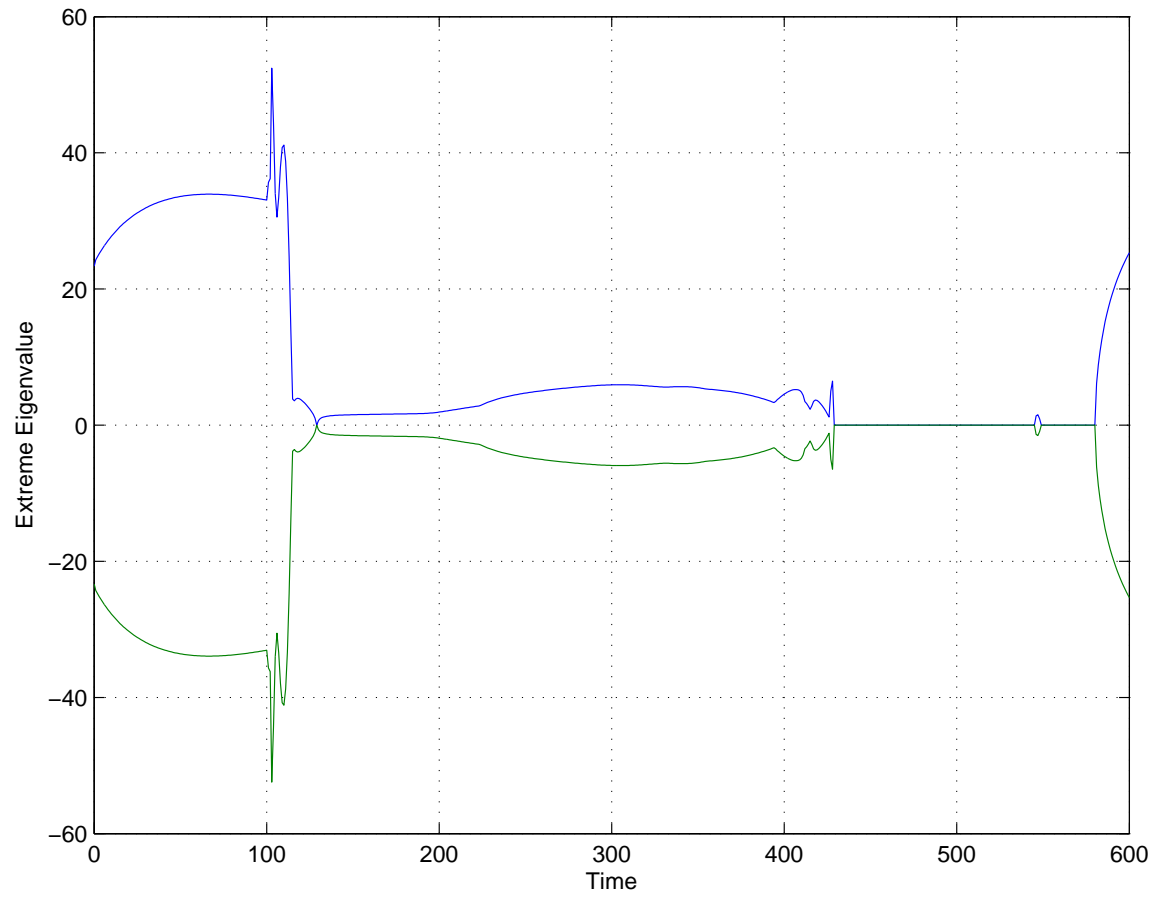


Figure 92: Extreme imaginary eigenvalues in the model of Sakmann et al. (2000) (Epicardial variant)

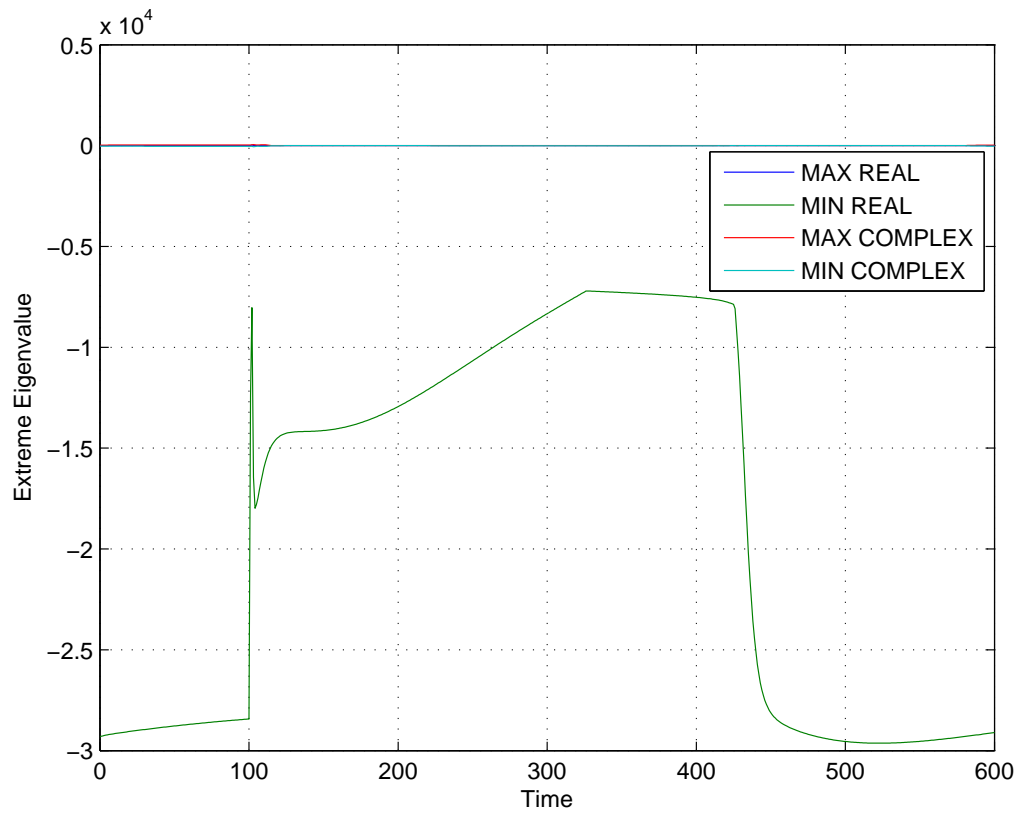


Figure 93: Extreme values of eigenvalues over time in the model of Sakmann et al. (2000) (Epicardial variant)

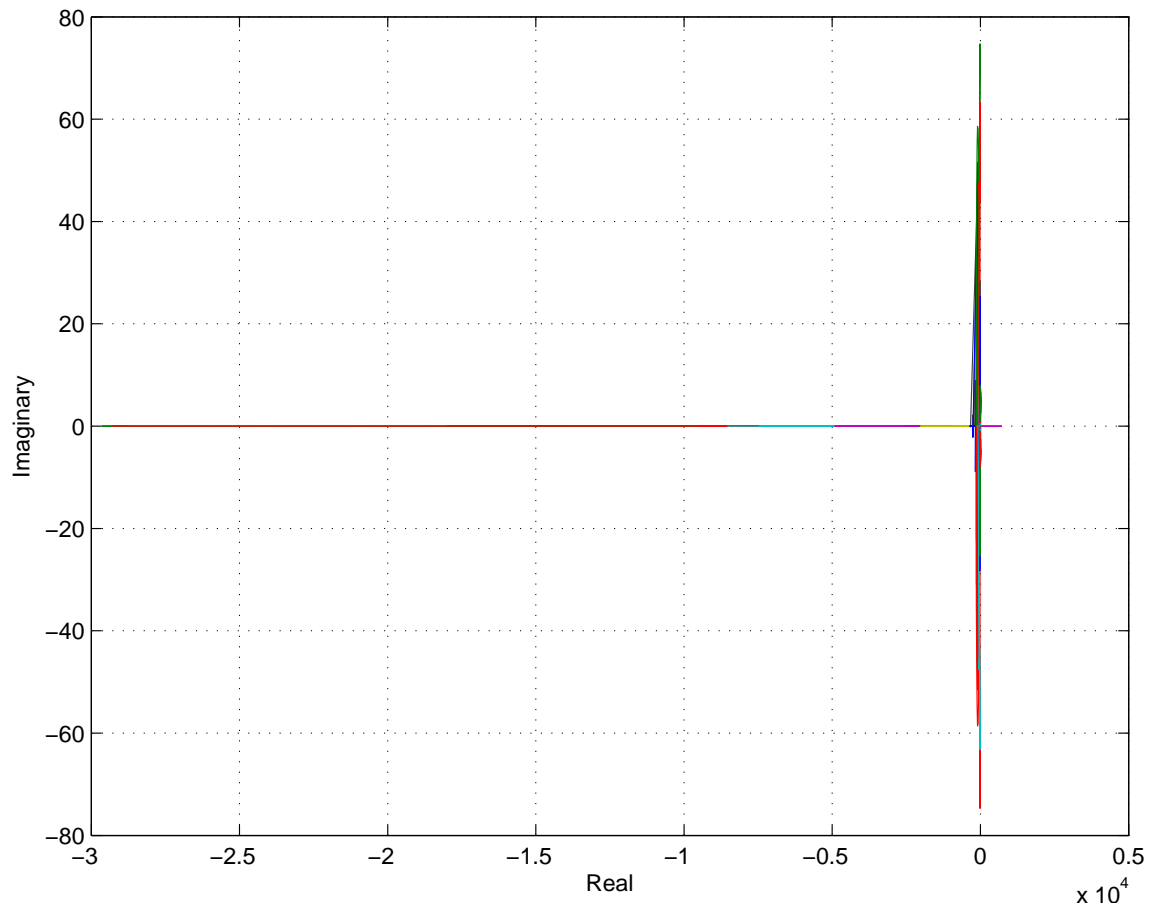


Figure 94: Plot of all eigenvalues at all times measured in the model of Sakmann et al. (2000) (Epicardial variant)

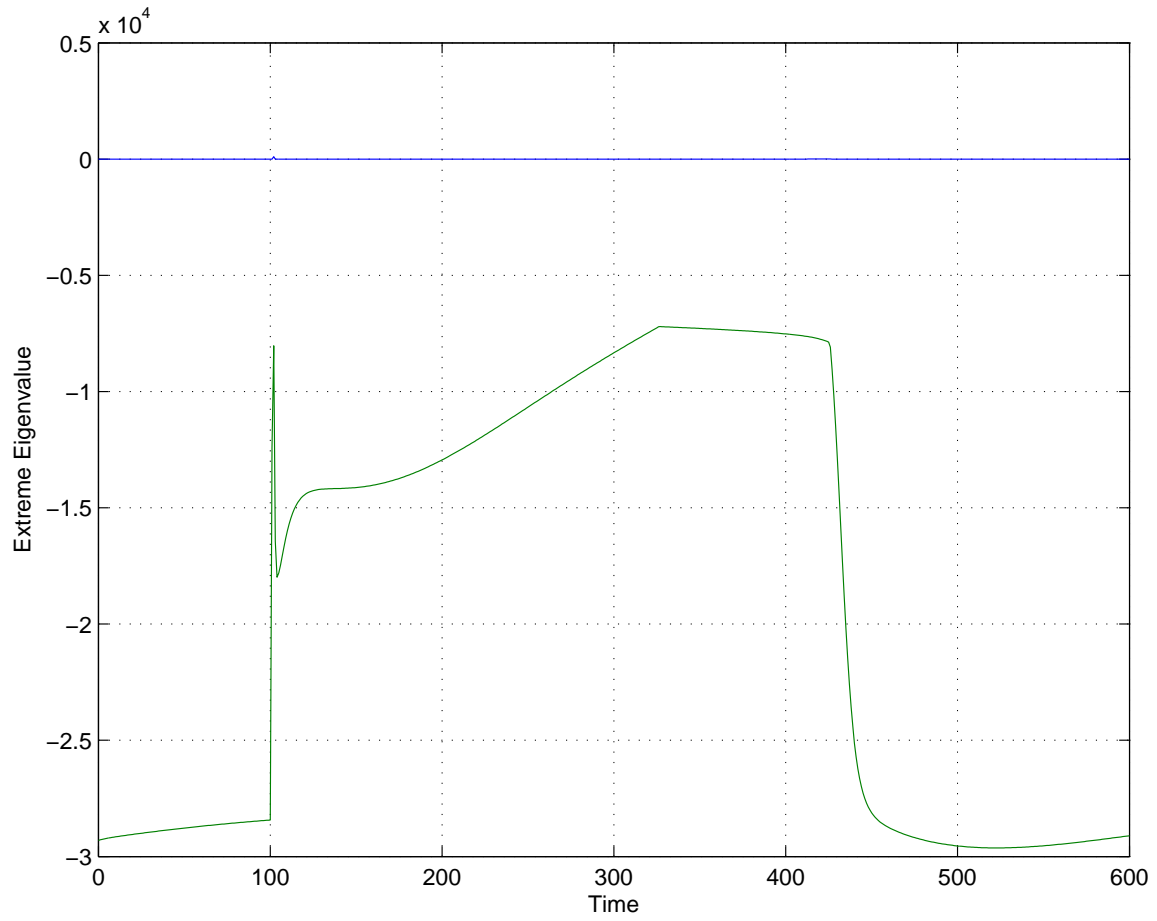


Figure 95: Extreme real eigenvalues in the model of Sakmann et al. (2000) (M-cell variant).

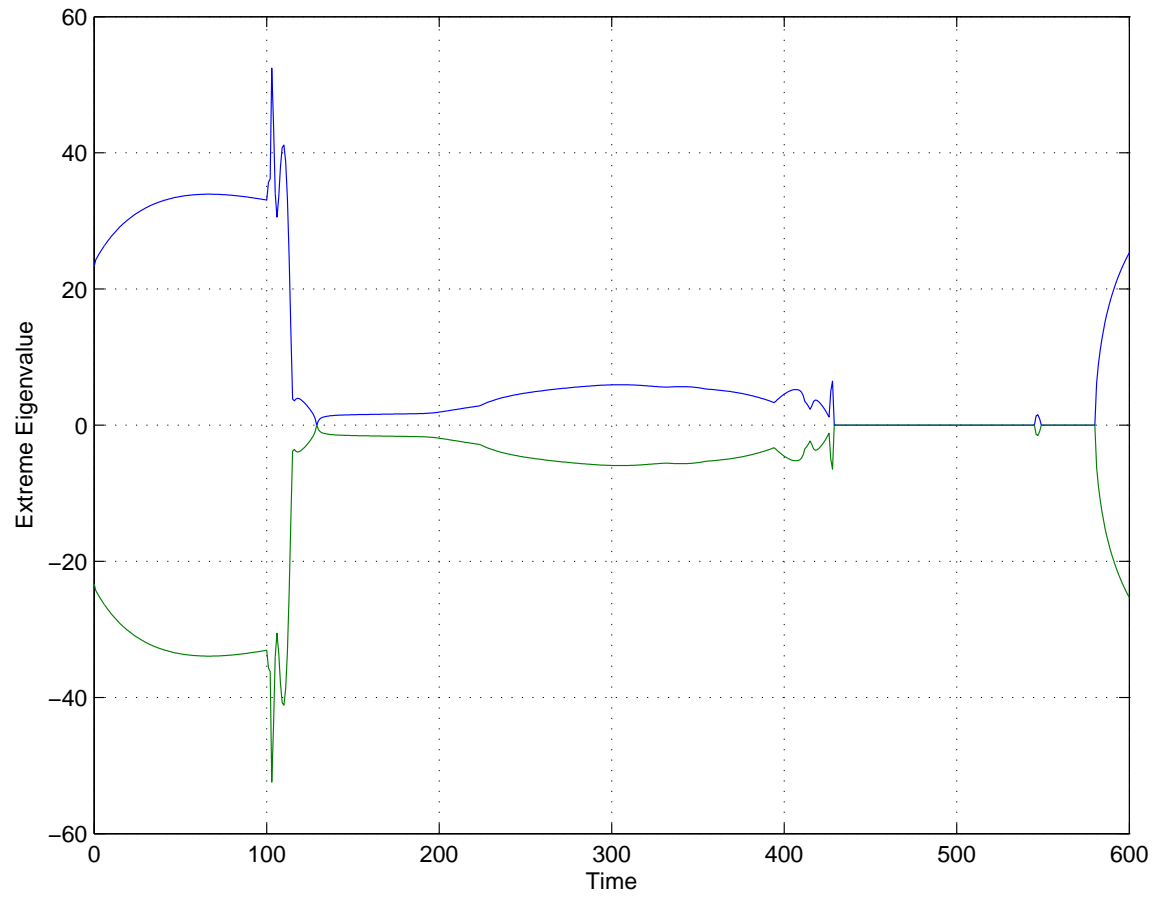


Figure 96: Extreme imaginary eigenvalues in the model of Sakmann et al. (2000) (M-cell variant).

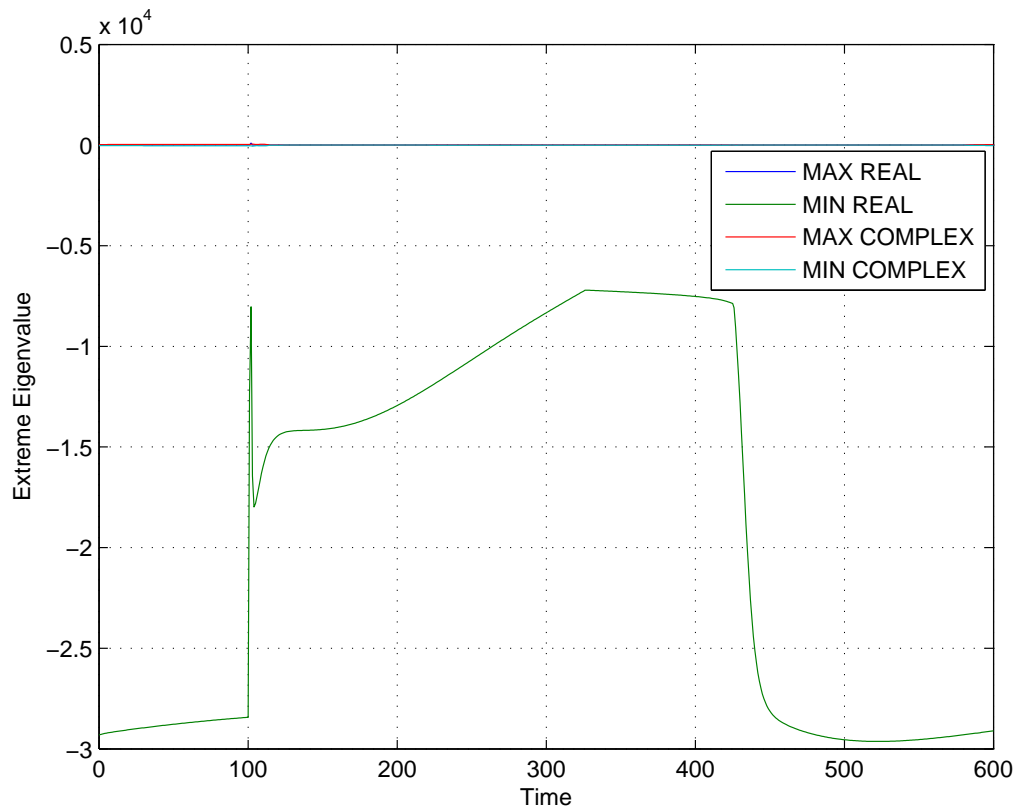


Figure 97: Extreme values of eigenvalues over time in the model of Sakmann et al. (2000) (M-cell variant).

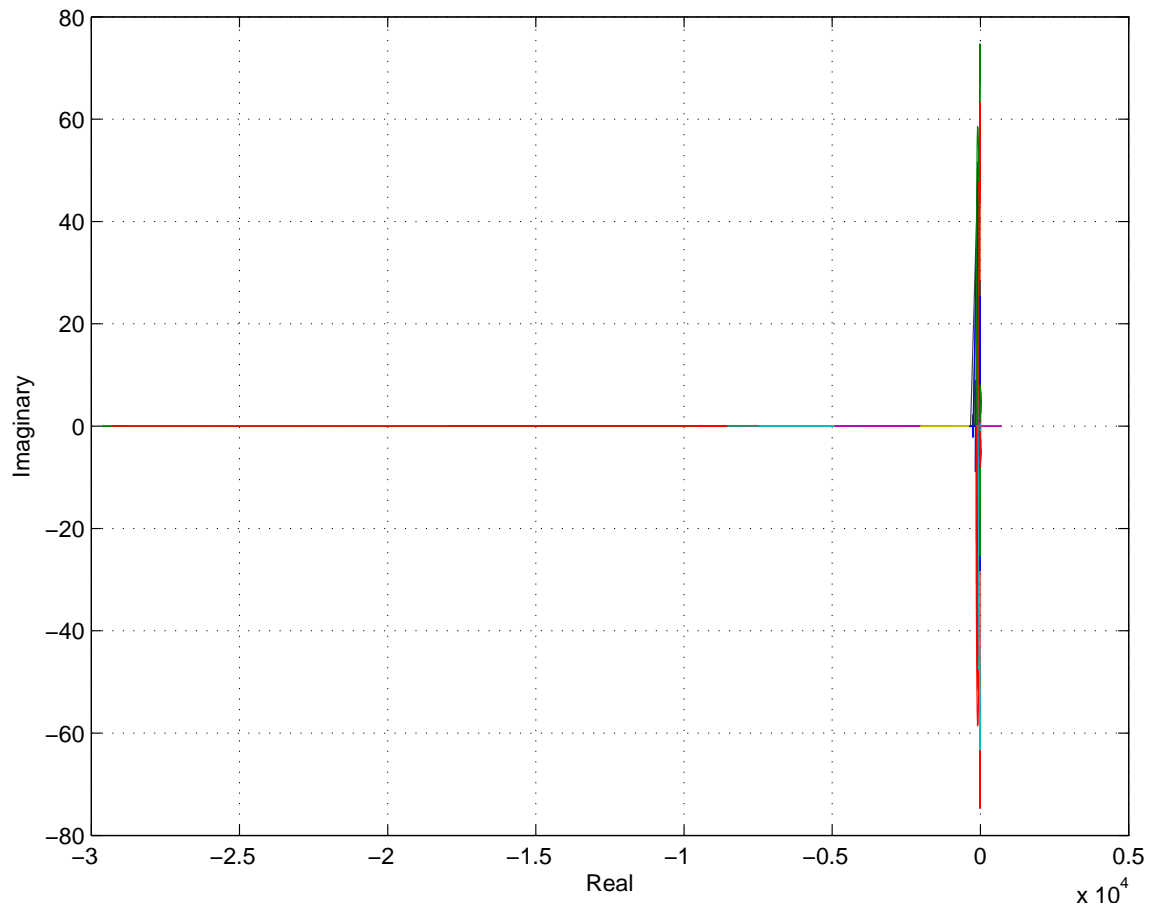


Figure 98: Plot of all eigenvalues at all times measured in the model of Sakmann et al. (2000) (M-cell variant).

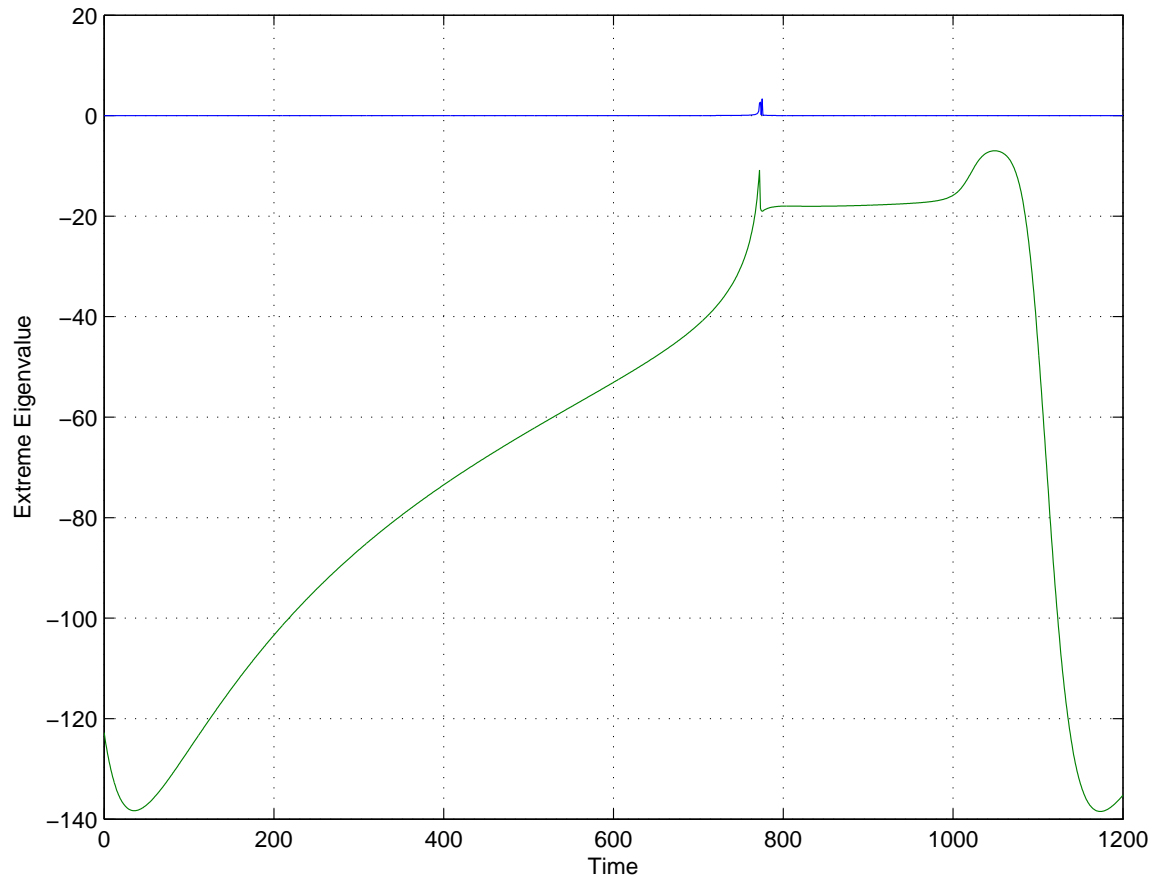


Figure 99: Extreme real eigenvalues in the model of Stewart et al. (2009).

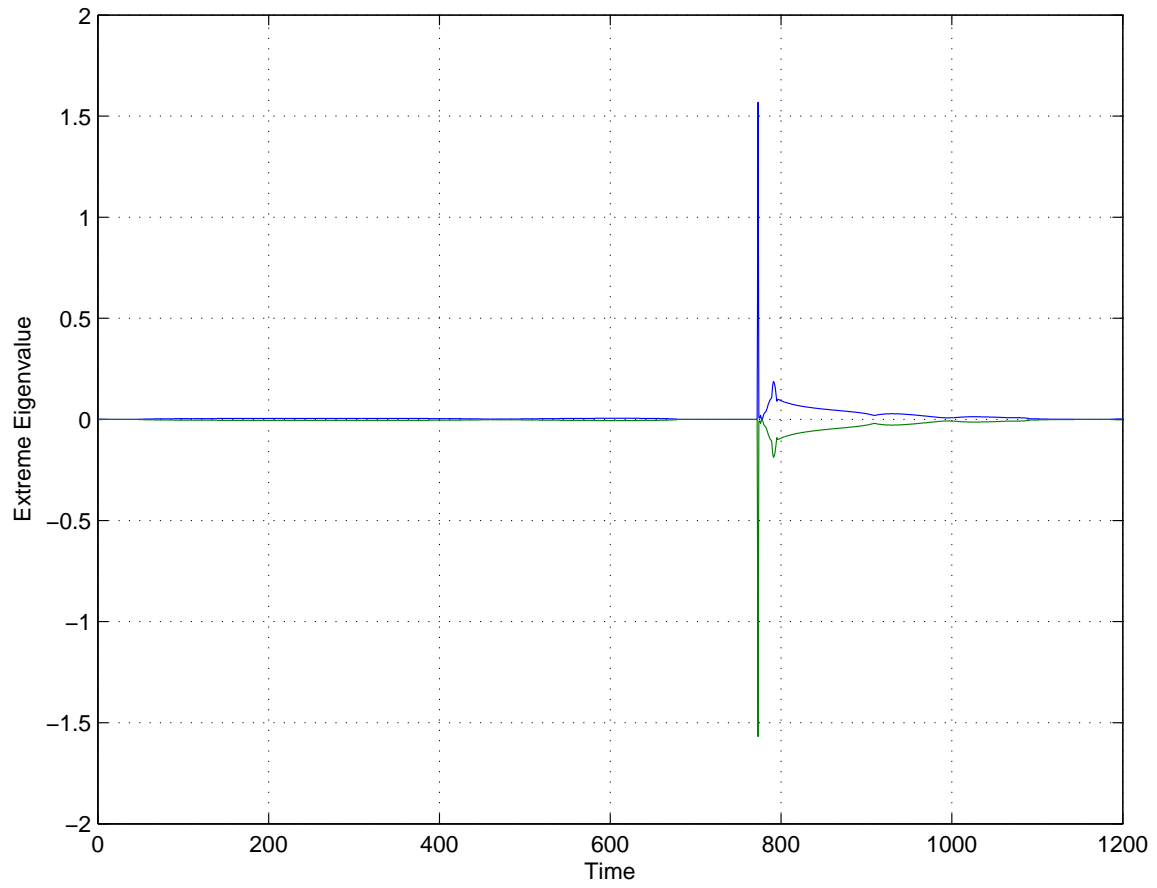


Figure 100: Extreme imaginary eigenvalues in the model of Stewart et al. (2009).

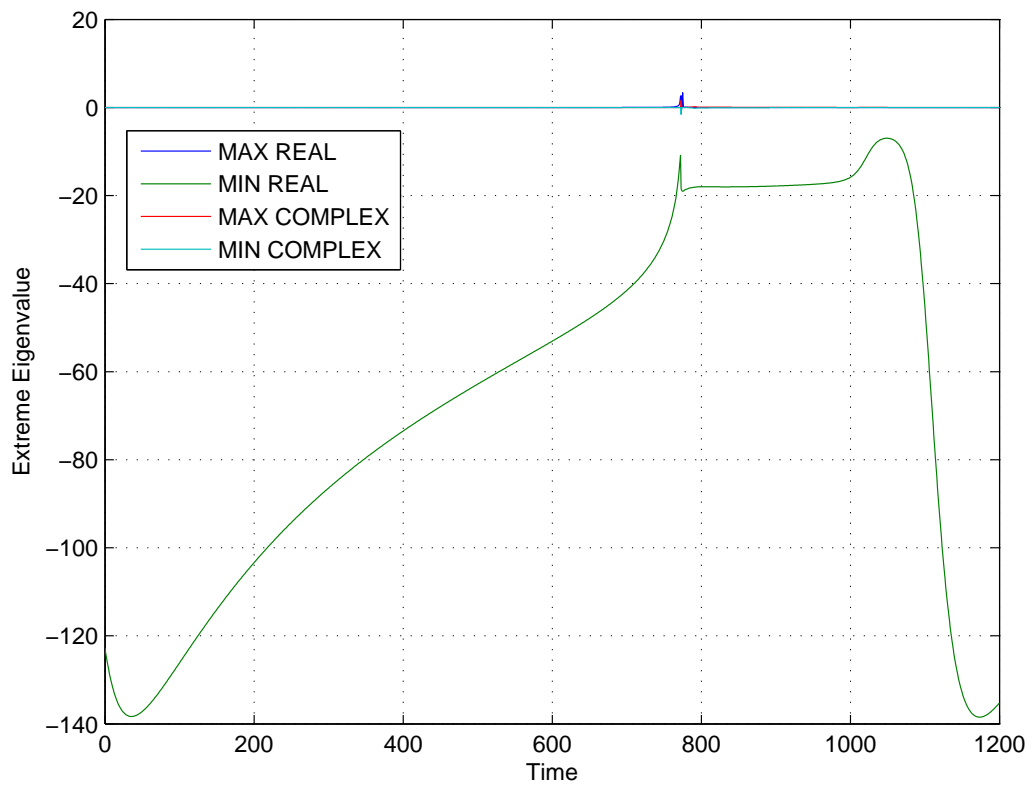


Figure 101: Extreme values of eigenvalues over time in the model of Stewart et al. (2009).

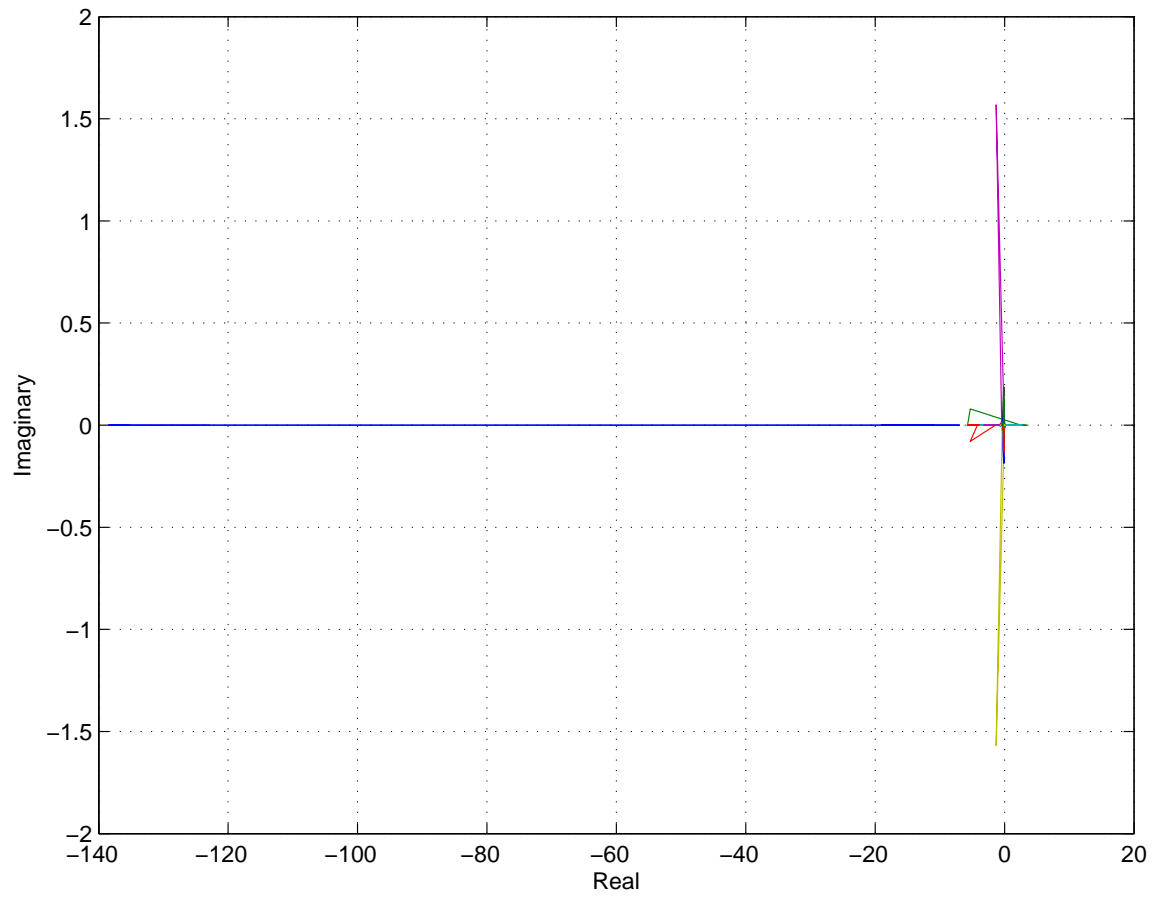


Figure 102: Plot of all eigenvalues at all times measured in the model of Stewart et al. (2009).

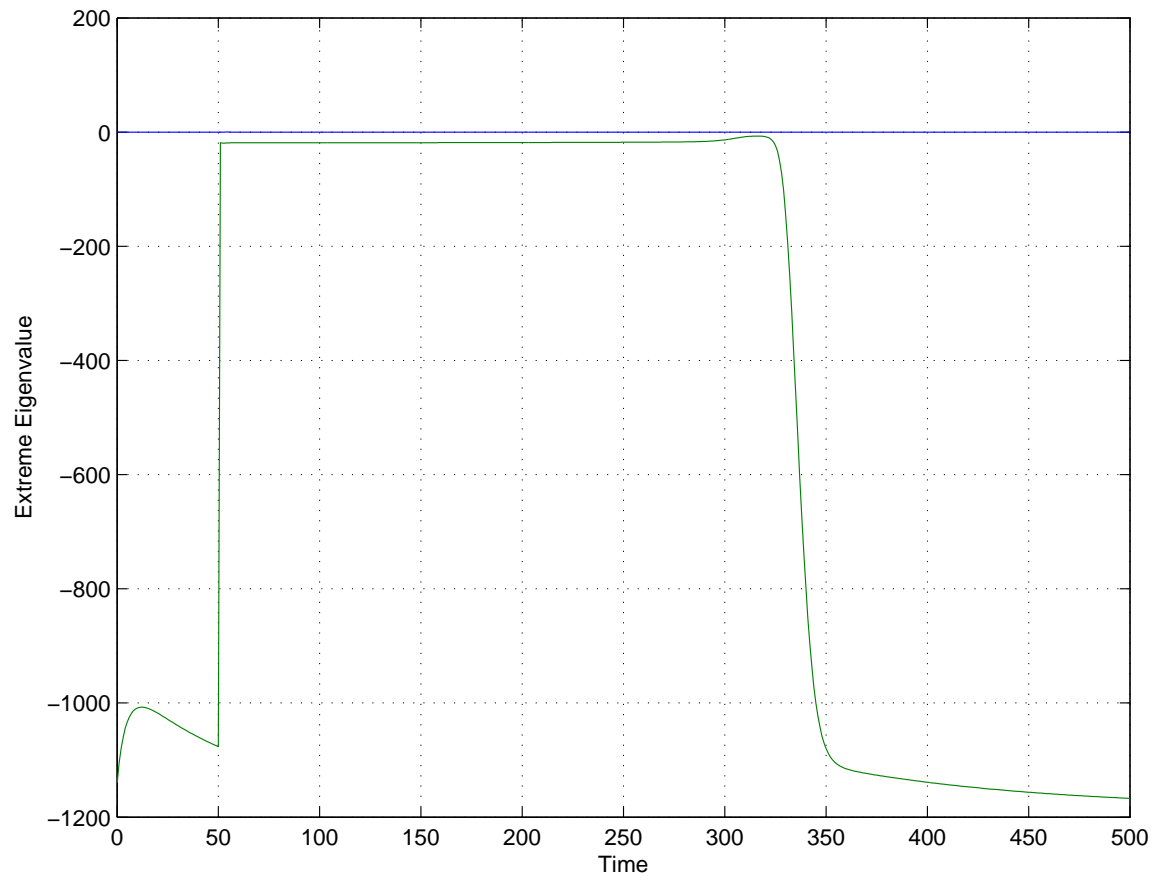


Figure 103: Extreme real eigenvalues in the model of Ten Tusscher et al. (2004) (Endocardial variant)

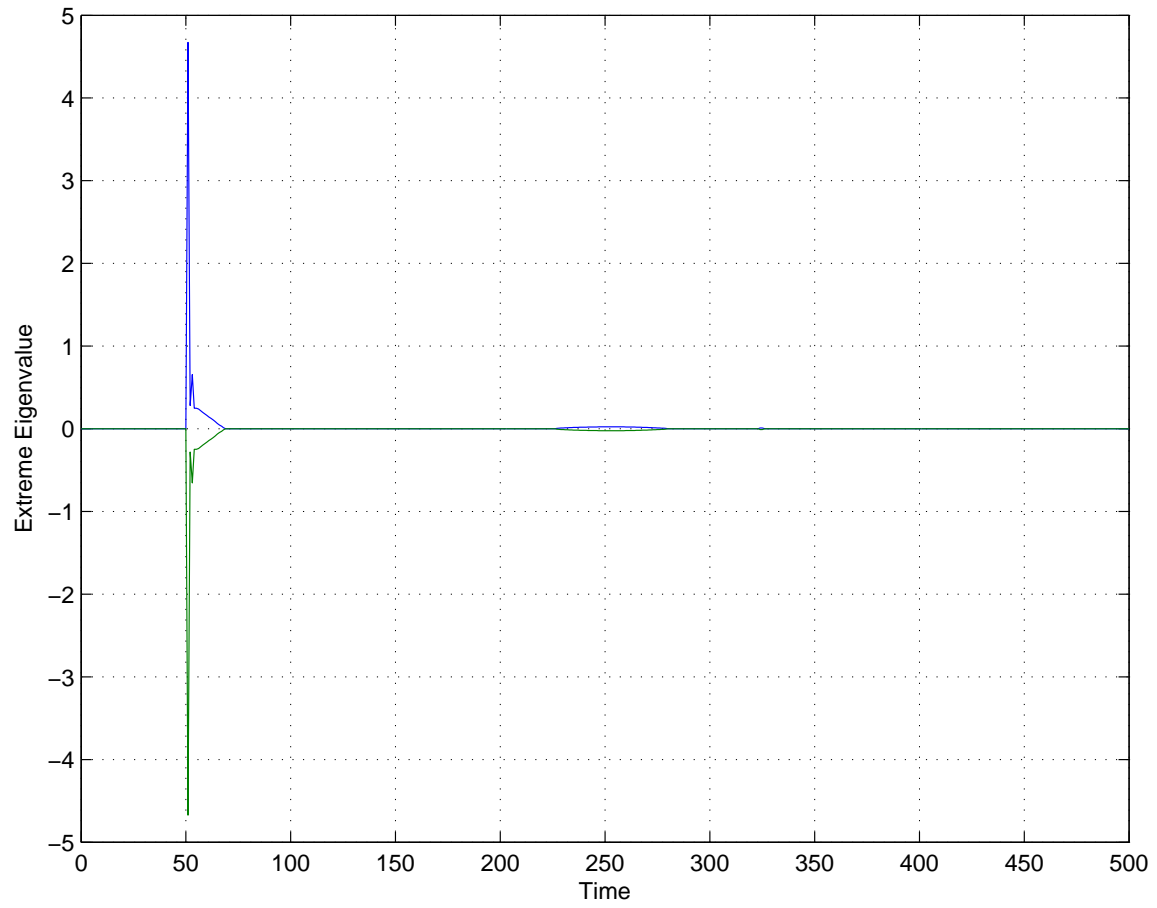


Figure 104: Extreme imaginary eigenvalues in the model of Ten Tusscher et al. (2004) (Endocardial variant)

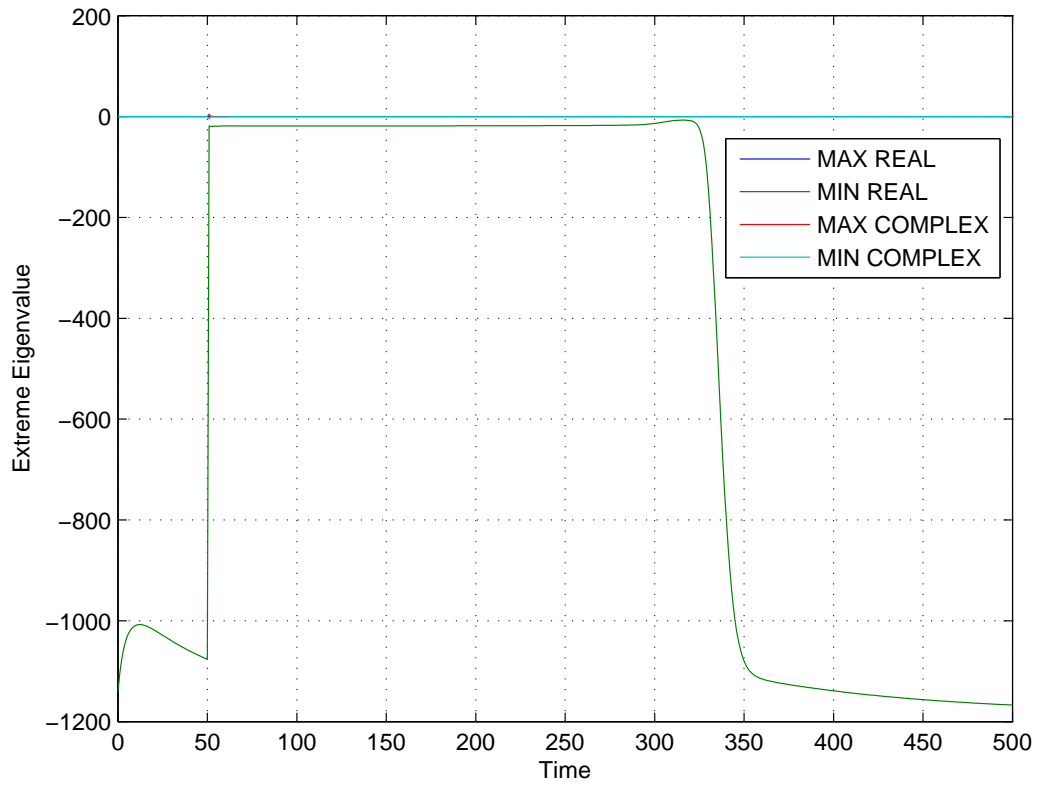


Figure 105: Extreme values of eigenvalues over time in the model of Ten Tusscher et al. (2004) (Endocardial variant)

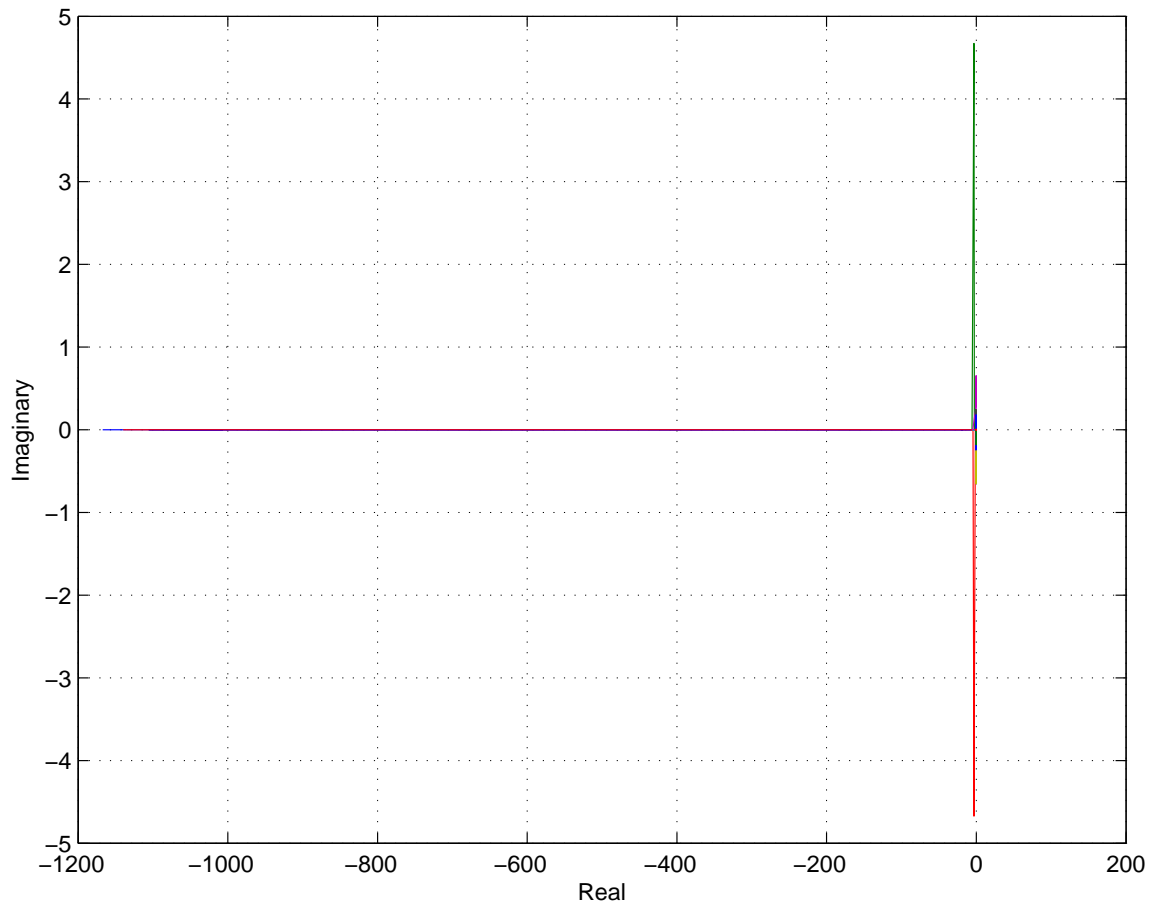


Figure 106: Plot of all eigenvalues at all times measured in the model of Ten Tusscher et al. (2004) (Endocardial variant)

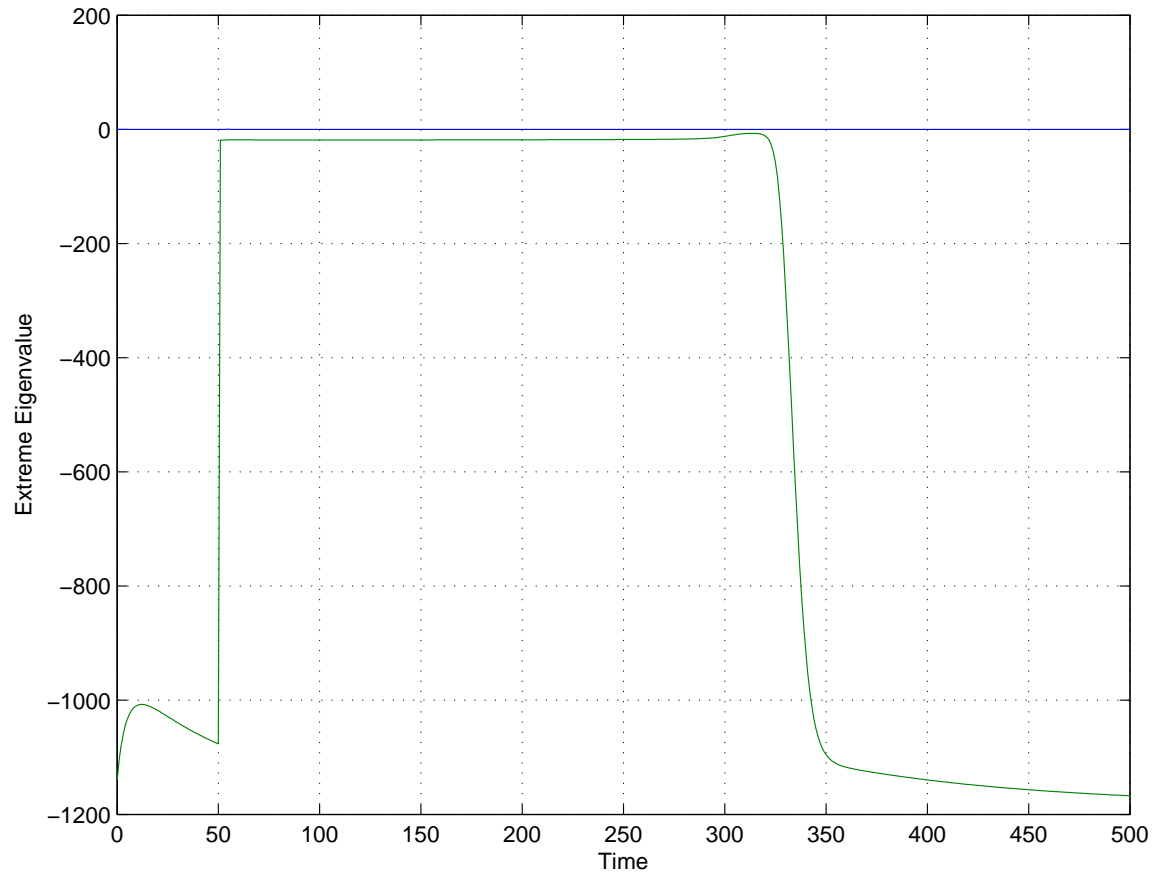


Figure 107: Extreme real eigenvalues in the model of Ten Tusscher et al. (2004) (Epicardial variant).

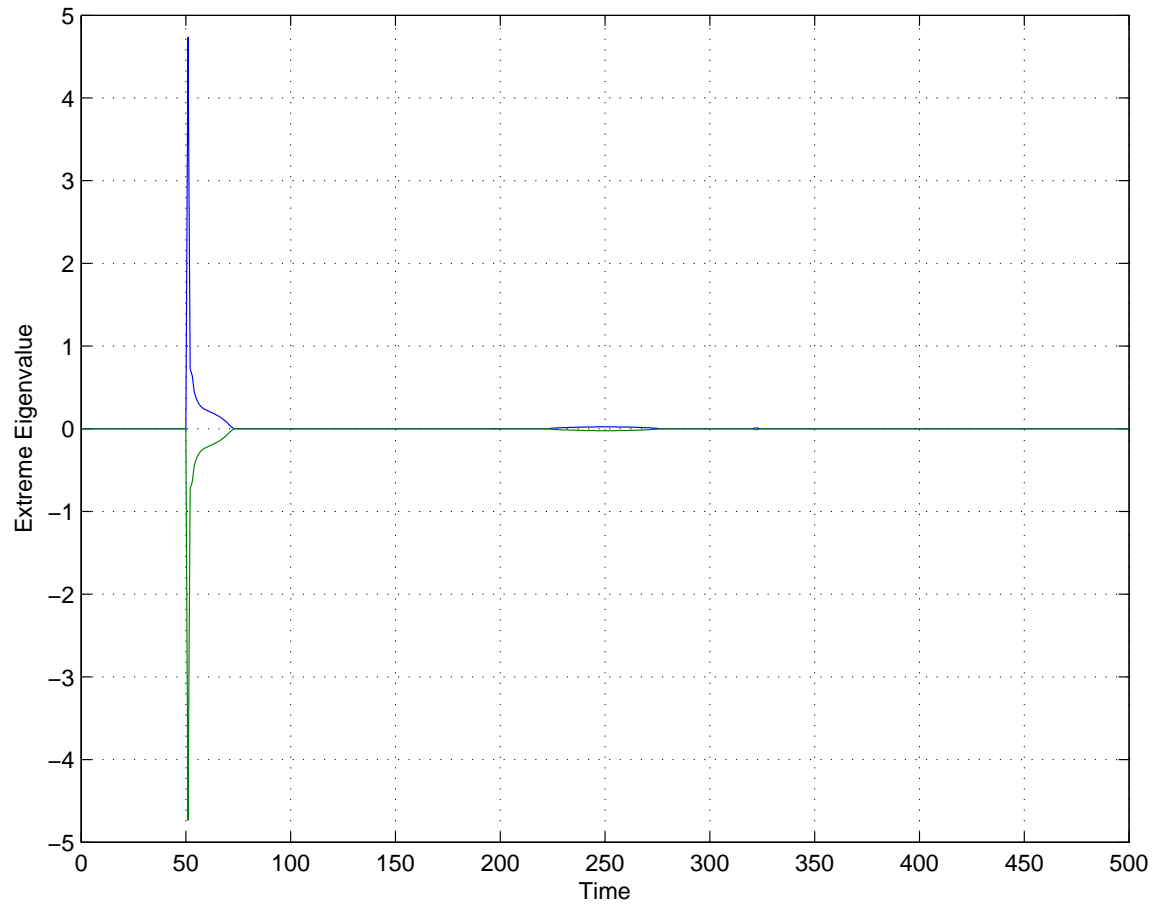


Figure 108: Extreme imaginary eigenvalues in the model of Ten Tusscher et al. (2004) (Epicardial variant).

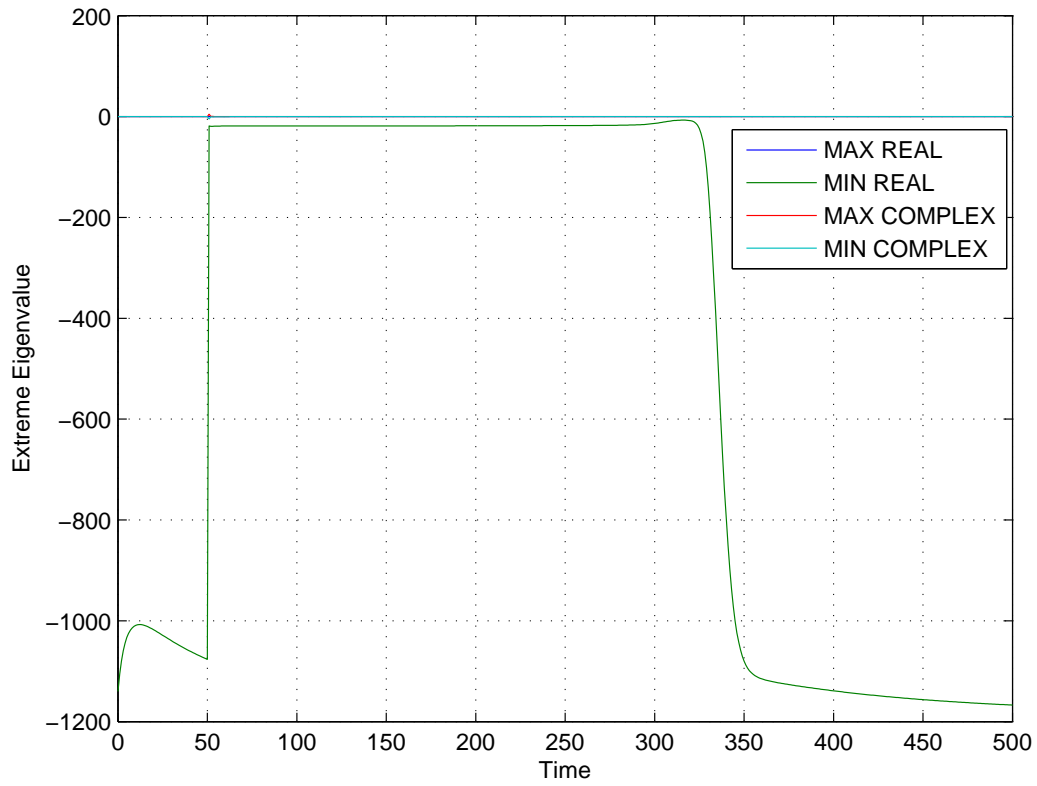


Figure 109: Extreme values of eigenvalues over time in the model of Ten Tusscher et al. (2004) (Epicardial variant).

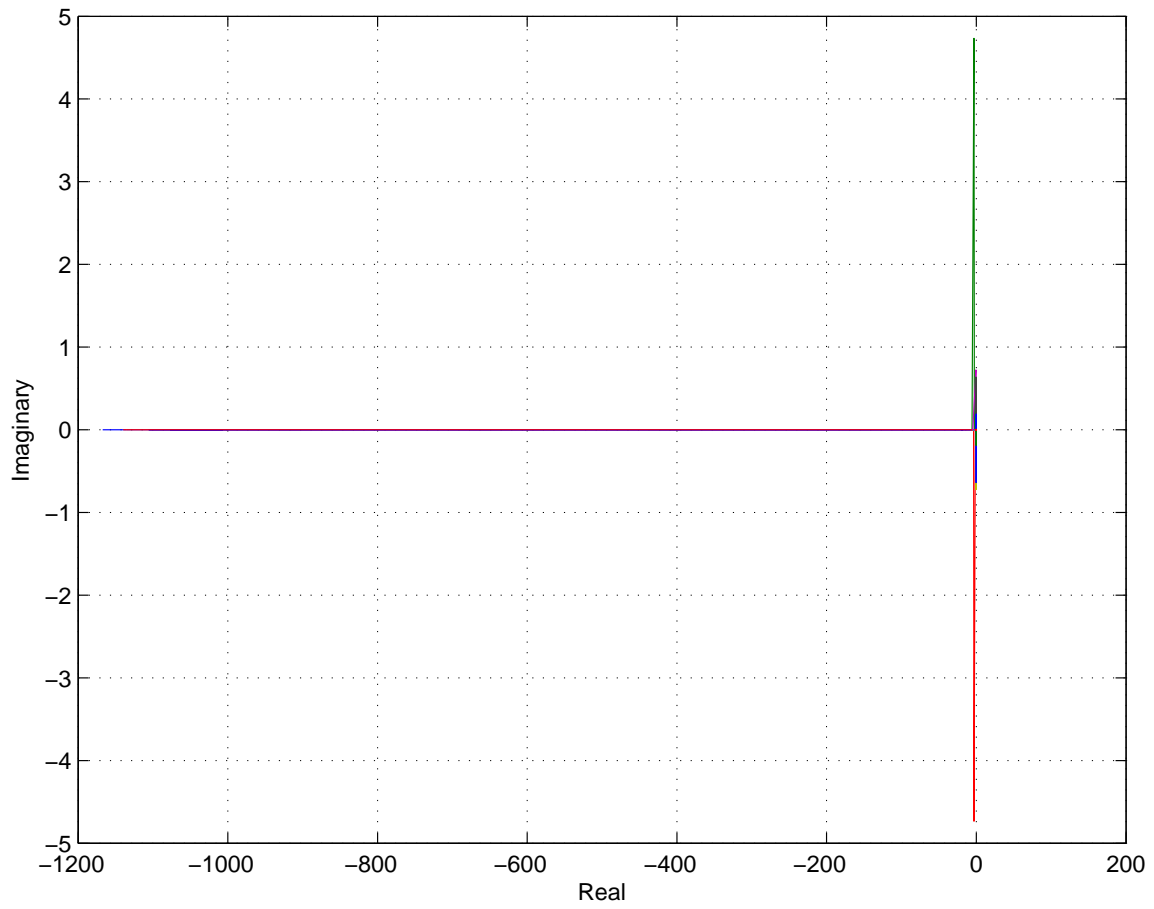


Figure 110: Plot of all eigenvalues at all times measured in the model of Ten Tusscher et al. Epicardial (2004) model.

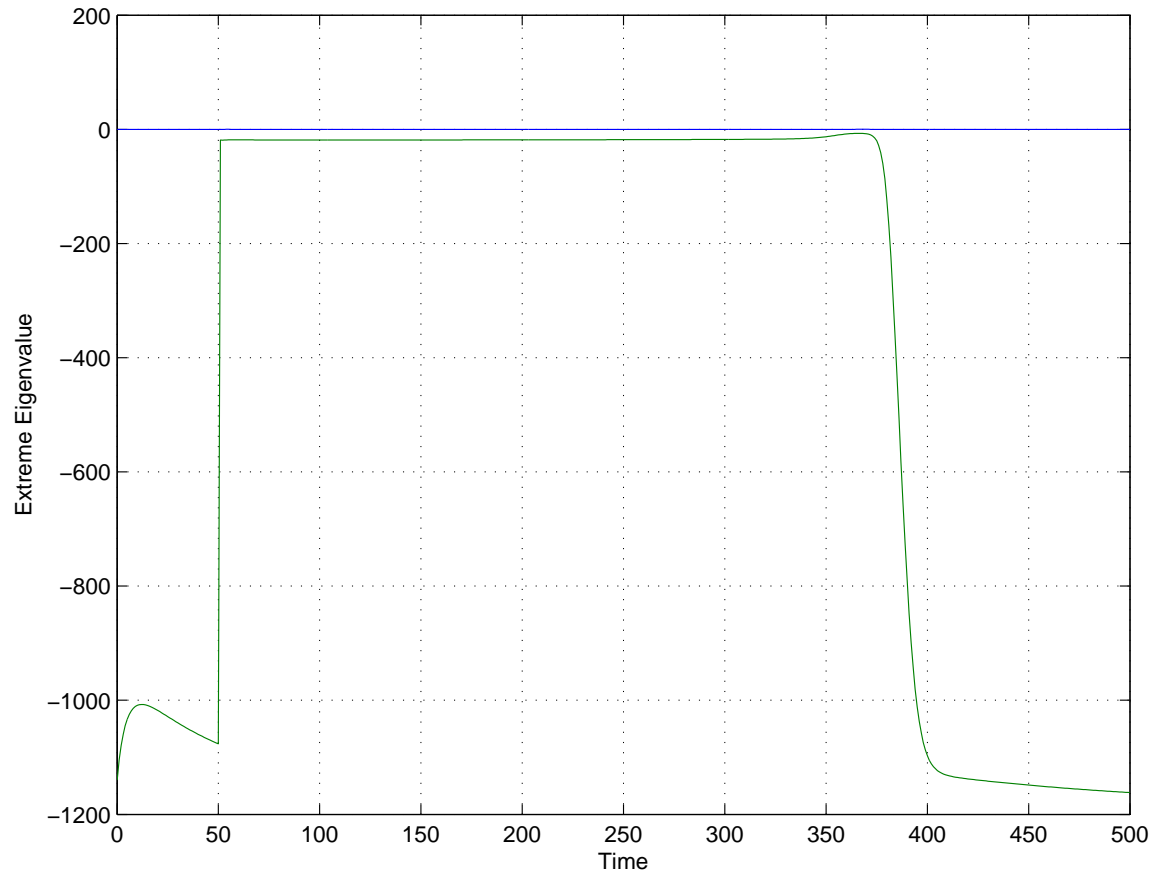


Figure 111: Extreme real eigenvalues in the model of Ten Tusscher et al. (2004) (M-cell variant).

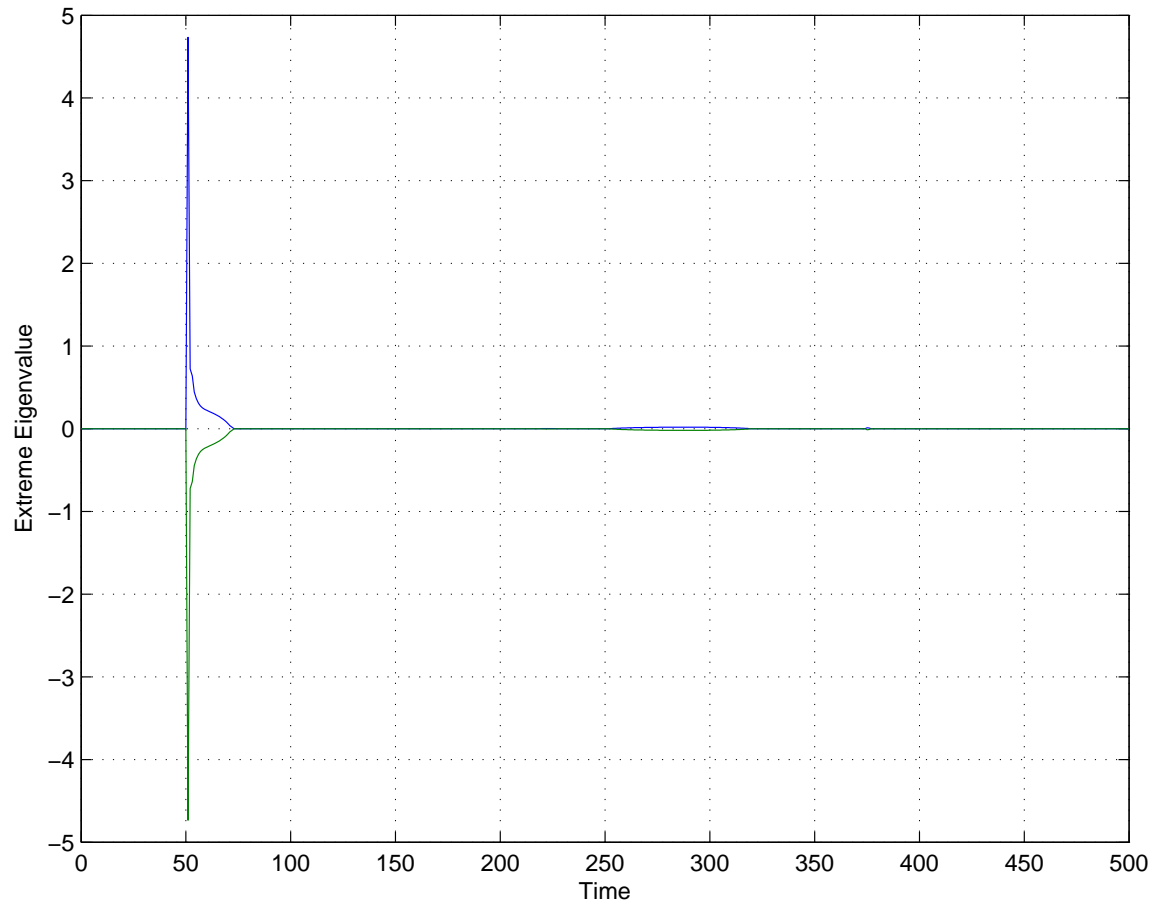


Figure 112: Extreme imaginary eigenvalues in the model of Ten Tusscher et al. (2004) (M-cell variant).

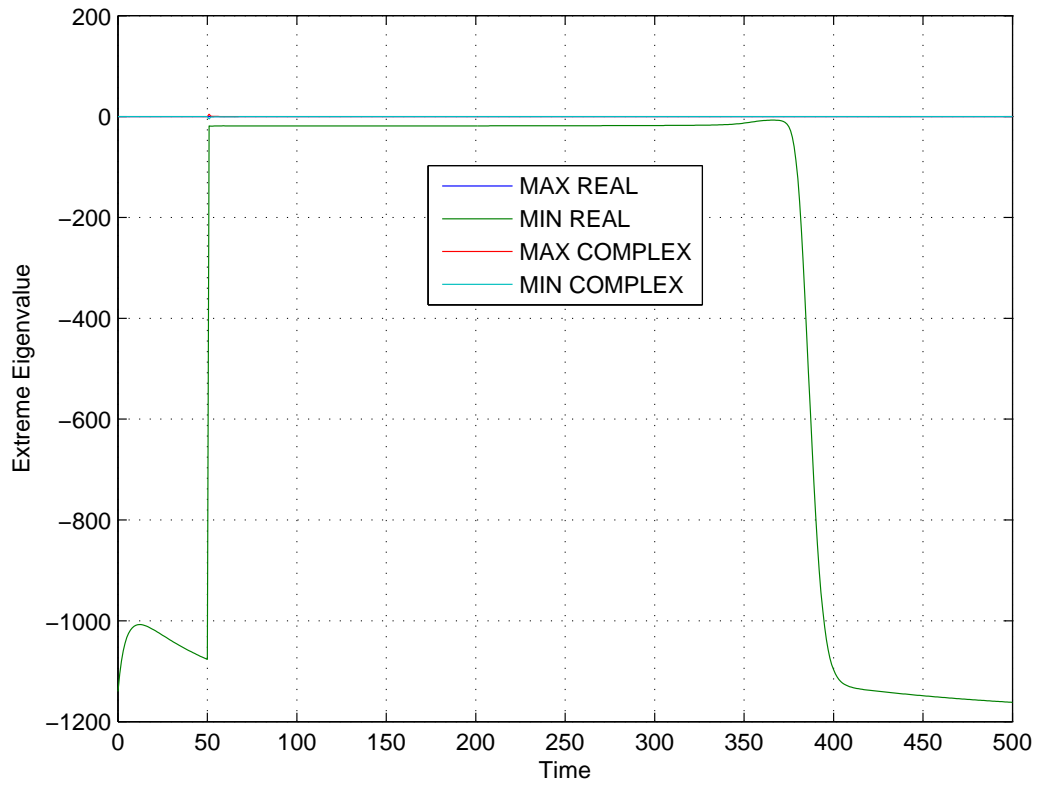


Figure 113: Extreme values of eigenvalues over time in the model of Ten Tusscher et al. (2004) (M-cell variant).

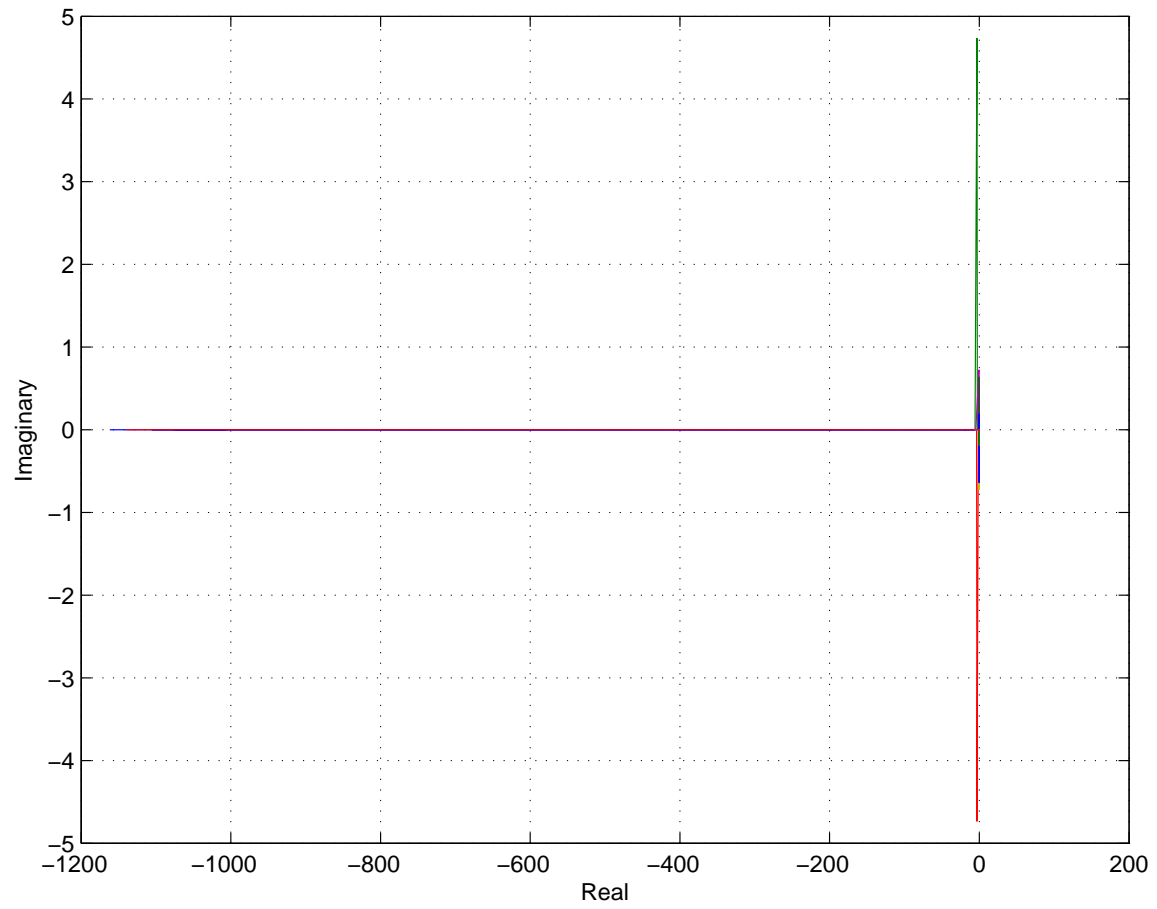


Figure 114: Plot of all eigenvalues at all times measured in the model of Ten Tusscher et al. (2004) (M-cell variant).

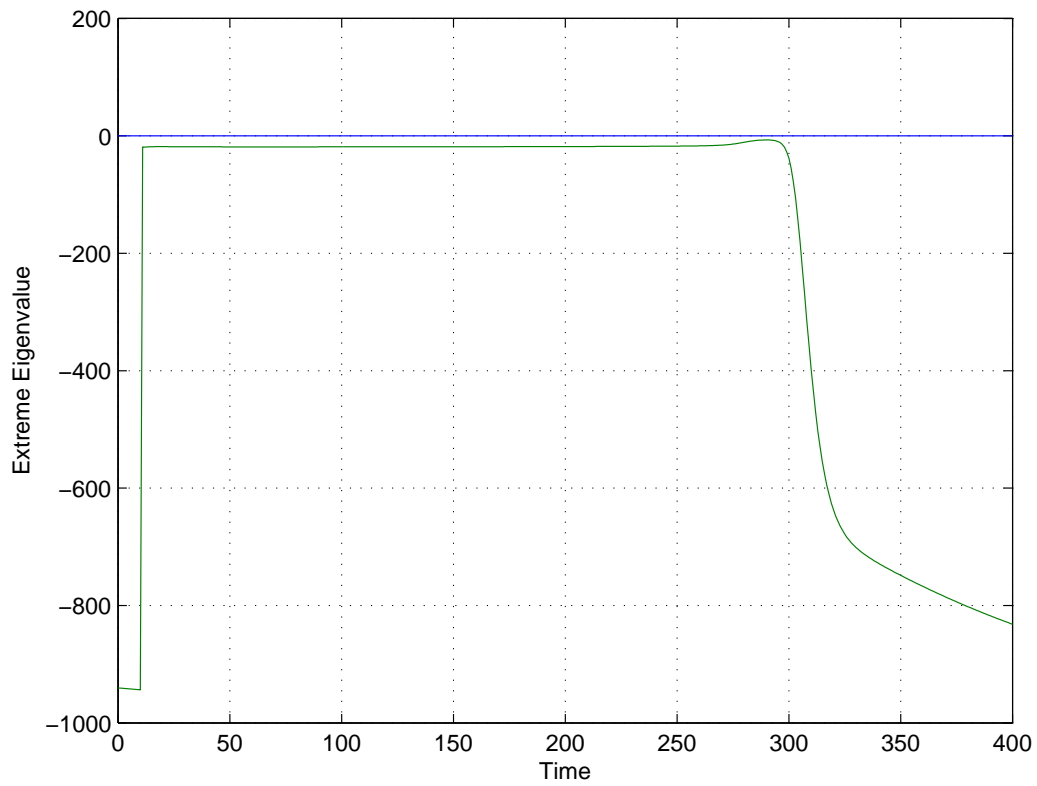


Figure 115: Extreme real eigenvalues in the model of Ten Tusscher et al. (2006) (Endocardial variant).

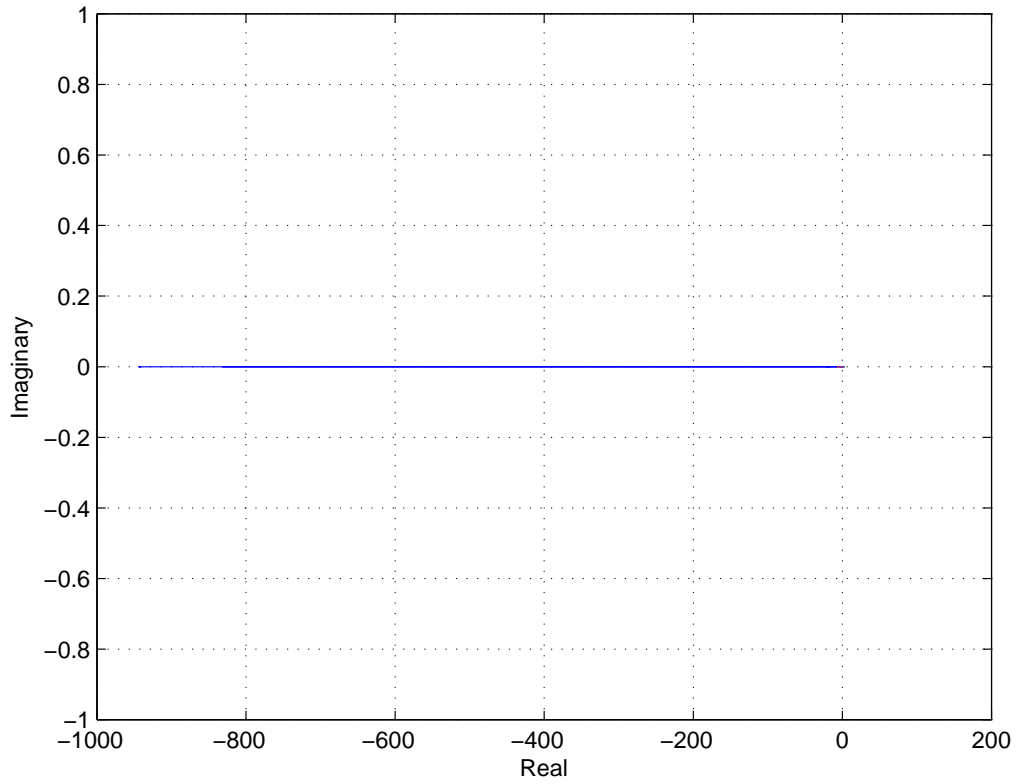


Figure 116: Plot of all eigenvalues at all times measured in the model of Ten Tusscher et al. (2006) (Endocardial variant).

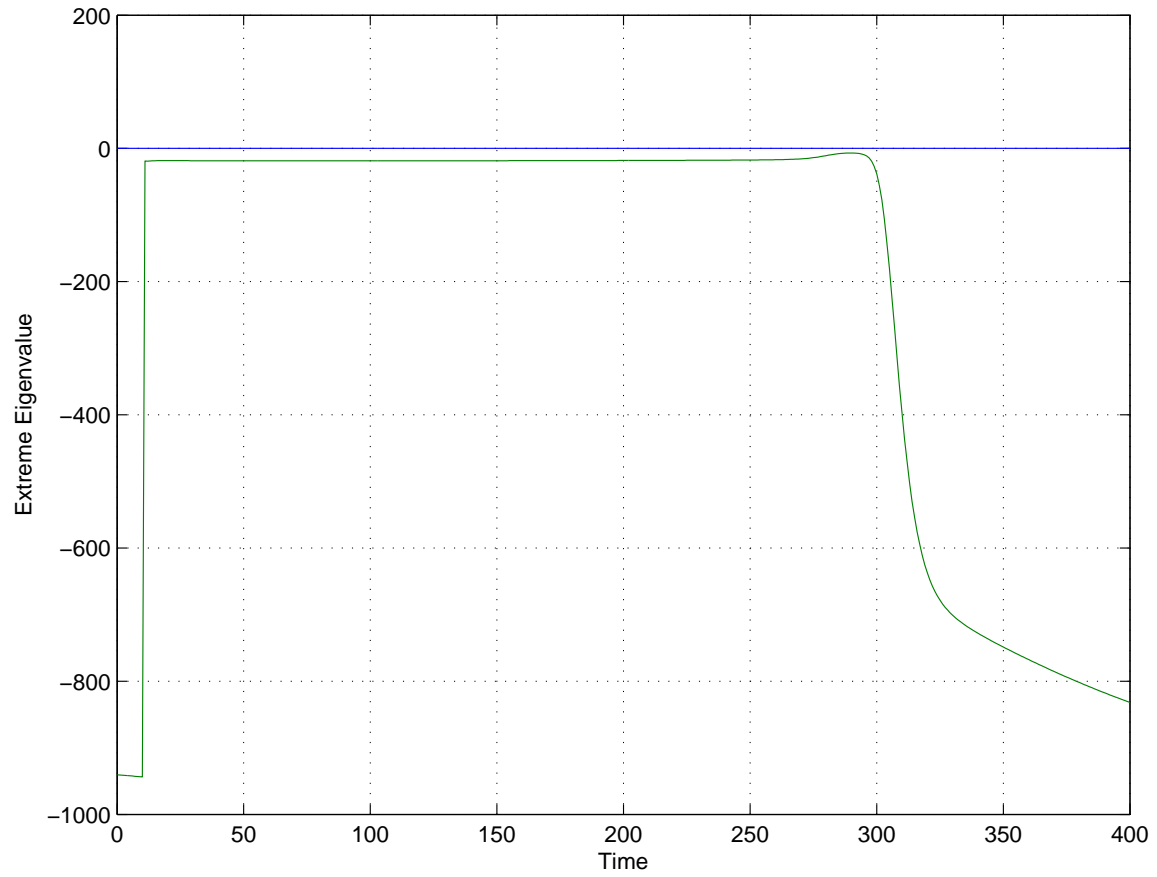


Figure 117: Extreme real eigenvalues in the model of Ten Tusscher et al. (2006) (Epicardial variant).

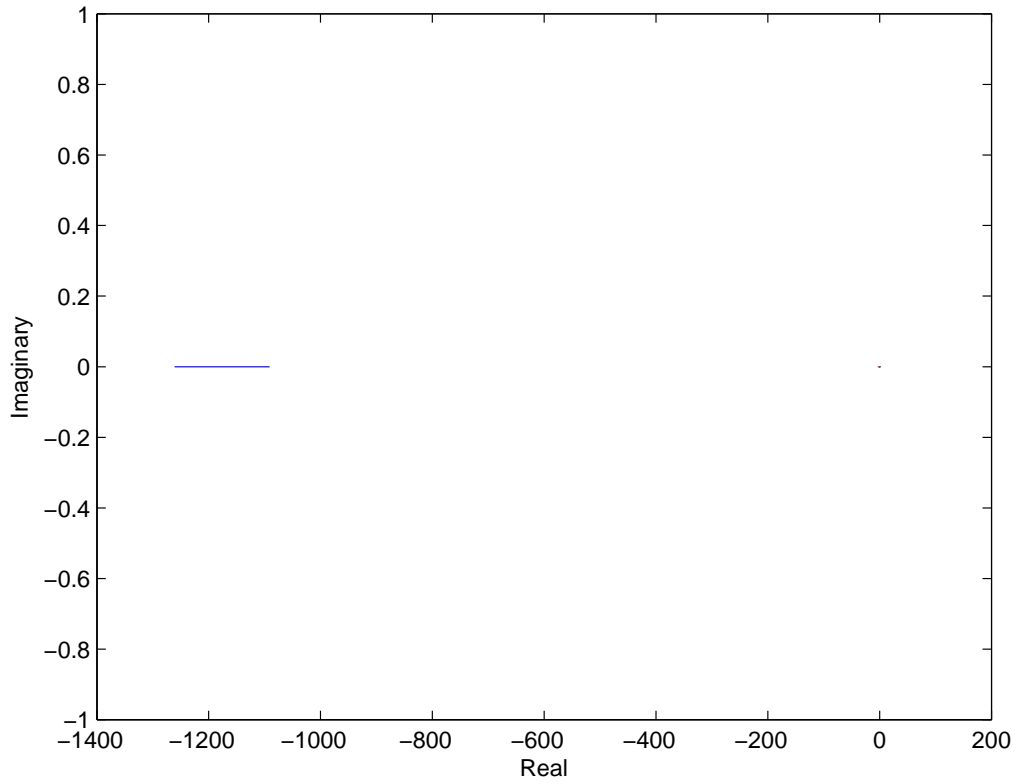


Figure 118: Plot of all eigenvalues at all times measured in the model of Ten Tusscher et al. (2006) (Epicardial variant).

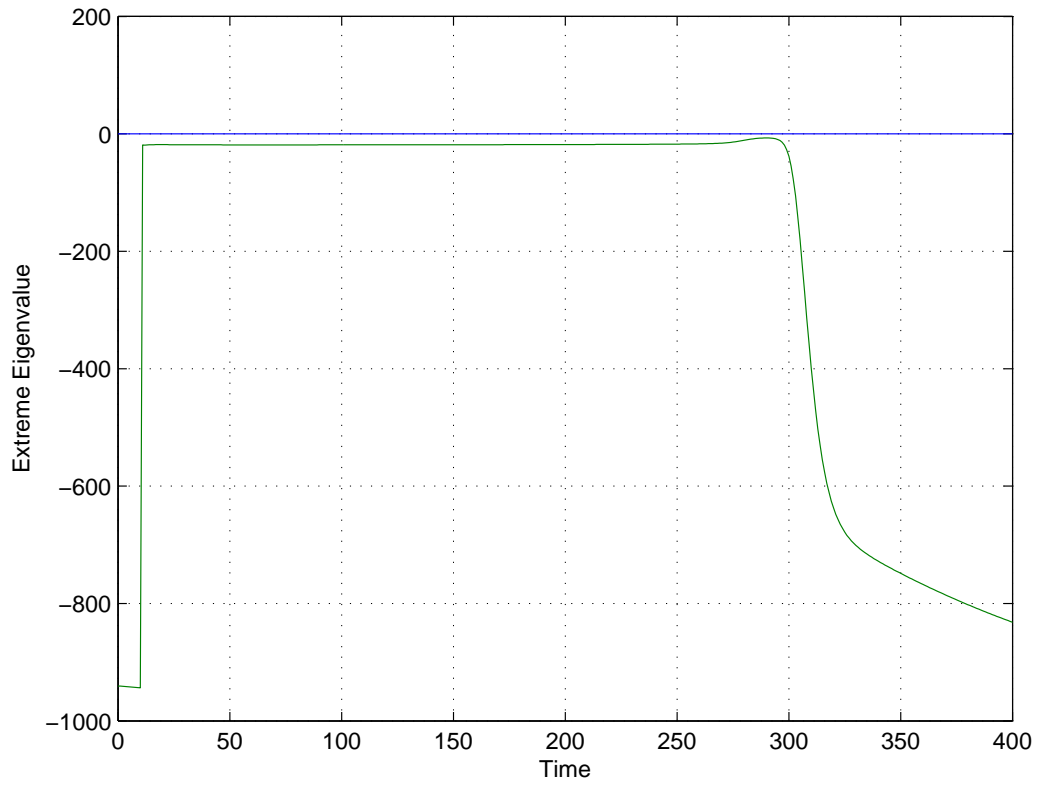


Figure 119: Extreme real eigenvalues in the model of Ten Tusscher et al. (2006) (M-cell variant).

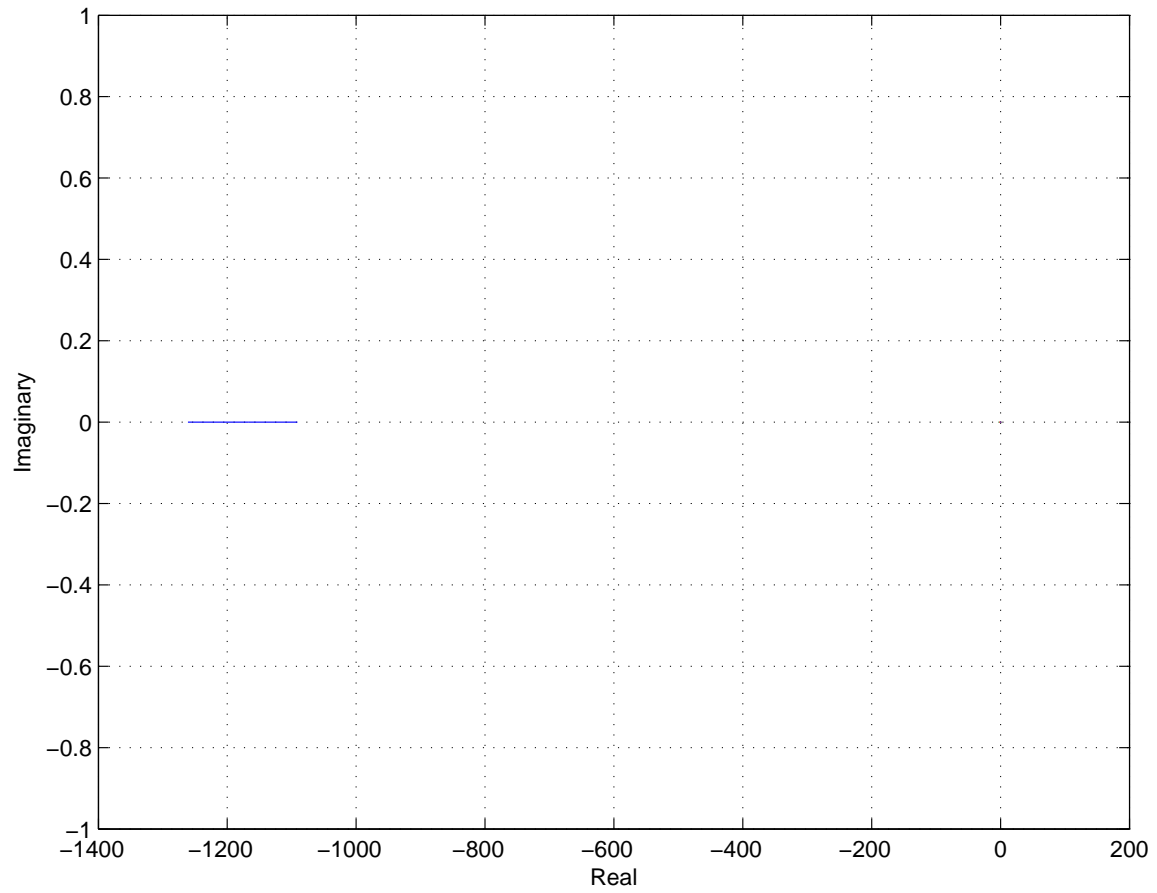


Figure 120: Plot of all eigenvalues at all times measured in the model of the model of Ten Tusscher et al. (2006) (M-cell variant).

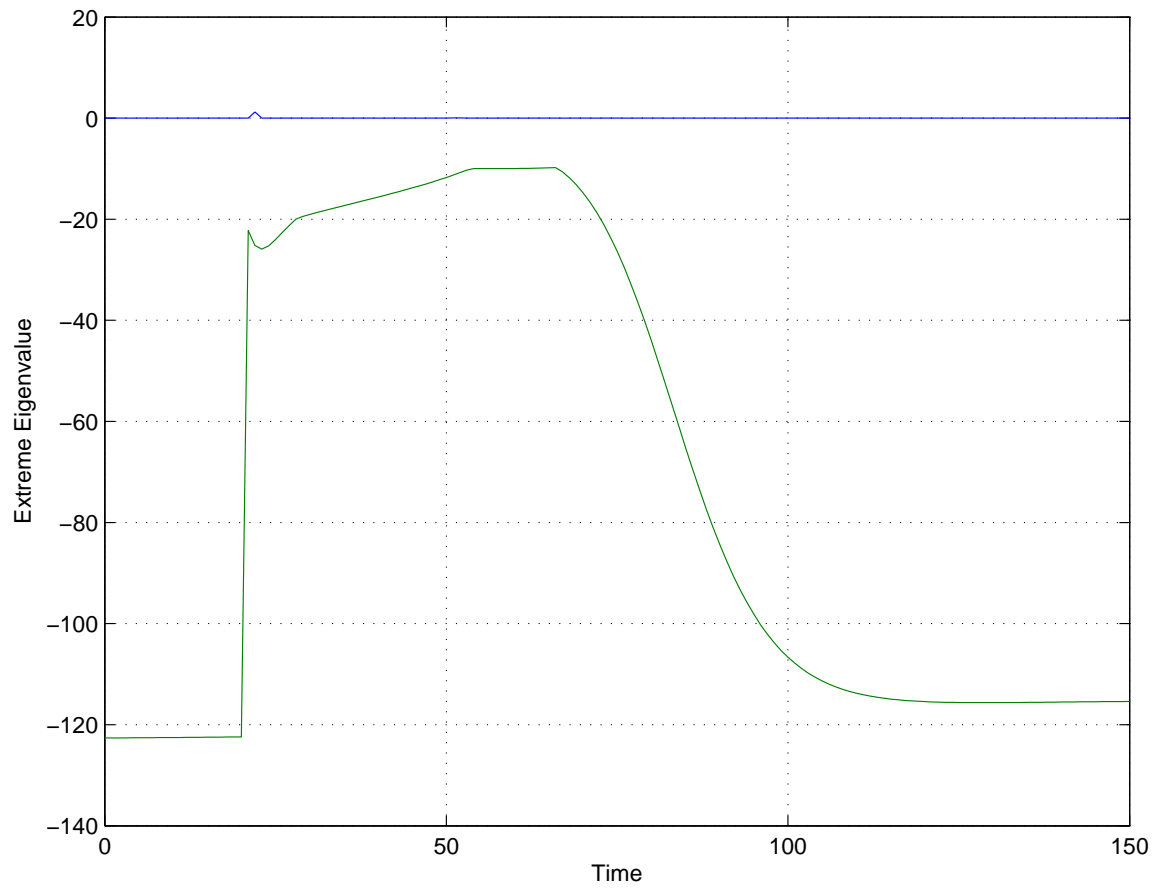


Figure 121: Extreme real eigenvalues in the Wang–Sobie model (2008).

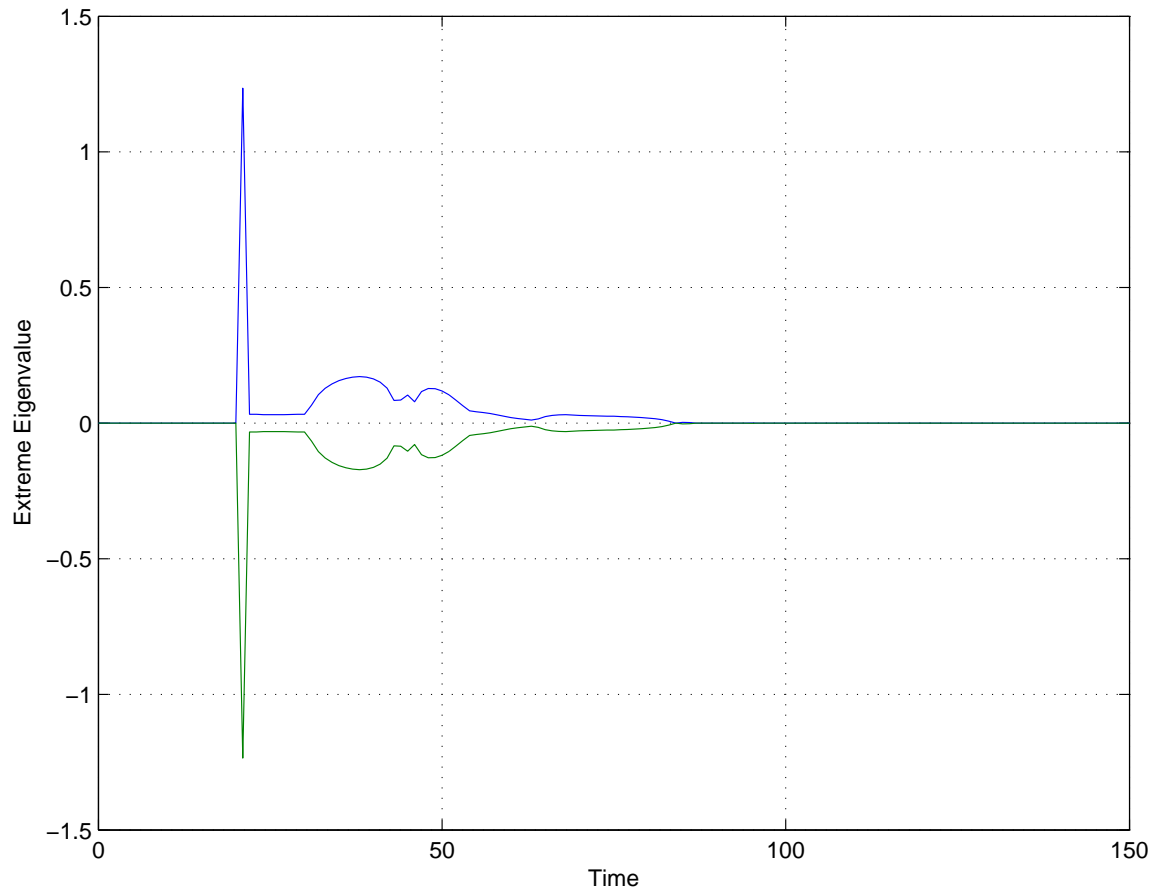


Figure 122: Extreme imaginary eigenvalues in the Wang–Sobie model (2008).

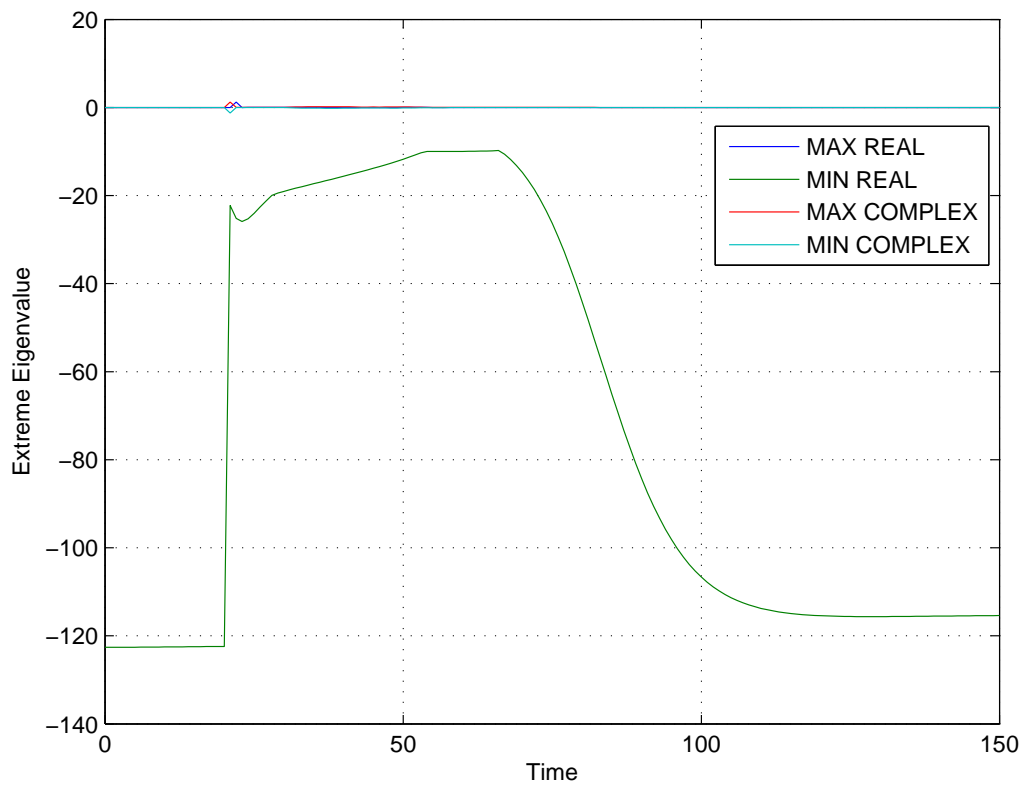


Figure 123: Extreme values of eigenvalues over time in the Wang-Sobie model (2008).

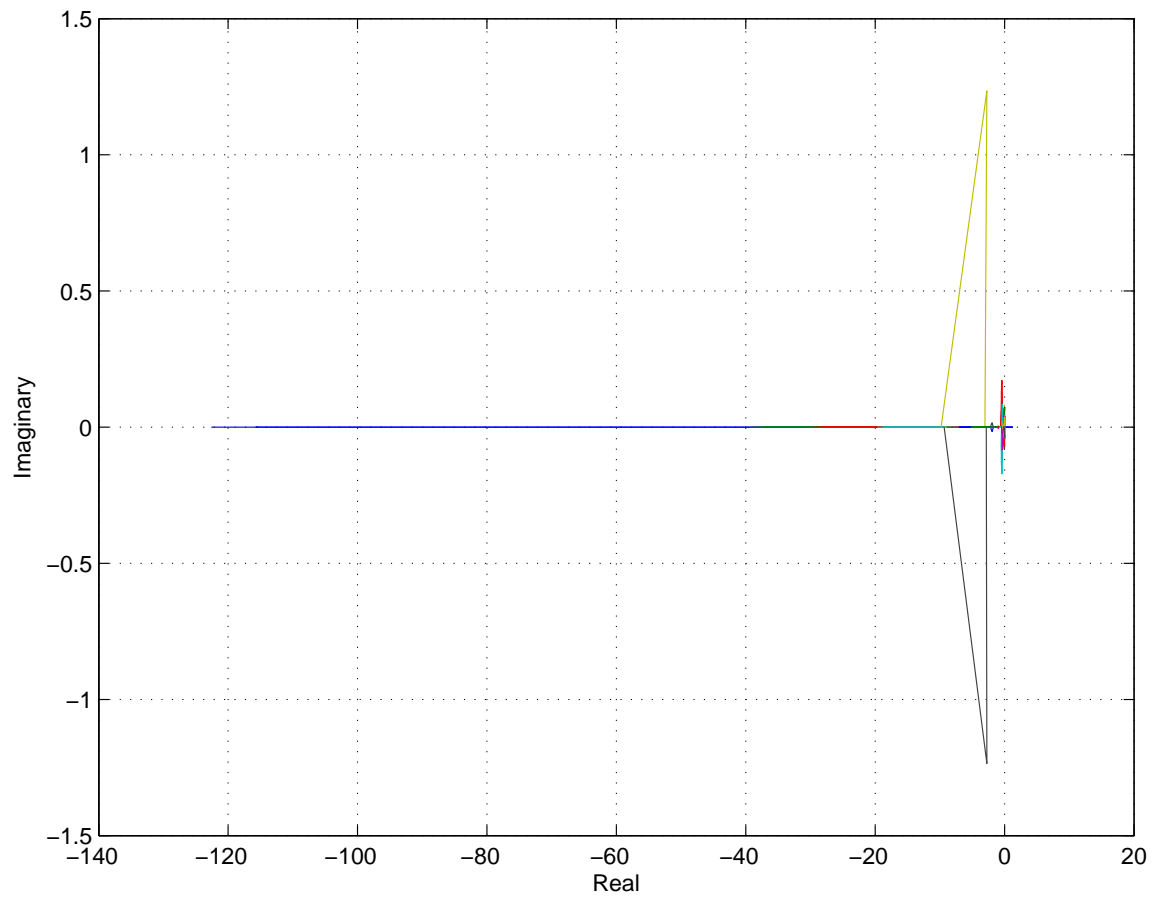


Figure 124: Plot of all eigenvalues at all times measured in the Wang–Sobie model (2008).

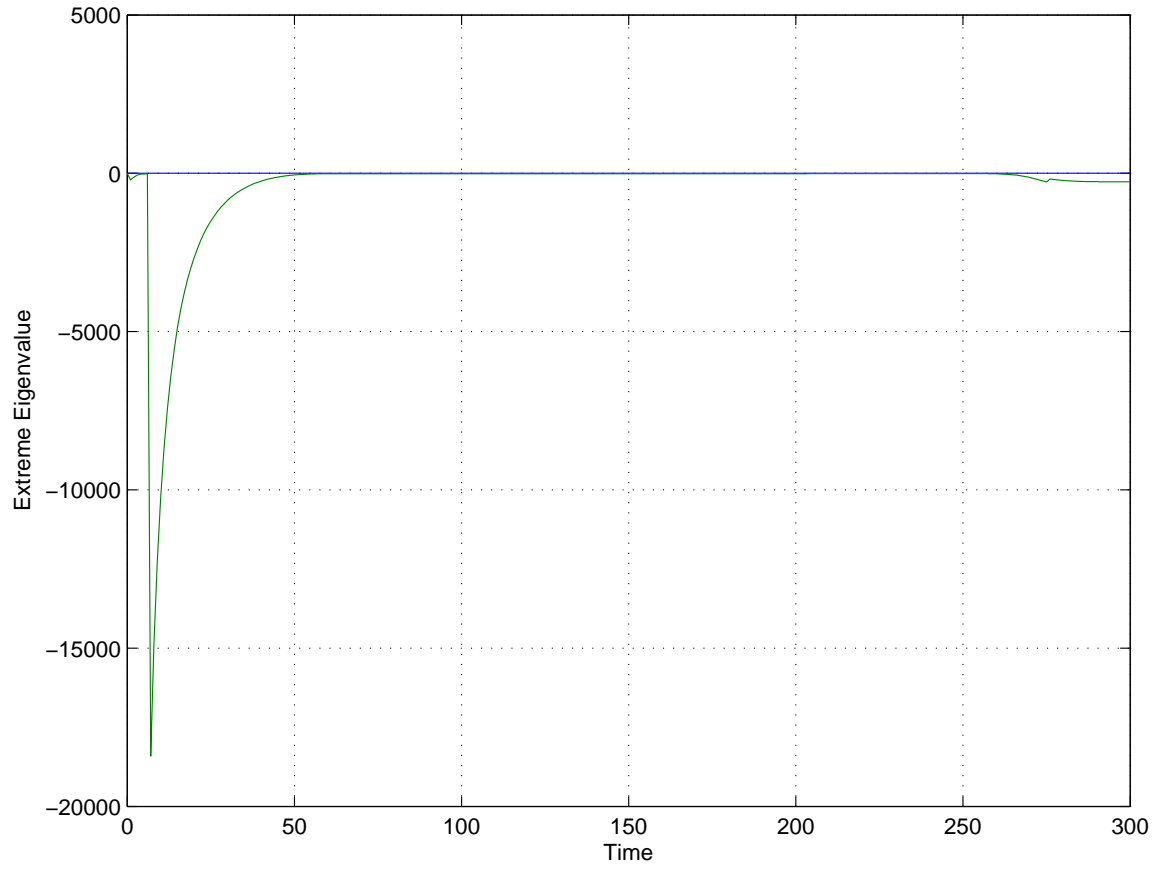


Figure 125: Extreme real eigenvalues in the model of Winslow et al. (1999).

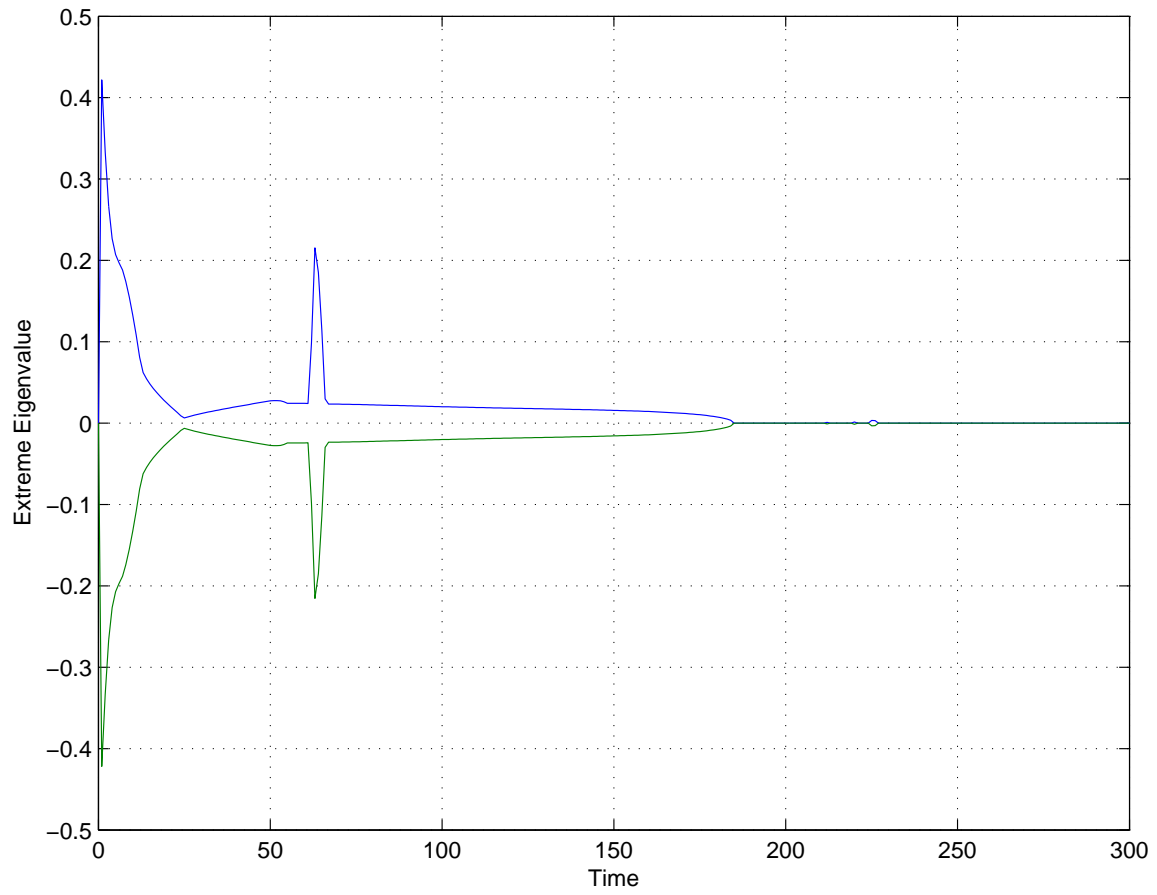


Figure 126: Extreme imaginary eigenvalues in the model of Winslow et al. (1999).

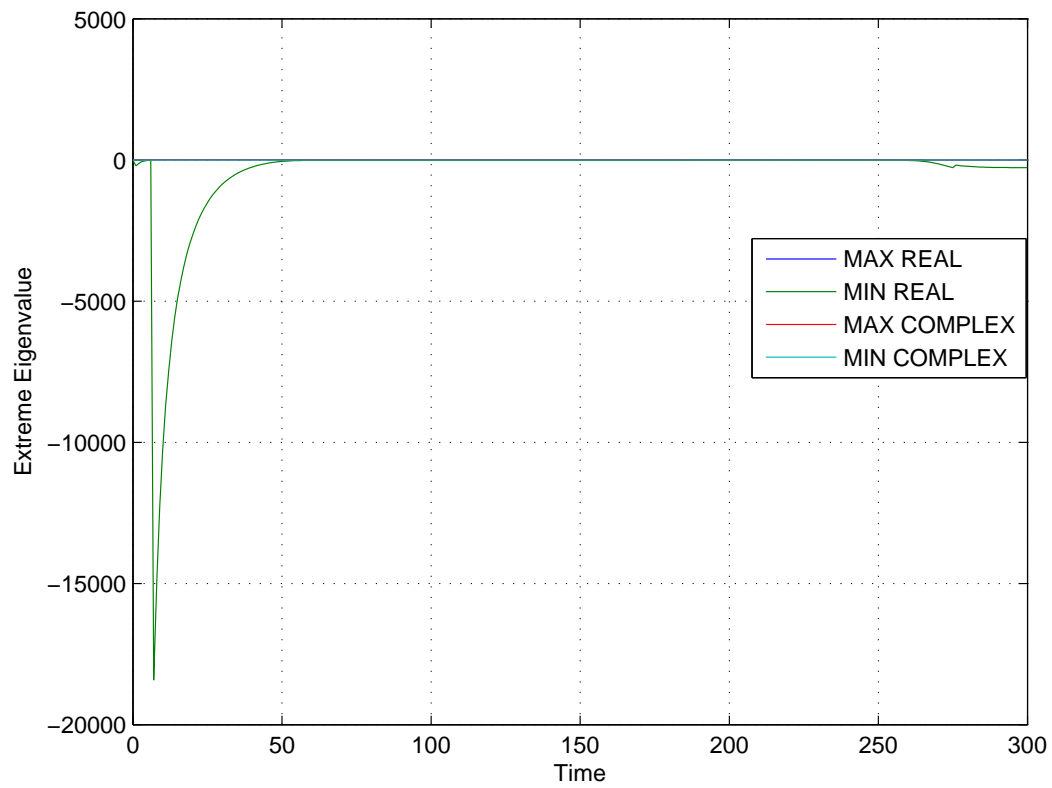


Figure 127: Extreme values of eigenvalues over time in the model of Winslow et al. (1999).

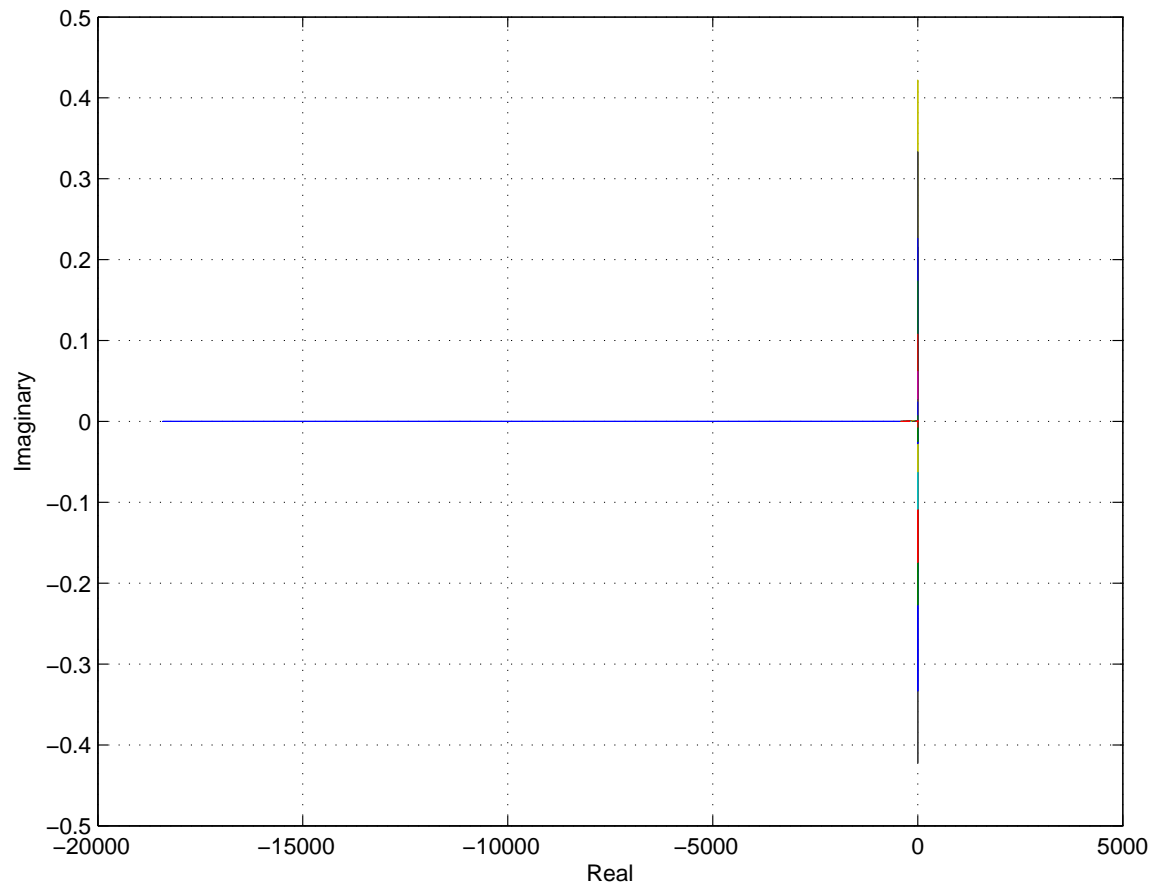


Figure 128: Plot of all eigenvalues at all times measured in the model of Winslow et al. (1999).

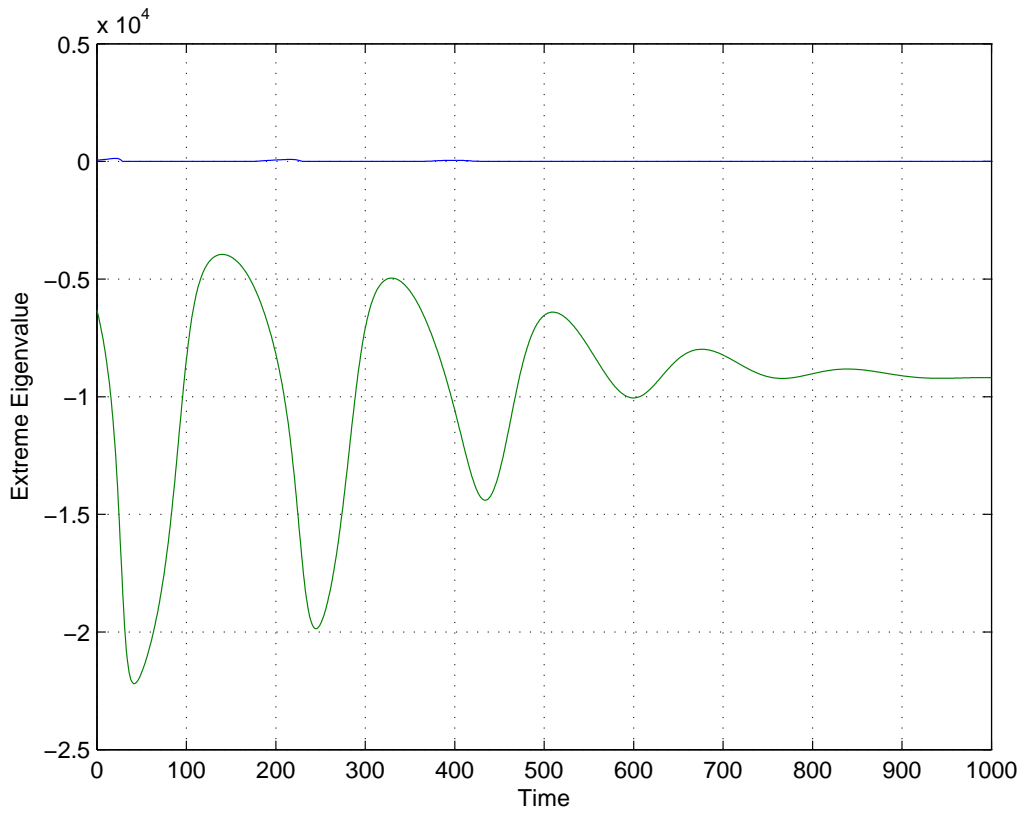


Figure 129: Extreme real eigenvalues in the model of Zhang et al. (2000).

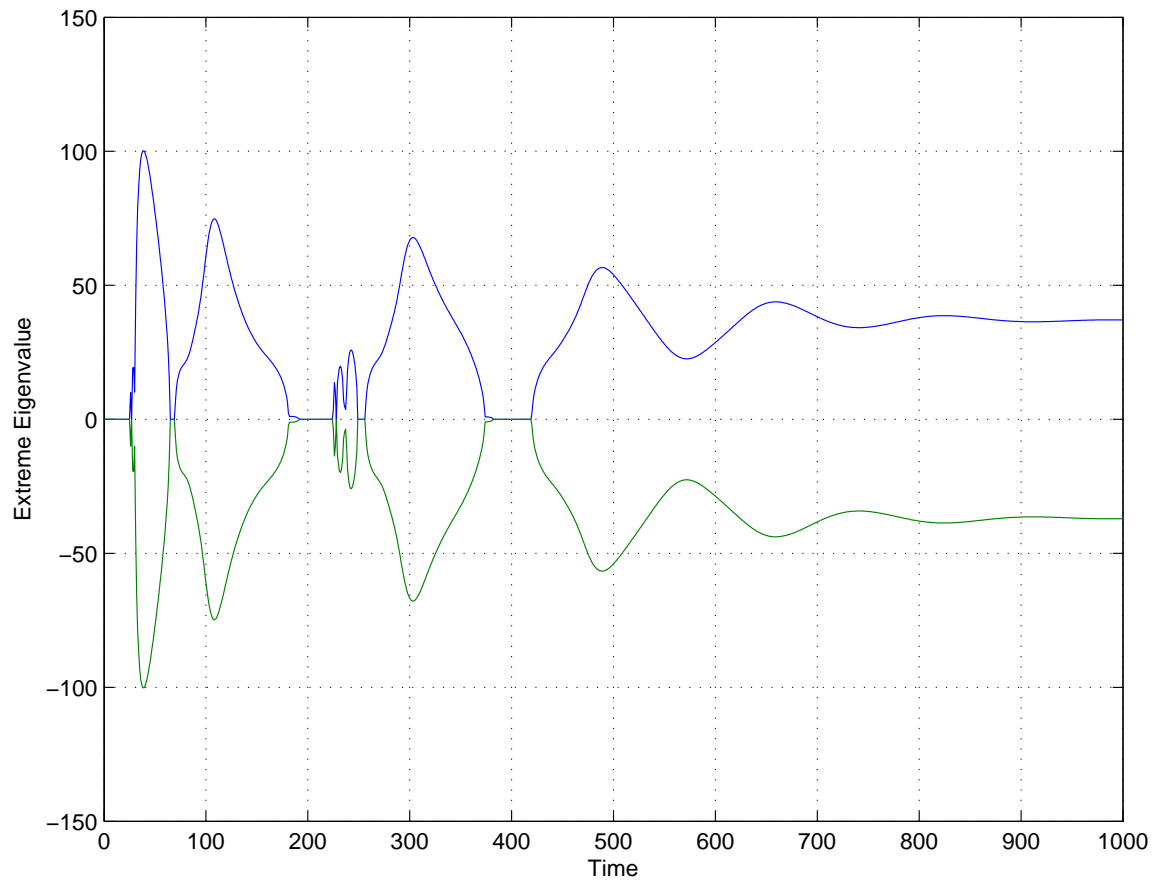


Figure 130: Extreme imaginary eigenvalues in the model of Zhang et al. (2000).

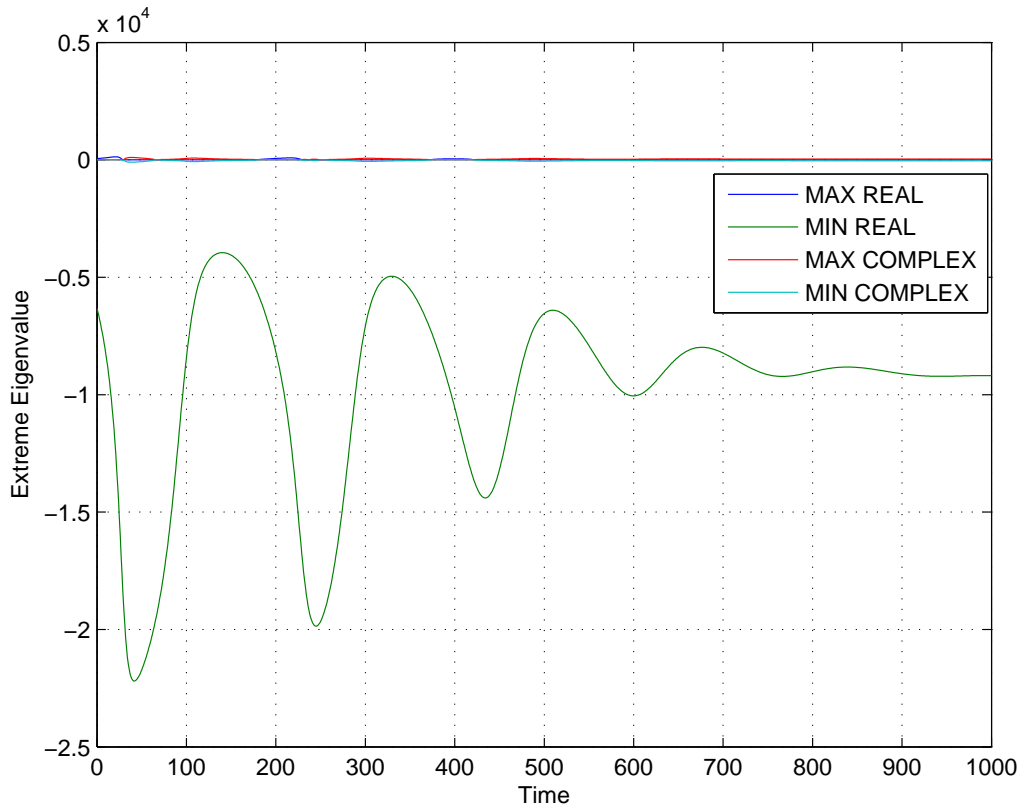


Figure 131: Extreme values of eigenvalues over time in the model of Zhang et al. (2000).

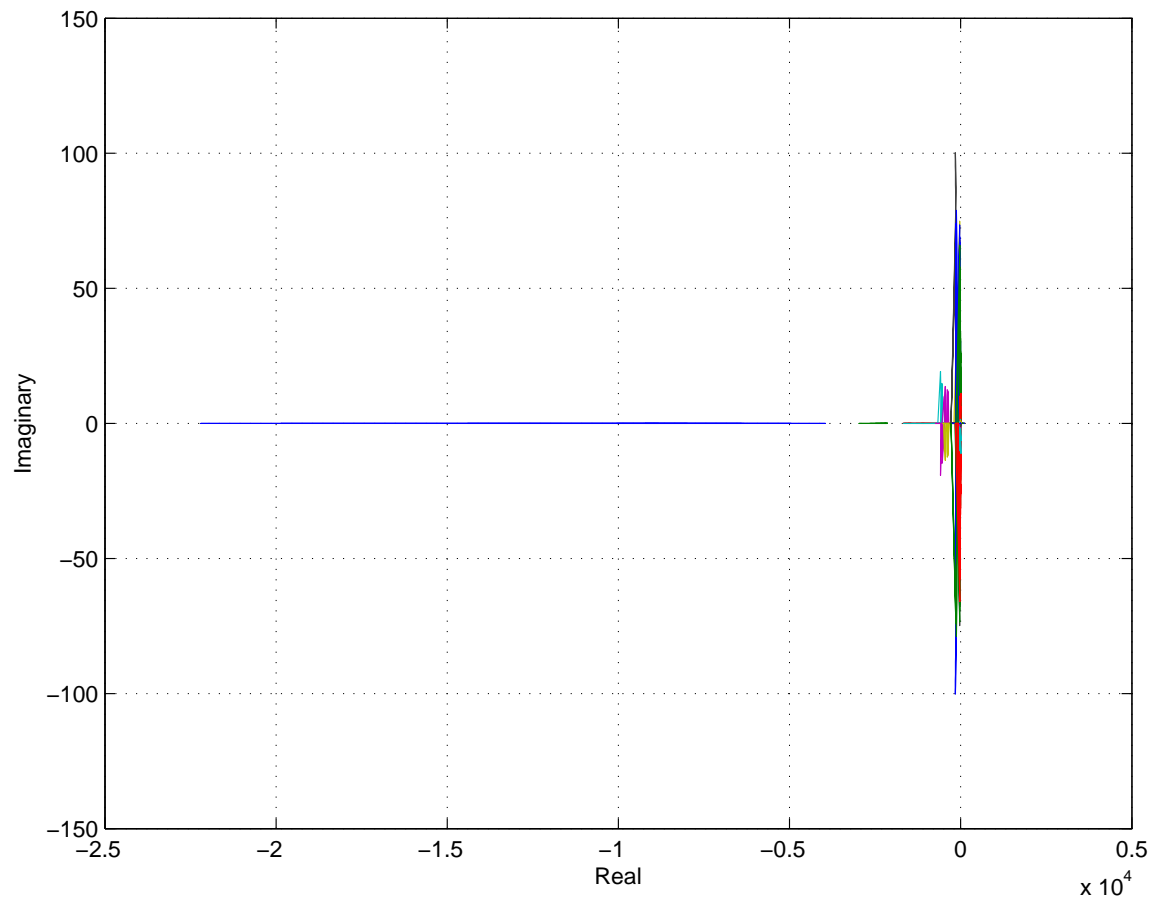


Figure 132: Plot of all eigenvalues at all times measured in the model of Zhang et al. (2000).